Dissertation zur Erlangung des Grades „Doktor der Naturwissenschaften“
am Fachbereich Chemie, Pharmazie und Geowissenschaften
der Johannes Gutenberg-Universität, Mainz
vorgelegt von
Dipl.-Chem. Karen Lienkamp
geboren in Freiburg im Breisgau

Synthesis and Characterization of Polyelectrolyte Brushes – Towards a Synthetic Model System for Human Cartilage

Contents

1. Motivation

1.1. Introduction

Self-organizing systems are ubiquitous in nature, the double-helix of DNA and the folding of protein structures being common examples. Another important example of self-organization in the human organism is the formation of proteoglycan aggregates with hyaluronic acid (Fig. 1.1.(left)[1]). These aggregates are found throughout all extracellular compartments. Specifically, tissues which are subject to constant mechanical strain, e.g. cartilage, contain large amounts. Being extremely resistant to mechanical impacts, these tissues are at the same time highly flexible. The most abundant proteoglycan-hyaluronic acid aggregate found in nature is the aggrecan-hyaluronic acid aggregate. Aggrecan is a linear polypeptide chain carrying a large number of anionic polysaccharide side chains, thus forming an anionic polymer brush. In living organisms, aggrecan and hyaluronic acid are synthesized separately in specialized cells of the cartilage and released into the extracellular compartment, where about 100 aggrecan molecules self-assemble with one hyaluronic acid molecule. The linker between aggrecan and hyaluronic acid is a positively charged, claw-shaped protein, which is covalently attached to the aggrecan molecule. Thus the whole aggregate is held together by electrostatic interaction of the positive link and the negatively charged hyaluronic acid[1, 2].

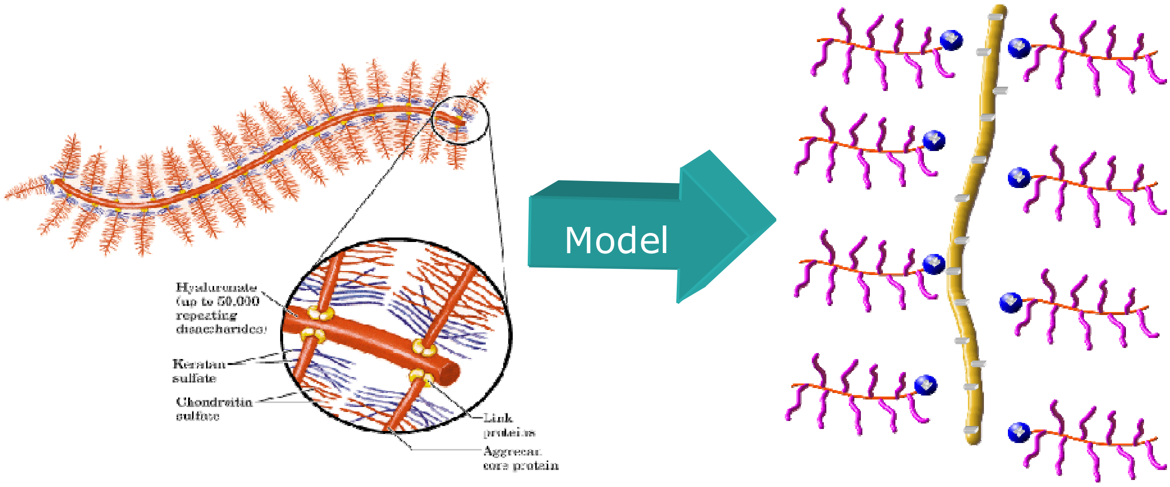

Fig. 1.1.: Cartoon representation of the proteoglycan-hyaluronic acid aggregates[1] in human cartilage (left) and a simplified synthetic model system for this structure (right)

In order to understand the unusual mechanical properties of these aggregates, which act as biological lubricants, and to mirror them in synthetic products, the aim of this work is to produce model compounds for the proteoglycan-hyaluronic acid complex (see Fig. 1.1.).

1.2. Objective

As a model for the proteoglycan, anionic polyelectrolyte brushes from poly(styrene sulfonic acid) will be synthesized (Fig. 1.2., left). This monomer has been chosen to imitate the polyelectrolyte properties of the original proteoglycan molecule. Their solution structure and aggregation behavior will be investigated. Ultimately, it is to be attempted to end-functionalize the polyelectrolyte brush with a positively charged linker (Fig. 1.1., right) and complex the resulting structure to negatively charged objects. The structure of these materials would be investigated by microscopic methods (TEM, SEM, AFM) and scattering techniques (static and dynamic light scattering, neutron scattering).

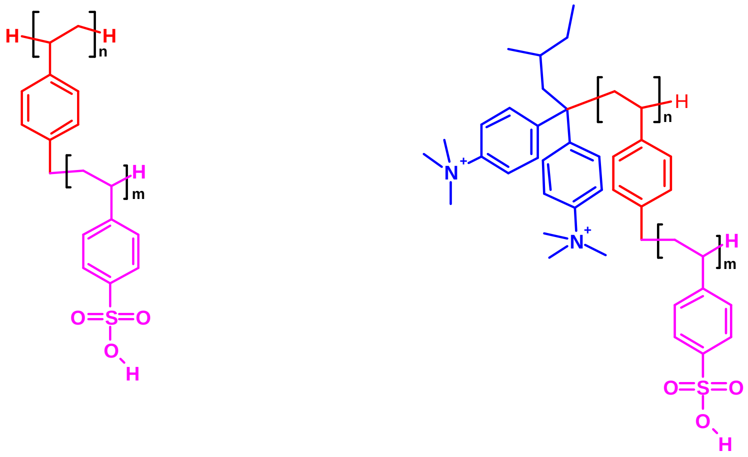

Fig. 1.2.: Target structure, unfunctionalized (left) and functionalized (right)

2. Polymerization Methods

2.1. *General Comments*

The literature available suggests for styrene-type monomers used in this work that polymerization by radicals (free and controlled), living anionic polymerization and cationic polymerization is possible. For the macromonomer polymerization, Suzuki polycondensation is a promising method. The advantages and disadvantages of these methods and their relevance for this work are discussed in the following sections.

2.2. *Free Radical Polymerization*

Free radical polymerization is by far the easiest polymerization method, as it does not demand for extreme monomer or solvent purity, tolerating even water as an impurity as well as many functional groups. Oxygen is to be excluded. In spite of this drawback, radical polymerization is widely used in industry. Its disadvantage is the lack of precise control over the reaction products, resulting in a broad molar mass distribution. This is due to the fact that radicals are highly reactive and unselective intermediates and suffer from termination reactions in a statistical fashion. Free radical polymerization consists of three basic mechanistic steps: initiation, propagation and termination. Further reaction steps such as inhibition and chain transfer complicate this simple picture. In the initiation step, a suitable initiator radical attacks the double bond of a vinyl monomer, resulting in a chain radical, as shown in Fig. 2.2.1..

The initiator radical can be generated by decomposition of a molecule containing a thermally labile bond. Other possibilities include photolytic cleavage, redox reactions or high energy radiation. In the propagation step, monomer molecules repeatedly react with the chain end radical, forming a linear polymer. Further reaction channels, e.g. termination reactions, limit the chain length of such a polymer. These include disproportionation of two radicals into an alkane and an alkene terminated macromolecule, as well as recombination of two radicals. The preferred termination step depends on the monomer and temperature. From the rate laws for these three reaction steps and application of the steady-state hypothesis for the concentration of radicals, the following overall polymerization rate can be derived:

$$v_p = k_p \cdot \sqrt{\frac{f \cdot [I] \cdot k_d}{k_t}} \cdot [M]$$

v_p = polymerization rate
k_i = reaction step rate constant
$[I]$ = initiator concentration
$[M]$ = monomer concentration
f = initiator efficiency

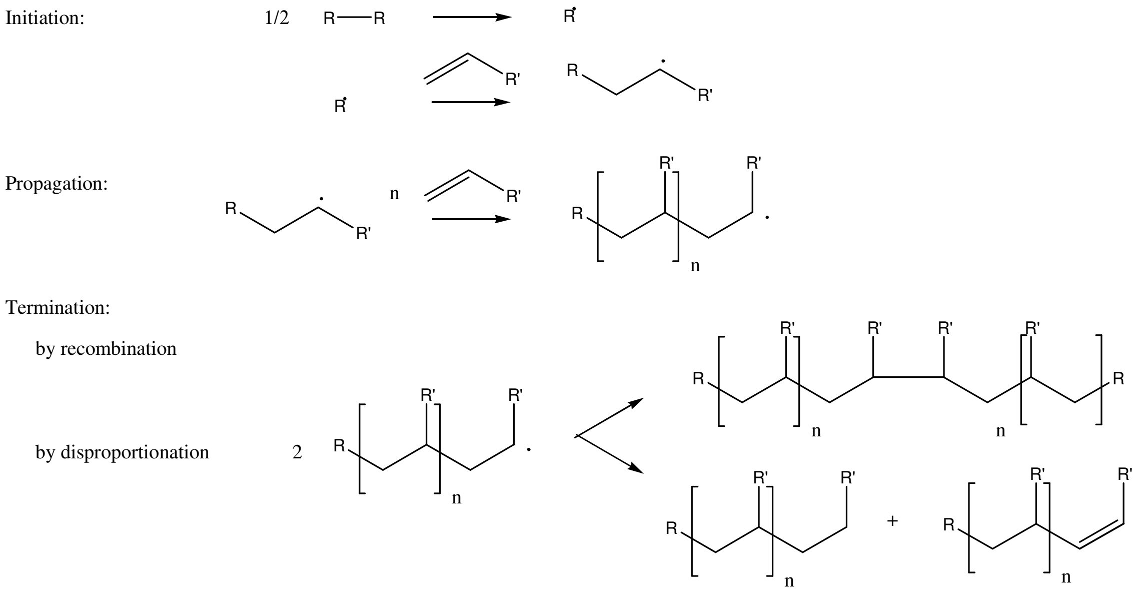

Fig. 2.2.1.: Mechanistic steps in free radical polymerization

As can be seen from this equation, the reaction rate is proportional to the monomer concentration and the square route of the initiator concentration, i.e. it can be manipulated by the variation of these parameters. The other parameters are intrinsic properties of the system and depend via the Arrhenius equation on temperature only. The kinetic chain length v is a measure of the average number of monomer units that react with the active chain end during its lifetime. It can be shown that

$$v = \frac{v_p}{v_i} = \frac{k_p^2 \cdot [M]^2}{2 \cdot k_t \cdot v_p}$$

As v is inversely proportional to the polymerization rate, an increase in v_p by raising the temperature results in a reduction of the kinetic chain length. Depending on the termination step, v is related to the number average degree of polymerization, x_n, by $2v \leq x_n \leq v$. For pure recombination, $x_n = 2v$, and for pure termination by disproportionation, $x_n = v$.[3] As mentioned above, chain transfer and inhibition steps complicate the simplified picture presented here. Chain transfer works as follows: on collision of the reactive species with another molecule (solvent, impurities, monomers, polymer chain etc.), the radical chain is able to extract an atom, most commonly an H atom, from the collision partner, thus transferring the radical onto it. Consequently, the chain is terminated, and the newly formed radical may initiate a new chain. This process limits the chain length, which can be exploited by deliberately adding a 'moderator' to the reaction mixture, which contains a weakly bonded atom and thus allows molar mass control by chain transfer. As to inhibition, reaction of the initiator with an inhibitor molecule leads to the formation of a more stable, i.e. less reactive radical. This influences initiation rate and thus the overall reaction kinetics. Due to the chain transfer and crosslinking, the synthesis of well-defined functionalized polymers with defined architecture by radical polymerization is not possible. It will be therefore not considered further.

2.3. Controlled Radical Polymerization

2.3.1. General Comments

Controlled radical polymerization techniques provide better control over the molar mass distribution. The key idea of controlled radical polymerization is to direct the reaction by lowering the radical concentration in the reaction mixture. Thus disproportionation and recombination as well as other side reactions discussed in section 2.2. can be suppressed, i.e. the kinetic chain lengths are increased. The concept of controlled radical polymerization includes an equilibrium between a so-called 'dormant' species (Fig. 2.3.1.1.), which can dissociate into an inactive, not polymerization inducing radical and an active, chain-carrying radical[4].

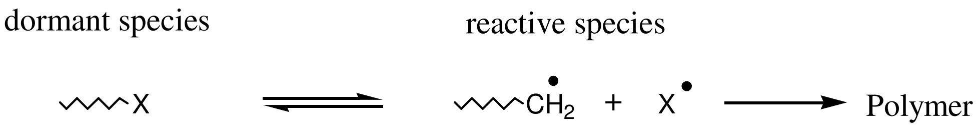

Fig. 2.3.1.1.: Principle of controlled radical polymerization

The equilibrium lies on the side of the dormant species, which is transformed into the reactive species by an external stimulus, e.g. by raising the temperature. This conversion is rapid and fully reversible. Thus each polymer chain has the same chance for undergoing a propagation step, which results in a relatively uniform molar mass distribution. The species $X^\cdot$ in reaction scheme 2.3.1.1., the so called capping reagent, has to meet certain criteria: it has to react rapidly (as fast as the propagation step, or faster) with the radical of the growing polymer chain, forming a covalent bond that can be cleaved homolytically to release the active species. Moreover, it should not react with the monomer. The actual initiator of the polymerization is a species that is similar to the dormant polymer chain (e.g. $Me_2CBr(CO_2R)$ for alkyl methacrylates; benzyl bromide for styrene-type monomers), which ensures that the initiation and propagation steps of the reaction have similar reaction rates. The three most common types of living radical polymerization are SFRP (stable free radical polymerization), ATRP (atom transfer radical polymerization) and RAFT (reversible addition-fragmentation chain transfer). These methods will be presented in the following sections. They all considerably increase the control over polymerization as compared to the free radical archetype; however these methods should be not considered as living polymerization systems. Even though the amount of side reactions has been significantly reduced, they have not been eliminated (which is the criterion for a living polymerization), therefore they must be considered as *controlled* rather than *living*[5].

2.3.2. Stable Free Radical Polymerization (SFRP)

SFRP, also called nitroxide-mediated polymerization (NMP), involves nitroxides as radical capping reagents. One of the first works which demonstrated the power of this method is by Georges et al., who obtained low polydispersity, high molecular weight poly(styrene) by polymerization at 130℃ in bulk, using 2,2,6,6-tetramethyl piperidine-1-oxyl (TEMPO) as a capping agent and dibenzoyl peroxide (DBPO) as initiator[6] (Fig. 2.3.2.1.). The TEMPO radical, which is a polymerization inhibitor at low temperatures, acts as a mediator at high temperatures due to the C-ON bond becoming labile. It thus reduces recombination and disproportionation reactions.

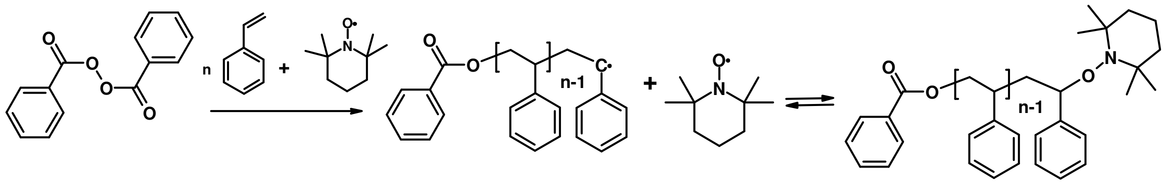

Fig. 2.3.2.1.: SFRP with TEMPO radicals

To avoid stoichiometry problems between initiator and capping agents, unimolecular initiators were developed, in which initiator and moderator were contained in the same molecule, i.e. these molecules have a built-in and correct stoichiometry. The disadvantage of SFRP reactions thus conducted are the high reaction temperatures, which are incompatible with many monomers (e.g. acrylates), and the long reaction times. To overcome this, nitroxides with lower thermal stability of the C-ON bonds were developed. Examples are given in Fig. 2.3.2.2.. With these, acrylates, acrylonitrile, acrylamides and dienes can be polymerized. Hawker gives a concise list of such nitroxide moderators[7]. Current research focuses on the improvement of the reactivity of those radicals.

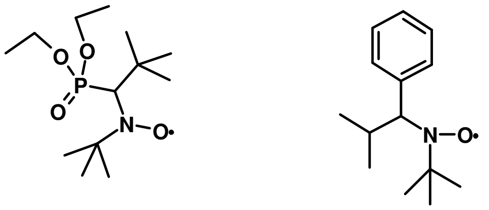

Fig. 2.3.2.2.: Nitroxide radicals as moderators for SFRP

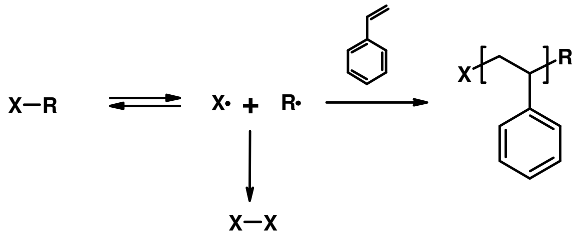

Fig. 2.3.2.3.: Mechanism of SFRP[7]

The reaction mechanism is shown in Fig. 2.3.2.3.. At the beginning of the reaction, some of the initiating radical **X**$^{\cdot}$ is consumed due to recombination, while this does not occur for the capping radical **R**$^{\cdot}$. Consequently, the concentration of **R**$^{\cdot}$ increases. Thus the reaction equilibrium is shifted towards the dormant species, which decreases the amount of termination by recombination. Although the reaction is not strictly living (see section 2.3.1.), a linear relation between molar mass and reaction conversion is observed. An important side reaction of SFRP is the loss of the nitroxide group due to the abstraction of a hydrogen atom from the polymer chain. The corresponding hydroxylamine and a dead polymer chain are formed. This side reaction limits the attainable molecular weight and increases the polydispersity.

SFRP can be used for the synthesis block and gradient copolymers, telechelic polymers, dendritic, hyperbranched and branched polymers, as well as for surface-initiated polymerization[8].

2.3.3. Atom Transfer Radical Polymerization (ATRP)

ATRP is the polymer version of the atom transfer radical addition (ATRA) reaction, in which alkyl halide-alkene adducts are formed by transition metal catalysis[9]. For a concise and detailed review, the reader is referred to the literature[10]. ATRP was developed by two independent research groups[11] by adjusting the ATRA conditions. A transition metal complex was designed that reversibly cleaves the C-halogen bond of an alkyl halide. The thus formed alkyl radical initiates polymerization. The term ‘atom transfer’ in ATRP refers to the halogen radical being transferred to the new chain end after each monomer insertion step to form the dormant species (see section 2.3.1.).. The mechanism for ATRP is given in Fig. 2.3.3.1.[12]. The first reaction step involves the reversible cleavage of the C-Br bond of the initiator, whereby a bipyridyl-ligated copper(I) species is oxidized to Cu(II). The benzyl radical thus formed starts the polymerization by attacking a monomer double bond. Due to the reaction equilibrium being located on the side of the dormant species ($k_{act} \ll k_{desact}$), the newly formed radical is immediately capped by a bromine atom. Initiation is much faster than the reversible deactivation step, thus uniformly growing chains are obtained, which allows good control over the structure of the polymer as well as its polydispersity. Termination is limited to about 5 % of all chains and mainly occurs at the beginning of the reaction, when it is not yet in a steady-state.

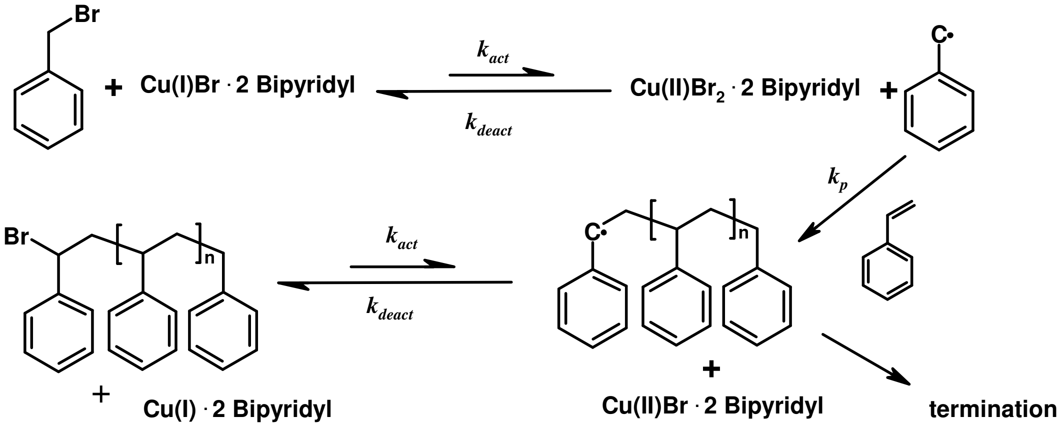

Fig.2.3.3.1. Mechanism of ATRP for the polymerization of styrene with CuBr/bipyridyl and benzyl bromide, k_{act} = rate constant of activation k_{desact} = rate constant of desactivation, k_p = rate constant of polymerization

The nature of the initiator, the metal species and its ligands, the monomer, the solvent polarity, the reaction temperature, the concentration of the components and their solubility in the reaction medium, as well as additives influence the reaction kinetics. All these parameters must be taken into account when designing a new ATRP reaction.

Neglecting the influence of termination, Matyjaszewski derived the following first order rate law for ATRP[12]:

$$r_p = k_p \frac{k_{act}}{k_{deact}} [M] \cdot [I]_0 \cdot \frac{[Cu^I]}{[BrCu^{II}]}$$

r_p = polymerization rate
k_i = reaction step rate constant
$[I]$ = initiator concentration
$[M]$ = monomer concentration
$[Cu^I]$ = concentration of copper(I)
$[BrCu^{II}]$ = concentration of copper(II)

As can be seen from this equation, the reaction is first order with respect to the monomer concentration, i.e. a plot of $\ln([M]/[M_0])$ versus time results in a straight line. The polydispersity for an ATRP reaction is typically between 1 and 1.5, and can be predicted as

$$\frac{M_w}{M_n} = 1 - \left(\frac{([RX]_0 - [RX]_t) \cdot k_p}{k_{desact} [Cu^{II}]} \right) \cdot \left(\frac{2}{p} - 1 \right)$$

M_w/M_n = polydispersity index
k_i = reaction step rate constant
$[RX]$ = initiator concentration
p = monomer conversion
$[BCu^{II}]$ = concentration of copper(II)

In real systems, the reaction kinetics are more complicated than in the simplified picture given above, as other factors influencing the reaction kinetics by inducing side reactions might be present.

For the initiator R-X (R = α-carbon substituted alkyl), the reactivity decreases from X = I to X = Cl. Chlorides and bromides are usually preferred, as iodides are light sensitive and prone to undergo heterolytic cleavage. Initiation should be fast and without side reactions. This depends on the nature of R.

The catalyst reactivity is influenced by the nature of the metal used - besides copper, Mo, Mn, Re, Fe, Ru, Co, Rh, Pd and Ni complexes in two oxidation states have been employed. The kind of ligand is also crucial, as it mediates the solubility of the catalyst in the reaction solvent and also influences the redox potential of the metal species. It should be strongly bound to the metal and still allow the expansion of the coordination sphere. The nature of the anionic species also influences the reaction kinetics: acetates are much faster than bromides, which are in turn faster than chlorides. Using an alkyl bromide as initiator and a copper(I) chloride salts can lead to halogen exchange in the initiation phase and thereby improve the reaction control. Additives such as copper(0) and copper(II) also influence the reaction kinetics. Copper(0) increases the reaction rate, copper(II) leads to a rate reduction. This can be exploited for tuning the reaction kinetics. In the presence of a large amount of Cu(0), the reaction may be even conducted in the presence of air. An increase in solvent polarity usually increases the reaction kinetics. This is attributed to changes in the coordination sphere of the metal center due to polar solvents. However, polar solvents might also induce side reactions. As in conventional free radical polymerization, higher temperatures increase the rate of propagation and decrease the rate of termination. However, they also increase the rate of chain transfer reactions. Conversion should be kept below 95 %. Otherwise, an increased loss of the chain end functionality is observed.

In reverse ATRP, a copper(II) species is used, together with a conventional radical starter (such as AIBN). ATRP, just as free radical polymerization, can be performed in bulk, solution or heterogeneous systems. Copper removal is complicated, which is a big drawback for industrial application of ATRP. ATRP is extremely versatile: by now, homopolymers, copolymers (block, graft, gradient, statistical) with linear, branched, hyperbranched or network-like topology have been synthesized. As ATRP is highly tolerant to functional groups, virtually any monomer containing a reactive double bond can be used.

2.3.4. Reversible Addtion-Fragmenation Chain Transfer Polymerization (RAFT)

RAFT, an acronym for Reversible Addition-Fragmentation chain Transfer polymerization, was developed in the late 1990s by Rizzardo et al.[13,14]. It is another controlled radical polymerization technique that yields narrowly distributed polymers with predetermined molecular weight. It is highly tolerant to many functional groups, including, alcohols, acids, amides, amines and sulfate groups. Like ATRP, RAFT can be performed in bulk, solution, emulsion and suspension. The mechanism is slightly more complicated than the one for SFRP and ATRP, which is outlined in Fig. 2.3.4.1.[15].

In RAFT, a chain transfer agent (RX-ZC=X in Fig. 2.3.4.1.), usually a dithioester, is added to the usual free radical polymerization system. By reaction with the growing polymer chain (**Pn**$^{\cdot}$), an alkyl fragment (**R**$^{\cdot}$) of the ester is reversibly expelled from the molecule, thus reducing the concentration of active chain ends. This equilibrium allows control over the molar mass distribution. The RAFT agent should have a high transfer constant. All intermediate radicals should fragment fast and without side reactions. The alkyl fragment in the RAFT agent should reinitiate polymerization rapidly. A typical system involves azoisobutyric acid nitrile (AIBN) as an initiator and 2-phenylprop-2-yl dithiobenzoate as the transfer agent[16]. Due to the rapidity of the chain transfer reactions, well-defined homopolymers, blockcopolymers and even star polymers ('away-from' process and 'attached-to' process, Ref. 15) can be obtained. However, a certain percentage of the chains always undergoes termination, which cannot be effectively suppressed. Due to that, and due to the fact that brush synthesis by RAFT is yet poorly established, the reaction will not be considered further in this work.

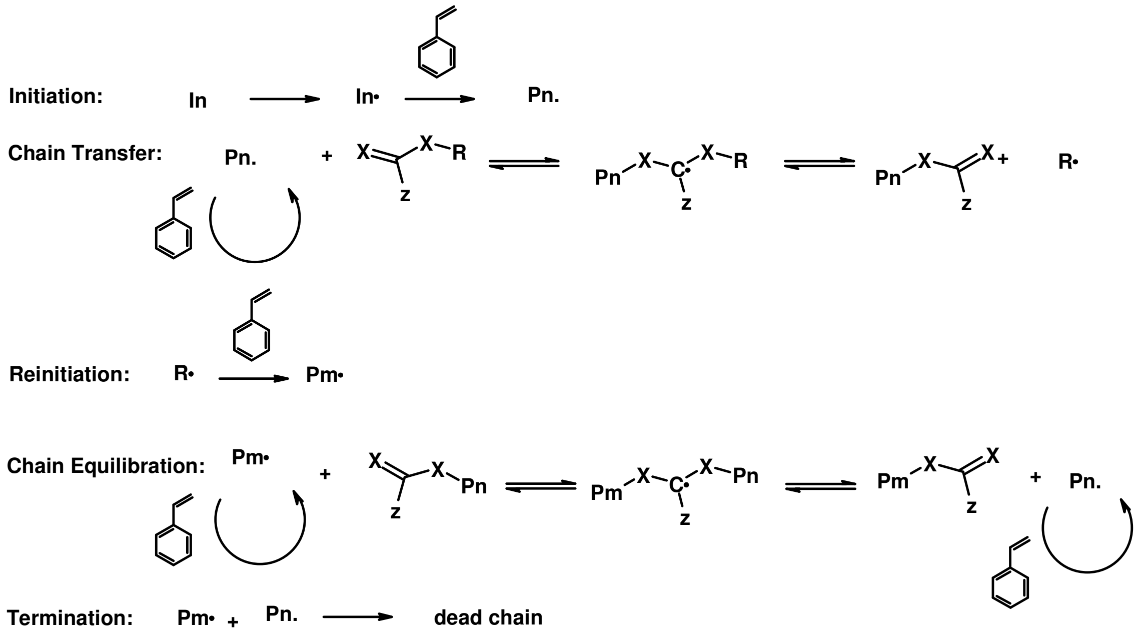

Pn. , Pm. = Macroradicals
In. = Initiator
R = free radical leaving group that is able to reiinitiate the polymerization
X = atom that leads to an active double bond, usually sulfur
Y = residue that can modify addition and fragmentation rates

Fig. 2.3.4.1.: Mechanism of RAFT polymerization

2.4. Anionic Polymerization

Anionic polymerization is useful for monomers carrying electron-withdrawing groups such as esters, nitriles or aromatics, which can stabilize a negative charge resulting from the attack of a carbanion on a monomer double bond. The mechanism assumed is presented in Figure 2.4.1.. While radical polymerization contains chain-ending steps, such as radical recombination and disproportionation, anionic polymerization does not have an intrinsic termination step. If impurities are completely excluded, living chains are obtained. Once initiated, polymer chains grow until all monomer is consumed. The anionic species remains on the chain end. This can be proven by adding further monomer – the same or a different one – and observing further chain growth. This phenomenon was first recognized as a living anionic polymerization by Szwarc et al.[17,18,19], who performed the reaction in a completely closed glass reactor. The mechanism of living anionic polymerization consists of two reaction steps: initiation and propagation. In ideal systems, there is no termination or chain transfer step, except by reaction with impurities: very little amounts of protic species, oxygen or carbon dioxide can end anionic chains. Deliberate termination by addition of a termination agent (e.g. an end group for macromonomer synthesis) is possible, making it very attractive in the synthesis of functionalized polymers. To obtain truly living systems, the following criteria must be met: there may be only one propagating species, or a fast equilibrium between several propagating species, which is much faster than the rate of propagation. Initiation must be faster than propagation, or at least equally fast. The propagation step must have the same reaction rate for different chain lengths, only then a uniform k_p is observed. If the first two criteria are fulfilled, the number of active species is constant, and the overall reaction shows a first order rate law:

$$v_{anionic} = -\frac{d[M]}{dt} = k_p \cdot [M] \cdot [P^-] = k_{overall} \cdot [M]$$

$$\text{Initiation:} \quad In^{\ominus} + M \xrightarrow{k_i} P_i^{\ominus}$$

$$\text{Propagation:} \quad P_i^{\ominus} + M \xrightarrow{k_p} P_{i+1}^{\ominus}$$

$$\text{Termination:} \quad P_i^{\ominus} + X \xrightarrow{k_t} P_i$$

Fig. 2.4.1.: Reaction mechanism of living anionic polymerization (k_i = rate constant of the reaction step indicated, ***In*** = initiator, ***M*** = monomer, P_i = polymer with *i* repeat units)

A deviation from first order kinetics is observed if the amount of active species decreases, either by reaction with impurities, or by aggregation of the active species, causing temporary or permanent deactivation. Polymers synthesized by living anionic polymerization methods have a Poisson-type molecular weight distribution[20]. Depending on the specific monomer, very low polydispersity indices can be obtained.

This makes anionic polymerization very attractive for molecular engineering. However, due to its sensitivity to impurities, industrial applications are rare.

While living anionic polymerization of non-polar molecules such as styrene and butadiene is well established[21], polar monomers, such as acrylates of styrene sulfonate esters, do not undergo living anionic polymerization when exposed to the same reaction conditions (metal alkyl initiators in polar or non-polar solvents). The resulting polymers show broad molecular weight distributions or very low molecular weights. This is due to the polar ester group of the monomer, which is prone to undergo side reactions and form aggregates. In alkyl(meth)acrylate polymerization, side reactions such as aggregate formation, nucleophilic attack of the ester group, termination by intra- and intermolecular reactions have been observed[22]. This can be suppressed by additives, such as crown ethers, cryptands, tertiary amines, alkyl aluminum compounds, alkali metal halides, perchlorates and alkoxides or alkoxyalkoxydes, aminoalkoxides and silanolates[23]. For monomers such as vinyl phosponate esters[24] and styrene sulfonate esters[25], only low molecular weight polymers have been obtained. For styrene sulfonate esters, the living polyanion is very stable and is believed to form inter and intramolecular complexes. As a result, yields are low and the polydispersities obtained are larger than for well-behaved anionic polymerization. This could not yet be successfully suppressed by additives, although research is much less advanced in this field than in the case of (meth)acrylates. Due to the inactivity of the living anion, polymer brush syntheses by either the ‘grafting onto’ or ‘grafting through’ approach (see Chapter 4) via anionic polymerization is not feasible. Polymer brush synthesis by anionic ‘grafting from’ could be attempted, yet the obtainable side chain length would be limited by the anion inactivity. As the establishment of reaction conditions for well-behaved anionic polymerization of styrene sulfonate esters would be too time-consuming, it was not attempted for this project.

2.5. Cationic Polymerization

Cationic polymerization is used for the polymerization of vinylic monomers with cation-stabilizing substituents, such as vinyl ethers and donor-substituted styrene derivatives. Additionally, heterocyclic monomers such as tetrahydrofuran can be cationically polymerized, where the driving force of the reaction is the release of ring strain energy. Due to the aggressiveness of the carbocationic intermediates, the solvent range for the reaction is limited to benzene, cyclohexane, chloroform etc., which do not undergo reactions with carbocations. The reaction is initiated with acids (Brønsted or Lewis acids) or carbocationic initiators. Side reactions include chain transfer, β-hydrogen elimination, rearrangement reactions (Wagner-Meerwein rearrangement), Friedel-Crafts type backbiting reactions etc.. Attempts to reduce these side reactions led to the development of controlled cationic polymerization, which can be achieved by the addition of nucleophilic counter anions, weak nucleophiles or salts. In spite of a general improvement of reaction control by these methods, a linear dependence of molar mass on conversion is rarely observed, indicating that the reaction is not truly living. While cationic polymerization is much more tolerant to impurities, especially water, than anionic polymerization, its disadvantage is that chain transfer cannot be completely suppressed, which makes it less useful for the synthesis of molecules with defined architecture[26]. Also, the styrene sulfonate derivatives used in this work are electron-withdrawing and thus destabilize the cationic reaction intermediate. It will be therefore not considered further.

2.6. Suzuki Polycondenzation

The reaction mechanisms that were discussed in the previous sections are all chain growth reactions. In contrast to that, the Suzuki polycondenzation is a step-growth reaction, i.e. the molecular weight obtained is proportional to the reaction conversion (see below). In this type of polycondenzation, monomers with sp^2 hybridized carbon atoms are connected to form conjugated poly(para-phenylene) polymers . In general, a boronic acid derivative on an sp^2-hybridized carbon atom is reacted with another sp^2 centre carrying a good leaving group (Br, I, tosylate or triflate). The reaction is highly tolerant towards many functional groups, including carboxylic acids, esters, aldehydes, alcohols, ethers and protected amines. The general reaction scheme is shown in Figure 2.6.1..

The reactive groups can be put onto two different monomers carrying two groups each (AA-monomers), which are copolymerized, or onto one monomer (AB-monomer), which is then homopolymerized. As a consequence of the general reaction kinetics of step-growth reactions, to obtain high molecular weights, the reaction conversion must be very high. The relation between chain length and reaction conversion is given by Carothers' equation[3]:

$$x_n = \frac{1}{1-p^*}$$

x_n = degree of polymerization
p^* = reaction conversion

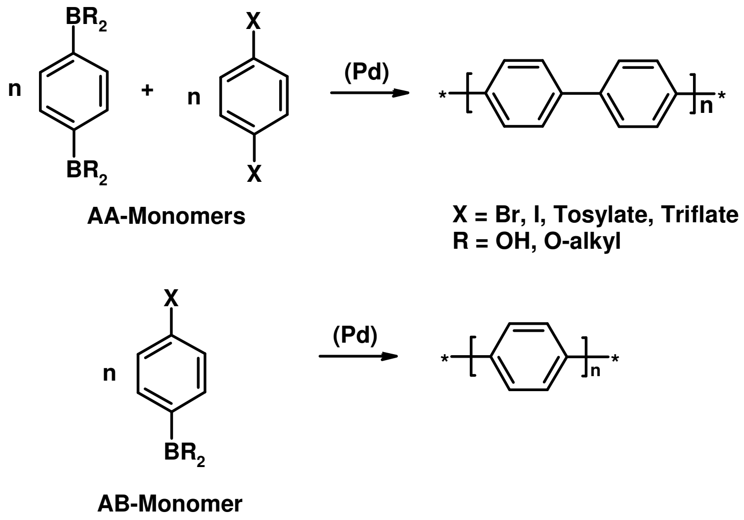

Fig. 2.6.1.: General reaction scheme of Suzuki polycondensation

For x_n = 100, p^* must be 0.99 (i.e. 99% conversion). Thus, in the case of the copolymerization of two AA-monomers, the monomer purity must be extremely high to obtain exactly the right reactant stoichiometry. For AB-monomers, this is less critical, as they have automatically the correct number of functional groups. The following catalytic cycle is assumed for Suzuki polycondenzation (Figure 2.6.2.)[27]: In this reaction cycle, the transmetallation is the rate determining step. Some of the reaction intermediates have been verified experimentally by Canary[28]. As catalyst, a palladium(0) species with a variety of ligands are used. Examples are phosphane, acetate or chloro ligands. Usually, 0.1 – 1 mol% is used. The reaction is performed in a two phase system of water and an organic solvent (e.g. THF, toluene, DMF). As a base, Na_2CO_3, K_2CO_3, NaOH or $Ba(OH)_2$, among many others, can be used. For polymerization, reactions can take a few hours to several days. After that time span, side reactions usually dominate: deboronification[29], homocoupling[30] and ligand scrambling[31] occur. These limit the reaction conversions and thus the degree of polymerization achieved. The range of polymers thus obtained include poly(para-phenylene)s substituted with alkyl, polyether, nitro, sulfonate and ammonium groups, among many others[32]. The literature on brush-shaped poly(macromonomers) obtained via Suzuki polycondensation is as yet very little and will be discussed in chapter 9.

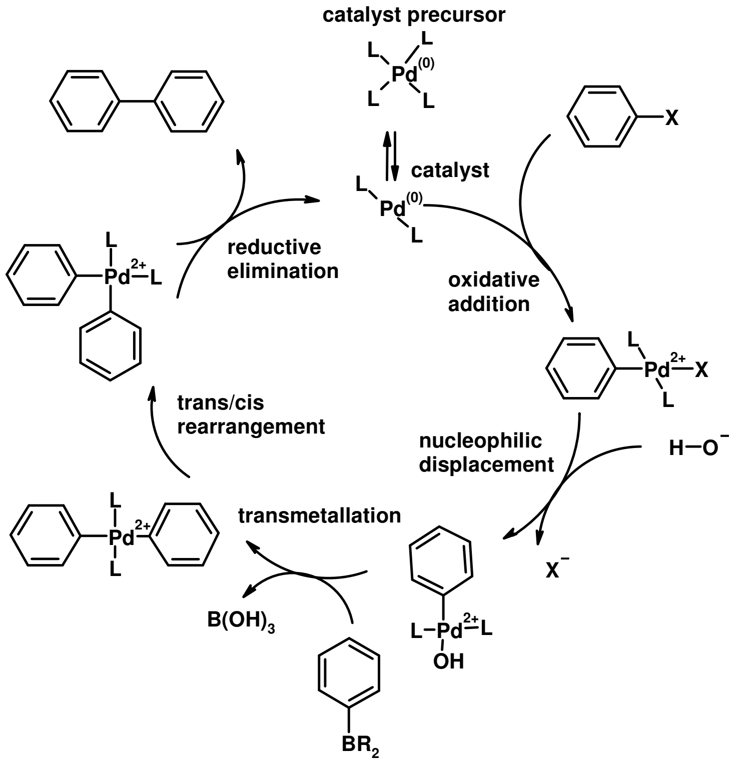

Fig. 2.6.2.: Catalytic cycle of Suzuki polycondenzation

3. Characterization Methods

3.1. *General Comments*

Due to the multitude of analytical methods used in this work, a complete description of the theoretical background of each method is beyond the scope of this thesis. The main characterization techniques and analytical problems pertaining to them are discussed in this chapter. For more information, the reader is referred to the literature.

3.2. *Scattering Methods*

3.2.1. Static Light Scattering (SLS)[33]

Static light scattering is one of the most common methods for the determination of the weight average molecular mass of a polymer. Moreover, information about the polymer structure, the structure of the solution and the second virial coefficient A_2, can be obtained from static light scattering measurements. The value of this method rests in the fact that it is an absolute method, i.e. it does not need any calibration.

In Fig. 3.2.1.1., the general set-up for a light scattering experiment is shown. A laser beam is focussed onto a sample cuvette by an optical lens. The larger part of the laser beam passes the sample unhindered, while a small portion is scattered at an angle θ. The scattered intensity is measured by a detector, typically a photomultiplier or and avalanche diode. This detector is placed on a goniometer which allows scanning through an angular range of 25° to 150°.

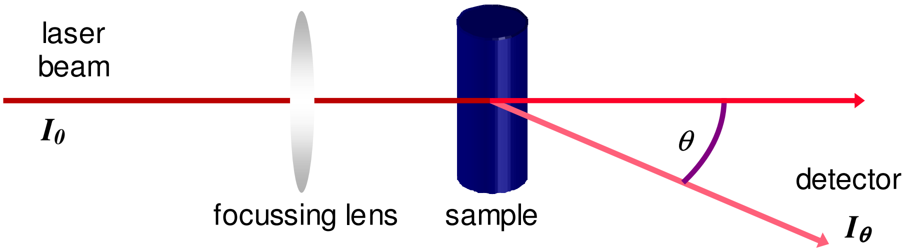

Fig. 3.2.1.1.: Light scattering set-up

When an electromagnetic wave hits a particle, it induces a dipole moment in the particle which oscillates and sends out electromagnetic waves. The magnitude of the dipole moment is proportional to the particle's polarizability and the electric field strength of the incoming beam:

$$\left|\vec{p}_{ind}\right| = \alpha \cdot E_0 \cos(\omega t - kx).$$

p_{ind} = inducted dipole moment
α = polarizability
E_0 = electric field strength
ω = angular frequency
t = time
k = wave vector = $2\pi/\lambda$

In polymer solutions, density and concentration fluctuations occur. The scattering is thus due to local fluctuations of the polarizability caused by these phenomena:

$$\delta\alpha = \left(\frac{\partial\alpha}{\partial\rho}\right)_{p,T}\delta\rho + \left(\frac{\partial\alpha}{\partial c_2}\right)_{p,T}\delta c_2$$

ρ = density
c_2 = concentration of the dissolved species
p = pressure
T = temperature

In data analysis, the density fluctuations are eliminated by subtraction of the solvent scattering data from the scattering data of the sample, thus only the concentration fluctuations described by the second term are relevant. Modelling a dilute solution as a 'pseudo gas', its polarizability is connected to the refractive index by the equation

$$n^2 - 1 = \frac{4\pi\cdot\alpha}{\delta V}\,.$$

n = refractive index of the solution
α = polarizability
δV = volume of a 'pseudo gas molecule'

Thus

$$\left(\frac{\partial\alpha}{\partial c_2}\right)^2 = \left(\frac{\partial\alpha}{\partial n}\right)^2\left(\frac{\partial n}{\partial c_2}\right)^2 = \frac{(\delta V)^2\cdot n^2}{4\pi^2}\cdot\left(\frac{\mathrm{d}n}{\mathrm{d}c_2}\right)^2,$$

with $\frac{\mathrm{d}n}{\mathrm{d}c_2}$ being the refractive index increment.

It follows that

$$(\delta\alpha)^2 = \frac{(\delta V)^2\cdot n^2}{4\pi^2}\cdot\left(\frac{\mathrm{d}n}{\mathrm{d}c_2}\right)^2(\delta c_2)^2$$

Using general thermodynamics theorems, it can be shown that

$$(\delta c_2)^2 = -\frac{k\cdot T\cdot c_2\cdot V_1}{dV\cdot\left(\frac{\partial\mu}{\partial c_2}\right)_{T,p}}$$

k = Boltzmann's constant
c_2 = concentration of the dissolved species
V_1 = solvent volume
μ = chemical potential

The term $(\delta c)^2$ contains the above mentioned concentration fluctuations, and a term containing the chemical potential can be related to the particle mass by

$$\left(\frac{\partial\mu}{\partial c_2}\right)_{T,p} = -RT\overline{V}_1\cdot\left(\frac{1}{M_2} + 2A_2c_2 + 3A_3c_2 + \ldots\right)$$

V = scattering volume
M_2 = particle mass
A_2 = second virial coefficient
A_3 = third virial coefficient

These equations are the first ingredients for the light scattering recipe and will be needed later. In the following, the relation between scattering intensity (which can be measured) and polarizability will be discussed. Using the model of a damped oscillator, combined with some general electrodynamics theorems, it can be shown that in the so-called Raleigh limit, $I_\theta \sim \lambda^4$ for a point scatterer and polarized light,

$$I_\theta = E_s(\omega)\cdot\left(E_s(\omega)\right)^* = I_0 \cdot \frac{\sin^2\phi}{r^2}\cdot\frac{16\cdot\pi^4}{\lambda^4}\cdot\alpha^2\ .$$

I_θ = Intensity of scattered light
$E_s(\omega)$ = electric field strength
I_0 = Intensity of incoming light
ω = angular frequency
ϕ = angle
r = radius
λ = wavelength
N = number of scattering centres

For many scattering centres,

$$\frac{I_\theta}{I_0} = N\cdot\frac{\sin^2\phi}{r^2}\cdot\frac{16\cdot\pi^4}{\lambda^4}\cdot\alpha^2\ .$$

Subtraction of this equation for the solvent from that for solution gives

$$\frac{I_{\theta,solution} - I_{\theta,solvent}}{I_0} = N\cdot\frac{\sin^2\phi}{r^2}\cdot\frac{16\pi^4}{\lambda^4}(\delta\alpha)^2$$

This is the second collection of ingredients, which will now be connected to the first set. Inserting the equation for $(\delta\alpha)^2$ gives

$$\frac{I_{\theta,solution} - I_{\theta,solvent}}{I_0} = N\cdot\frac{\sin^2\phi}{r^2}\cdot\frac{4\pi^2}{\lambda^4}\cdot(\mathrm{d}V)^2\left(\frac{\mathrm{d}n}{\mathrm{d}c}\right)^2(\delta c)^2\ .$$

Combined with the expression for $(\delta c_2)^2$ and $\left(\frac{\partial\mu}{\partial c_2}\right)_{T,p}$, the result is

$$\frac{I_{\theta,solution} - I_{\theta,solvent}}{I_0} = \frac{n^2\cdot V}{N_A}\cdot\frac{\sin^2\phi}{r^2}\cdot\frac{4\pi^2}{\lambda^4}\cdot\left(\frac{\mathrm{d}n}{\mathrm{d}c_2}\right)^2 c_2\cdot\left(\frac{1}{M_2} + 2A_2c_2 + 3A_3c_2 + \ldots\right)^{-1}$$

The Rayleigh Ratio ***R(θ)*** and the optical constant ***K*** are introduced to put the equation into a more user-friendly shape:

$$R(\theta) = \frac{r^2\,\frac{I_{s,solution} - I_{s,solvent}}{I_0}}{V\cdot\sin^2\phi}$$

$$K = \frac{4\pi^2 n_0^2}{N_A\lambda_0^4}\cdot\left(\frac{\mathrm{d}n}{\mathrm{d}c_2}\right)^2\ .$$

This leads to

$$\frac{K\cdot c_2}{R(\theta)} = \left(\frac{1}{M_2} + 2A_2c_2 + 3A_3c_2 + \ldots\right),$$

which is the fundamental equation of light scattering for small particles. A plot of ***c_2*** vs ***$Kc_2/R(\theta)$*** yields ***M_2*** as the inverse y-axis intercept and 2 ***A_2*** as slope.

So far, we have assumed that there is only one scattering centre per particle. For polymers, and in general particles larger than $\lambda/20$, there is more than one scattering centre per particle. This causes intramolecular interference, which leads to a dependence of the scattering intensity on the scattering angle, i.e. the angle between the incoming beam and the sample-detector axis. This is described by introducing the form factor ***P(q)***:

$$\frac{K \cdot c_2}{R(\theta)} = \left(\frac{1}{M_2} + 2A_2 c_2 + 3A_3 c_2 + \ldots \right) \cdot P(q)$$

P(q) = form factor
q = scattering vector

The scattering vector ***q***, is defined as

$$q = \frac{4 \cdot \pi \cdot n}{\lambda_0} \sin\left(\frac{\theta}{2} \right)$$

q = scattering vector
n = refractive index of the medium
θ = scattering angle

With the form factor, information about the particle shape can be obtained, which makes static light scattering a powerful tool for obtaining detailed information about particles in solution. It has been shown by Guinier (see below) that the form factor of a particle is related to its radius of gyration by

$$P(q) = 1 - \frac{R_g{}^2 \cdot q^2}{3} \text{ if } R_g \cdot q < 1.$$

R_g = radius of gyration

Inserting this equation into the fundamental equation of light scattering gives

$$\frac{K \cdot c_2}{R(\theta)} = \cdot \frac{1}{M_2} \left(1 + \frac{R_g{}^2 \cdot q^2}{3} \right) + 2A_2 c_2 + \ldots.,$$

which is the Zimm equation. By plotting $\frac{K \cdot c_2}{R(\theta)}$ versus $q^2 + kc_2$, where k is an arbitrary constant, extrapolation to $c_2 = 0$ and $q^2 = 0$ (open circles in Fig. 3.2.1.2.) gives M_w, A_2 and R_g as indicated.

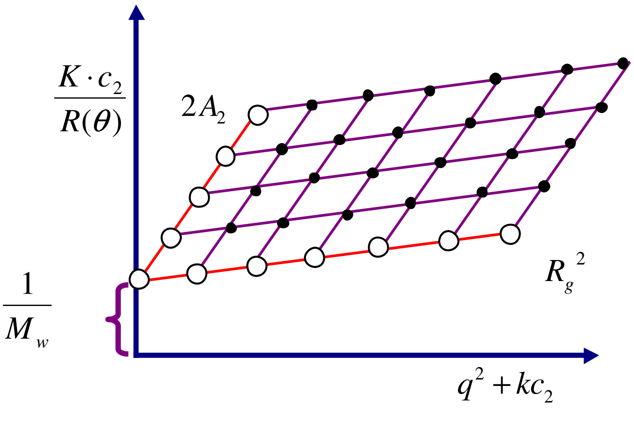

Fig. 3.2.1.2.: Zimm plot for M_w determination

When information about the polymer shape is required, the scattering intensity must be looked at in more detail. The total scattering intensity can be split into two terms: *intra*molecular and *inter*molecular interference. Scattering from the same object is summed up as the form factor **$P(q)$**, while intermolecular scattering is combined in the structure factor **$S(q)$**. It can be shown that the scattering intensity of light scattered from N scattering centres is given by

$$\frac{I(q)}{N \cdot b^2} = z^2 \cdot P(q) + N \cdot z^2 S(q)$$

b = contrast factor
N = number of particles
z = number of scattering centres per particle

For dilute solutions, i.e. $N \to 0$, the second term is zero and the intensity only depends on the form factor. However, the form factor cannot be calculated directly from the intensity, as $I(q) \sim \boldsymbol{A}^2$, where $\boldsymbol{A}$ is the scattering amplitude. Thus the phase information of the scattered wave is lost by squaring. This is called the 'phase problem' of light scattering. Form factors are therefore determined by comparing calculated form factor curves with the measured data. By averaging over all possible orientations of the particle, it can be shown that, for randomly orientated particles,

$$P(q) = \frac{1}{z^2} \sum_{i=1}^{z} \sum_{j=1}^{z} \left\langle \frac{\sin(q \cdot r)}{q \cdot r} \right\rangle_r .$$

For small particles the expansion of the sine function by a Taylor series and including the definition of the radius of gyration,

$\left\langle R_g^2 \right\rangle = \frac{1}{z} \sum_{i=1}^{z} \left\langle r_i^2 \right\rangle$, the form factor becomes

$P(q) = 1 - \frac{R_g{}^2 \cdot q^2}{3}$, which is the Guinier approximation used above.

This approximation is valid for all particle shapes if $R_g \cdot q < 1$. For specific particle shapes, special form factors have been calculated and tabulated in the literature. For these, special plots for data analysis can be determined:

- Guinier plot: $\ln(I(q))$ vs $\boldsymbol{q^2}$, linear for spheres, slope = $-\frac{1}{3} R_g^2$
- Cross-section Guinier plot: $\ln(q \cdot I(q))$ vs $\boldsymbol{q^2}$, linear for rods, determination of $R_{g,c}$ by splitting the scattering function in to a 'cross-sectional part' and 'length part'. The cross-sectional part can be expressed as $I_c(q) = I_{c,0} \exp\left(\frac{-q^2 R_{g,c}{}^2}{2}\right)$, thus the slope is - $\frac{1}{2} R_{g,c}^2$.

- Double logarithmic plot: log $\boldsymbol{I}$ vs log $\boldsymbol{q}$, for coils $P(q)=\frac{2}{q^2R_g^2}$, thus the slope is -2; for rods $P(q)=\frac{\pi}{q\cdot L}$, where $\boldsymbol{L}$ is the rod length, i.e. the slope is -1.
- Holtzer plot: $q\cdot I(q)$ vs $\boldsymbol{q}$, constant for thin rods, determination of mass per unit length
- Kratky plot: $q^2\cdot I(q)$ vs $\boldsymbol{q}$, linear for rods, maximum for branched molecules

3.2.2. Dynamic Light Scattering (DLS)

By dynamic light scattering (DLS), information on Brownian motion, i.e. diffusion processes of particles in a solution, is obtained. This is done by analyzing fluctuations of the scattered light intensity at a fixed angle. These are caused by concentration fluctuations of the solution. The density fluctuations are usually so fast that they do not interfere with the diffusion coefficient measurement, therefore the solvent need not be considered further. A typical example for $I(q,t)$ vs time is shown in Fig. 3.2.2.1..

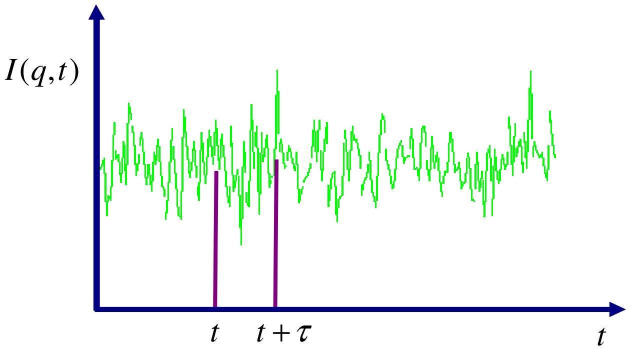

Fig. 3.2.2.1.: Intensity as a function of time

From this measured function, the so-called intensity autocorrelation function $g_2(\tau)$ is calculated. It is defined as

$$g_2(\tau)=\frac{\langle I(q,t)\cdot I(q,t+\tau)\rangle_t}{\langle I(q)\rangle^2_t}.$$

τ = time interval after t
$g_2(\tau)$ = intensity autocorrelation function
$I(q,t)$ = intensity

It compares the value of $I(g,t)$ with $I(g,t+\tau)$, i.e. it correlates these two values. For $\tau\rightarrow 0$, $g_2(\tau)$ approaches 1, as the probability that the particle moved in small time intervals is very low. For large τ, the function approaches zero, as a correlation between the two intensity values becomes more improbable with increasing time span, as shown in Fig. 3.2.2.2..

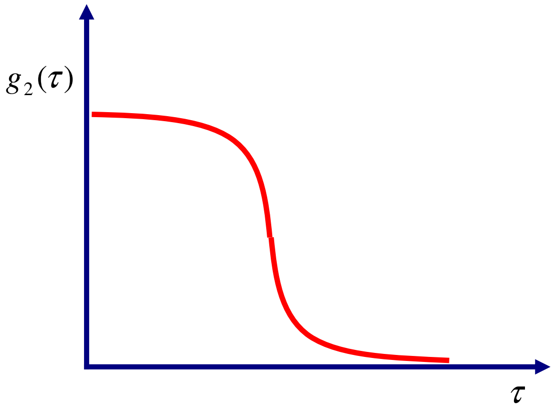

Fig. 3.2.2.2.: Intensity autocorrelation function

$g_2(\tau)$ is related to $g_1(\tau)$, the amplitude autocorrelation function, by the Siegert relation

$$g_2(q,\tau) = 1 + const \cdot \left| g_1(\tau) \right|^2,$$

thus, $g_1(\tau)$ can be calculated from $g_2(\tau)$. The phase problem is not relevant in dynamic light scattering. In the case of dilute solutions, the amplitude autocorrelation function $g_1(\tau)$ correlates each particle with itself by

$$g_1(q,\tau) = \frac{1}{N}\sum_{i=1}^{N}\left\langle \exp\left(-i\vec{q}\left[\vec{r}_i(0) - \vec{r}_i(\tau)\right]\right)\right\rangle = \frac{1}{N}\sum_{i=1}^{N}\left\langle \exp\left(-i\vec{q}[\Delta r(\tau)]^2\right)\right\rangle,$$

where $\left\langle [\Delta r(\tau)]^2 \right\rangle$ is the mean square displacement, i.e. measure of the particle displacement in a certain time span. This parameter is related to the diffusion coefficient: $g_1(q,\tau) = \exp\left(-D \cdot q^2 \cdot \tau\right)$

Thus a plot of $\ln\left[g_1(q,\tau)\right]$ vs τ yields a straight line with the slope $-D \cdot q^2$, which allows the determination of the diffusion coefficient. For spherical molecules, the diffusion coefficient is related to the hydrodynamic radius R_h via the Stokes-Einstein equation:

$$D = \frac{k_B \cdot T}{6\pi \cdot \eta \cdot R_h}$$

k_B = Boltzmann’s constant
T = temperature
η = viscosity

The equations above are strictly valid for monodisperse particle systems only. For polydisperse samples, $g_1(t)$ is transformed by an inverse Laplace transformation into the distribution of relaxation rates $A(\Gamma)$, which accounts for the polydispersity of the system. The relaxation rate, Γ, is related to the correlation time by the relation

$$\Gamma = \frac{1}{\tau} = D \cdot q^2,$$

which, after extrapolation to zero scattering angle and concentration, provides, via the Stokes-Einstein equation, the distribution of hydrodynamic radii. This is summarized in Fig. 3.2.2.3..

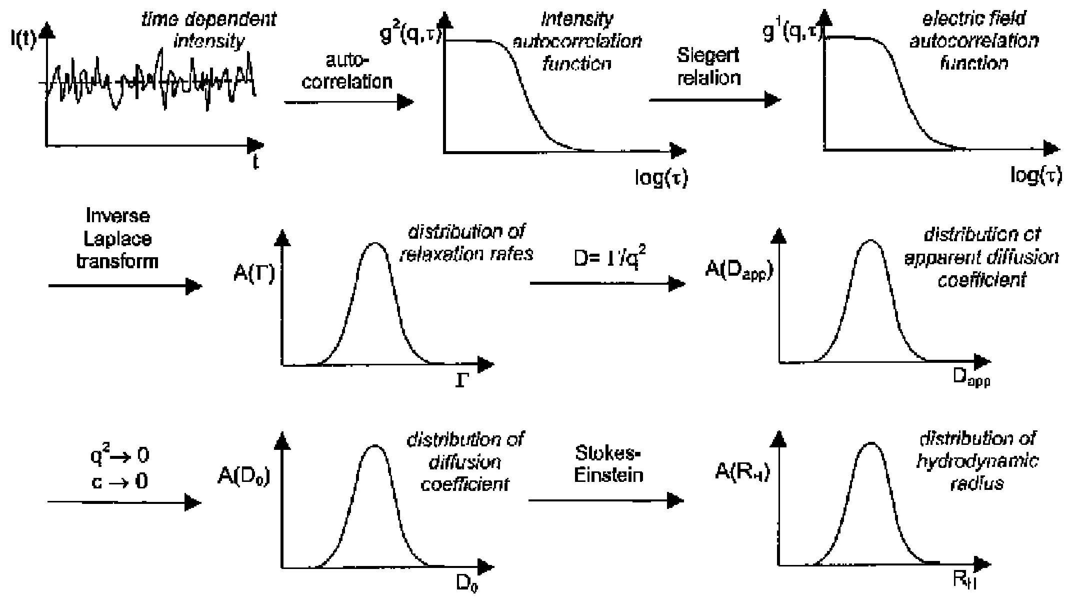

Fig. 3.2.2.3.: Data evaluation in dynamic light scattering[34]

When dynamic and static light scattering is available for the same sample, the ratio R_g/R_h, , the so-called ρ-ratio, gives information about the particle shape. For rod-like particles, the ρ-ratio is equal or larger than 2.

3.2.3. Small Angle Neutron Scattering (SANS)

For small angle neutron scattering, the principle is the same as for static light scattering; only the origin of the scattering as well as the experimental set-up is different. As thermal neutrons are generated in a nuclear reactor, there are only a few sites where SANS experiment can be performed (e.g. in Grenoble, France; Villigen, Switzerland or Jülich, Germany). While light is scattered at an oscillating dipole, neutrons are scattered at the nuclei of the atoms. The contrast in light scattering is due to differences in polarizability and refractive index increment of sample and solvent. In SANS, the contrast is caused by differences in the scattering lengths and amplitudes of the nuclei, which are characteristic constants for each element isotope. As it is particularly large between hydrogen and deuterium, deuterated solvents are used for scattering of polymer solutions. The scattered neutrons are detected e.g. by a He-detector, where the absorption of a neutron produces a charged particle, which is measurable. Thus, plots $I(q)$ versus q are obtained, which can be evaluated analogously to light scattering data. Due to the difference in wavelength between laser light and neutrons, a different q range is covered. With neutrons, much larger q values are reached, thus neutron scattering allows to look into the fine structure of a polymer coil, while static light scattering looks at the molecule as a whole.

3.3. Gel Permeation Chromatography (GPC) and Coupled Methods

3.2.1. GPC[35,36]

Gel Permeation Chromatography, also known as Size Exclusion Chromatography (SEC), is a quick and reliable analytical technique to characterize the molecular weight distribution of a polymer sample. The key components of the instrumental setup are shown in Fig. 3.3.1.1. In a GPC experiment, the sample is dissolved in a solvent (mobile phase), which is passed through a column filled with a stationary phase of a macroporous material. While the small molecules can penetrate most of the pores of the stationary phase, larger molecules are unable to enter them at all (Fig. 3.3.1.2.), thus they are eluted more quickly. In contrast to common chromatographic techniques, GPC does not exploit the enthalpic interaction between the column material and the sample, but separates molecules by their hydrodynamic volume. Consequently, chemically distinct polymers with the same hydrodynamic volume are eluted simultaneously (Fig. 3.3.1.3.). A UV and/or refractive index detector at the end of the column detects the retention volume, i.e. the volume at which a compound is eluted.

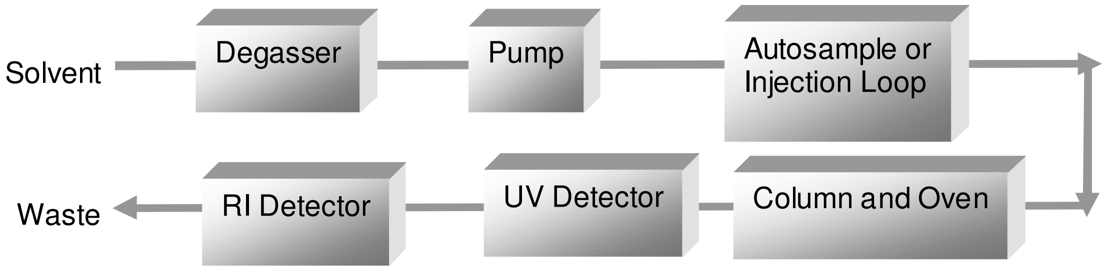

Fig. 3.3.1.1.: Experimental setup

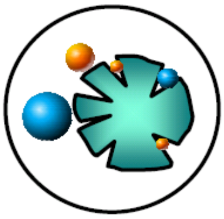

Fig. 3.3.1.2.: Principle of size exclusion

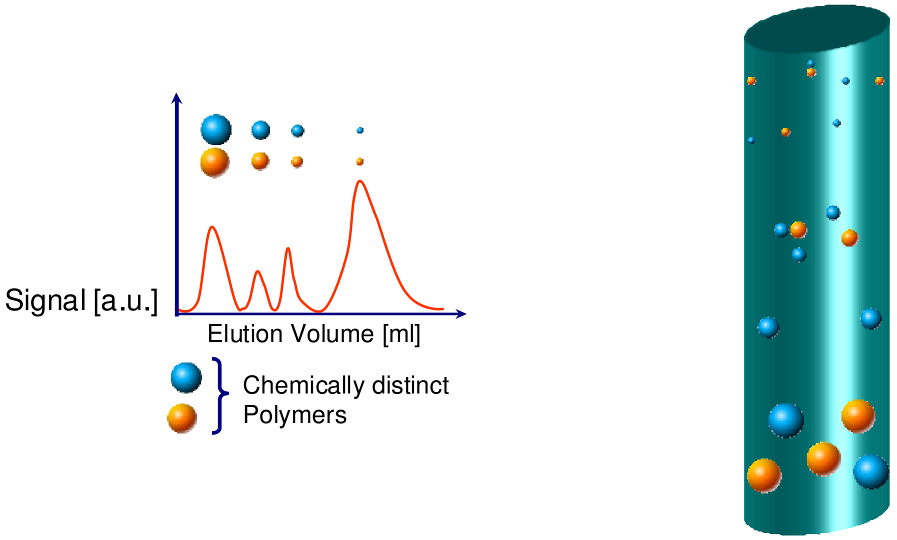

Fig. 3.3.1.3.: Separation mechanism of GPC: Plot of detector intensity vs. elution volume (left), molecule separation on a GPC column (right)

The driving force of the separation is a change in Gibbs free energy, i.e.

$$\Delta G = \Delta H - T\Delta S = -RT \ln K_{GPC}$$

ΔG = change in Gibbs free energy
ΔH = change in enthalpy
ΔS = change in entropy
T = temperature
R = universal gas constant = 8.314 [J/mol K]
K_{GPC} = equilibrium constant

Ideally, no enthalpic interactions occur, thus $\Delta H = 0$, which leads to

$$K_{GPC} = \exp\left(\frac{\Delta S}{R}\right)$$

Physically, the separation range is limited by the pore size of the column material by the so called exclusion limit (Fig.3.3.1.4.). The upper exclusion limit depends on the maximal pore size. Molecules larger than that cannot be resolved (total exclusion), for those, $K_{GPC} = 0$. The lower exclusion limit is determined by the minimal pore size. Molecules smaller than the smallest pores permeate the whole column volume (total permeation) and thus cannot be separated, i.e. $K_{GPC} = 1$. Within these limits, separation of polymer molecules by molecular weight is achieved:

$$V_e = V_0 + K_{GPC} \cdot V_h$$

V_e = elution volume
V_0 = interstitial volume
V_h = hydrodynamic volume of the molecule

The separation range of the setup can be extended by connecting several columns with different pore size ranges in series, or by using a ‘mixed bed’ column containing material of different pore sizes.

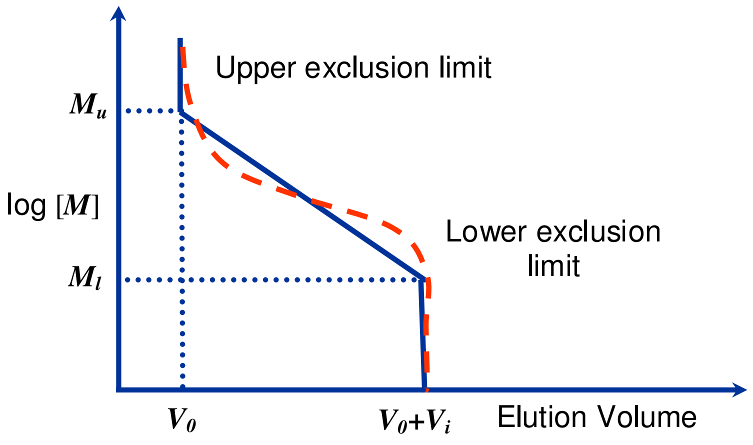

Fig. 3.3.1.4.: Exclusion limits: plot of log $[M]$ vs V_e, $[M]$ = number average molar mass, M_u = maximal mass resolved, M_l = minimal mass resolved, - = experimental curve. - = theoretical curve

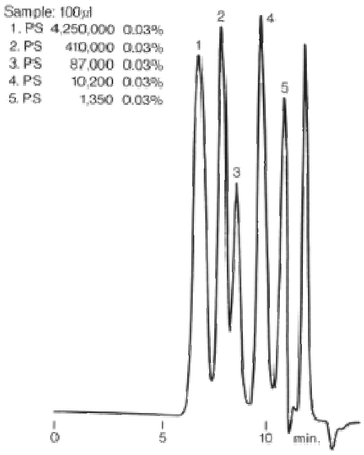

Fig. 3.3.1.5.: Elugram (elution time vs. detector intensity) for poly(styrene) standards[38]

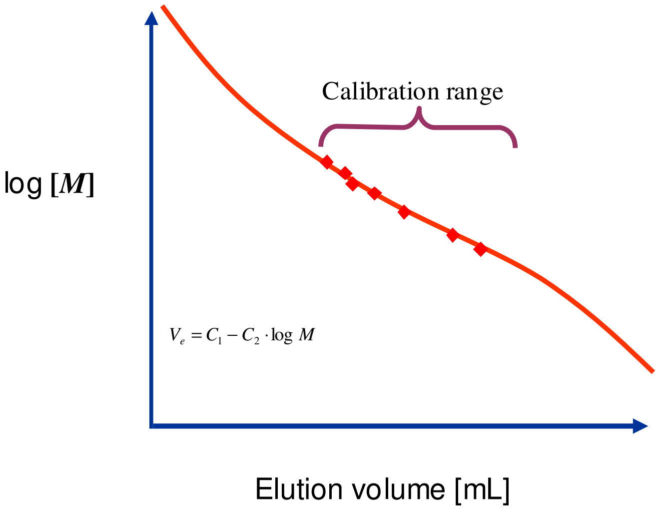

Fig. 3.3.1.6.: Calibration curve for GPC, C_1, C_2 = Constants determined from the linear range of the calibration C_1 = y axis intercept, C_2 = slope

As GPC is not an absolute method, calibration with a standard of known molecular weight is necessary. The elugram obtained for a series of narrowly distributed GPC standards, the masses of which were previously determined by static light scattering, is shown in Fig. 3.3.1.5.. With the knowledge of the elution volumes of these samples, a plot of log $[M]$ versus V_e (Fig. 3.3.1.6) can be used to determine the molecular weight of unknown polystyrene samples. This plot is only valid for the same type of linear polymer in the same solvent. For other polymers in different solvents, calibration curves are imprecise as the hydrodynamic volumes are different. This limits the applicability of GPC for chemically new polymers. With a knowledge of the calibration curve (Fig. 3.3.1.6.), in combination with the elugram, the number average molecular mass distribution of the polymer can be calculated (Fig. 3.3.1.7.).

As the hydrodynamic volume of a substance is defined as

$$V_h = const \cdot [\eta] \cdot M$$

V_x = hydrodynamic volume of the molecule
$[\eta]$ = intrinsic viscosity
M = number average molecular weight of the molecule

the elution volume depends on molecular structure through the intrinsic viscosity $[\eta]$, which is lower for branched molecules than for linear ones.

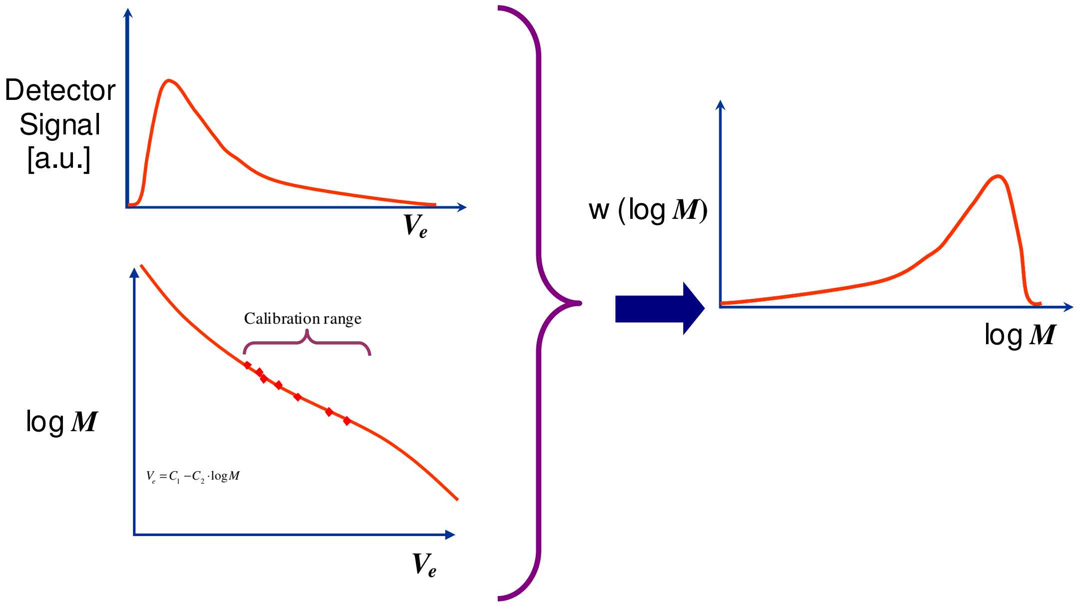

Fig. 3.3.1.7.: Derivation of the molecular mass distribution from the GPC elugram and the calibration curve; w (log M) = weight fraction

The elution volume of the sample may be further influenced by structural parameters of the polymer sample. If there is enthalpic interaction of the column material with the sample, this will cause an elution delay, i.e. V_e is increased and the molecular weight calculated will be too small. If the sample and the column material are identically charged and no salt is added to the eluent, ion exclusion occurs. The sample cannot enter the pores due to electrostatic repulsion, i.e. V_e is decreased and the molecular weight obtained is too high. If the sample has a highly branched structure, it might be stretched, deformed or even fragmented due to entanglement of the side chains in the column pores. This process, called degradation, also results in misleading GPC results.

From an instrumental point of view, the following factors limit the quality of GPC results: A constant flow rate is crucial, as a small error in the elution volume leads to large errors in M_n determined. The solvent quality must be kept constant, as differences in water content limit the reproducibility. The material, the separation range and the particle size of the column as well as the solvent used must be adjusted to the structural properties of the polymer to be investigated. Temperature and pressure need to be constant for reproducible results, otherwise baseline instabilities occur. Axial dispersion due to band broadening occurs if the flow is too slow, which leads to large errors in the M_n determination. If the flow is too fast, the resolution is decreased. The samples must be completely soluble in the GPC solvent, preferentially from the same bottle as the GPC eluent. The sample concentration depends on the molecular weight ($c \approx 0.25$ w% for M = 50 000 – 100 000 g/mol), it is filtrated through a 0.5 µm filter prior to injection.

With water as an eluent, GPC is less straight forward. Water does not swell or wet conventional styrene-based column materials, thus materials such as poly(dextrans) or poly(acrylamides) are used. For those, there is a pressure limitation, as they are soft gels. Frequently, adsorption of the macromolecules due to electrostatic interactions, hydrogen bonding or enthalpic interactions with the column material occur. To suppress these, deactivation agents (salts, small percentage of organic solvents) are added. Reliable and reproducible results are only obtained if the eluent properties (pH, ionic strength, amount of organic solvent) are carefully chosen. Some of these problems were overcome by new column materials that are more water-compatible (Suprema, MCX columns by PSS Company, Mainz). For the analysis of polyelectrolytes in water, the issues discussed above are particularly critical, as the reproducibility of GPC on polyelectrolytes depends also on charge number, the counter-ions, the solvent polarity and electrical screening properties of the solvent. Due to osmotic swelling, solvent molecules diffuse into the polyelectrolyte molecule, and a small part or the counter ions diffuses into the bulk solvent (Fig. 3.3.1.8.). This changes the hydrodynamic volume of the sample. The effect can be suppressed by addition of strong electrolytes (sodium trifluoroacetate, LiBr, $NaNO_3$ etc.).

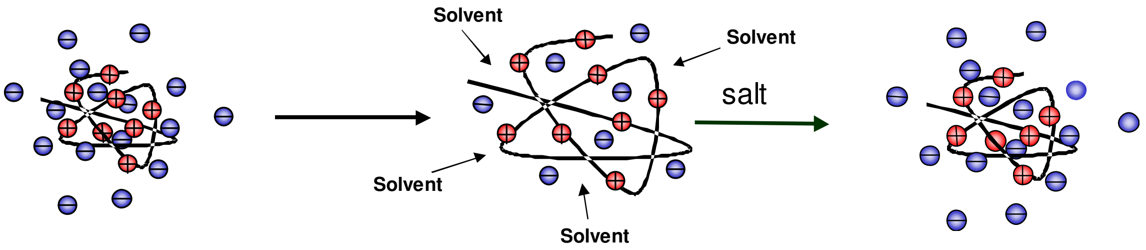

Fig. 3.3.1.8.: Swelling of polyelectrolytes in water[37], effect of salt addition

3.3.2. Universal Calibration[38]

As discussed in the previous section, GPC is intrinsically a relative method, i.e. the molar mass distribution curve is obtained by calibration. However, it is possible to obtain a universal calibration curve with a reference compound. As discussed above, the product of the molar mass of a sample and its intrinsic viscosity $[\eta]$ are proportional to the hydrodynamic volume of the substance. If $\log[\eta]_s \cdot M_s$ is plotted vs. V_e, the elution volume, with the relation $\log[\eta]_x \cdot M_x = \log[\eta]_s \cdot M_s$, V_e can be related to the molecular weight M_x of the sample, if the intrinsic viscosities of sample and reference compound are known. Thus, GPC can be used for a more reliable estimation of the molecular weight of a compound. As shown in Fig. 3.3.2.1., plots of $\log[\eta] \cdot M$ vs. V_e coincide for many structures, no matter what the chemical identity or the structure of the polymer is.

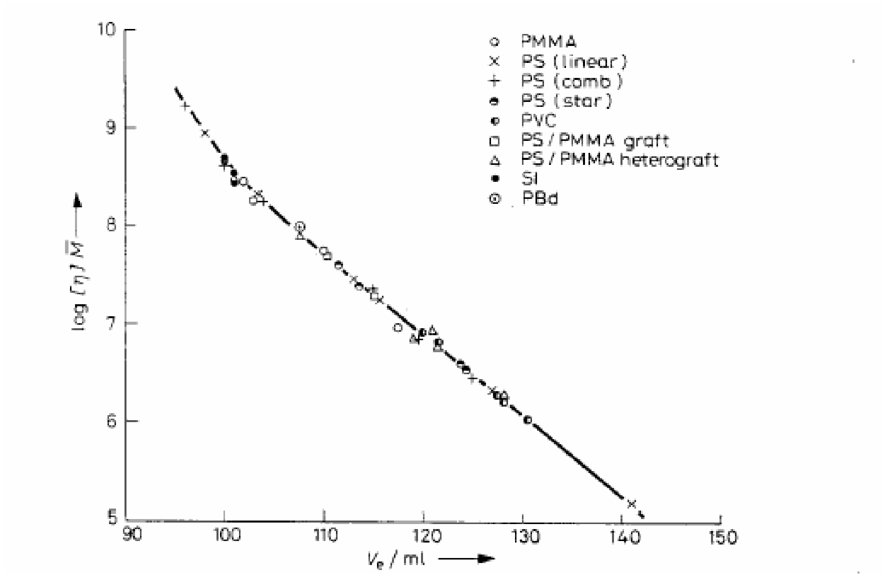

Fig. 3.3.2.1.: Universal calibration[38]

3.3.3. GPC-MALLS[39,40,41]

GPC can be coupled with other analytical techniques, such as light scattering methods, viscosimetry or NMR. Thus, each peak in the GPC elugram can be more profoundly characterized. In the following section, the coupling of GPC with static light scattering will be discussed. GPC-MALLS refers to GPC coupled with a multi-angle laser light scattering (MALLS) detector. For this experiment, the same setup as shown in Fig. 3.3.1.1. is used, only the UV detector is replaced by a MALLS detector. In contrast to UV and RI detectors, which are concentration sensitive, the MALLS detector is mass sensitive. In off-line static light scattering, the molecular weight is determined by measuring the angular dependence of Kc/R_θ. The extrapolation to $c = 0$ and $q^2 = 0$ yields M_w. In GPC-MALLS, Kc/R_θ is measured for defined small volume elements along the GPC elugram. As the concentration in each volume element is very small (typically 10^{-5} g/L), it can be approximated as $c = 0$. For each volume element, extrapolation to $q^2 = 0$ yields a value M (Fig. 3.3.3.1., left). Summation over all M values and weighting (with reference to the concentration-sensitive, previously calibrated refractive index signal, see Fig. 3.3.3.1., right) gives the M_w value for the whole sample.

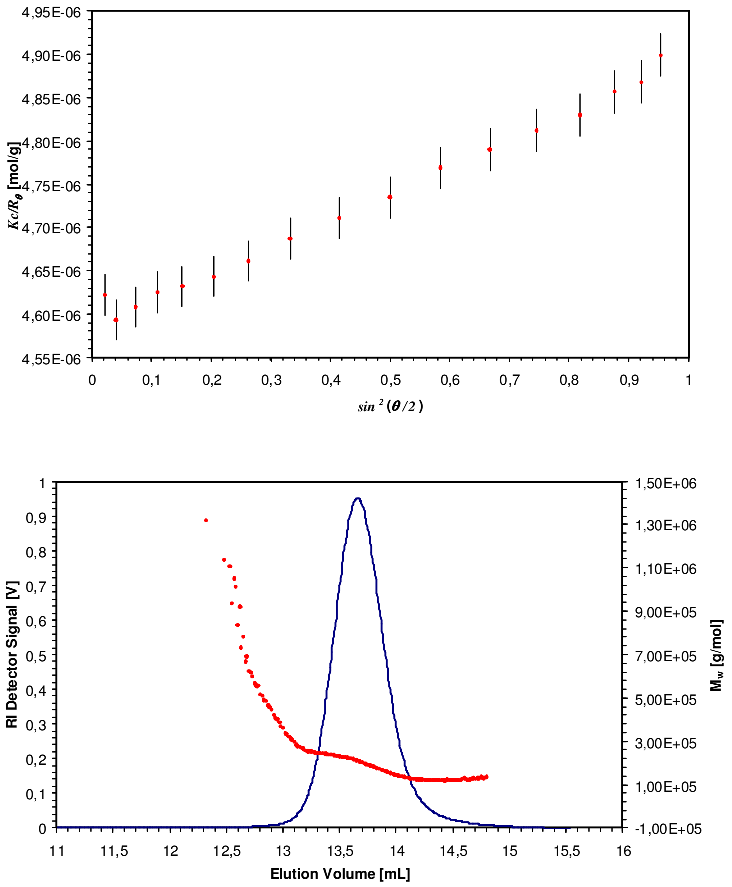

Fig. 3.3.3.1.: Zimm plot (left) for an individual slice from the GPC-MALLS elugram (right) for the macroinitiator precursor **PpMS11**

As shown in Fig. 3.3.3.1., right, there is an approximately linear relation between M_w and V_e, indicating that the separation of the polymer is indeed by hydrodynamic volume. The deviation at the tails of the chromatogram is due to instrumental issues, as discussed by Radke and Müller[42]. Fig. 3.3.3.2. shows a plot of radius of gyration vs. molecular weight. For a separation by molecular weight only, there should be a linear correlation between these two parameters. This is indeed found for non-branched molecules (Fig. 3.3.3.2., left).

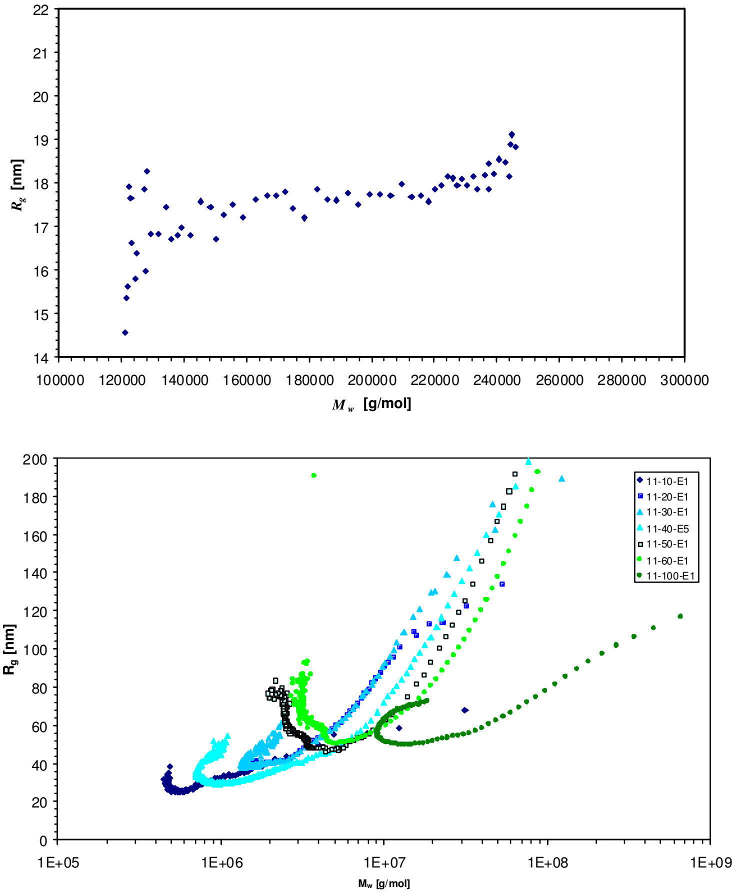

Fig. 3.3.3.2.: Plot of radius of gyration versus M_w for a linear molecule (left) and polymer brushes (right, see also chapter 8.6.)

For branched structures, such as polymer brushes, anomalous behaviour is observed (Fig. 3.3.3.2., right). It was found that with branched samples, strong tailing on the lower molar mass flank of the GPC curve occurred. GPC-MALLS revealed that, in contradiction to normal GPC behaviour, in this tailing, the molar mass of eluting molecules *increased* with elution volume. This was explained as follows: additionally to the normal GPC separation process, a second mechanism occurs which delays the molecules and lets them elute much later than expected for their molecular weight. This causes co-elution of these molecules with smaller ones, which leads to nonlinearity of the R_g vs. M_w curves. Such effects are usually attributed to an overloading of the column or adsorption of the polymer on the stationary phase. As the effect does not occur with linear polymers of the same chemical identity, and does not vanish upon reduction of the column loading by an order of magnitude, Schmidt et al.[43] concluded that this was due to a 'sieving effect'. It was found that the radius of gyration of the poly(methylmethacrylate) brushes investigated was of the same size as the voids between the particles of the stationary phase. Thus, it was assumed that large branched molecules 'reptate' through these voids and are thus retarded, which causes their elution at higher elution volumes. This indicates that GPC alone is not suitable for the analysis of polymer brushes. A coupling of GPC with the MALLS detector gives much more meaningful information for this analytical issue. Ideally, polymer brushes should be characterized by triple detection, i.e. by GPC coupled with RI, MALLS and viscosity detector. Thus M, $[\eta]$ and R_g are determined across the entire distribution. The processing of these signals together at each data slice gives information about the degree of branching of the sample. As an additional information, the refractive index increment is necessary for GPC-MALLS, which can be obtained from off-line refractive index increment measurements. With this information, the recovery rate of the polymer can be calculated (recovery rate = mass found/mass injected). This is a very important parameter as it gives information about significance of the results obtained. Low recovery rates (0 to 0.6) indicate that the polymer distribution observed is only a fraction of the polymer injected, i.e. a good part of the sample is filtered out by the column or other setup components. The results obtained are then not representative for the polymer distribution that is to be investigated.

3.4. Analytical Ultracentrifugation (AUC)[44,45,46]

With analytical ultracentrifugation, molecular parameters such as mass, mass distribution, sedimentation coefficient, diffusion coefficient and the osmotic virial coefficient can be determined. There are two measurement modes: sedimentation velocity and sedimentation equilibrium. Only the first method was used in this work, therefore the sedimentation equilibrium will not be discussed further.

In the sedimentation velocity experiment, by fast rotation (up to 60 000 rpm) the molecules are subject to a centrifugal force. Depending on their mass and molecular shape, the molecules sediment at different rates. The centrifugal force is opposed by a frictional force, which is proportional to the sedimentation velocity, plus the buoyant force:

$$F_c = F_f + F_b \Leftrightarrow M\omega^2 r = f'\frac{\mathrm{d}r}{\mathrm{d}t} + M\upsilon\rho\omega^2 r$$

F_c = centrifugal force
F_f = frictional force
F_b = buoyant force
M = molar mass
ω = angular frequency
ρ = density of the solvent
υ = partial specific volume
r = radius
f' = frictional coefficient
t = time

This rearranges to

$$M(1-\upsilon\rho)\omega^2 r = f'\frac{\mathrm{d}r}{\mathrm{d}t}$$

For an ideal solution, the frictional coefficient is related to the diffusion coefficient by

$$f' = \frac{RT}{D}$$

R = universal gas constant
T = temperature
D = diffusion coefficient

Including the definition of the sedimentation coefficient,

$$s = \frac{\frac{\mathrm{d}r}{\mathrm{d}t}}{\omega^2 r}$$

s = sedimentation coefficient
$\mathrm{d}r/\mathrm{d}t$ = sedimentation velocity

the Svedberg equation is obtained

$$\frac{D}{s}(1-\upsilon\rho) = \frac{RT}{M}.$$

Thus, to calculate the molar mass, the diffusion coefficient, the sedimentation coefficient, the density of the solvent and the partial molar volume of the molecule must be known. The latter is related to the density of the particle. To obtain meaningful results, it must be known to a high precision. The sedimentation velocity is measured by tracking the sedimentation front in the sample. It follows from the Svedberg equation that, for a distribution of molar masses, a distribution of sedimentation coefficients is obtained. This is expressed as a plot of $g(s)$ vs. s, where $g(s)$ is the relative amount of molecules with a sedimentation coefficient s. A typical example for such a distribution is given in Fig. 3.4.1.. From the Svedberg equation it can be seen that the sedimentation coefficient is directly proportional to the molar mass. Consequently, the s distribution looks reciprocal to a GPC elugram.

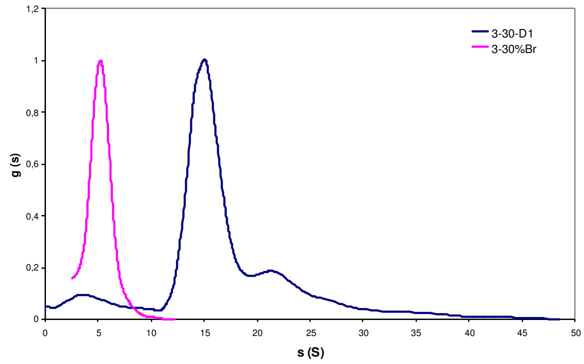

Fig. 3.4.1.: Sedimentation coefficient distribution for macroinitiator **3-30%Br** and polymer brush **3-30-D1**

3.5. Imaging Techniques

3.2.1. Transmission Electron Microscopy (TEM)[47]

The basis for all optical imaging methods, whether they are performed by photons or electrons, is Abbe's imaging theory (Fig. 3.5.1.1.).

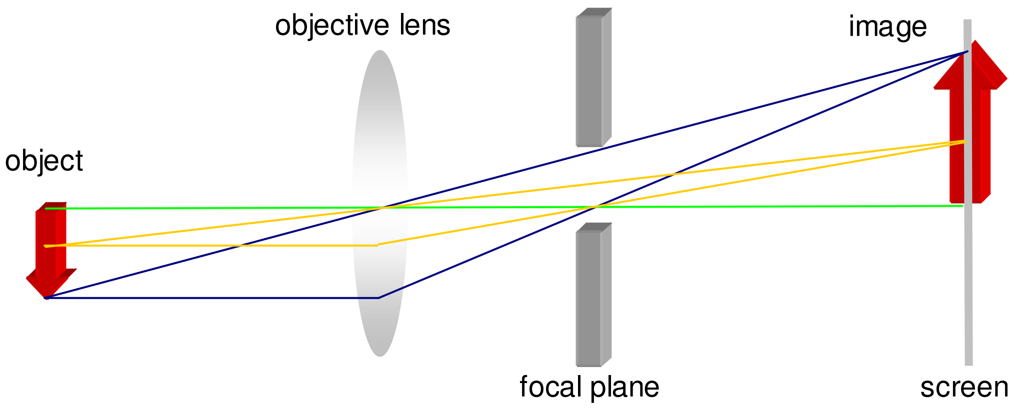

Fig. 3.5.1.1.: Abbe's imaging theory

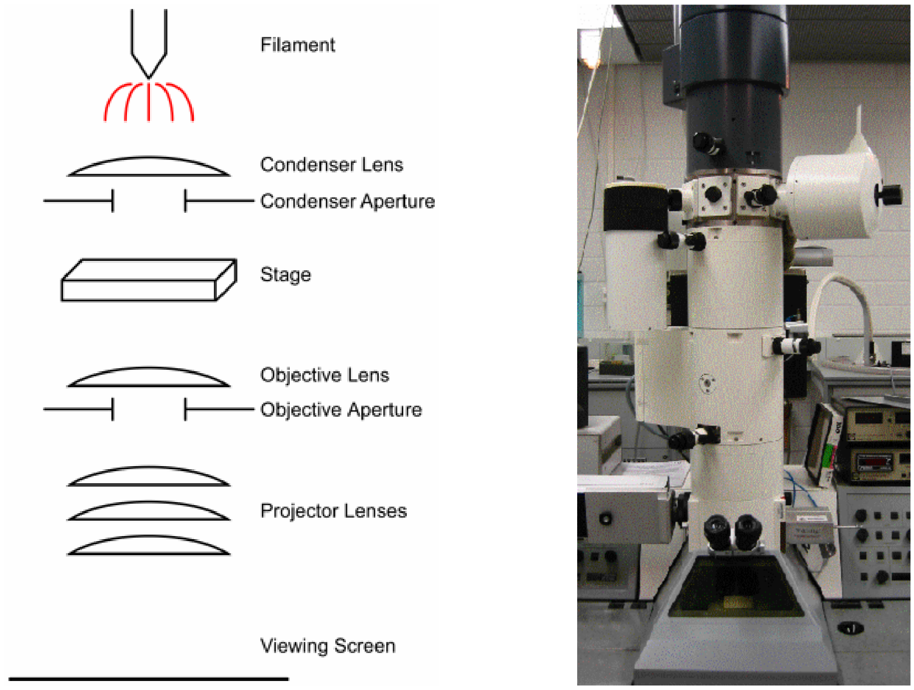

Fig. 3.5.1.2.: Principle of a transmission electron microscope (left), Electron microscope LEO 912 from ZEISS (right)

According to Abbe's theory, the object scatters light, which is collected by the objective lens and focussed on the focal plane. In the focal plane, the diffraction pattern of the object is formed, which contains all the information about the object that will be contained in the image. At the image plane, the scattered light interferes and forms an inverted image of the object. This is the principle of the set-up of a transmission electron microscope, which is shown in Fig. 3.5.1.2.[48]. The whole set-up is placed in a vacuum chamber to minimize scattering of the electron beam in the atmosphere.

The main difference is that, besides electrons being used instead of light, the lenses are electromagnetic coils. The electrons are created by the filament of the electron gun, which is typically operated with 100 to 1000 kV, and parallelized by the condenser lens. The condenser aperture selects the central beam of these parallelized beams. The specimen, placed on the stage, diffracts the electrons. These are focused by the objective lens. The objective aperture is placed in the back focal plane of the object and selects the beams of the diffraction pattern which will contribute to the image. The widely diffracted beams carry the information about the fine details of the object. Thus a big aperture increases the resolution, while a small one increases the contrast at the expense of structural details. With the spectrometer and the slit, which is placed between the objective aperture and the projection lenses (not contained in Fig. 3.5.1.2., left), inelastically scattered electrons can be selected according to their energy loss and thus assigned to specific atoms contained in the sample. The projection lenses focus either the image or the diffraction pattern on the viewing screen. Theoretically, the resolution of an electron microscope is limited by the electron wavelength used and the quality of the lenses. While the wavelength of the electrons (0.04 Å at 100 kV acceleration voltage) is small enough to image objects on the sub-angström length scale, the resolution is limited by the quality of the electromagnetic lenses to an effective resolution of 1.5 Å. This is due to the failure of the electromagnetic lenses to preserve both the amplitude and the phase of all diffracted beams during recombination. This effect is stronger for the widely scattered beams. It can be partially compensated by a slightly defocusing the objective lens.

With the objective aperture, special areas of the diffraction pattern can be selected for imaging. When the transmitted beam is selected, so-called bright field images are formed. When one of the diffracted beams is selected, a dark field image arises, which shows inverse contrast to the bright field images. Dark field images have more contrast and less intensity than bright field image. By positioning the aperture at a specific position in the diffraction image of the sample, specific crystalline areas of the sample can be imaged. For amorphous samples, dark field images do not give further information.

The spectrometer suppresses inelastically scattered electrons for bright field and dark field images, as they would contribute to the background noise. By selecting different energy losses ΔE with the spectrometer, the interaction of the electrons with defined elements in the sample can be imaged. The energy loss is specific for each element, as it corresponds to the energy difference of an electronic transition between two shells in the atom. This technique is called electron energy loss spectrometry (EELS).

The contrast in TEM is due to different electron densities in the sample, which have different scattering powers for the incident electrons. Crystalline samples give a diffraction contrast, amorphous materials give a mass contrast. Polymeric materials have usually low atomic number atoms and are thus weakly scattering. They are beam sensitive – crosslinking and chain scission occur. This can be counteracted by using higher acceleration voltages and cooling the sample. The samples imaged in electron microscopy must be thin enough to be transparent for the electron beam. Certain features of the sample can be emphasized by special preparation techniques to improve the electronic contrast of these features to the background. These techniques include polishing, staining, etching, replication, application of a conductive coating or embedding of the sample into a matrix. Most of these methods were established for imaging bulk substances or thin films. For imaging single molecules, different preparation methods are used. The simplest preparation method involves drop-casting of the polymer solution on a carbon film that is mounted on a copper grid. The carbon film is prepared by vacuum evaporation of graphite onto a glass substrate and floating off of the carbon film on water. Such a film is hydrophobic and can be used for drop-casting from organic solvents. With aqueous solvents, de-wetting is observed. To increase the hydrophilicity of the carbon film, it is exposed to a glow discharge in a partially evacuated evaporation chamber. To improve the contrast in polymer solutions, the sample can be stained with lead, tungsten, molybdenum, vanadium, caesium or uranium. This is called negative staining, as the object will appear lighter than the surrounding stain due to its lower electron density. After drying, samples prepared are ready for imaging. The advantage of this preparation technique is that it is very fast. However, in many cases, the contrast is poor as the carbon film causes background noise and has a similar electron density as the polymer. To improve the contrast, the sample can be shaded with platinum/carbon or tungsten/tantalum. For that purpose, the samples are shaded at an angle of 30° to 60° by evaporation of the shading agent, thus hills of the samples are covered with the shading agent on one side, while valleys remain unstained. This gives a plastic impression of the surface topology. The disadvantage of these methods is that the shape of the molecules imaged strongly depends on the nature of the supporting surface, and the dimensions measured from such an object cannot be directly related to the structure of the object in solution. For aqueous solutions, two methods are available that image a polymer “as in solution”. The first is embedding of the polymer into a trehalose matrix. Trehalose is a disaccharide that forms films upon drying. When mixing the sample solution with an aqueous solution of trehalose (1%) and placing the mixture on a carbon grid or holey carbon film, during drying the trehalose solidifies, which stabilizes the polymer. At the same time, it dehydrates the polymer, as it is strongly hygroscopic. As the molecule does not have any time or space to change its conformation, it is imaged in its native state. The advantage of this method is that it is fast. However, due to the chemical structure of the trehalose film, the contrast to unstained polymeric species is usually poor. However, the method can be combined with negative staining to improve the contrast. The same principle is applied in cryo-TEM. An aqueous solution of the sample is frozen in liquid ethane on a holey carbon film. The frozen sample parts in the holes can then be imaged. The disadvantage of this method is that the sample preparation is tedious. However, the noise due to the solvent film is low.

3.2.2. Scanning Electron Microscopy (SEM)

The main difference between TEM and SEM is that, while TEM is a projection of the entire object, SEM gives information about the sample surface. When using SEM, samples are usually first coated with a metal that readily reflects electrons. This coating also provides a conducting surface for electrons to avoid charging of the sample. The image is formed by scanning along the sample surface. The sample is imaged by the electrons that are emitted from the sample by interaction with the primary beam (secondary electrons). These low energy electrons are then collected onto the imaging screen. Another fraction of electrons from the primary beam is reflected (backscattered electrons). The intensity of both processes is sensitive to the surface topography, i.e. the angle at which the beam strikes the sample. Heavy atoms in a sample lead to a larger proportion of back scattered electrons. Additionally, x-rays are emitted in the imaging process. These can be used for quantitative chemical microanalysis.

3.2.3. Atomic Force Microscopy (AFM)[49,52]

After the development of Scanning Tunnelling Microscopy in 1982[50], which allowed imaging conducting surfaces on the atomic scale, there was an increasing need for an analytical technique that could image non-conducting samples. This can be done by measuring the forces between a nanometre-sized tip and a sample surface by atomic force microscopy (AFM). It was first applied to polymer samples in 1988[51]. The tip can be used to probe the mechanical, adhesive, magnetic, electric, optical and/or thermal properties of the sample. In the context of this work, only mechanical probing will be considered. For imaging the surface of a polymer sample without damaging it, week mechanical interactions of the sample with the tip are needed. Therefore, rather than scratching with the tip across the sample surface (ContactMode^{TM}), oscillations of the tip are excited and the amplitudes of these oscillations while scanning across the sample surface are measured. In this mode, the so called TappingMode^{TM}, the sample is imaged without or with little damage.

A typical AFM is shown in Fig. 3.5.3.1. (left) The principle of AFM operation is revealed schematically in Fig. 3.5.3.1. (right) and Fig. 3.5.3.2.. The scanning tip is connected to a cantilever spring. It scans the sample surface by moving point by point along a defined area of the specimen. This motion is driven by a piezo scanner. A laser beam is focused on the cantilever. The reflections of this beam are directed to a position sensitive photodetector that measures the laser light intensity and correlates the intensity with the cantilever amplitude. With this height information, together with the two scanning directions, a three-dimensional image of the sample surface is obtained. A projection of this image to a contour plot gives the two dimensional AFM image. The tip is usually made from Si_3N_4 or from Si; its diameter can be down to a few nanometers and is typically 10 nm for a standard tip. The tip is triangular or conically shaped and has a spring constant from 0.1 to 500 N m^{-1} depending on the application. Softer cantilevers are used for contact mode to avoid surface deformation. The resonance frequency of the cantilever ranges from 10 to 500 kHz. Two sets of information can be derived from tapping mode AFM. First, with the amplitude, a height profile of the surface is obtained. Secondly, by measuring the forces between the tip and the sample, information about the mechanical or adhesive properties of the sample are obtained. The image thus obtained is called the phase image. Usually, height and phase images are recorded simultaneously. Phase images should be interpreted with care, as the origin of the phase contrast can be manifold.

The advantage of AFM over TEM is that the measurement can be performed under ambient conditions and that the samples need not be ultra-thin. Also, there is no need for staining or coating. However, extremely smooth surfaces are needed. These can be prepared for bulk samples by cutting or breaking, for samples in solution by drop-casting or spin-coating. Measurement artifacts are very common in AFM, therefore images obtained should be treated with the necessary care. The most common artifacts come from dull, dirty or multiple tips. Optical interference, resulting in a wavelike pattern on the surface, is due to poor laser alignment. Maladjustment of the feedback parameters may lead to “tailing” in the direction of scanning near prominent surface features.

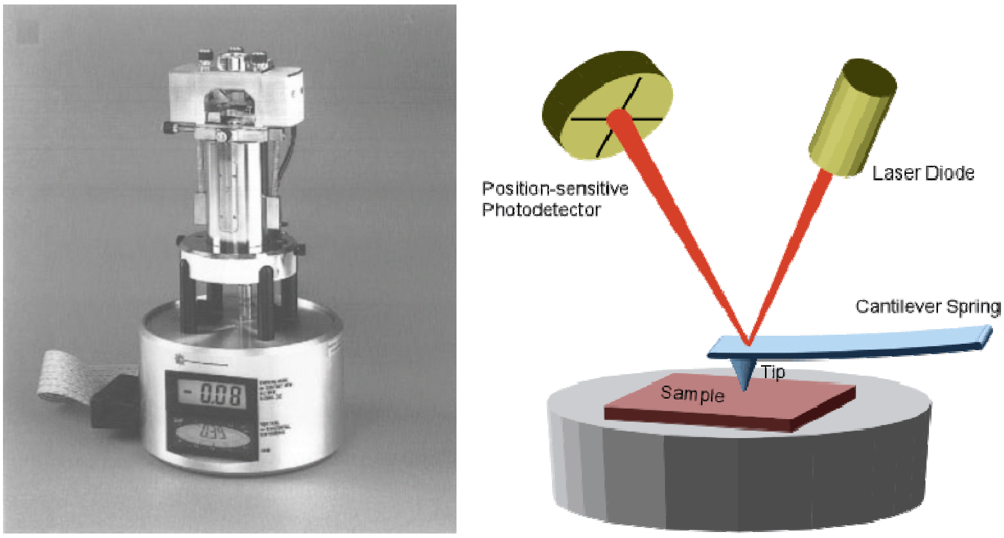

Fig. 3.5.3.1.: Nanoscope II Multimode AFM (left)[52], principle of AFM operation (right)[53]

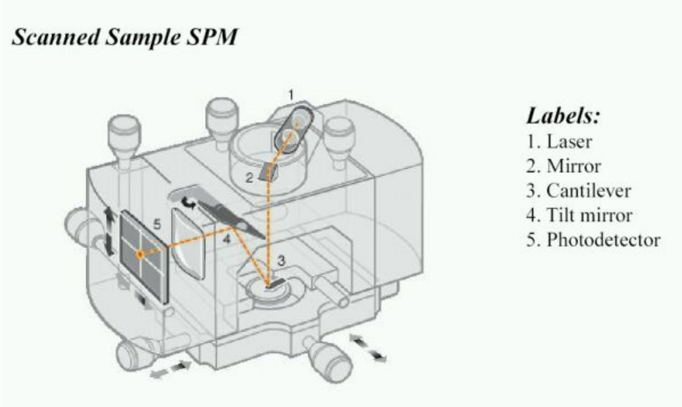

Fig. 3.5.3.2.: AFM Sample holder and detector[54]

3.6. MALDI-TOF Mass Spectrometry

MALDI-TOF MS is an acronym for “Matrix-Assisted Laser Desorption and Ionization Time-Of-Flight Mass Spectrometry”. This method was developed for high molar mass molecules, whose molecular ion peaks cannot be detected in conventional mass spectrometry due to fragmentation. The aim of MALDI-TOF MS thus is to get the entire macromolecule into the gas phase without fragmentation. As high molar mass compounds disintegrate before evaporating, thermal treatment followed by ionization, as done in conventional mass spectrometry, is inadequate. Therefore, the compound is mixed with a low molar mass matrix, which has a strong absorption band at a specific wavelength. When exposed to a laser beam of that wavelength, the energy transfer into the matrix is so efficient that it evaporates so fast that the macromolecule is pulled into the gas phase by the evaporating matrix molecules. An ionizing agent, in most cases a salt, has been added to the matrix-macromolecule mixture to ensure that the neutral macromolecule is ionized by complexation to the cation. Thus, the entire molecule can be accelerated in the electromagnetic field of the spectrometer and is detected by the time-of-flight detector. This device relates the flight time to the molar mass by the following equation, which is derived by equating the formulae for the kinetic energy of a moving particle and its energy due to the electric field:

$$\frac{M}{z'} = \frac{2 \cdot U \cdot t^2}{s'^2},$$

M_n = number average molar mass
z' = molecule charge
U = accelerating voltage of the electric field
s' = flight path length
t = time of flight

The method can be used for samples with M_n up to about 100 000 g/mol. Common MALDI-TOF mass spectrometers can be run in two different modes, the linear and the reflectron mode. In the linear mode, the sample is directly accelerated onto the detector. In the reflectron mode, the macromolecule ions are passed through a system of magnetic fields that perform a recalibration before hitting the detector. Thus, the reflectron mode is more precise than the linear mode. Less stable macromolecule ions can be detected more easily in the linear mode.

As in any analytical method, sample preparation is crucial. Unlike conventional mass spectrometry, where sample mixtures can be analyzed without difficulty, MALDI-TOF samples have to be extremely pure, otherwise desorption is not possible. This refers to low molecular weight impurities as well as to the molar mass distribution of the polymer itself. If low molecular weight compounds are present, these are desorbed preferentially, thus there may not be enough energy left for the macromolecule to be carried into the gas phase. Only for samples with narrow molecular weight distribution ($M_w/M_n < 1.5$), good quality spectra are obtained. The heavier the molecule that is to be analyzed, the narrower the distribution needed. Additionally, it must be assured that a homogeneous mixture between cationizing agent, matrix material and polymer is obtained. For most purposes, this is achieved by dissolving all three components in a volatile solvent, e.g. THF or CH_2Cl_2. After evaporation of the solvent, the sample is ready for measurement. However, phase separation may occur during the drying process. This may prevent the evaporation of the molecule.

While MALDI-TOF MS is a useful tool for analyzing the chemical identity of a macromolecule (e.g. the repeat unit of the polymer, end groups), it cannot be used to analyze molar mass distributions. It has been reported by Montaudo et al.[55] that desorption as well as detection are dependent on the mass, which means that low molecular species are more easily observed. Moreover, ionization appears to be chemically selective, i.e. a side product of the reaction may be ionized more easily than the main product. As only a small fraction of the sample actually reaches the detector anyway, the main distribution in the MALDI-TOF mass spectrum is not necessarily the main reaction product. Also, the complex stability of cation and polymer and thus the spectrum quality strongly depends on the cation used. It is also possible that labile groups in the molecule are eliminated during desorption or flight. MALDI-TOF MS does not reveal whether this fragmentation is caused by the analytical method itself or happened in synthesis. Thus, in some cases, the chemical identity of a substance cannot be determined with MALDI-TOF MS alone, and complementary methods have to be referred to. However, it is a quick and efficient method, requiring very little material (less than 1 mg).

4. Polymer and Polyelectrolyte Brushes

4.1. Polymer Brushes

In the last 20 years, macromolecular research has turned from conventional polymers, i.e. polymers with the usual coil or network structure, to polymers with more sophisticated architectures. Among these, star shaped polymers with a single core, dendrimers, polymer brushes and highly branched polymers such as dendrons attached to a flexible backbone[56] have to be mentioned. The subject of polymer brushes has been summarized very recently in reviews[57] and monographs[58]. Literature uses the term 'polymer brush' synonymously for three entirely different architectures (see Fig. 4.1.1.). Cylindrical brushes consist of a linear backbone, to which polymeric side chains are connected. Two dimensional polymer brushes consist of polymeric side chains attached to a surface. In the case of three dimensional polymer brushes, the side chains are linked to a three dimensional object, e.g. a sphere. Ballauff[59] defines a 2D brush as a polymeric layer gafted to a surface, with a radius of gyration that is much larger than the grafting density. Since this work is limited to cylindrical polymer brushes, the term 'polymer brush' will be used for this type only.

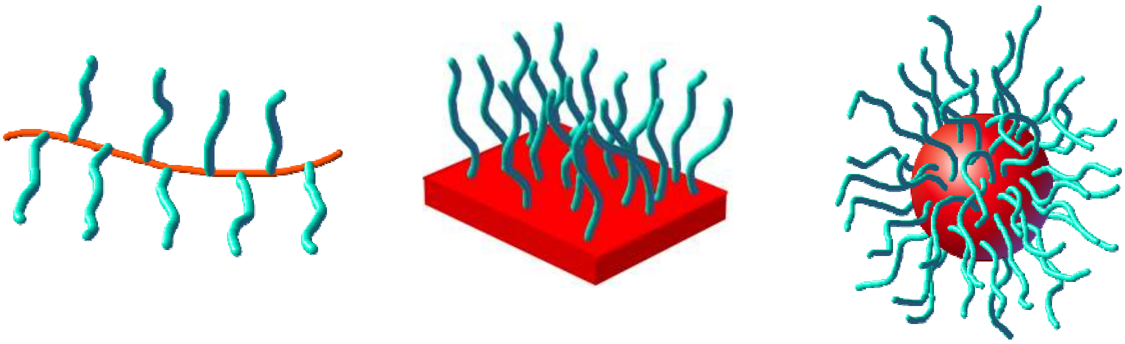

Fig. 4.1.1.: Polymer brush architectures with different 'cores'– cylindrical (1D) brush, planar (2D) brush, spherical (3D) brush

Polymer brushes are intrinsically interesting compounds. Their properties both in bulk and solution differ exceedingly form those of their linear analogues. Compared to linear polymers of similar molecular mass, polymer brushes are smaller and more compact. Their solution conformation depends on the length ratio of the side chains and the backbone, as displayed in Fig. 4.1.2.. At constant side chain length and increasing backbone length, there is a transition from star-like geometry via cylindrical (wormlike and rod-like) to a swollen coil-like shape, where the backbone is so long that its conformation is not affected by the mutual repulsion of the side chains[60,66,61]. At constant backbone length, the conformation changes from coil via expanded coil to cylindrical shapes[62].

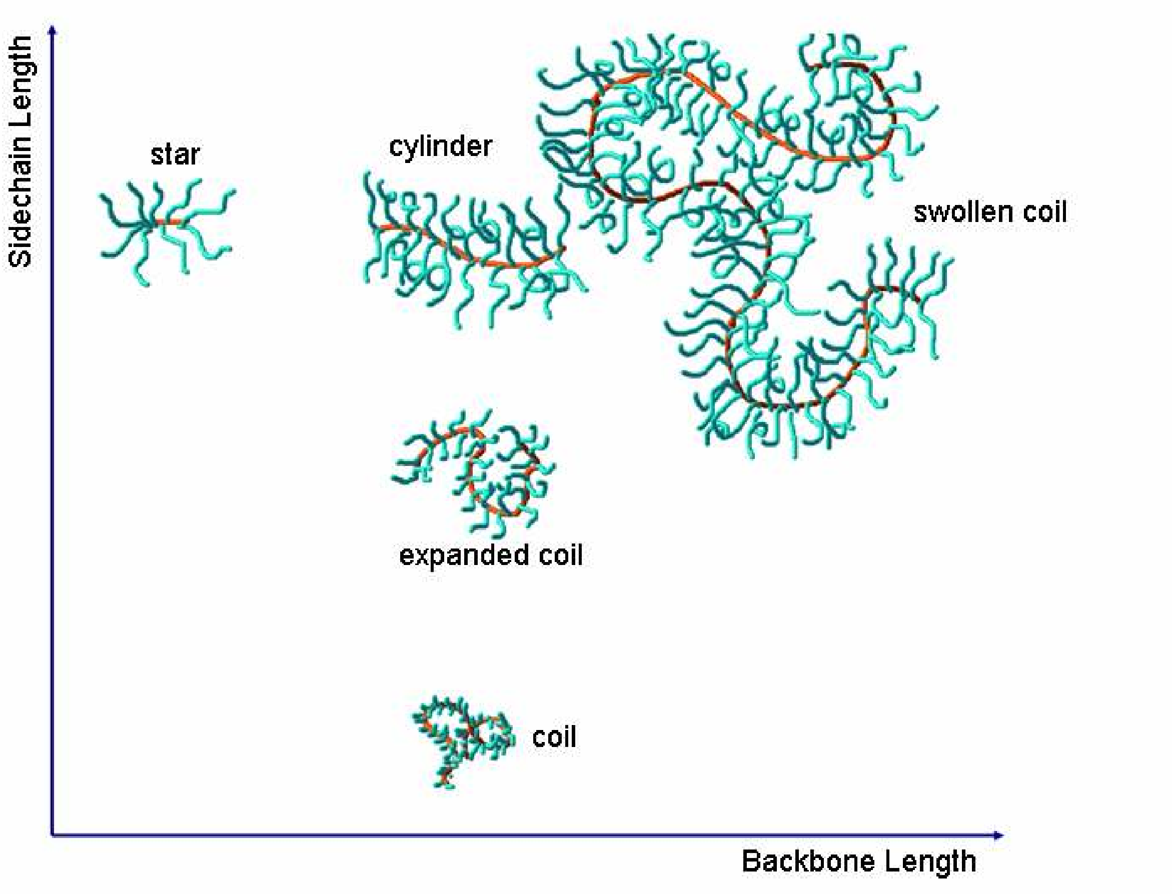

Fig. 4.1.2.: Solution conformation of polymer brushes

More specifically, Schmidt et al.[63] showed that for brushes with identical side chain length and different backbone lengths, the dependence of the radius of gyration on the molecular mass follows the wormlike chain model of Kratky and Porod. Müller et al.[64] showed that the radius of gyration of polymer brushes with identical backbone lengths is proportional to the side chain length $(\boldsymbol{n})^{0.57\pm0.05}$. Schmidt et al.[65] report that the Kuhn statistical segment length $\boldsymbol{l_k}$ as well as the overall contour length of the main chain increases with increasing side chain length, until a limiting value is reached above which no further backbone stretching is observed. Thus the backbone of a polymer brush should be considered as a spring, whose driving force for contraction is entropy. This is counterbalanced by the steric repulsion (excluded volume interaction) of the side chains[66]. In concentrated solutions, some polymer brushes were found to form lyotropic phases[67,68].

In bulk, liquid crystalline phases were found[69]. It was confirmed by SAXS[70], AFM[71] and rheology[72] that polymer brushes are not entangled in the bulk state. Therefore, films made from polymer brushes are very brittle. The glass transition temperature of polymer brushes, compared to their linear analogues, is lower. These are chain end effects, as polymer brush has a much higher chain end concentration compared to linear polymers. The glass transition temperature scales linearly with the side chain length and is almost independent of the backbone length[73].

Polymer brushes can be obtained by the following synthetic strategies:

- ***'Grafting onto'*** refers to the reaction of an end-functionalized polymer (side chain precursor) with a reactive site on the polymer backbone precursor (Fig. 4.1.3.). Both components can be synthesized with low polydispersity by living polymerization methods and analyzed separately prior to the grafting reaction. From these precursors, polymer brushes with well defined molecular dimensions are obtained. However, 'grafting onto' comprises all the disadvantages of a polymer-polymer reaction. With growing conversion, it is increasingly difficult for the side chain precursors to diffuse to the remaining reactive sites on the backbone precursor due to an increase in the local viscosity at the reactive sites (steric repulsion). Entropically, the reaction is unfavourable due to the loss of conformational degrees of freedom of the polymer chains (chain stretching). From a point of view of synthesis, the reaction is limited to monomers tolerating both the living reaction conditions of the precursor synthesis, and the highly reactive functional groups used for the actual grafting. Therefore, the reaction is, up to now, limited to non-polar monomers such as isobutylene, styrene and methyl styrene[74,75,76,77]. Another drawback is that, as the side chain precursor is used in large excess to obtain high grafting densities, purification is tedious.

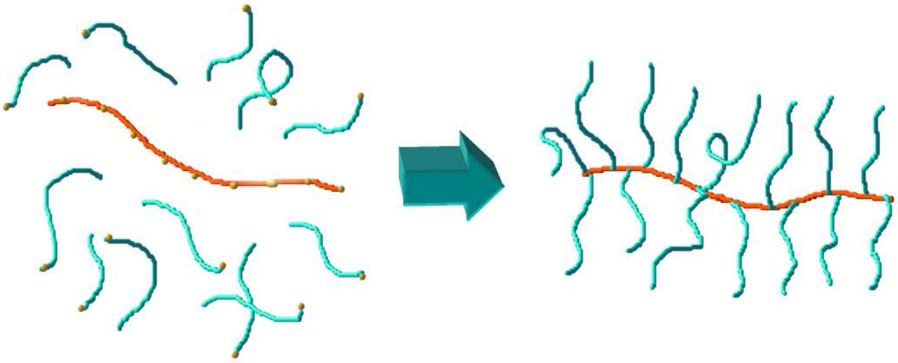

Fig. 4.1.3.: Synthesis of polymer brushes via 'grafting onto'

- ***'Grafting from'***: In the 'grafting from' approach, the side chains of the brush are grown from the polymer backbone precursor carrying initiating sites at regular intervals (Fig. 4.1.4.). These initiate polymerization of an added monomer, most commonly via atom transfer radical polymerization (ATRP). With this method, well-defined brushes with high branching densities and narrow molecular weight distributions have been obtained[78,79,80,81]. ATRP is tolerant to many functional groups, both polar and non-polar. Thus, a wide range of chemically different brushes have been obtained, including acrylates, methacrylates, styrenes, acrylamides and, only very recently, polypeptides[82] and sugars[83]. Polymer brushes synthesized by this strategy are comparatively easy to purify as there is no separation of polymeric species involved. However, if the brush is grown by ATRP, quantitative removal of the catalyst system, especially with polar monomers, is a challenge. Additionally, ATRP with a macroinitiator often leads to gelation due to intermolecular crosslinking. Therefore, the reaction conditions influencing the kinetics (copper and ligand species, solvent, concentration) have to be chosen very carefully, and conversion is to be kept low. If the initiation step is slow compared to the propagation step, incomplete initiation occurs[84], leading to less densely grafted brushes.

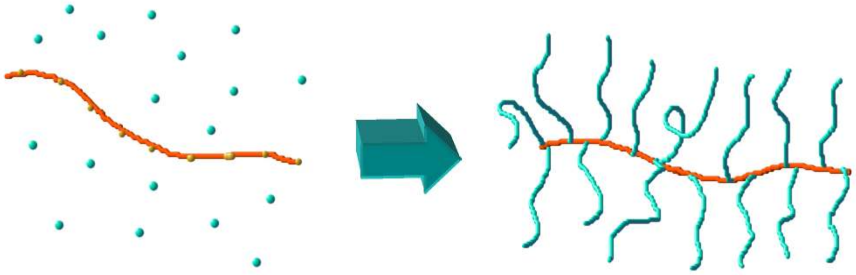

Fig. 4.1.4.: Synthesis of polymer brushes via ‘grafting from’

- ***‘Grafting through’ (Macromonomer route)***: In the macromonomer approach, a polymer containing a polymerizable group (macromonomer) is homopolymerized to get a poly(macromonomer) (Fig. 4.1.5.). In contrast to the above mentioned routes towards polymer brushes, the macromonomer route provides the advantage that the polymer brush obtained has a regular side chain density (one chain per backbone monomer). This cannot be achieved by the above mentioned grafting techniques. The polydispersity of the side chains is low if living polymerization methods are used for their synthesis. The poly(macromonomer), however, is traditionally obtained by free radical polymerization[85,86,87,88,89,90] of the macromonomer in highly concentrated solutions. Therefore, the mass distribution of the backbone is difficult to control and usually broad, yielding a mixture of globular and brush-shaped species, besides the unreacted macromonomer. Consequently, the work up is even more tedious as in the case of ‘grafting onto’. Living polymerization methods such as anionic polymerization[91] and ROMP[92,93] have yet failed to yield high molecular weight polymer brushes.

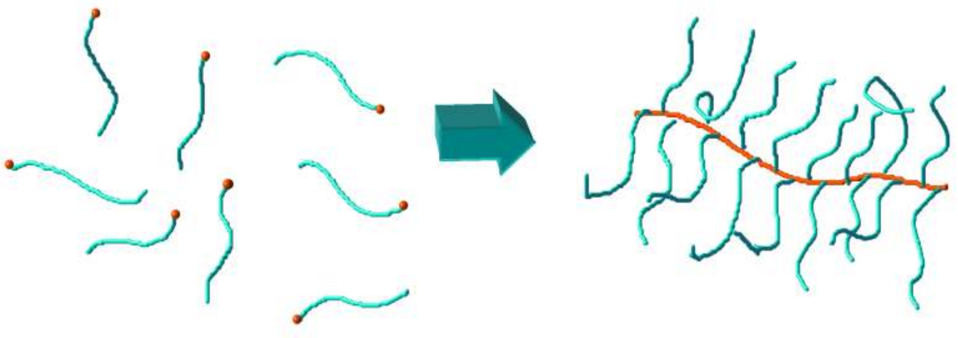

Fig. 4.1.5.: Synthesis of polymer brushes via ‘grafting through’

Although polymer brushes have been studied for more than 15 years by now, the number of applications is still limited, possibly due to the sophisticated synthesis of such molecules. Presently, research focuses on the use of polymer brushes and their polyelectrolyte analogues (see below) as templates in self-assembly as well as for the production of nanowires and conducting, semiconducting and superparamagnetic hybrid nanocylinders for nanoscale devices[94,95,96,97,98]. Additionally, polymer brushes responsive to external stimuli, such as temperature[99] or solvent change[66,100] are being investigated[101]. Their development towards molecular machines is considered. Biological applications, such as attempts to use polymer brushes complexated to DNA for gene transfection, are currently developed[102]. These experiments are still in their infancy, and while it may be possible to use such brushes for gene transfection at a coincidental position of a genome, it is improbable that a directional gene transfection, e.g. for applications in gene therapy, with such simple systems will be successful, as even sophisticated biological systems such as viruses have their limitations in this respect. Applications of polymer brushes for drug delivery[103] and ‘walking molecules’[104] seem more promising.

4.2. Polyelectrolyte Brushes

4.2.1. Polyelectrolytes and their properties

Polyelectrolytes are key compounds in life, as they comprise such important classes of compounds as DNA, RNA and proteins. In industry, they find widespread application, for instance as superabsorbers, ion exchangers and flocculants[105]. However, their properties are not easy to quantify or predict, as they are the result of a combination of polymeric and electrolyte properties: restricted motional freedom caused by the polymer chain, repulsion of the charged repeat units due to electrostatic interactions, long-range intermolecular electrostatic interactions between polyelectrolyte chains, and the influence of condensed or freely moving counterions.

In general, linear polyelectrolytes have larger molecular dimensions than the corresponding neutral polymeric precursors. This is attributed to the electrostatic repulsion of the repeat units. According to Manning[106], linear polyelectrolytes behave differently to conventional electrolytes. They do not dissociate completely, even if their repeat units are strong (completely dissociating) electrolytes. A fraction ***f*** of the counterions is forced to stay close to the polyelectrolyte (Manning condensation), whereas the remaining (1- ***f***) counterions diffuse freely in the surrounding solution. The size of ***f*** is determined by the Bjerrum length $\boldsymbol{l_B}$, defined as

$$l_B = \frac{e^2}{4\pi\varepsilon_o\varepsilon_r k_B T} .$$

l_B = Bjerrum length
e = elementary charge of the electron
ε_0 = dielectric constant in vacuo
ε_r = dielectric constant of the solvent
k_B = Boltzmanns's constant
T = temperature

For two charges at a distance $\boldsymbol{l_B}$ from each other, the electrostatic repulsion is exactly balanced by the thermal energy of the charges. Thus, thermodynamics admit only one charge per Bjerrum length. The surplus counter ions have to remain condensed to the polyelectrolyte.

The osmotic properties of polyelectrolyte solutions are also more complicated than those of uncharged macromolecules. In membrane osmometry measurements on polyelectrolyte solutions containing low molecular weight salt in one chamber versus water in the second chamber, the salt ions migrate into the water chamber until the chemical potentials in both chambers are balanced. This leads to a higher salt concentration in the second chamber due to the presence of the macroion in the first chamber. Consequently, an additional component to the osmotic pressure, the socalled Donnan effect[107] (the second term in the equation for the reduced osmotic pressure), can be measured.

$$\frac{\Pi}{c_p} = RT \cdot \left(\frac{1}{M_n} + \frac{z^2}{4M_n c_s} c_p \right) = \frac{\Pi}{c_p} = RT \cdot \left(\frac{1}{M_n} + A_2 c_p \right)$$

Π = Osmotic pressure
c_p = polymer concentration
R = universal gas constant
M_n = number average molecular weight
c_s = salt concentration
z = charge
A_2 = second virial coefficient

As can be seen from this equation, the Donnan effect influences the second virial coefficient A_2, which also plays a crucial role in light scattering measurements. For the determination of the weight average molecular weight M_w, therefore, the light scattering measurements have to be conducted at high salt concentrations to make this effect negligible. Vrij[108] et al. pointed out that, unless polyelectrolyte solutions have been prepared by isoionic dilution, only apparent values for A_2 and M_w are obtained. The refractive index increment should also be determined in the Donnan equilibrium. In solutions containing no additional salt, the coulomb interactions between polyelectrolyte molecules are hardly shielded and consequently long ranged. This electrostatic repulsion leads to a regular array of polyelectrolyte molecules in solution, which can be found as an intermolecular structure peak in static light scattering measurements[109]. From the position of this structure peak maximum, the inter-molecule distance d_{exp} can calculated by combining the definition of the scattering vector with the Bragg equation [110]:

$$q = \frac{4 \cdot \pi \cdot n}{\lambda} \sin(\vartheta)$$

$$\mathrm{n} \cdot \lambda = 2 \cdot d \cdot \sin(\vartheta)$$

q = scattering vector
n = refractive index
λ = laser light wavelength
ϑ = scattering angle
d = intermolecular distance
n = scattering order

This yields

$$d_{\mathrm{exp}} = \frac{2\pi}{q_{\mathrm{max}}}.$$

d_{exp} = measured intermolecular distance
q = scattering vector
q_{max} = q value at the maximum of the scattering curve (in a plot of I vs q)

The position of the maximum q_{max} is independent of the molecule shape. Assuming a cubic lattice and a uniform particle distribution, the theoretical distance between particles in solution can be calculated as

$$d_{theory} = \sqrt[3]{\frac{M_w}{c_p \cdot N_A}}$$

d_{theory} = calculated intermolecular distance
M_w = weight average molecular weight
c_p = polymer solution concentration
N_A = Avogadro's number

When comparing this value and the experimentally determined molecule distance, it is found that d_{exp} is much smaller than d_{theory}. This is attributed to the coexistence of zones where the polyelectrolyte molecules are close to each other due to electrostatic interaction, and dilute zones where the molecule density is much lower.

The diffusion coefficient of linear polyelectrolytes, which can be measured by dynamic light scattering, depends on the salt concentration of the solution. At high salt concentration, only one diffusion process is found, which splits into two processes at low salt concentration. This is called the 'ordinary-extraordinary transition'. This is shown in Fig. 4.2.1.1. (right): a plot of the salt concentration (c_s) vs. D, the diffusion coefficient, at constant polymer concentration features a transition from the two-mode region to a one-mode region at high salt concentration, i.e. the second mode can be quenched by the addition of salt. In Fig. 4.2.1.1. (left), a plot of c_p vs the diffusion coefficient in “salt free” solution is shown. It clearly indicates the same kind of transition with increasing polyelectrolyte concentration. As reviewed by Förster and Schmidt[110], the phenomenon has been found for many different types of polyelectrolytes. While early studies attributed the phenomenon to a cross-over from the dilute to the semi-dilute region, more recent investigations show that the overlap concentration of the polyelectrolyte molecules, which characterizes the dilute/semi-dilute cross-over, is at much higher concentrations than the ordinary-extraordinary transition.

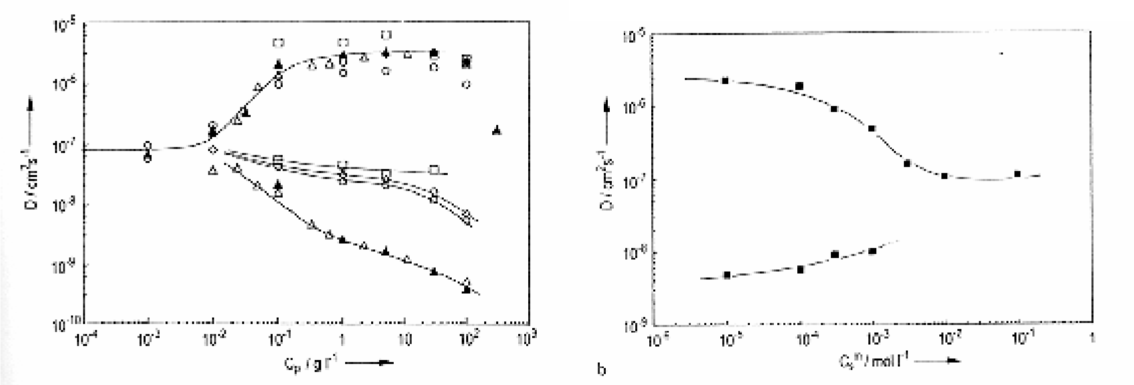

Fig. 4.2.1.1.: Diffusion coefficient (D) as a function of polyelectrolyte concentration (c_p) and added salt concentration (c_s). Left: quarternized poly(vinylpyridine) with different contour lengths and degrees of quarternization[111], right: quarternized poly(vinylpyridine), M_w = 820 000 g/mol, c_p = 0.33 g/L[112]

This led to the interpretation that the smaller of the two diffusion coefficients, the so-called ‘fast mode’, represents the coupled motion of the macroion with its counterions. The nature of the other diffusive process, the ‘slow mode’, is not yet fully understood. It is assumed that it arises from the coupled diffusive motion of polyelectrolyte domains in the solution.

4.2.2. Polyelectrolyte Brushes and their Properties

For highly branched polyelectrolytes such as polyelectrolyte brushes, the issue becomes even more complicated. As far as Manning condensation is concerned, it has been shown by charge density measurements on poly(vinylpyridinium) brushes that the effective charge density of polyelectrolyte brush side chains is much smaller than that of the corresponding linear polyelectrolytes[113], whereas the charge density of the brush along the contour length is significantly larger than that for a linear flexible chain[114]. Consequently, a larger fraction of counter ions is condensed to the polymer brush. In static light scattering experiments, the intermolecular structure peak expected for dilute, salt free solutions of linear polyelectrolytes is not found for dilute solutions of polyelectrolyte brushes, as the electrostatic interactions of the macroions are shielded due to the increased Manning condensation[114]. In dynamic light scattering, the 'ordinary-extraordinary' transition is only found at much higher macroion concentrations as compared to solutions of linear polyelectrolytes[115,116]. This is shown in Fig. 4.2.2.1.. The transition value of c_p/c_s for the linear polyelectrolyte (solid line) is almost two decades lower than that of the branched polyelectrolytes (dashed line).

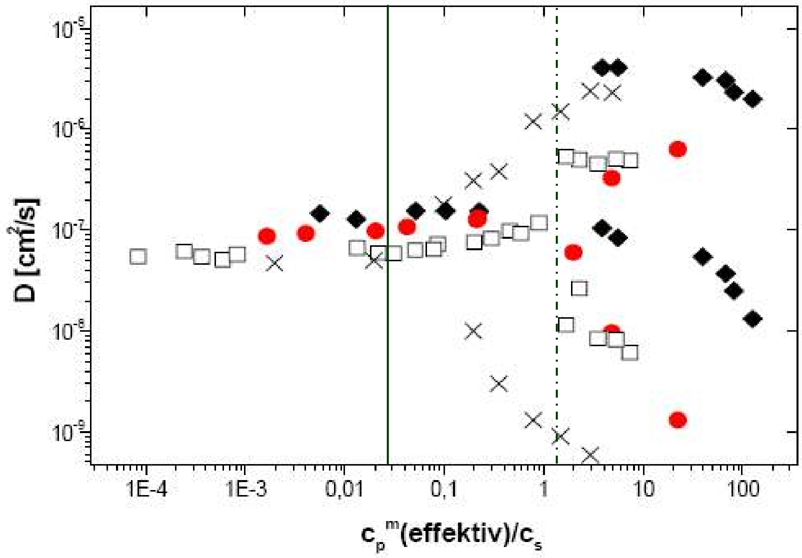

Fig. 4.2.2.1: Ordinary-extraordinary transition for linear poly(vinylpyridinium) (x) and cylindrical poly(vinylpyridinium) brushes (other symbols)[116].

As far as chain expansion due to electrostatic repulsion is concerned, it has as yet not been found for polyelectrolyte brushes. Whereas the transformation of linear poly(vinylpyridine) into its charged pyridinium salt causes chain expansion, neutral poly(vinylpyridine) brushes and their quarternized polyelectrolyte analogues have the same hydrodynamic radii (measured in dynamic light scattering experiments). This is attributed to the already expanded structure of the polymer brushes due to steric repulsion of the side chains. The additional repulsion by electrostatic interaction or osmotic swelling is apparently not large enough to further increase the molecular dimensions[114].

From SANS experiments on poly(methacrylic acid) brushes and poly(styrene sulfonate) brushes obtained by sulfonation of poly(styrene) brushes, the cross-sectional radius of gyration was found to be independent of the added salt concentration, indicating an insignificant influence of osmotic swelling on the side chain conformation. The neutral poly(styrene) brushes had cross-sectional radii of gyration similar to their poly(styrene sulfonate) analogues, confirming that additional electrostatic interactions affect the molecular dimensions[114].

5. Ionic Self-Assembly in Nature and Research

5.1. Synthetic Structures by Ionic Self-Assembly

Structure formation by combination of charged molecules (‘ionic self-assembly’) has been extensively investigated in the past decade, as well-defined nanosized structures can be obtained via this approach. In general, nano- and mesostructured materials are obtained by two different synthetic strategies, the so called ‘bottom up’ and the ‘top down’ method. The ‘top down’ approach deals with the carving of fine structures into unstructured bulk material. This is difficult and expensive. One of the supporting pillars of the ‘bottom up’ method is self-assembly[117], i.e. the formation of ordered structures from specially designed building blocks by non-covalent supramolecular interactions. This can be achieved by e.g. hydrogen bonding[118] or by ionic interaction between molecules[119]. Nature makes use of both of these principles, and others, as can be seen in the hierarchical ordering principles involved in protein folding. In this work, we will concentrate on ionic interactions.

Ionic self-assembly is to be understood as the coupling of structurally different, charged building blocks (‘tectons’) by electrostatic attraction. With this approach, highly ordered nanoscale structures can be generated. An appropriate combination of these tectons (e.g. organic and inorganic ions, oligopeptides, surfactants, lipids, polyelectrolytes, charged polypeptides, DNA, charged chromophores and dyes) yields, for example, supramolecular salts, catanionic surfactant systems, simplexes, polyelectrolyte-supported liquid crystals, DNA-lipid complexes or polyelectrolyte-surfactant complexes[119]. Especially, complexes of polyelectrolytes with surfactants[119] and liquid crystals[120] have been investigated in detail. The latter are expected to find application in molecular electronics. Polyelectrolyte-dye complexes are used in polyelectrolyte analytics. Aqueous complexes are highly organized, forming vesicles and supramolecular rods[121].

5.2. Proteoglycan-Hyaluronic Acid Aggregates in Human Cartilage as an Example for Ionic Self-Assembly in Nature

One important example of self-organization in vertebrates is the formation of aggregates of proteoglycans with hyaluronic acid. A cartoon representation of such aggregates is given in Fig. 1.1.. Fig. 5.2.1. gives selected examples of such aggregates imaged by TEM and AFM. They are found in load bearing tissues such as human cartilage, which is highly resistant to mechanical impacts and at the same time flexible. Due to their ability to absorb large amounts of water and form gels, these complexes form a tissue that can undergo reversible compression in articular cartilage, giving elasticity to blood vessels and contributing to the structural integrity of many tissues such as skin or brain[122].

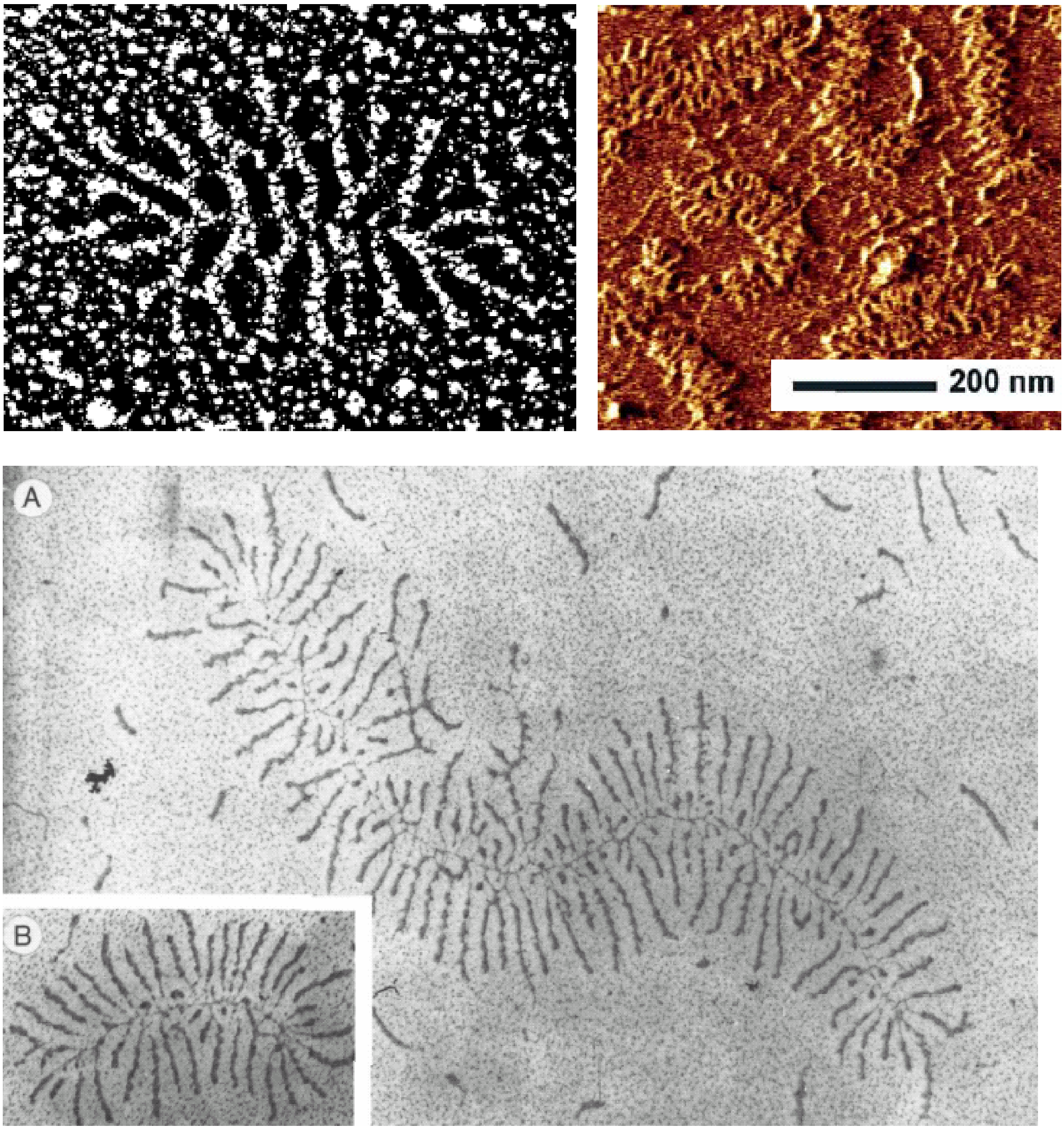

Fig. 5.2.1.: TEM image of the proteoglycan-hyaluronic acid aggregate in human cartilage[123] (top left, no µm scale available); AFM image of bovine nasal proteoglycan-hyaluronic acid aggregate[124] (top right), TEM image of bovine nasal cartilage[125] (bottom; A 32 600x, backbone length ~ 2µm, B 42 000x)

Hyaluronic Acid (hyaluronan) is a glycosaminoglycan consisting of a disaccharide repeat unit (D-glucuronic acid and N-acetylglucosamine, Fig. 5.2.2.). It has a molar mass of approximately 10^6 to 10^7 g/mol. Due to its polyanionic nature, it is a linear rod-like molecule of 2-25 µm length[126]. Besides being a structural component of connective tissues, it forms loose hydrated matrices that enable cell division and migration, adhesion of immune cells and it plays a role in intracellular signalling[122]. Hyaluronan is involved in these processes is due to the ability of many proteins to bind to it. One such protein is contained in proteoglycans. These are anionic polyelectrolyte brushes consisting of a core protein, to which heteropolysaccharide side chains are attached. They are produced in the cell by the Golgi apparatus by glycosilation of the core protein: first, a tetrasaccharide is attached, then glycolsyl transferases add one sugar molecule after the other (which is much like a grafting-from reaction), followed by sulfonation of the sugar side chains[2]. The side chains of aggrecan, the proteoglycan found in human cartilage, consist of chondroitin sulphate (Fig. 5.2.3., left) and keratane sulphate (Fig. 5.2.3, right).

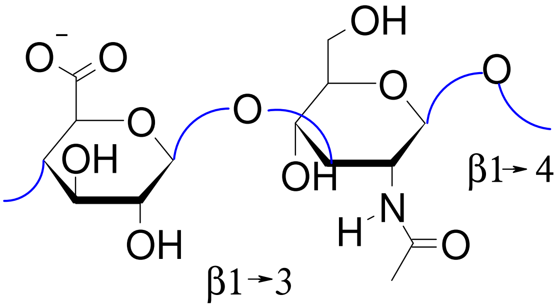

Fig. 5.2.2.: Hyaluronic acid (hyaluronan) repeat unit

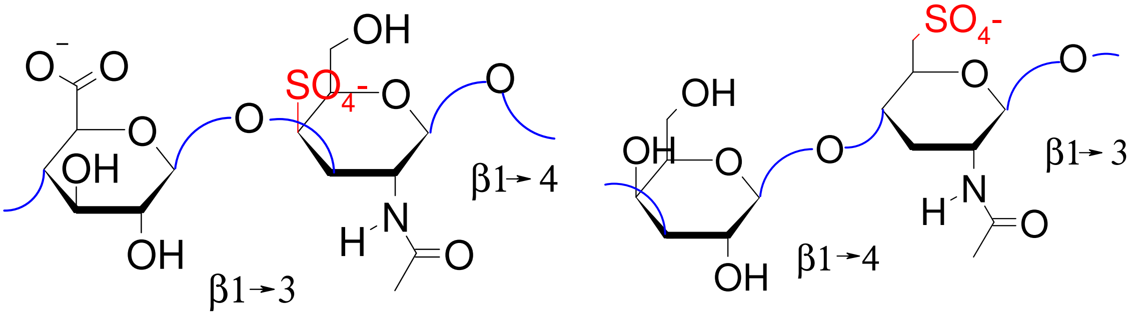

Fig. 5.2.3.: Chondroitin sulfate repeat unit (left) and keratane sulfate repeat unit (right)

A typical aggrecan brush consists of 150 side chains, each having a molar mass of 20 000 g/mol[1] (about 80 repeat units), making a total of 3 000 000 g/mol for the whole molecule. In living organisms, aggrecan and hyaluronic acid are synthesized separately and released into the extracellular compartment, where the aggrecan molecules bind to the hyaluronic acid molecule. The aggregates are non-dissociating and non-displaceable under physiological conditions[127]. Other aggrecan molecules remain anchored on the plasma membrane or become a component of mucus on epithelia[2]. The link between aggrecan and hyaluronic acid is a positively charged, claw-shaped link protein (Fig. 5.2.4.), which is covalently attached to the aggrecan molecule. The binding between the link protein and hyaluronan is mainly due to the formation of ionic bonds between about eight basic amino acids of the protein and the carboxylic acid groups of hyaluronan[128]. Besides the ionic component of the binding, there is evidence that hydrogen bonding and van der Waals forces also play a role[129]. In other hyaluron binding proteins, it was found that there is also the possibility of covalent binding between the protein and hyaluronic acid via an ester bond. To the best of our knowledge, there are as yet no publications on the attempt to mimic these structures by synthetic polyelectrolyte brushes.

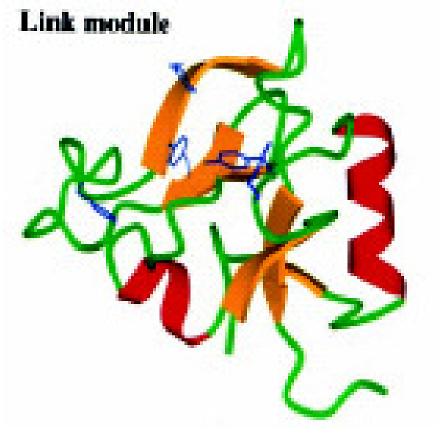

Fig. 5.2.4.: 3D-structure of the link protein in human cartilage, consisting of 2 α-helices and four β-sheets. Four of the amino acids contributing to the ionic binding are marked in blue[122].

6. Synthetic Strategy

6.1. Synthesis of Poly(styrene sulfonate) Brushes in the Literature

Poly(styrene sulfonate) was chosen to model the polyelectrolyte properties of chondroitin sulfate and keratane sulfate, which make up the proteoglycan molecule. The sulfonate groups in poly(styrene sulfonate) were meant to imitate the polyelectrolyte properties of these sulfate-bearing polysaccharides. The carboxylic acid groups also present in chondroitin sulfate are ignored, as their additional incorporation in the model polymer would comprise a series of further complications. This somewhat arbitrary choice was made because of the lack of monomers with more likeliness to the natural heteropolysaccharide. There are reports on the polymerization of methacrylated sugar molecules, including one very recent report of a polymer brush from sugar[130,131,132,133,134]. However, since the sugar molecules in these products are all connected to a synthetic polymer, there is also no structural likeliness between these sugars and the natural 1,4-polycondensated heteropolysaccharides. The synthesis of such monomers, their polymerization and sulfonation to obtain the desired polyelectrolyte brushes would be much more involved and is therefore beyond the time-frame of this work.

In the literature, only few examples of polyelectrolyte brushes made from poly(styrene sulfonate) exist. The majority of these works focuses on two-dimensional polyelectrolyte brushes. Most groups prepared poly(styrene sulfonate) brushes by sulfonation from poly(styrene) brushes attached to surfaces[135,136,137,138]. The big disadvantage of polymers thus obtained is that the functional group distribution is not homogeneous, which causes structure distortions by hydrophilic-hydrophobic interactions. Hugenberg[139] showed that the complete sulfonation of cylindrical poly(styrene) brushes leads to intermolecular crosslinking, making these structures difficult to characterize by light scattering methods. Partially sulfonated cylindrical poly(styrene-co-styrene sulfonate) brushes were not crosslinked, however these systems are also not yet well understood. Ding et al. [140] produced macromonomers from sodium styrene sulfonate and by stable free radical polyermization (SFRP) end-functionalized them with divinylbenzene. Polymerization of these was assumed to lead to poly(styrene sulfonate) brushes, however the authors did not shown that the high molecular weight material obtained actually had brush like properties rather than network characteristics (see below). It has as yet not been show convincingly that polymer brushes can be directly synthesized from styrene sulfonic acid or its derivatives. The reason for this probably is that these monomers are delicate to handle in all living polymerization methods available:

- **Anionic polymerization:** Whicher et al. [141] found that styrene sulfonic acid esters can be successfully initiated by anionic initiators, but due to intramolecular complexation between the living anion and neighbouring sulfonate groups, conversions and degrees of polymerization remained low (10-15%). Upon quenching, the red color of the macroanion persisted, indicating that the termination reaction was slow. Thus, functionalization of poly(styrene sulfonic acid esters) by termination does not seem feasible, which excludes the formation of macromonomers from poly(styrene sulfonic acid ester) by anionic polymerization. There are no publications of functionalization by initiation of this monomer.
- **Stable Free Radical Polymerization (SFRP):** The first report on nitroxide-mediated radical polymerization of sodium styrene sulfonate was by Keoshkerian et al.[142]. Unimodally distributed polymers with M_n from 7 200-762 700 g/mol and M_w/M_n = 1.12-1.96 (GPC) were obtained. Nowakowska et al.[143] obtained high molecular weight poly(sodium styrene sulfonate) based block copolymers. Block-copolymers with low-molecular weight poly(sodium styrene sulfonate) segments (M_n = 2 940-5 700 g/mol, M_w/M_n = 1.25-1.50 (GPC)) were synthesized by Bouix et al.[144]. Ding et al. produced poly(sodium styrene sulfonate) macromonomers by end-functionalization with divinylbenzene (see above). Polymerization of these allegedly led to graft copolymers, however the authors' structural characterization of the products was limited to GPC, FT-IR and DSC measurements[140]. Since molecular shape determinations by, for example, light scattering experiments, have not been carried out, it remains unclear whether the polymer obtained has brush-like structure, or rather is a polymer network, as a result of the incorporation of more than one divinylbenzene unit per polymer chain.
- **Atom Transfer Radical Polymerization (ATRP):** ATRP is extremely tolerant of many functional groups[145], even acidic, water soluble monomers can be used[146,147,148]. ATRP reactions in water are possible, but sensitive to the pH-value of the solution. Below pH=6, protonation of the nitrogen ligand occurs. As a result, the copper species is not complexed and thus not solubilized, i.e. the catalyst complex does not form, leading to failure of the polymerization reaction[149]. There are a few reports in the literature on the aqueous polymerization of sodium styrene sulfonate. However, in all these cases, the macroinitiator for "grafting from" needs to be water soluble. As yet there are no such initiators reported in literature.

- **Radical Addition Fragmentation Chain Transfer (RAFT):** Living Free-Radical Polymerization by Reversible Addition-Fragmentation Chain Transfer was successfully applied to polymerize sodium styrene sulfonic acid with low molecular weights (8 000 g/mol) and low polydispersities (M_w/M_n = 1.13).[150] However, functionalization by RAFT is difficult to achieve and significant effort is to be put into the chain transfer agent synthesis. Thus, there has as yet been no report on polymer brushes obtained by RAFT.

6.2. Non-functionalized Polyelectrolyte Brushes as Model Compounds

Before a selective end-functionalization of one end of the brush was be attempted, non-functionalized polyelectrolyte brushes were synthesized and investigated as model compounds.

6.2.1. Functional Monomer Incorporation versus Sulfonation by Polymeranalogous Reaction

It is frequently reported in the literature that post-polymerization sulfonation of polystyrene, whether as single molecule or attached to a surface, leads to changes in the polymer topology. Hugenberg[139] reports that, for polymer brushes from polystyrene, quantitative sulfonation with sulfonic acid and phosphorus pentoxide leads to intermolecular crosslinking. If milder reaction conditions (Ac_2O, H_2SO_4) are used, only partially sulfonated brushes were obtained. However, due to their partially hydrophobic character, analysis in solution was difficult. Due to these findings, it was decided that, in this work, post-polymerization sulfonation is to be avoided. Consequently, the desired functional group had to be incorporated in the monomer. As the polymerization of styrene sulfonate by ATRP in water is yet only poorly controlled, organosoluble styrene sulfonate esters were chosen as a monomer. The solubility of these monomers and the resulting polymers depends on the ester residue: while the poly(styrene sulfonate ethyl ester) is soluble in acetonitrile, N,N-dimethylformamide and acetone, the corresponding dodecyl ester polymers can be dissolved in dichloromethane, tetrahydrofuran and acetone. The synthesis and polymerization of such monomers has been studied in detail by Woeste[151]. The saponification of these esters leads to the desired polyelectrolyte molecule. Another advantage of this synthetic pathway is that the polymer brushes obtained can be characterized in organic solvents, thus avoiding the additional analytical complications in aqueous solution. The results of the polyelectrolyte characterization in water can be then compared to the results obtained from the neutral precursors.

6.2.2. Polyelectrolyte Brush: Synthesis Plan

The target polyelectrolyte is a cylindrical polymer brush with poly(styrene sulfonate) side chains. The nature of the backbone is only of secondary importance, making various synthetic routes possible. Of all theoretically possible alternatives, the following were identified as the most promising. A detailed account of each approach is given in chapters 7 and 9.

Macromonomer Approach

A macromonomer bearing functional groups that are polymerizable by the Suzuki cross coupling reaction was to be synthesized. This was realized as shown in Fig. 6.2.2.1.:

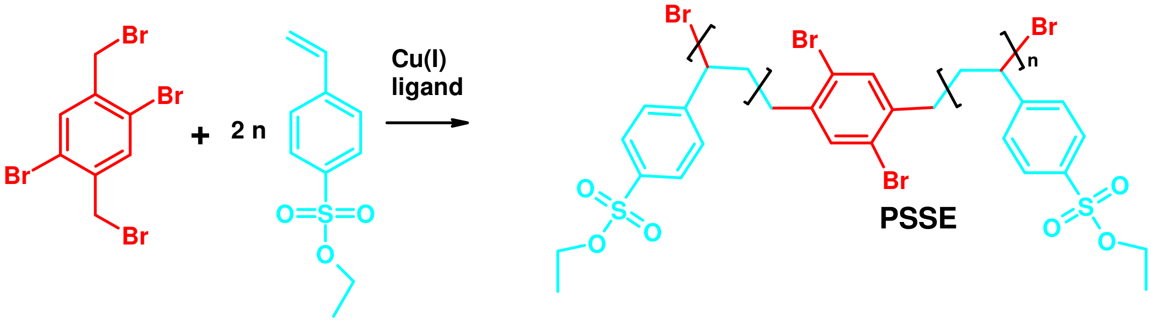

Fig. 6.2.2.1.: **PSSE** AA-macromonomer

Figure 6.2.2.1. shows the synthesis of an AA-macromonomer, whose saponification and copolymerization with benzene diboronic acid would lead to the desired polyelectrolyte brush with a regular grafting density of one side chain per two benzene units. The corresponding AB-macromonomer, which was also synthesized, is shown in Figure 6.2.2.2.. The saponification and homopolymerization of this macromonomer would lead to a polyelectrolyte brush with precisely one branch per benzene unit of the backbone. However, attempts to polymerize both macromonomers were unsuccessful, for reasons to be discussed in chapter 9. Yet, pursuing the macromonomer approach helped to establish the polymerization of styrene sulfonate esters by ATRP and gave vital information on the reaction kinetics of these monomers.

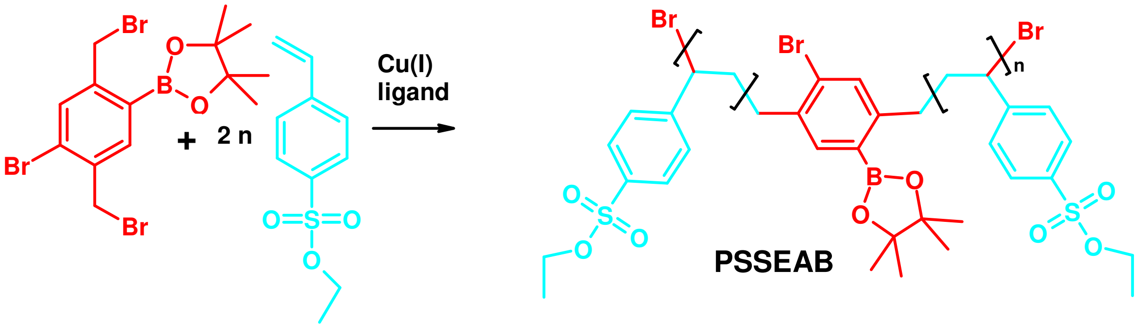

Fig. 6.2.2.2.: **PSSE** AB-Macromonomer

Macroinitiator Approach

As the macromonomer approach proved to be unsuccessful, the synthesis of the polyelectrolyte brush by the macroinitiator approach was attempted. The synthesis of a macroinitiator was attempted by bromination of anionically polymerized methyl styrene (Fig. 6.2.2.4., step 1 and 2) according to a method described by Janata[152].

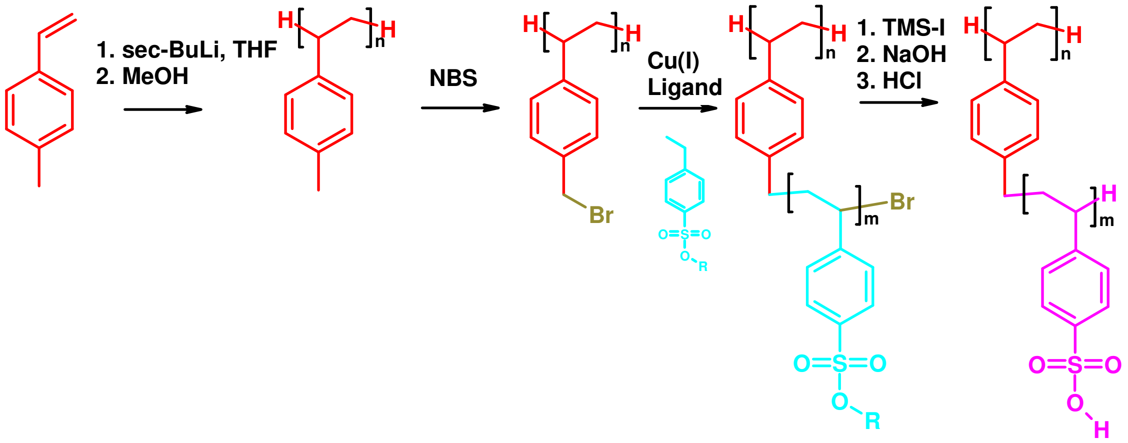

Fig. 6.2.2.4.: Synthesis of the non-functionalized polyelectrolyte brush

The resulting macroinitiator was successfully used to initiate the polymerization of two styrene sulfonate esters via ATRP (Fig. 6.2.2.4., step 3). The polymer brushes thus obtained from styrene sulfonate dodecyl ester (R = $C_{12}H_{25}$) had a broad polydispersity and were polymodal, and the reaction was very slow. Additionally, these products were difficult to characterize, as GPC, GPC-MALLS and static light scattering could not be applied (no elution from the column and negative slope in the Zimm plots as discussed in chapter 7.4.). However, imaging techniques (AFM and TEM) confirmed the brush-like nature of these molecules. Saponification (Fig. 6.2.2.4., step 4) was less straight forward than expected. Four different saponification methods were attempted, yielding the sodium salts of the polyelectrolyte. After an ion exchange, the corresponding free acid was obtained. The corresponding polymer brushes obtained from styrene sulfonic acid ethyl ester (R = C_2H_5) were easier to characterize. GPC and GPC-MALLS were available, however off-line static light scattering showed anomalous Zimm plots for reasons to be discussed in chapter 7. The molar mass distributions of the polymer brushes were relatively narrow and monomodal. Saponification yielded the corresponding polyelectrolyte brushes. A detailed account on the synthesis and characterization of both the polymer brushes and polyelectrolyte brushes obtained via the macroinitiator approach is given in chapter 7.

7. Macroinitiator Approach

7.1. ATRP Macroinitiators for Polymer Brushes in the Literature

Figure 7.1.1. displays some of the ATRP macroinitiators that have been used for polymer brush synthesis by “grafting from” in the literature. The first example, (2-(2-bromoisobutyryloxy)ethyl methacrylate) (PBIEM)[153], was shown to be able to initiate both acrylic and styrene-type monomers. It can be obtained from 2-hydroxyethylmethacrylate in a two step synthesis[154] and has been used for the synthesis of the majority of the polymer brushes described in the literature. The advantage of this macroinitiator is that, due to its ester linkage, the side chains can be hydrolyzed. This simplifies the characterization of the entire polymer brush tremendously, as the side chains and the backbone can be analyzed separately. As the polyelectrolyte brush synthesis in this study includes the cleavage of styrene sulfonate esters in the presence of a base, which would be also hydrolyzing the ester bond of the macroinitiator, PBIEM cannot be used. A macroinitiator leading to an all-carbon side chain was necessary. Such a macroinitiator (**II**) was described by Janata et al.[155]. It is obtained by anionic polymerization of methyl styrene, followed by bromination with N-bromosuccinimide. However, to the best or our knowledge, no case of its application to the synthesis of polymer brushes by ATRP was yet reported. However, a similar copolymer (poly(isobutylene-*alt*-p-bromomethylstyrene)) was used by Matyjaszewski for the synthesis of branched polymers[156]. Another similar macroinitiator (**III**) can be obtained by the polymerization of vinylbenzyl chloride[157] by SFRP and has been used to for the synthesis of branched polymers previously[158], however the benzyl chloride group, being a chain transfer agent, suggests that these molecules might be branched in the main chain. Only very recently, a styrene-type macroinitiator that can be used for polymer brush synthesis by photoinitiated ATRP was reported (**IV**)[159].

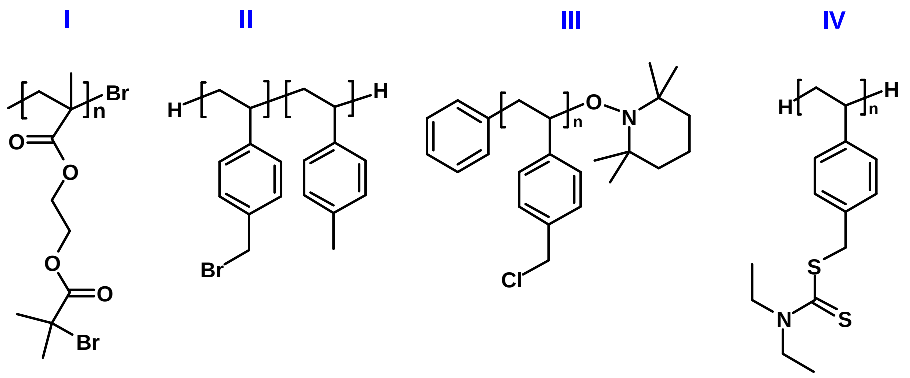

Fig. 7.1.1.: Macroinitiators for densely grafted polymer brushes by ATRP

7.2. *Macroinitiator Synthesis and Characterization*

Due to the (apparently) straight forward synthetic procedures involved, macroinitiator **II** (Fig. 7.1.1.) was focused on. Poly(vinylbenzylbromide) macroinitiators (**II**) were obtained in a two-step procedure by living anionic polymerization of p-methylstyrene, followed by selective bromination of the benzylic position with N-bromosuccinimide, as shown in Figure 7.2.1.. By this procedure, three poly(p-methylstyrene) macroinitiator precursors (**PpMSX**) and three series of macroinitiators with varied bromine content (**X-Y%Br**, where **X** is the number of the macroinitiator precursor and **Y** the targeted bromine content) were obtained. Table 7.2.1. summarizes the results obtained for the macroinitiator precursors.

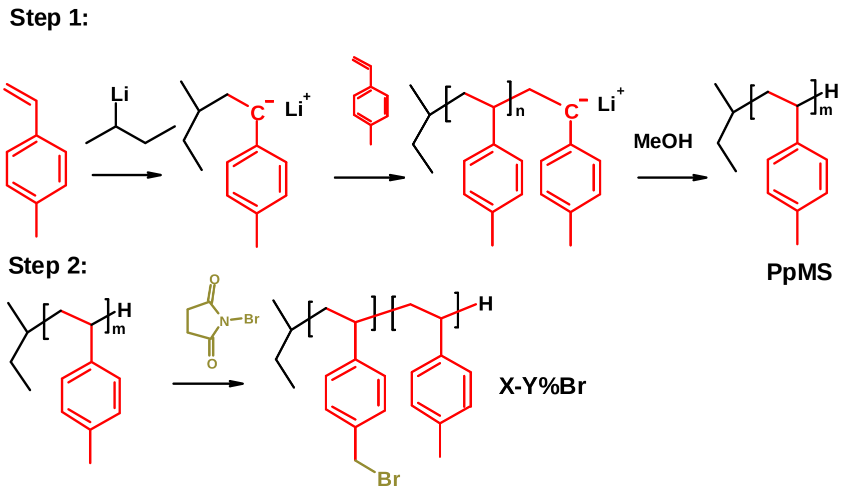

Fig. 7.2.1.: Anionic polymerization of p-methylstyrene followed by bromination

Table 7.2.1.: GPC-MALLS results for poly(p-methylstyrene) macroinitiator precursors (THF)

Sample	$M_{w,\ GPC\text{-}MALLS}$ **[g/mol]**	$M_{n,\ GPC\text{-}MALLS}$ **[g/mol]**	M_w/M_n	$n_{n,\ calc}$
PpMS3	70 400	67 700	1.04	573
PpMS7	25 000	23 400	1.07	198
PpMS11	200 000	187 000	1.07	1 582

The results of the macroinitiator characterization are given in Table 7.2.2. The bromine content by ^{1}H-NMR was obtained by integrating the signal of the aromatic protons (7.5 - 6.0 ppm) versus the peak of the benzylic protons of the brominated repeat unit at 4.3 ppm (Fig. 7.2.2.). By stoichiometric weighting, the bromine content is obtained as

$$\% \, \mathrm{Br} = \frac{2 \cdot \int \mathrm{Br\text{-}CH_2}}{\int \mathrm{aromatics}} \cdot 100$$

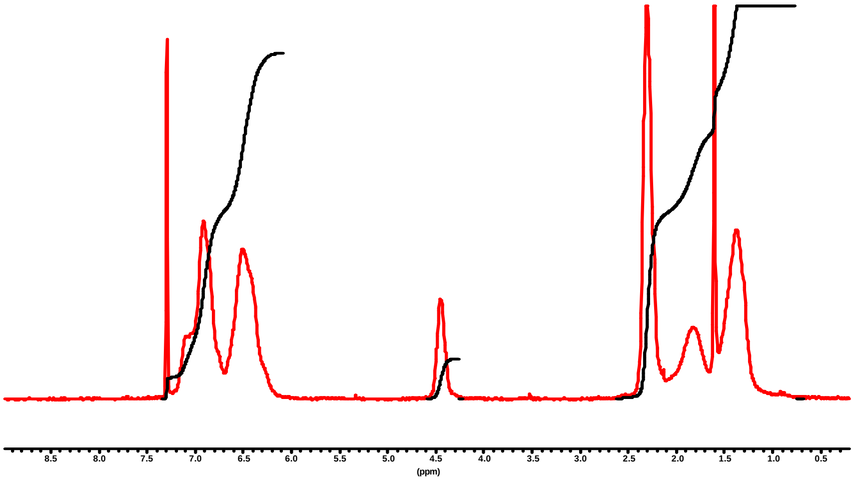

Fig. 7.2.2.: ^{1}H-NMR spectrum of macroinitiator 3-30%Br

As shown in Tab. 7.2.2., the polydispersity of the sample increases with increasing bromine content. This is due to continuously increasing enthalpic interacation with the column material and, in the case of **11-80%Br** and **11-100%Br**, due to partial crosslinking. The bromine content of the polymer was calculated from the GPC-MALLS results. First, the refractive index increment of the macroinitiators was determined as described in chapter 12. The results are given in Fig. 7.2.3.. The trend of these values is counterintuitive. Reference refractive index values (n_D^{20}) from the literature[160] for toluene (1.4961), benzyl chloride (1.5391) and benzyl bromide (1.5752) suggest that the refractive index, and thus also ***dn/dc***, should increase with increasing degree of bromination. However, this was not found. As can be seen from Fig. 7.2.3., the values scatter widely. Comparison with the reference values indicates that the scattering is on the same order of magnitude as the difference in ***dn/dc*** that would be theoretically expected. This can be only partially attributed to the experimental method. ^{1}H-NMR suggests that - within the accuracy of the method - the samples were free of the bromination agent (N-bromosuccinimid as well as the reaction side product, succinimide). However, small amounts of impurities not detectable by NMR could cause these deviations (the refractive index of succinimde is 1.418[160]). Thus, these results carry an error of approximately 15%.

Additionally, bromine was determined by elemental analysis. From these results, it can be seen that high molecular weight macroinitiators with degrees of bromination ranging from 10-96% bromination (according to elemental analysis) were obtained. The discrepancies between the values of elemental analysis, NMR and static light scattering can be explained as follows: the light scattering values show that there is a trend to increasing degrees of bromination from the **11-10%Br** sample to the **11-100%Br** sample. In between, individual results strongly deviate from the expected values. This is due to the general imprecision of the method (experimental error of ~20%) combined with the dependence on the results in the refractive index increments, as discussed above. As the molecular weight determined is proportional to $(dn/dc)^{-2}$, small deviations in this parameter lead to large experimental errors. Additionally, ***dn/dc*** is determined for the whole sample, while the MALLS detector only sees the specific ***dn/dc*** of the current fraction of the elugram. Thus, impurities with low molecular weight can severely influence the ***dn/dc*** measurement, while these are not seen in the high molecular weight range by the MALLS detector. Even a correction of these values by linear regression did not improve the results obtained. As can be seen from the recovery rates (calculated mass/injected mass) in Tab. 7.2.3., the total mass found by the MALLS detector is systematically larger than the mass injected. This is also due to imprecision in the ***dn/dc*** measurements.

The NMR values, while matching the expected values and the elemental analysis results for low degrees of bromination, deviate systematically from the expected values for higher degrees of bromination. This could be due to incomplete proton relaxation on the timescale of the NMR experiment as the polymer backbone gets more and more crowded.

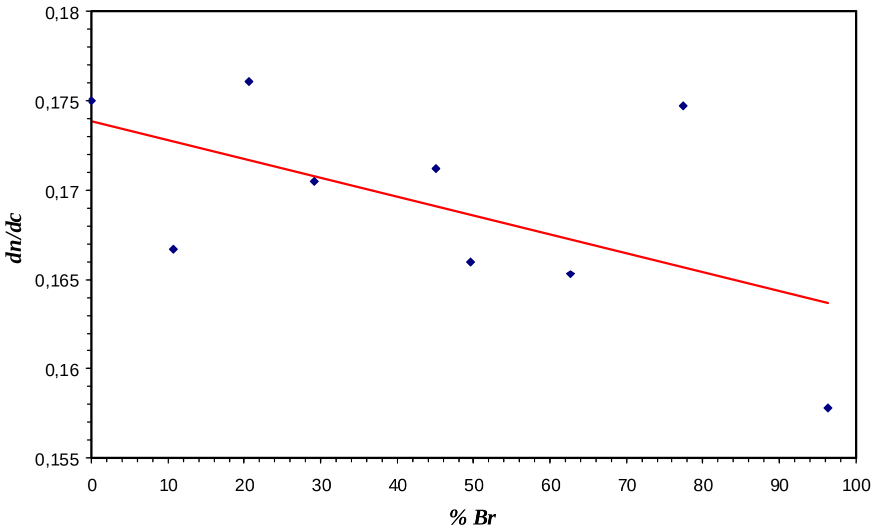

Fig. 7.2.3.: ***dn/dc*** values for the **11-**macroinitiator series (measured as described in chapter 12)

Table 7.2.2.: Analytical results for brominated poly(p-methylstyrene) macroinitiators from GPC-MALLS (THF), elemental analysis and ^{1}H-NMR

Sample	$M_{w,\ GPC\text{-}MALLS}$ [g/mol]	recovery rate	M_w/M_n	$n_{Br,calc}$	% Br		
					^{1}H-NMR	Elemental Analysis	GPC-MALLS
3-10%Br	69 800	1.04-1.07	1.04	-	9	-	-
3-20%Br	71 600	0.98-1.11	1.04	-	17	-	-
3-30%Br	74 600	1.05	1.04	-	23	-	-
7-20%Br	30 700	1.01	1.04	-	17	-	-
7-40%Br	34 200	1.02	1.04	-	35	-	-
7-60%Br	37 100	1.10	1.05	-	52	-	-
7-80%Br	40 100	1.00	1.05	-	64	-	-
11-10%Br	206 000	1.08-1.14	1.07	181	9	10.6	15
11-20%Br	211 400	1.10-1.11	1.07	351	18	20.6	19
11-30%Br	227 000	1.11-1.15	1.08	495	25	29.1	31
11-40%Br	221 300	1.08	1.11	767	34	45.1	26
11-50%Br	257 000	1.01-1.08	1.12	844	40	49.6	52
11-60%Br	220 300	1.11-1.12	1.27	1067	50	62.7	26
11-80%Br	269 300	1.25	1.24	1319	65	77.5	62
11-100%Br	329 200	-	1.45	1641	68	96.4	107

Literature reported that the bromine contents determined by NMR were lower than expected[155,163]. However, the conclusion that bromination is incomplete seems to be erroneous in the light of the values determined by elemental analysis. These values should be more precise than the NMR results. They were cross-checked by independent carbon and hydrogen determination, yielding comparable results for the remaining bromine content. As NMR spectra reveal that the bromination agent was quantitatively removed from all samples during work-up, the possibility that these values are too high due to amounts of impurities containing bromine can be ruled out. Thus elemental analysis is considered to be the most reliable method for the determination of the degree of bromination, and these values were used in the following sections for the calculation of side chain lengths and other parameters.

7.3. Synthesis of Polymer Brushes from Poly(styrene sulfonate dodecyl ester)

7.3.1. Synthesis of Polymer Brushes from Styrene Sulfonate Dodecyl Ester

The brominated macroinitiator described in chapter 7.2. was used to polymerize styrene sulfonate dodecyl ester (Fig. 7.3.1.1.). While initial experiments with the ethyl ester were not successful due to phase separation, the non-polar ester residue of **SSD** led to a phase compatibilization, and a homogeneous reaction system was obtained.

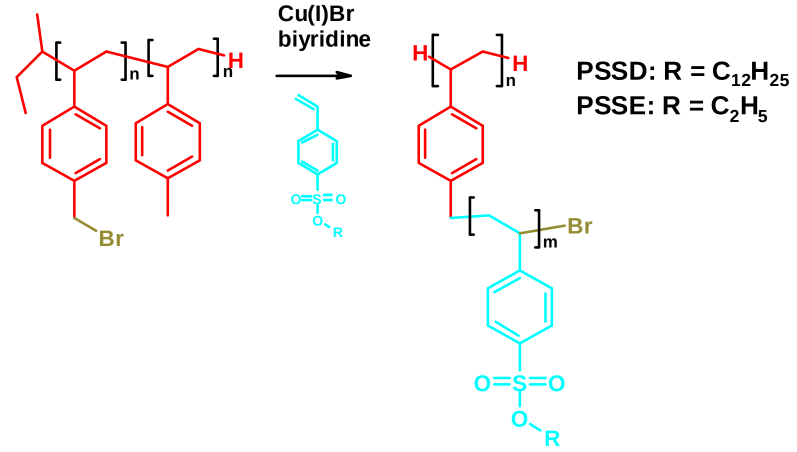

Fig. 7.3.1.1.: Polymer brush synthesis

To determine the reaction conversion, samples were drawn at regular intervals and investigated by ^{1}H-NMR. The conversion was determined by integration of the vinyl signals of the monomer versus the α-CH_2 group of both monomer and polymer repeat unit. The results of this are summarized in Fig. 7.3.1.2.-7.3.1.4..

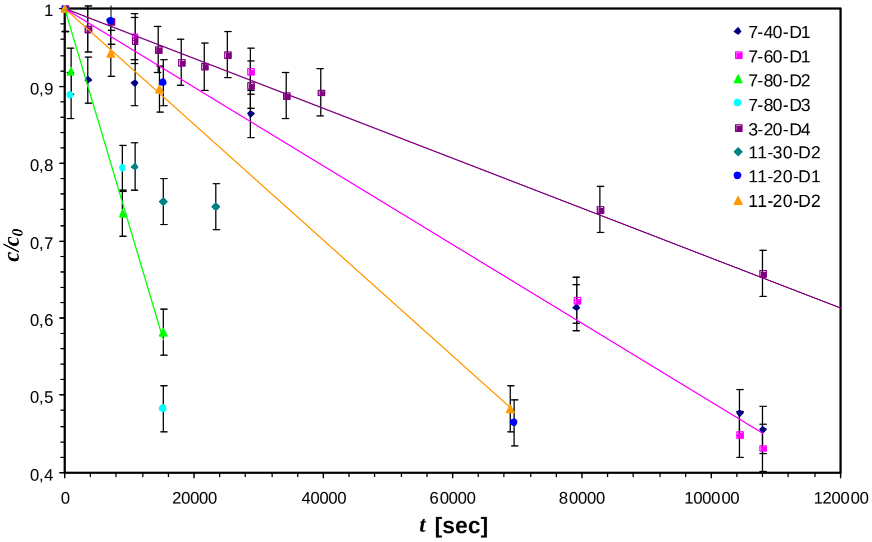

Fig. 7.3.1.2.: Polymerization of **SSD** with different macroinitiators – Plot of conversion versus time

In Fig. 7.3.1.2, the normalized reaction conversion of **SSD** polymerization with different macroinitiators is plotted versus time. Fig. 7.3.1.3. displays a logarithmic plot of the same data. From the overall curve shape, it is difficult to determine whether the reaction is first or zeroth order with respect to monomer concentration. Linear regressions for the curve fits shown in Figs. 7.3.1.2. and 7.3.1.3. indicate that the coefficients of determination (R^2) are closer to unity for the linear fits than for the logarithmic ones (Tab. 7.3.1.1.). An exception of this is sample **7-80-D2**, which is based on three data points only and will be therefore not considered further. From this data, it seems justified to assume that the reaction is rather zeroth order with respect to monomer concentration. This is surprising as ATRP is usually first order with respect to monomer concentration (chapter 2). Also, the kinetic data for the polymerization of styrene sulfonate *ethyl* ester with bifunctional initiators (Chapter 9) is first order. Apparently, the proximity of the reactive sites to each other has an influence on the reaction rate.

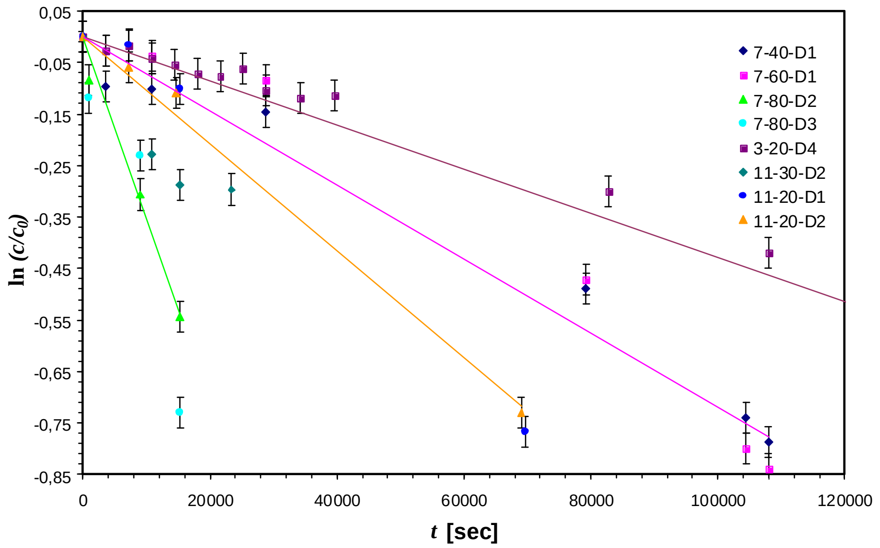

Fig. 7.3.1.3.: Polymerization of **SSD** with different macroinitiators – Logarithmic plot of conversion versus time

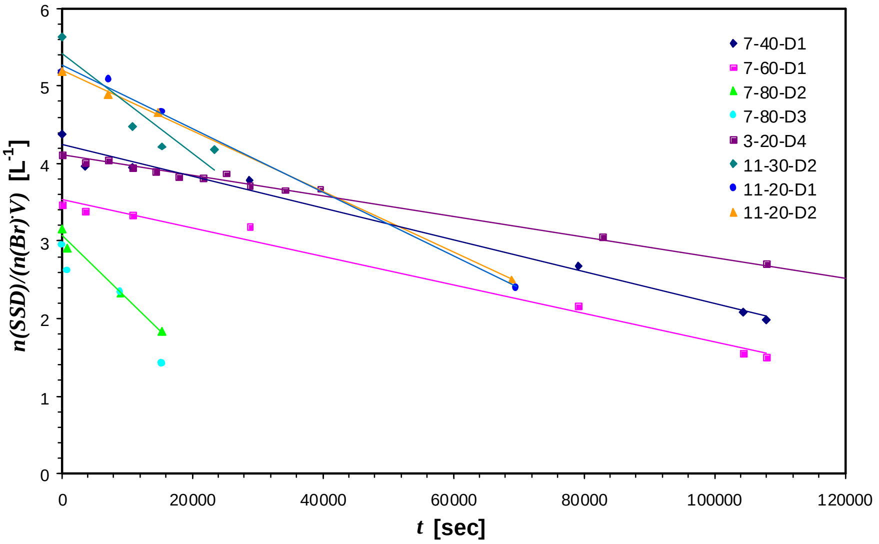

Fig. 7.3.1.4.: Polymerization of **SSD** with different macroinitiators – normalized plot of conversion versus time

Tab. 7.3.1.1. Coefficients of determination of the linear regressions for Figs. 7.3.1.2 and 7.3.1.3.

Sample	R² (linear)	R² (logarithmic)
3-20-D4	0.9950	0.9691
7-60-D1	0.9842	0.9615
11-20-D2	0.9997	0.9935
7-80-D2	0.9695	0.9843

Table 7.3.1.2.: Kinetic parameters of **SSD** polymerization with different macroinitiators

Sample	c_{SSD} [mol/L]	k_0 [sec^{-1}]	$t_{\frac{1}{2}}$ [sec]
7-40-D1	2.11	$2.39 \cdot 10^{-4}$	$2.09 \cdot 10^{3}$
7-60-D1	2.26	$2.70 \cdot 10^{-4}$	$1.85 \cdot 10^{3}$
7-80-D2	2.40	$1.25 \cdot 10^{-4}$	$4.00 \cdot 10^{3}$
7-80-D3	2.25	$1.25 \cdot 10^{-4}$	$4.00 \cdot 10^{3}$
3-20-D4	2.07	$7.30 \cdot 10^{-5}$	$6.85 \cdot 10^{3}$
11-30-D1	3.74	$2.18 \cdot 10^{-5}$	$2.29 \cdot 10^{4}$
11-30-D2	5.63	$5.95 \cdot 10^{-4}$	$8.40 \cdot 10^{2}$
11-20-D1	5.16	$3.81 \cdot 10^{-4}$	$1.31 \cdot 10^{3}$
11-20-D2	5.19	$3.70 \cdot 10^{-4}$	$1.35 \cdot 10^{3}$

To make the data comparable, the stoichiometric ratio of monomer to initiator as well as the solution concentration must be taken into account. In Fig. 7.3.1.4., a plot of $\frac{n_{SSD}}{n_{Br} \cdot V}$ is presented, where n is the molar amount of monomer (**SSD**) and initiator (**Br**), respectively. V is the total volume of the solution. From this data, the qualitative conclusion can be drawn that, within a series of initiators of the same backbone length, higher degrees of bromination lead to faster reaction rates. This could be attributed to higher local temperatures at the reactive sites due to the polymerization enthalpy released. For more quantitative statements, further investigations would be necessary.

7.3.2. Reaction work up

As mentioned in chapter 2, quantitative copper removal after ATRP is not trivial, especially for polar monomers in polar solvents, if both the monomer and the solvent have a tendency to act as ligands for copper[161]. For the system under investigation, filtration (in THF) over silica gel or aluminum oxide, which works reasonably well for non-polar polymers and solvents resulted in partial copper removal. After repeated precipitation of the polymer into methanol (from CH_2Cl_2 or THF), copper was also still present. It was then tried to extract the water soluble copper species from the organic phase in a two phase system with N,N,N',N',N''-pentametyldiethylentriamine (PMDETA), a water soluble ligand. With that method, copper was removed, but the polymer was irreversibly contaminated by the ligand. Finally, by ion exchange in acetone on an acidic ion exchange resin (Amberlyst 15, Fluka or DOWEX MSC-1, Fluka) copper could be almost quantitatively removed. The copper content after the ion exchange was determined by atom absorption spectroscopy. The amounts determined were 0.12 – 0.50 mass percent.

7.4. Characterization of Polymer Brushes from Poly(styrene sulfonate dodecyl ester)

7.4.1. Molar Mass Distributions

The characterization of polymer brushes from poly(styrene sulfonate dodecyl ester) was more complicated than expected, as it was not possible to analyze these polymer brushes by gel permeation chromatography. A number of combinations of different solvents ($CHCl_3$, THF, acetone), column materials (SDV, GRAM, GRAL, Suprema) and additives were tested, yet unsuccessfully. The maximum recovery rate of one of the less densely branched samples (**3-10-D4**) was ~10 %. The more densely grafted samples were not eluted at all. This was attributed to the amphiphilicity of the monomer, which lead to absorption both in polar and non-polar systems. The range of solvents available was limited, as the sample was insoluble in other solvents. To get a qualitative idea about the molar mass distributions obtained, the sedimentation coefficient distribution of the samples was measured by analytical ultracentrifugation (AUC) at the MPI for Colloid and Interface Research, Golm. The results of these experiments are shown in Fig. 7.4.1.1. to 7.4.1.6.. The molar mass distributions are monomodal for samples with low grafting density (Fig. 7.4.1.1.) and low conversions (**3-20-D2**, **3-20-D3** in Fig. 7.4.1.2.). For higher degrees of branching and higher conversions, additional maxima appear in the sedimentation coefficient distribution curve (**3-20-D4** in Fig. 7.4.1.2., Figs. 7.4.1.3. – 7.4.1.4.). These peaks have a higher molecular mass than the main maximum and indicate that there is some kind of crosslinking in the sample, possibly due to radical recombination. In the case of **11-80-D1** (Fig. 7.4.1.6.), this side reaction is quite prominent due to the high bromine content of the initiator. As shown for the case of **11-30-D2** and **11-40-D1**, these maxima can be almost suppressed if higher dilution conditions are chosen for the reaction. In the case of **11-80-D1**and **11-100-D1**, however, additional peaks appear at lower s values than the maximum of the macroinitiator. This must be due to homopolymer formation. For all samples, the curves are broad, indicating that the polydispersity of the samples is high.

These results are only qualitative. Theoretically, it would be possible to obtain quantitative results by first measuring the density increment of the solution, followed by a sedimentation equilibrium experiment. This was not attempted as the samples contained impurities in the lower *s* range from unconsumed initiator or homopolymer. These would spoil the precision of the density measurement, which is crucial for the molar mass distribution calculation. Consequently, the *s* distributions obtained were only used for qualitative information about the overall shape of the polymer distribution and the relative weight of the polymer brush samples. The molar masses were estimated from ^{1}H-NMR measurements only.

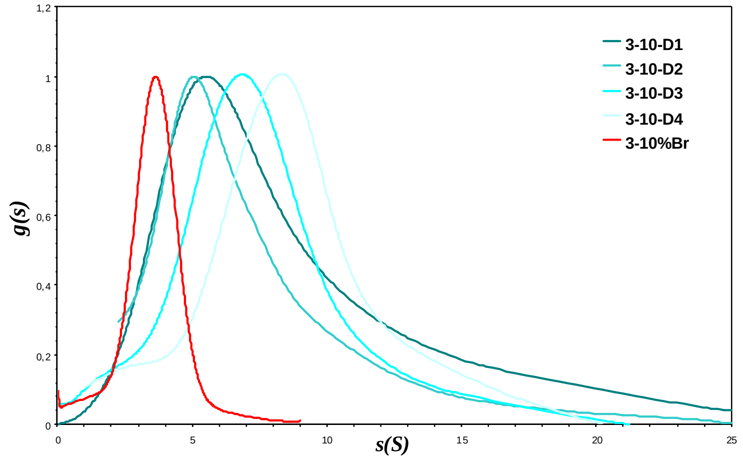

Fig. 7.4.1.1.: *s(S)* distribution for the **3-10-DX** series (red: macroinitiator, blue: polymer brushes)

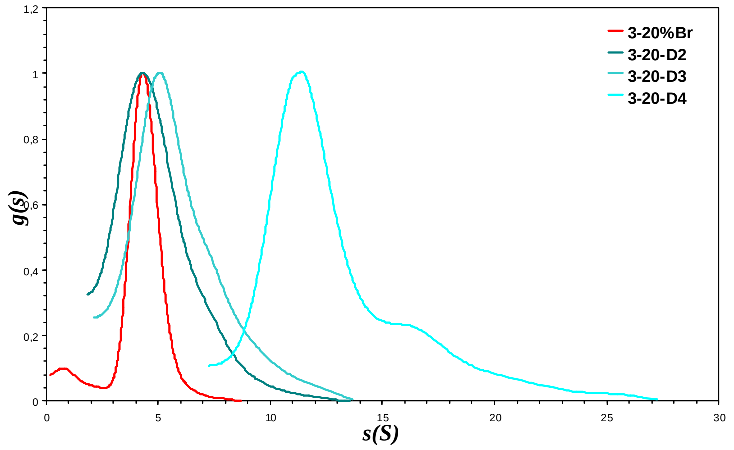

Fig. 7.4.1.2.: *s(S)* distribution for the **3-20-DX** series (red: macroinitiator, blue: polymer brushes)

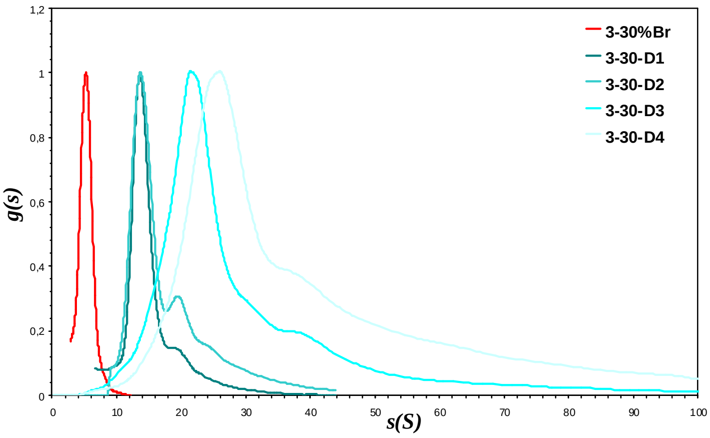

Fig. 7.4.1.3.: *s(S)* distribution for the **3-30-DX** series (red: macroinitiator, blue: polymer brushes)

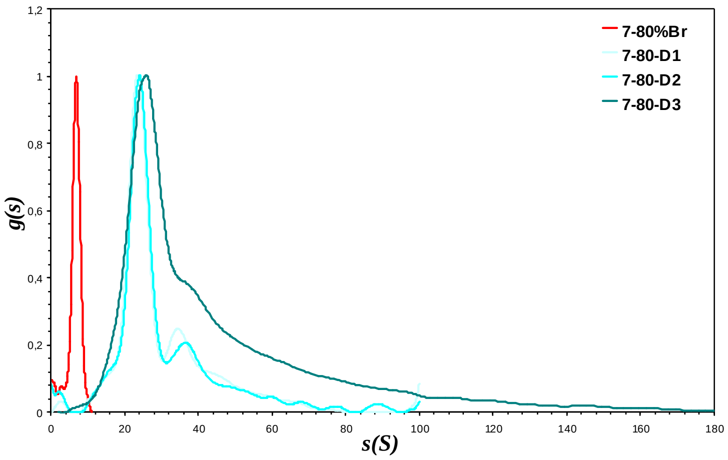

Fig. 7.4.1.4.: *s(S)* distribution for the **7-80-DX** series (red: macroinitiator, blue: polymer brushes)

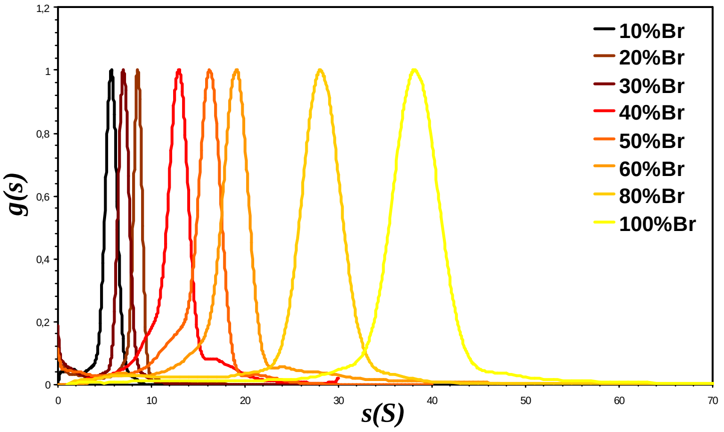

Fig. 7.4.1.5.: *s(S)* distribution for the initiators of the **11-XBr** series

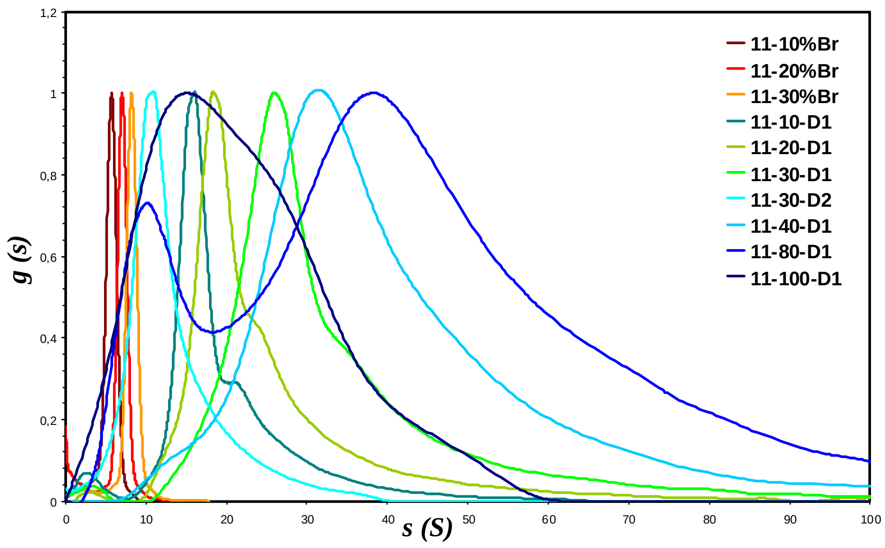

Fig. 7.4.1.6.: *s(S)* distribution for the **11-XX-DX** series (red: macroinitiator, blue/green:

7.4.2. Characterization by Static Light Scattering

It is known from literature that the homopolymers of styrene sulfonate esters cause problems in static light scattering experiments. Woeste[162] showed that already the homopolymers of these esters have negative slopes in the Zimm plot. The same was found for the polymer brushes from styrene sulfonate dodecyl ester (Fig. 7.4.2.1.), which were measured in THF, chlorobenzene and toluene. There are two possible explanations: If some of the ester groups of the polymer brushes are lost during work-up, there would be electrostatic interactions between the anionically charged samples, which could result in an intermolecular structure peak in static light scattering. The other possibility would be structure formation due to aggregation, e.g. by interaction of the dodecyl ester side chains.

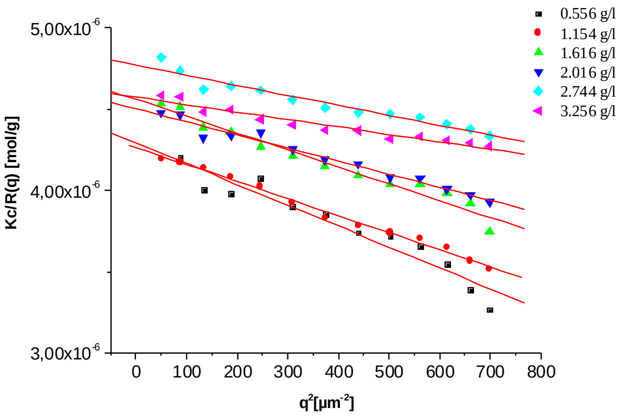

Fig. 7.4.2.1.: Static light scattering on **PSSD** brushes: plot of Kc/R_θ vs q^2

As the peculiar curve shape did not vanish upon salt addition (LiBr, LiCl, NaCl; c = 10^{-3}–1 g/L) to the sample, electrostatic interaction as the main contribution can be ruled out. Further dilution of the sample by a factor of 10 and 100 as well as further efforts to break possible aggregates (heating, stirring, ultrasound) did not affect the shape curves. As these samples did not elute from GPC columns (chapter 7.4.1.), fractionation by GPC and investigation of the fractionated samples was not possible. Therefore, it was not possible to determine the molecular weight of these samples by static light scattering.

7.4.3. Side Chain Length Determination by ^{1}H-NMR

The side chain length of the polymer were calculated from ^{1}H-NMR spectra. As the initiator peak from 4.2 to 4.5 ppm vanished, 100 % initiation efficiency was assumed. The reaction conversion was determined from the raw spectrum of the reaction mixture by integration of the vinyl monomer peaks versus the sum of the α-CH$_2$ groups of both monomer and polymer. From the conversion, together with the monomer input and the previously determined bromine content of the macroinitiator, the side chain length was calculated:

$$n_{\text{n, side chain}} = \frac{n_{\text{monomer}} \cdot \text{conversion}}{n_{\text{bromine}}}$$

Alternatively, in the cases where no raw spectrum was available, the side chain length was calculated from the spectrum of the pure substance by integration of all aromatic protons versus the α-CH$_2$ groups of the polymer. The peak of the α-CH$_2$ group is then set to a constant value. The relative amount of Y and Z (Fig. 7.4.3.1.) is determined by subtracting twice the integral of the α-CH$_2$ group (2 protons) from the total integral of the aromatics of X, Y and Z (4 protons each)

.

$$\int(\text{aromatics Y} + \text{Z}) = \int \text{all aromatics} - 2\int \alpha\text{-CH}_2$$

From the knowledge of the bromine content of the initiator, the ratio between Y and Z can be calculated:

$$\int(\text{aromatics Z}) = \text{bromine content} \cdot \int(\text{aromatics Y} + \text{Z})$$

The integral of the α-CH_2 group in X (2 protons) multiplied by 2, divided by the integral of the aromatics of repeat unit Z (4 protons) then yields the side chain length.

$$n_{\text{n, side chain}} = \frac{2 \cdot \int \alpha\text{-}CH_2}{\int (\text{aromatics Z})}$$

The results of these calculations are given in Tab. 7.4.3.1., together with the maxima of the sedimentation coefficient distributions from the analytical ultracentrifugation measurements.

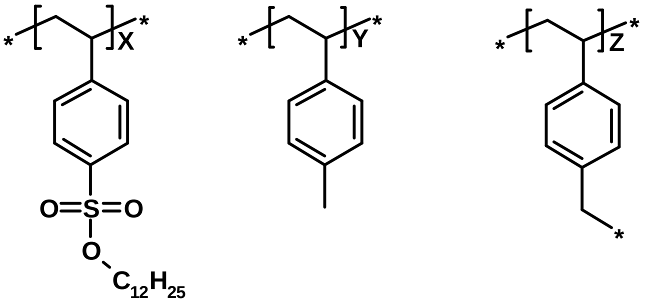

Fig. 7.4.3.1.: Repeat units in **PSSD** polymer brushes

The following assumptions limit the precision of the results obtained. First, it was assumed that the initiator efficiency is 100%, which is almost certainly not correct due to side reactions during polymerization (bromine loss etc.). Thus, the chain lengths obtained are minimum values, as fewer initiating sites result lead, for a given conversion, to longer side chains. Also, the mass fraction of the backbone compared to the side chains decreases with increasing grafting density to a value near the precision limit of ^{1}H-NMR (3-5%) – for high grafting densities, the experiment does not 'see' substantial amounts of the backbone, resulting in too high values for the side chain lengths and molecular masses. When determining the conversion, it is assumed that no homopolymer is formed, which is not true for the samples with 80% and 100% bromination. Bearing all these inaccuracies in mind, the values should be treated as best estimates rather than absolute figures.

By comparison with the results of the ***s(S)*** maxima form AUC (Tab. 7.4.3.1.), it was found that the results do not exactly coincide. Within one initiator series, the general trends in molecular weight are represented correctly: in the **3-series**, ***s(S)*** increases with increasing molecular weight, as do the samples from the **11-series**, with the exception of **11-30-D1**. This is not surprising: the *s(S)* distribution does not depend on M_n only, but also structural parameters such as density and viscosity. This sample has shorter side chains than many other sample of the **11-series**, which decreases the frictional force exerted by the surrounding medium during sedimentation and thus the *s(S)* value. Thus, the results obtained are in reasonable, yet only qualitative agreement.

Table 7.4.3.1.: Side chain length determination by ^{1}H-NMR and *s(S)* maxima from AUC, * = crosslinking

Sample	Side Chain Length (n_n)	$M_{n, calc}$ [g/mol]	Maxima *s(S)*
3-20-D4	13	585 000	11.5
3-30-D1	18	1 008 000	13.6
3-30-D3	55	3 079 000	21.2
11-10-D1	37	2 565 000	16.2
11-20-D1	26	3 215 000	18.2
11-30-D1	15	2 620 000	25.8
11-30-D2	-	-	11.1
11-40-D1	24	6 493 000	32.3
11-80-D1	9	4 222 000	15.0
11-100-D1	5	2 879 000	39.1*

7.4.4. Single Molecule Imaging by AFM, SEM and TEM

Microscopic imaging techniques were employed to determine the molecular dimensions of single polymer brush molecules on a solid support. Especially atomic force microscopy (AFM) was extremely useful for the determination of the contour length, the molecule diameter and the molecule height. All AFM pictures presented were measured in the tapping mode. The samples were dissolved in THF and spread on a solid support by spin-coating. After initial experiments with silica wafers, graphite and mica, it was found that the molecules only spread on and adhere to the polar mica surface. Table 7.4.4.1. summarizes the results of the diameter and contour length measurements on selected polymer brush samples. The molecules lie flat on the surface and tend to aggregate end to end even at low concentrations. Thus, the contour length measurements in AFM were not as precise as the accuracy of the method itself would allow. This is revealed in the relatively large standard deviation.

The results (Fig. 7.4.4.1.). show that, for samples with the same number of repeat units in the polymer backbone, an increase in the branching density of the polymer brush leads to an increased contour length. Between the samples **11-10-D1** (10.6% branching) and **11-20-D1** (20.6% branching), this increase is quite drastic (57%

backbone stretching). For higher degrees of branching (samples **11-30-D1** and **11-40-D1**), the increase is relatively small, i.e. no significant additional backbone stretching is observed. This effect is reflected in the molecule heights (Fig. 7.4.4.7.): Going from **11-10-D1** to **11-40-D1**, there is a minimum of the molecule height for sample **11-20-D1**: as the backbone is more stretched than for sample **11-10-D1**, the side chains have enough space to lie flat on the surface rather than on top of each other, consequently the height is diminished. When going from **11-20-D1** to **11-40-D1**, the backbone stretching is less pronounced, consequently the increased number of side chains cannot be accommodated on the mica surface and the height increases. For the molecule diameters, such a clear tendency is not observed, as the diameter does not only depend on the state of the backbone (coiled or stretched), but also on the side chain length, which is not as uniform for these samples as the backbone lengths. Interestingly, samples **11-20-D1** and **11-40-D1** have similar backbone and side chain lengths, and almost identical diameters. Some representative AFM images are shown in Figs. 7.4.4.2. to 7.4.4.6.. Higher degrees of branching were not observed due to sample instabilities (gel formation) with the 80% and 100% samples.

Table 7.4.4.1.: Contour length and diameter determination of **PSSD** brushes by AFM

Sample	Contour Length [nm]	Diameter [nm]	Height [nm]
3-10-D1	51.3 ± 8.0	15.0 ± 3.0	0.70 ± 0.09
3-30-D1	78.5 ± 11.9	11.6 ± 2.2	1.04 ± 0.10
11-10-D1	97.7 ± 18.7	15.6 ± 3.0	1.07 ± 0.12
11-20-D1	152.9 ± 40.8	22.3 ± 3.9	0.80 ± 0.10
11-30-D1	166.3 ± 32.3	28.1 ± 3.6	1.64 ± 0.14
11-40-D1	174.8 ± 36.3	21.6 ± 2.7	1.73 ± 0.15

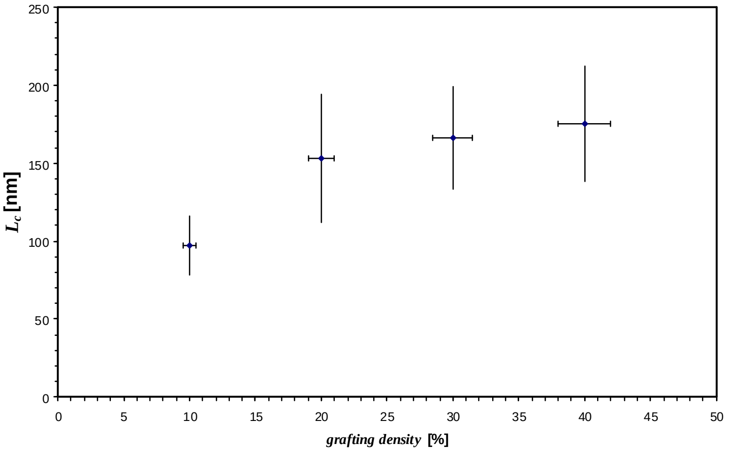

Fig. 7.4.4.1.: Correlation between contour length and grafting density

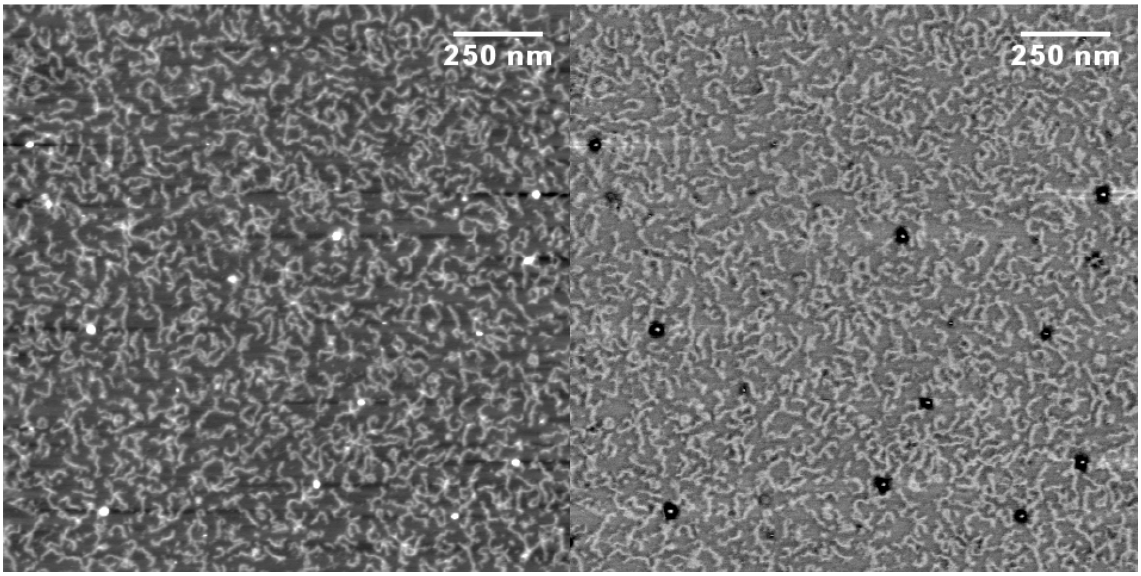

Fig. 7.4.4.2: **3-30-D1** on mica (height and phase image)

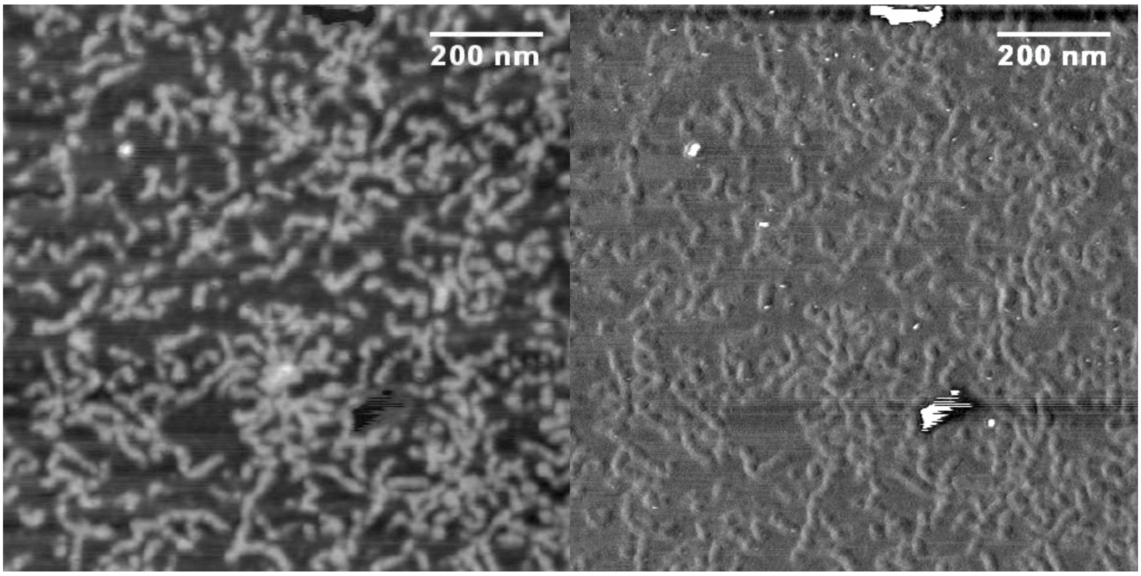

Fig. 7.4.4.3: **11-10-D1**, 10% branching, on mica (height and phase image)

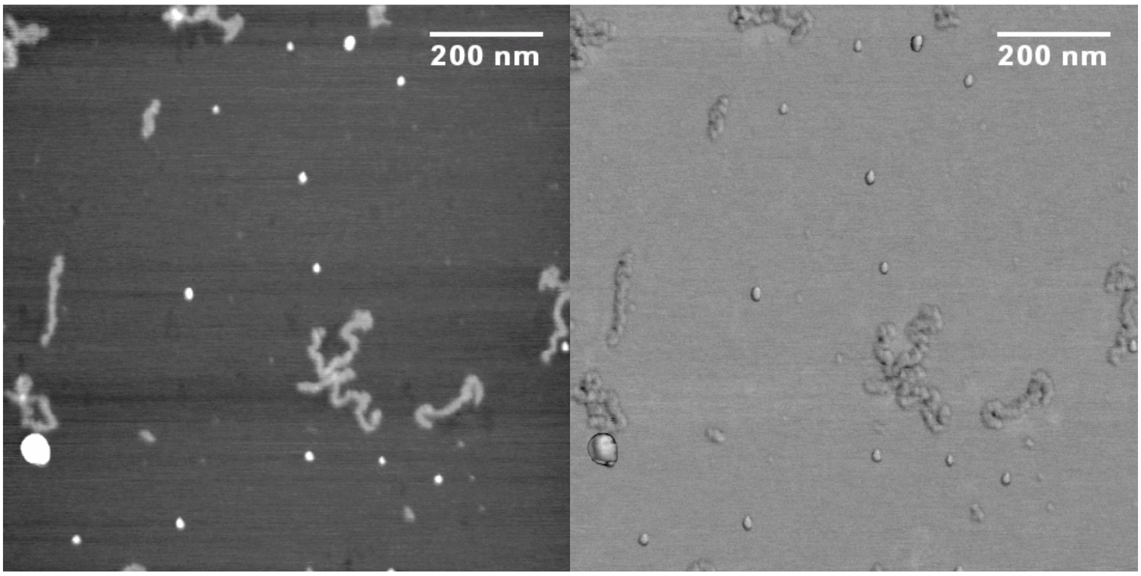

Fig. 7.4.4.4: **11-20-D1**, 20% branching, on mica (height and phase image)

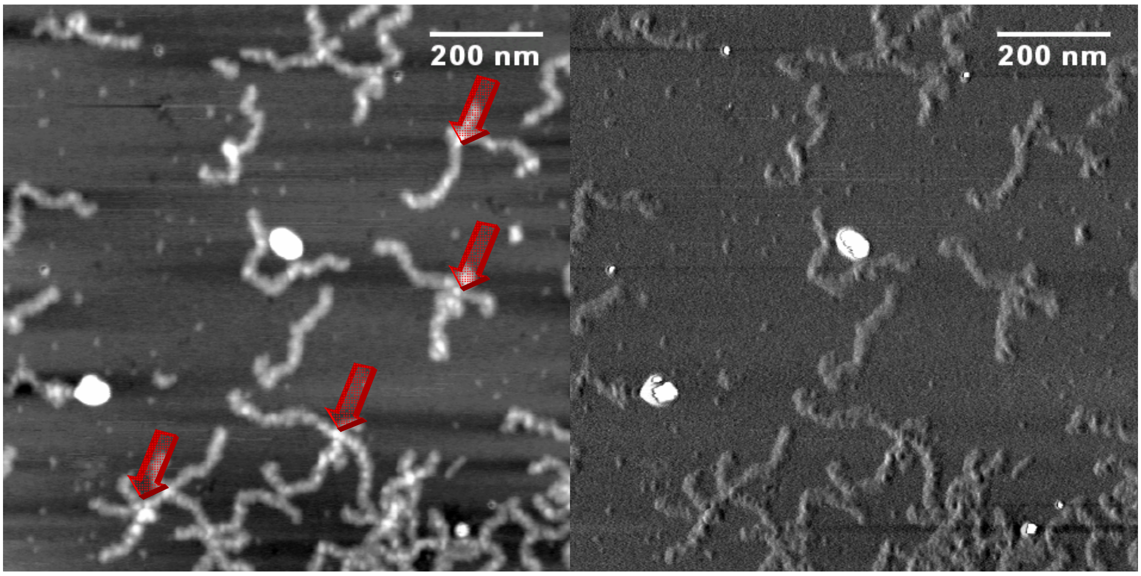

Fig. 7.4.4.5: **11-30-D1**, 30% branching, on mica (height and phase image)

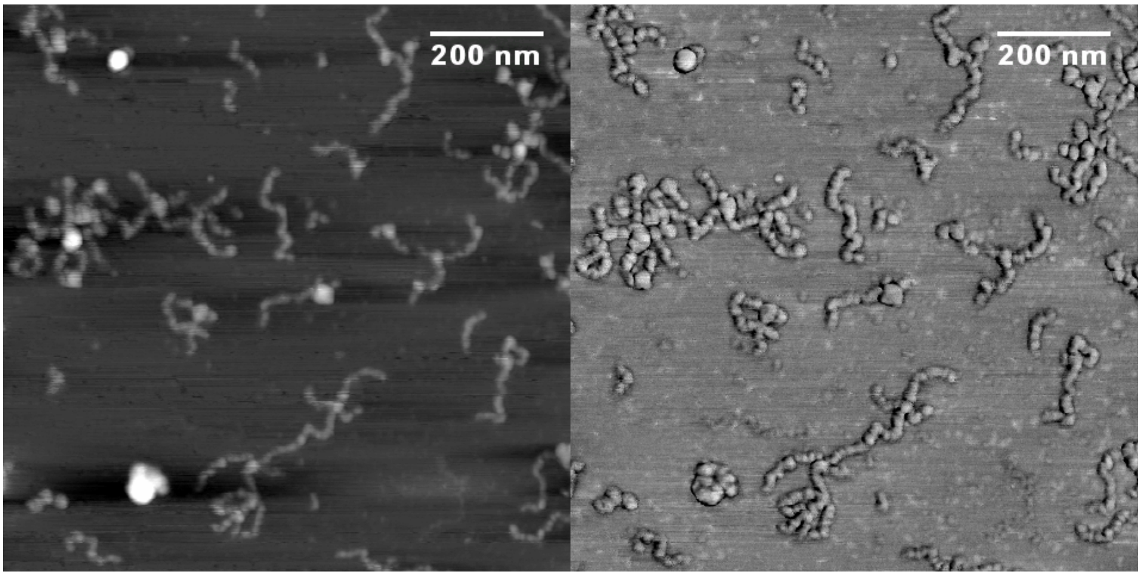

Fig. 7.4.4.6: **11-40-D1**, 40% branching, on mica (height and phase image)

In all images, crossing points of single molecules are observed. Some of these points have been highlighted in Fig. 7.4.4.5.. At these crossings, the height values of the samples (Tab. 7.4.4.1.) are doubled. Therefore, this cannot be due to backbone nonlinearity (branching). Other explanations would be intermolecular cross-linking due to radical recombination, which some of the AUC curves indicate (Fig. 7.4.1.6.), or just a coincidental piling up of the molecules. Morphologically, it was observed that the less densely grafted polymer brushes behave more wormlike than the brushes with higher degrees of branching. This is most striking when comparing the AFM images of **11-20-D1** (Fig. 7.4.4.4.) and **11-30-D1** (Fig. 7.4.4.5.). Thus, it is observed that, besides the lengthening of the backbone for higher degrees of branching, there is also an increase in the Kuhn segmental length of the backbone.

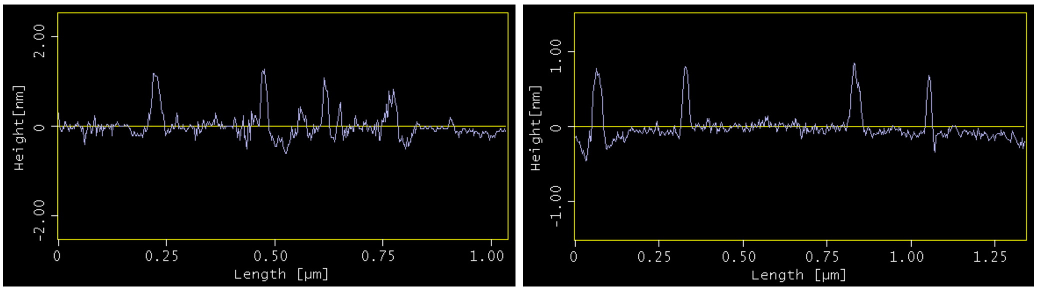

11-10-D1 **11-20-D1**

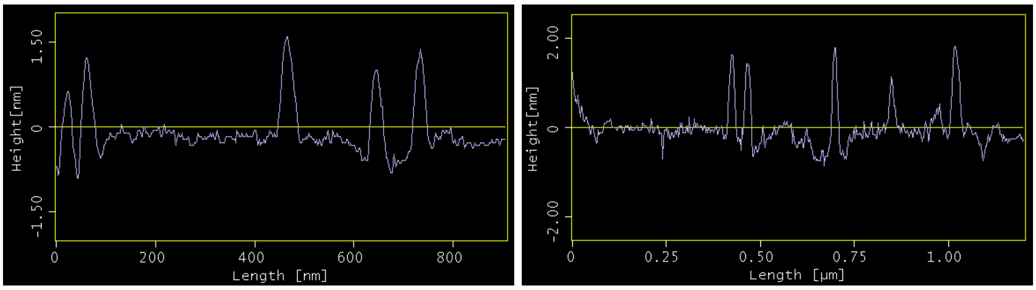

11-30-D1 **11-40-D1**

Fig. 7.4.4.7.: Sections through AFM height images for selected polymer brushes

In AFM, the probe size limits the resolution of the images. The AFM images presented so far have all been measured with a “standard” cantilever with a probe diameter of approximately 5-10 nm. This limits the lateral resolution of the images. It was precise enough to measure the molecular dimensions; however the molecule side chains could not be resolved. For a better resolution, a “supercantilever” with a tip size of approximately 1 nm was used. However, besides being scurrilously expensive, these cantilevers are extremely sensitive and prone to contamination and breaking. Therefore, only two samples were measured. The results are displayed in Figs. 7.4.4.8. to 7.4.4.10.. In these high resolution AFM images, the corona of side chains around the polymer backbone is visible. From the varying molecule diameter within one molecule, it can be assumed that the side chain length distribution is rather broad. This is in accordance with the findings of the AUC measurements.

The results from AFM can be further related to the results obtained by other analytical techniques. This is exemplified in the discussion of the results obtained for sample **3-30-D1**. The backbone length of the macroinitiator precursor **PpMS3**, and thus of the macroinitiators **3-10%Br** to **3-30%Br** was determined to be ≈ 600 repeat units by static light scattering. The side chain length of **3-30-D1**, as determined by ^{1}H-NMR, is 18.

Assuming an all-zigzag conformation and a C-C bond length of 1.5 Å, a fully stretched backbone with 600 repeat units would be 156 nm long. For a fully stretched side chain of 18 repeat units, a molecular diameter of 2 · 4.5 nm = 9 nm would be expected. Comparing these results with the above values for the contour length and molecule diameter (Table 7.4.4.1.), it appears that the backbone is not fully stretched (which is reasonable for a polymer brush with only 29% branching density). The side chain length calculated from NMR and the measured diameter from AFM are in reasonable agreement. For the series of brushes derived from **PpMS11**, the number of repeat units in the backbone is ≈ 1 580. For a fully stretched backbone in all-zigzag conformation, a total length of 387 nm would be expected. Even for the 45% branched polymer brush **11-40-D1**, the measured contour length is well below this value.

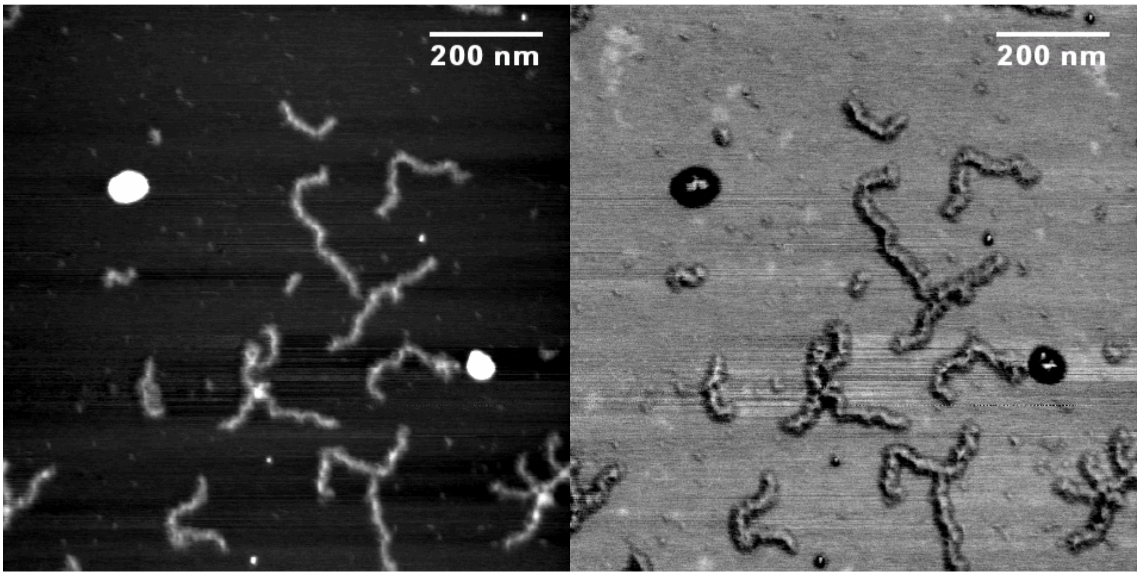

Fig. 7.4.4.8: “Supercantilever” AFM image of **11-30-D1** on mica (height and phase image)

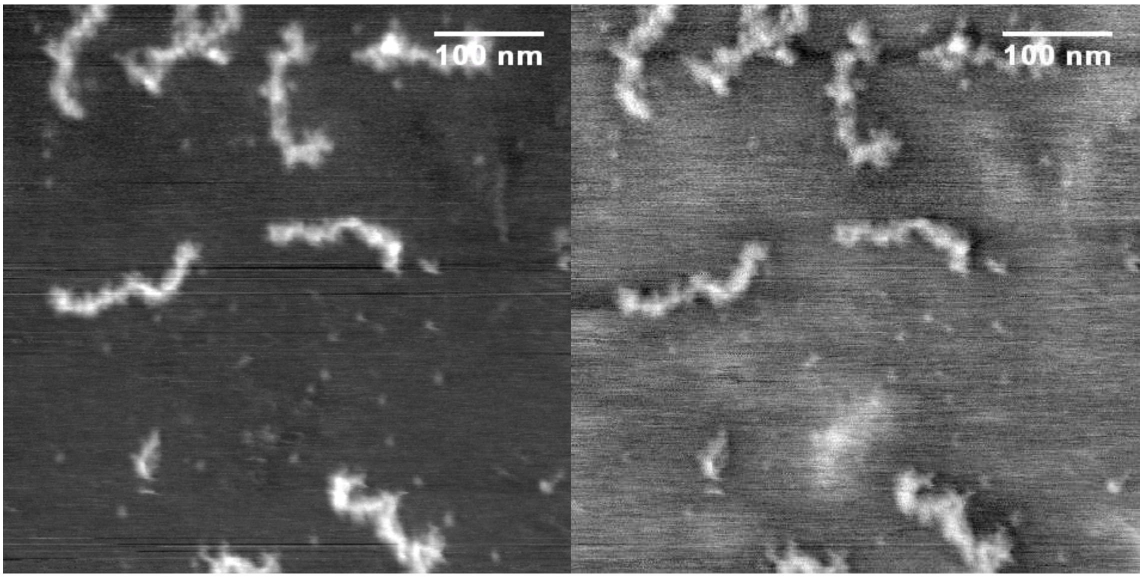

Fig. 7.4.4.9: “Supercantilever” AFM image of **3-30-D1** on mica (height and phase image)

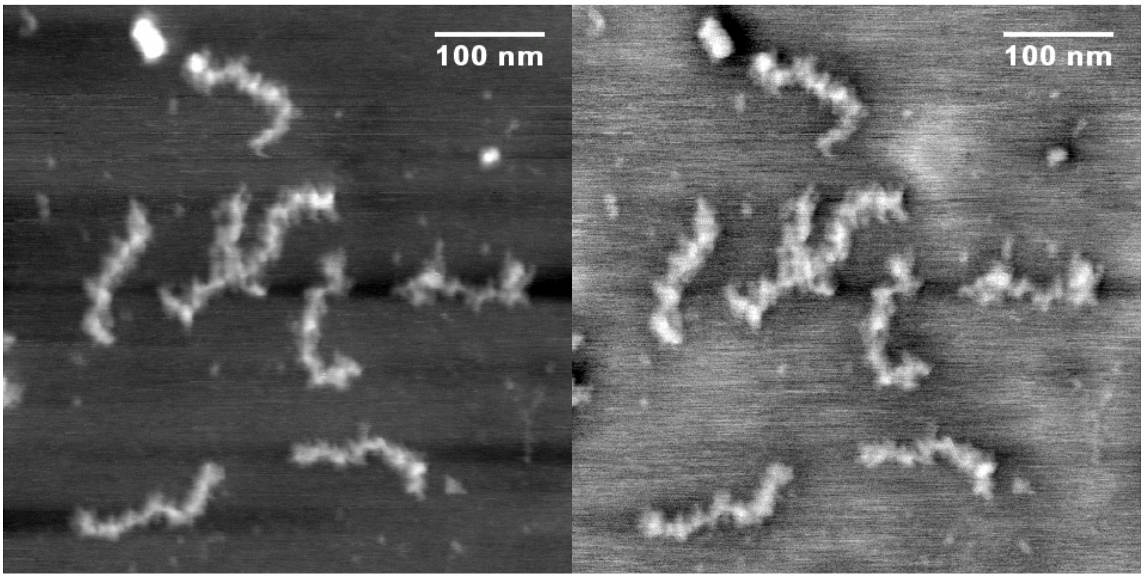

Fig. 7.4.4.10: “Supercantilever” AFM image of **3-30-D1** on mica (height and phase image)

To confirm the results obtained by AFM, the samples were investigated by scanning electron microscopy (SEM), as shown in Fig. 7.4.4.11.. The polymer brush morphology obtained in these measurements is similar to the AFM results, and the molecule dimensions are the same. However, due to the low conductivity of the mica substrate, the image quality was quite poor. Also, the size of the molecule diameter is at the limit of SEM resolution, i.e. the diameters cannot be measured from such images.

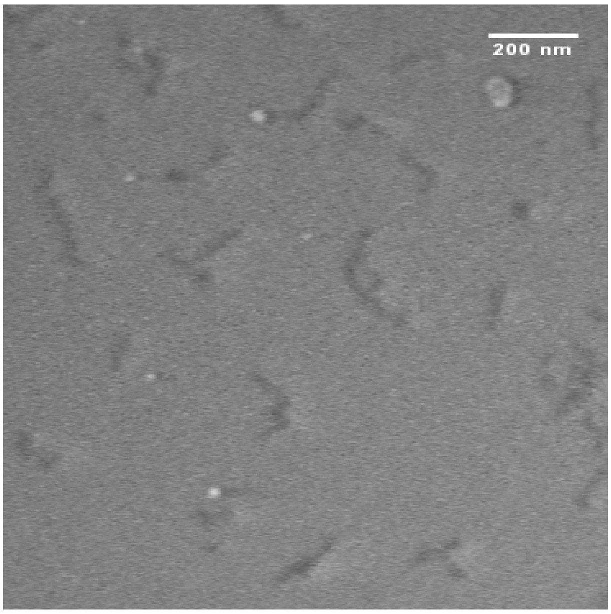

Fig. 7.4.4.11.: SEM image of **11-20-D1** on mica

The polymer brush samples were also investigated by transmission electron microscopy (TEM). As samples for TEM need to be extremely thin to be transparent for the electron beam, the AFM preparation could not be copied for the preparation of the TEM samples. Sample preparation by drop casting from solution onto thin carbon films only yielded molecule clusters (Fig. 7.4.4.12.). To improve this, samples were spin-coated on a thin carbon film on a mica substrate. The sample was then shaded with a tungsten-tantalum coating by electron beam evaporation. It was floated off on a water surface and placed on a copper grid. The images obtained from sample **3-30-D1** are shown in Figs. 7.4.4.13. and 7.4.4.14.. As with AFM, it was found that the polymer brushes aggregate end to end. On the coal film, this is even more pronounced than on the mica surface. It is therefore not possible to measure the length of individual molecules from the TEM pictures. The molecular diameter could be determined. For sample **3-30-D1**, 11.0±1.6 nm were measured, which is in excellent accordance with the 11.6±2.2 nm determined for the same sample from AFM.

The values determined by the various imaging techniques as discussed above give an estimate of the relative sizes of the **PSSD** polymer brushes. However, one has to bear in mind that these are dimensions of molecules on a solid support – in solution, these molecules will have totally different molecular dimensions.

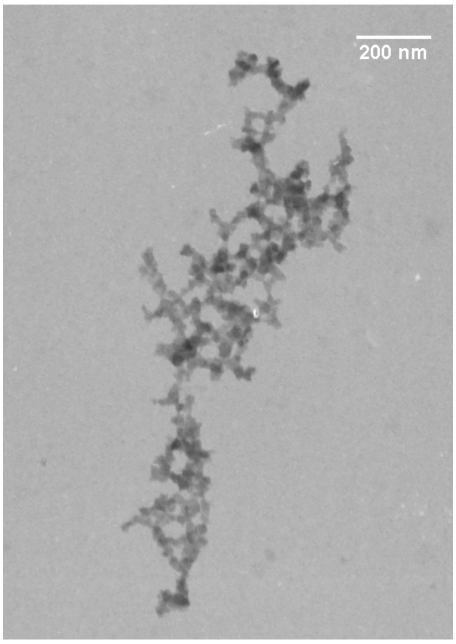

Fig. 7.4.4.12.: TEM image of **11-30-D1**, dropcasted on carbon

Fig. 7.4.4.13.: TEM image of **3-30-D1**, spin-coated on mica/carbon, shaded with W/Ta

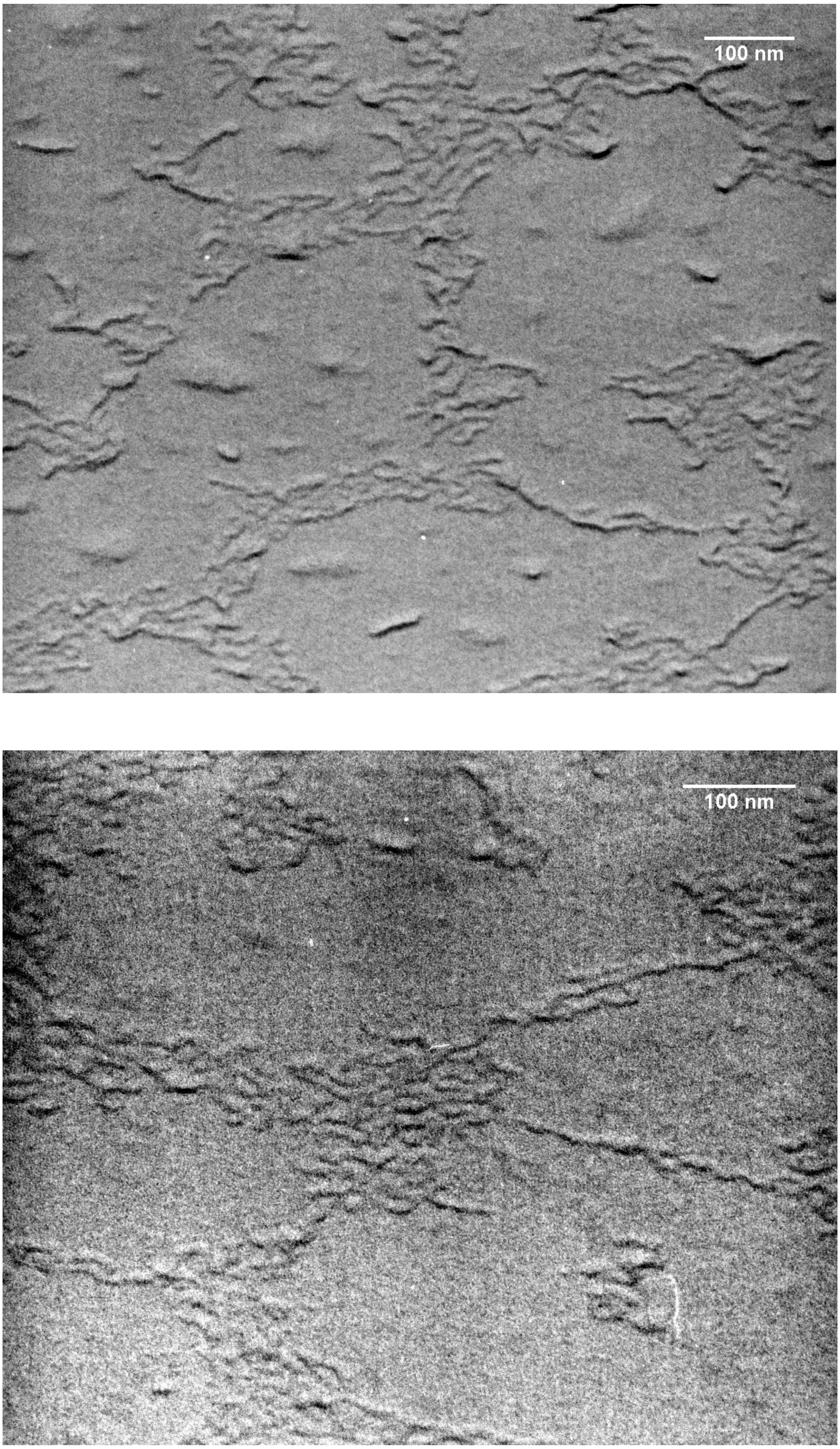

Fig. 7.4.4.14.: TEM image of **3-30-D1**, spin-coated on mica/carbon, shaded with W/Ta

7.5. Synthesis of Polymer Brushes from Poly(styrene sulfonate ethyl ester)

As has been discussed above, the polymer brushes obtained from poly(styrene sulfonate dodecyl ester) were structurally ill-defined (broad side chain length polydispersity, not strictly monomodal) and extremely difficult to characterize, as GPC and static light scattering could not be employed. Moreover, quantitative hydrolysis of the **PSSD** brushes (see chapter 7.7.) was difficult. For that reason, the problem of polymerization of styrene sulfonate *ethyl* ester with macroinitiators was revisited. When applying the same reaction parameters as in the polymerization of the **SSD** monomer to the polymerization of **SSE**, only polymer gel was obtained. The polymerization rates of this monomer were found to be much faster than those of the corresponding **SSD** ester. After systematic variation of the solvent, the reaction temperature and the dilution conditions, polymer brushes from poly(styrene sulfonate ethyl ester) were obtained. Cu(I)Cl/N,N'-dinonylbipyridine was used as a catalyst system and a mixture of chlorobenzene and acetone as solvents, with a solvent to monomer ratio of 1:2 (v/v). For higher degrees of branching, the system was further diluted. The conversion was kept below 10% in all cases. Above this value, gel was obtained. Figs. 7.5.1. and 7.5.2. show the monomer conversion for samples **11-40-E3** and **11-40-E4**, which were measured by *in situ* ^{1}H-NMR spectroscopy. As can be seen from the curves in the linear plot of conversion versus time (Fig. 7.5.1.), there is a change in gradient at 8% and 5% conversion, respectively. As in the case of **PSSD** brushes, it is difficult to decide whether the reaction is first or zeroth order with respect to monomer concentration. Table 7.5.1. gives the coefficients of determination for linear and logarithmic fits to both parts of the curves.

Tab. 7.5.1. Coefficients of determination of the linear regressions for Figs. 7.5.1. and 7.5.2.

Sample	R² (linear)	R² (logarithmic)
11-40-E3 (first part)	0.8964	0.89929
11-40-E3 (second part)	0.9888	0.99549
11-40-E4 (first part)	0.9216	0.92236
11-40-E4 (second part)	0.9943	0.99762

For the second part of each curve, the R^2 parameters are closer to unity for the logarithmic fit than for the linear fit, indicating that the reaction is first order with respect to monomer concentration. This is consistent with the results from bulk and solution polymerization of **SSE** with bifunctional initiators (chapter 9). For the first part of the curves, neither first nor zeroth order fits gave R^2 parameters close to unity. The following explanation is suggested: at the beginning of the reaction, the reaction rate is limited by monomer diffusion to the polymer backbone, which is crowded with initiating sites. Once the chains reach a certain length and make the reactive sites more approachable, the reaction proceeds with its expected first order kinetics. In the light of these results, the strange results from macroinitiator-initiated **SSD** polymerization (chapter 7.3.1.) can be re-interpreted. For these polymerizations, only one regime was found, which was zeroth order with respect to **SSD** concentration. As the long alkyl chains slow down the diffusion of the monomer to the reactive sites, it is assumed that the reaction is at all times diffusion-controlled.

Table 7.5.2. gives the kinetic parameters for samples **11-40-E3** and **11-40-E4**. The value determined for **SSE** polymerization in DMF at 333.15 K (chapter 9) was $5.5 \cdot 10^{-5}\ s^{-1}$. In spite of the different solvents and catalyst systems of both experiments, these values are on the same order of magnitude.

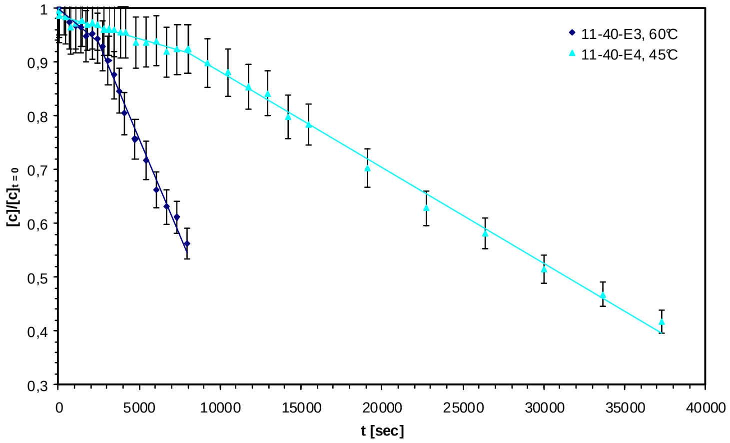

Fig. 7.5.1.: **SSE** polymerization: conversion versus time

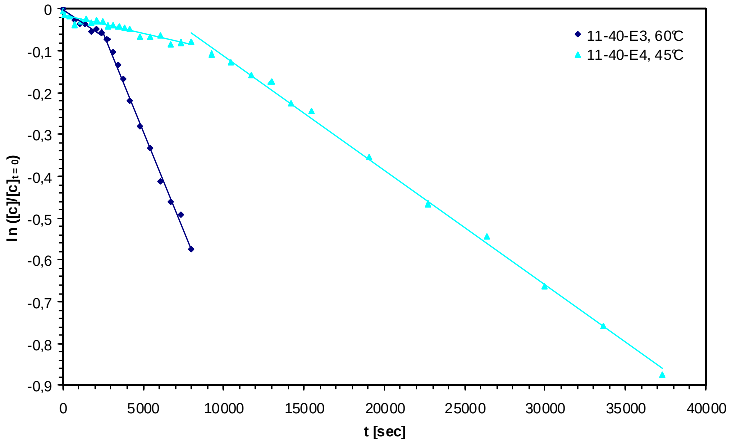

Fig. 7.5.2.: **SSE** polymerization: conversion versus time (logarithmic plot)

From the scarcity of the two data points of table 7.5.2., an activation energy of 73.4 kJ/mol was estimated. This is slightly higher than the 60.1 kJ/mol determined for **SSE** bulk polymerization, which explains the lower reaction rates as compared to polymerization in bulk.

Tab. 7.5.2. Kinetic parameters for **SSE** polymerization

Sample	T [K]	K [s^{-1}]
11-40-E3	318.15	$2.7 \cdot 10^{-5}$
11-40-E4	333.15	$9.6 \cdot 10^{-5}$
Activation energy E_a		73.4 kJ/mol

GPC reveals that for macroinitiator-initiated **SSE** polymerizations, at 60℃ high molecular weight polymer gel is formed. At 45℃, the desired polymer brushes with a monomodal molecular weight distribution (Fig. 7.6.1.1.) could be obtained if the reaction was quenched at low conversions. At room temperature, a large amount of homopolymer is formed as a side product (Fig. 7.5.3.). Consequently, there is a narrow temperature window for **SSE** polymerization with macroinitiators.

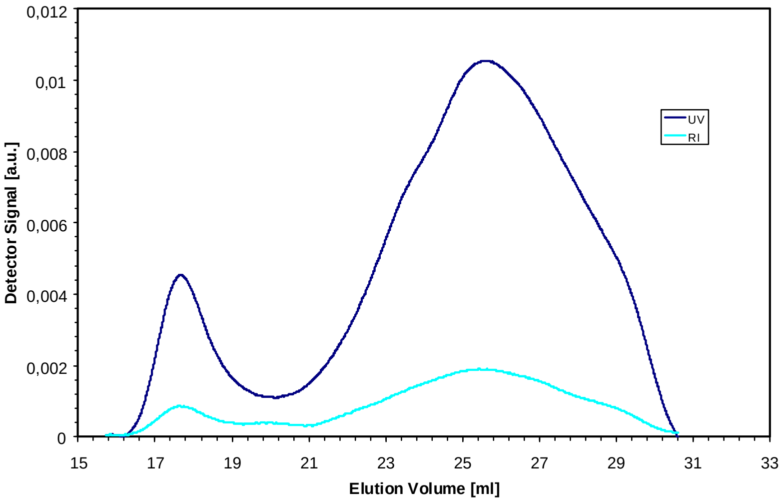

Fig. 7.5.3.: GPC elugram of SSE polymerization at 45℃

7.6. *Characterization of Polymer Brushes from Poly(styrene sulfonate ethyl ester)*

7.6.1. Molar Mass Distribution: GPC and GPC-MALLS

Unlike the **PSSD** polymer brushes, the **PSSE** brushes were eluted from the GPC column and thus could be analyzed by GPC-MALLS. The advantage of GPC-MALLS over off-line static light scattering is that, due to the separation by molecular weight on the GPC column, aggregation has not such a drastic effect on the molar mass determination as in off-line static light scattering. In off-line static light scattering, the molecular weight is determined by measuring the angular dependence of $K\,c/R_\theta$. The extrapolation to $c = 0$ and $q = 0$ yields M_w. In GPC-MALLS, $K\,c/R_\theta$ is measured in small volume elements along the GPC elugram. As the concentration in each volume element is very small (typically 10^{-5} g/L), it can be approximated to $c = 0$. For each volume element, extrapolation to $q = 0$ yields a value M. Summation over all M values and weighting (with reference to the concentration-sensitive refractive index signal) gives the M_w value for the whole sample. The results obtained for the **PSSE** polymer brushes are given in Table 7.6.1.1.. M_w and M_n were calculated from the GPC-MALLS measurement. As the M_w/M_n values from GPC only gives meaningful values if there is normal elution behaviour, which is not the case here (Fig. 7.6.1.2.), the polydispersity indices were taken also from the GPC-MALLS results. The values for M_w were obtained using the internal calibration constant of the RI detector and off-line measured refractive index increment (dn/dc) values. As a cross-check, the injected mass and the calculated mass were compared, yielding a recovery rate between 82 to 107 %, i.e. most samples were quantitatively eluted from the GPC column.

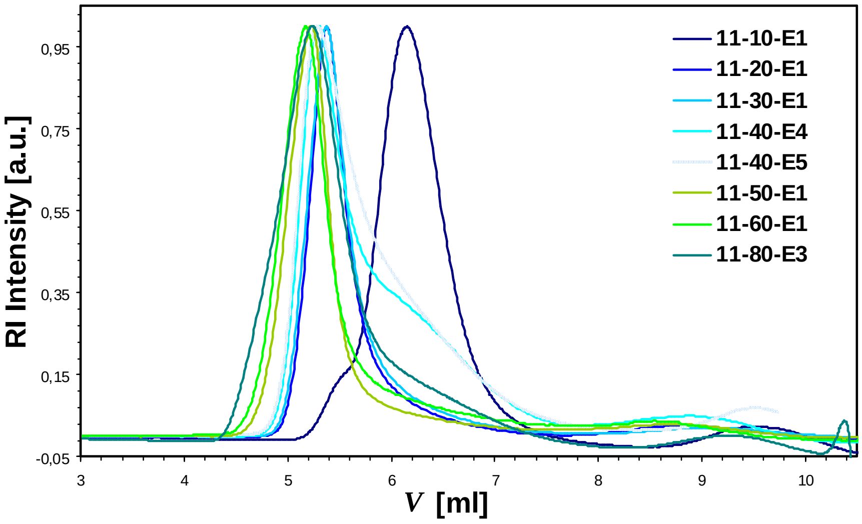

Fig. 7.6.1.1.: GPC elugrams of **PSSE** polymer brushes

Fig. 7.6.1.1. shows the GPC elugrams of the **PSSE** brushes. In most cases monomodal polymer brushes were obtained. Additional, a negligible amount of homopolymer is formed. Sample **11-10-E1** is an exception, as it shows a shoulder at the high molecular weight flank, which could be due to a small percentage of inter-brush crosslinking. The other samples show tailing on the low molecular weight flank.

This is an indication that the separation of the sample on the GPC column in not strictly by size exclusion - there seems to be some additional enthalpic interaction to the column material, which increases with increasing grafting density, as do the M_w/M_n values.

Table 7.6.1.1.: GPC-MALLS results of the **PSSE** brushes

Sample	M_w [g/mol]	M_n [g/mol]	M_w/M_n	$R_{g,z}$ [nm]	recovery rate	side chain length (n_n)
11-10-E1	637 000	562 000	1.13	27.8	1.08	11
11-20-E1	2 739 000	2 377 000	1.16	51.2	1.03	32
11-30-E2	2 736 000	2 312 000	1.21	52.2	0.90	22
11-40-E4	3 256 000	1 490 000	2.12	64.4	1.03	9
11-40-E5	2 972 000	1 723 000	1.73	62.4	1.03	10
11-50-E1	5 578 000	3 178 000	1.76	55.8	0.82	18
11-60-E1	1 577 000	702 000	2.26	60.5	0.87	3
11-80-E1	6 096 000	3 847 000	1.59	107	-	14
11-100-E1	22 260 000	9 945 000	2.24	139	-	30

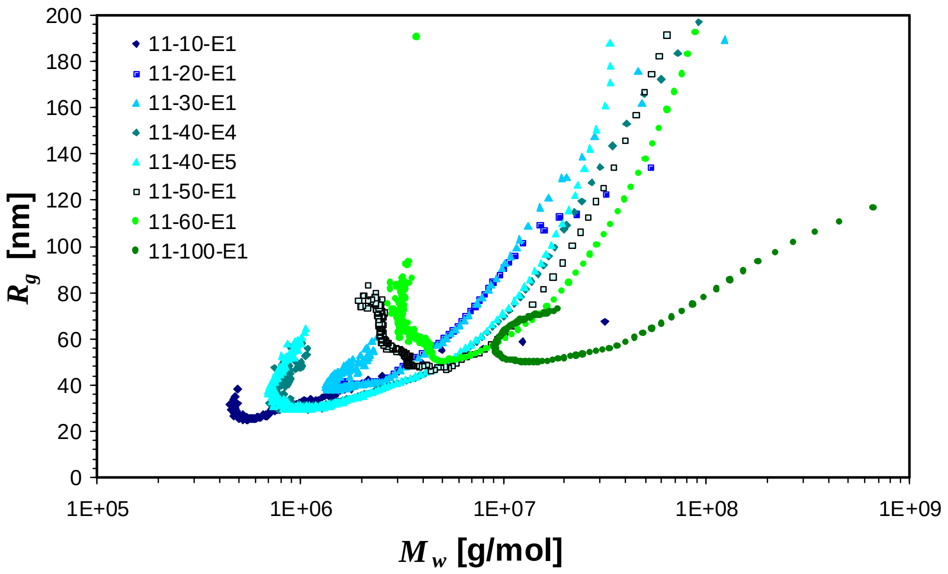

Fig. 7.6.1.2.: Plot of radius of gyration $R_{g,z}$ versus M_w

The dn/dc values for some **PSSE** samples are given in Fig. 7.6.1.4.. For the other samples, the values were extrapolated. The plot of the radius of gyration (determined for each volume element along the GPC-MALLS elugram, versus M_w measured at that volume slice (Fig. 7.6.1.2.)), shows that there is non-linear elution behaviour for the **PSSE** polymer brushes. This is consistent with reports of GPC-MALLS measurements on other polymer brushes in the literature, which also have anomalous elution behaviour[163,164]. This is typical for highly branched systems, however the phenomenon has not yet been sufficiently explained. This is discussed further in section 7.8. When looking at the Zimm plot for the individual volume elements of the GPC-MALLS measurements (Fig. 7.6.1.3.), they feature the usual positive gradient and a linear q^2 dependency expected for such a plot. This is contrary to the findings in off-line static light scattering on poly(styrene sulfonate esters) (Fig. 7.4.2.1.), where a negative gradient was observed. As electrostatic interactions (due to partial hydrolysis of the sample) were suppressed by salt addition in these off-line measurements, it can be concluded that the origin of the negative Zimm slope is structure formation in solution. This was not present in the GPC-MALLS experiments, as any structures were broken by the shear forces on the GPC column or filtered out.

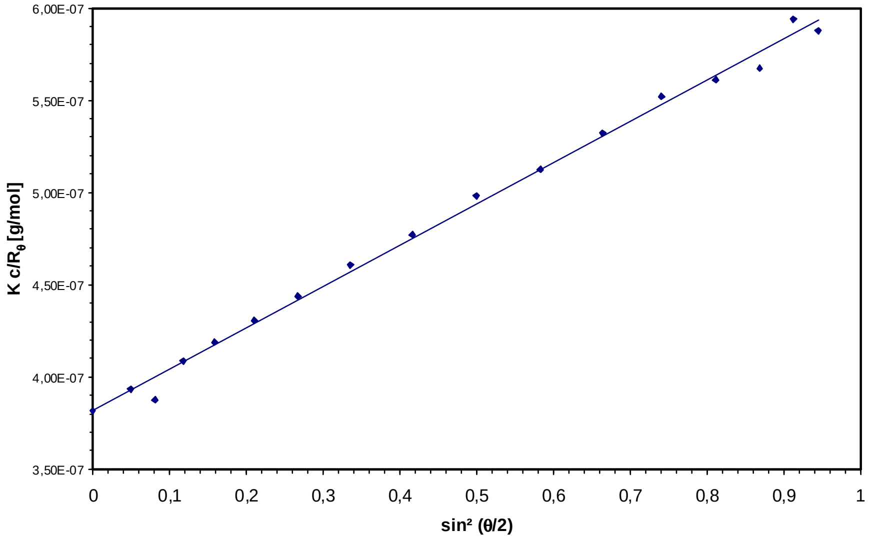

Fig. 7.6.1.3.: Zimm plot for an arbitrary volume element from sample **11-50-E1**

To test this hypothesis, sample **11-40-E5** was fractioned by GPC into a light scattering cuvette. The result is presented in Fig. 7.6.1.5.: after fractionation, a positive slope is obtained in off-line static light scattering, indicating that no aggregates are present. By estimating the concentration to 0.03 g/L and extrapolating to $q = 0$, the molecular weight M_w was estimated to be around 2 300 000 g/mol, which is on the same order of magnitude as the results presented in Tab. 7.6.1.1. . The angular dependence from GPC-MALLS of the other samples is given in the Appendix as supporting information. In previous works on polymer brushes, the Kuhn segment length was determined from the plot of $R_{g,z}$ vs M_w[163] for each GPC-MALLS slice. As pointed out by Wahnes[165], this is only possible for samples with a broad polydispersity and was therefore not done for these samples. In Fig. 7.6.1.6., the radii of gyration (*z*-average) of the whole sample are plotted versus the grafting density of the samples. Although the side chain length and the molar masses are disregarded in this plot, there is and interesting correlation between $R_{g,z}$ and the grafting density, which apparently levels off for higher degrees of branching, as no further stretching of the backbone is observed. This corresponds to the findings by Wahnes[165], who investigated the stretching of poly(styrene) brushes with increasing grafting density, as well as to the results from the AFM measurements on **PSSD** brushes (Fig. 7.4.4.1.).

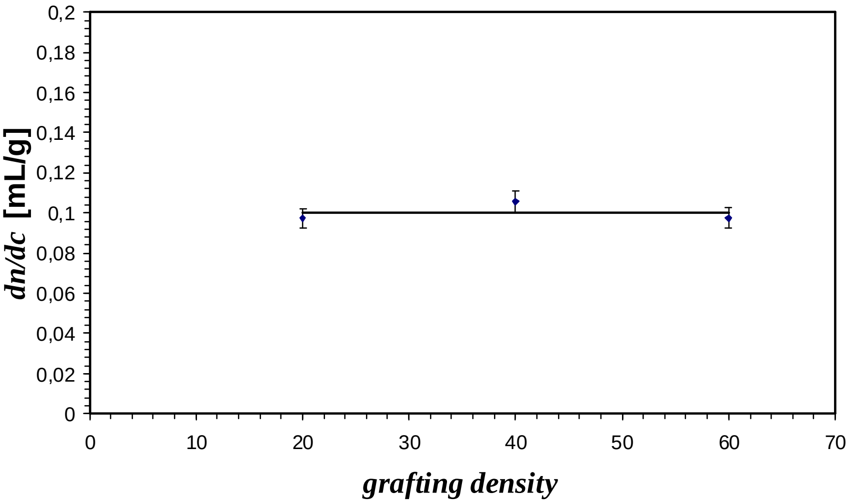

Fig. 7.6.1.4.: *dn/dc* values for **PSSE** brushes

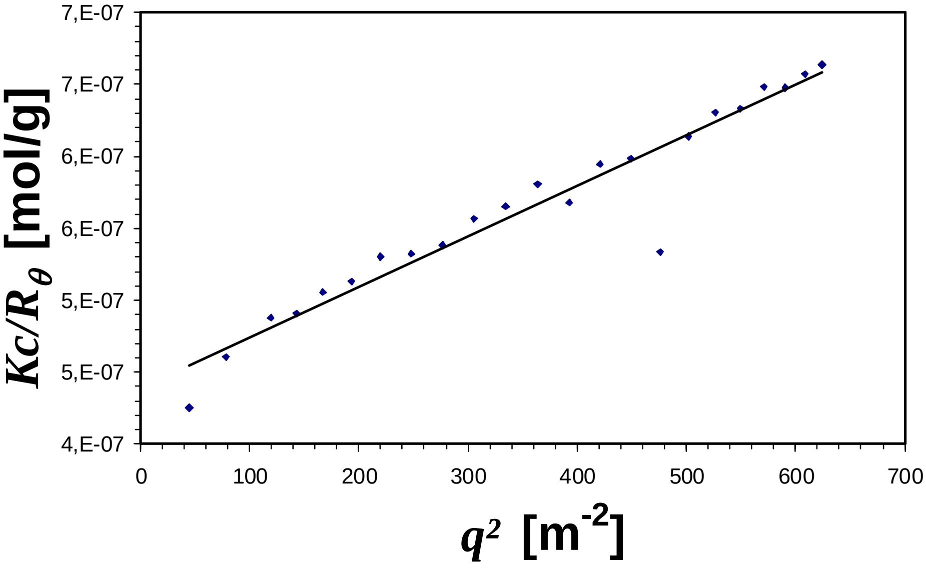

Fig. 7.6.1.5.: Off-line static light scattering of sample **11-40-E5**, after fractionation

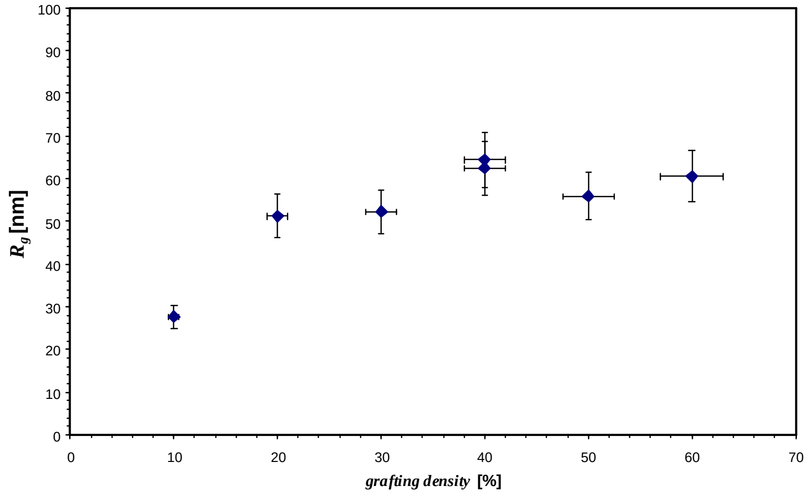

Fig. 7.6.1.6.: Correlation between radius of gyration ($R_{g,z}$) and the grafting density

7.6.2. Side Chain Length Determination by ^{1}H-NMR

The side chain lengths of the **PSSE** brushes and the corresponding molar masses M_n were determined by ^{1}H-NMR as described in chapter 7.4.3.. The results are presented in Table 7.6.2.1..

Table 7.6.2.1.: Side chain length determination by ^{1}H-NMR

Sample	side chain length (n_n), (GPC-MALLS)	side chain length (n_n), (NMR)	M_n [g/mol]
11-10-E1	11	6	396 000
11-20-E1	32	19	1 388 000
11-30-E2	22	17	1 661 000
11-40-E4	9	40	4 848 000
11-40-E5	10	11	1 484 000
11-50-E1	18	41	5 935 000
11-60-E1	3	24	4 391 000
11-80-E1	14	34	7 775 000
11-100-E1	30	40	9 469 000

As can be seen by comparison with the results from GPC-MALLS, as far as rough orders of magnitude go, the trends are the same for both methods: **11-10-E1** has by far the smallest molecular weight; **11-20-E1** and **11-30-E2** have approximately the same M_w and M_n, respectively; **11-80-E1** and **11-100-E1** have the largest molecular weights. Otherwise, the values deviate. This can be made plausible by the following considerations: for the ^{1}H-NMR values it is assumed that all protons relax quantitatively on the timescale of the ^{1}H-NMR experiment, which might not be the case due to the molecule structure. Also, the error from NMR increases with increasing mass fraction of the side chains because the relative contribution of the backbone protons to the integral of the aromatics decreases to a percentage near the limit of the method (3-5%). Tab. 7.6.2.2. is a rearrangement of the values obtained, including the M_n values from NMR and M_w values from GPC-MALLS, thus the values can be compared without the bias due to inaccurate M_w/M_n values. For comparison, the M_w/M_n value has been calculated from the results displayed.

Table 7.6.2.2.: Molecular weight of **PSSE** brushes: M_n determination by ^{1}H-NMR, M_w from GPC-MALLS, M_w/M_n calculated

Sample	$M_w/M_{n,\ calc}$	M_n [g/mol]	M_w [g/mol]
11-10-E1	1.61	396 000	637 000
11-20-E1	1.97	1 388 000	2 739 000
11-30-E2	1.65	1 661 000	2 736 000
11-40-E4	0.67	4 848 000	3 256 000
11-40-E5	-	-	2 972 000
11-50-E1	0.94	5 935 000	5 578 000
11-60-E1	0.36	4 391 000	1 577 000
11-80-E1	0.78	7 775 000	6 096 000
11-100-E1	2.35	9 469 000	22 260 000

For the first three samples, the results are reasonable. For the brushes with higher degrees of branching, the value becomes smaller than unity, which is physically meaningless. This is due to the experimental error from NMR, which increases with increasing branching density and thus simulates M_n values that are too high. It is therefore more plausible to calculate the side chain lengths from the GPC-MALLS results. These values have been included in Table 7.6.2.1.. For branching densities from 40% upwards, the NMR error becomes dominant, thus considerable deviations are observed, while the trends and orders of magnitude are similar for the samples with lower degree of branching. As the side chain length determinations by GPC-MALLS and NMR assume 100% initiation efficiency, which is certainly an overestimation, the values obtained are minimum values.

7.6.3. Single Molecule Imaging by AFM and TEM

Imaging of the **PSSE** esters was found to be much more difficult than in the case of the **PSSD** esters. The reasons for this lie in the chemical and physical properties of the ester residue. The **PSSD** brushes are more hydrophobic due to the dodecyl ester group. On mica, these hydrophobic side chains adhere to the surface. As a result, the single molecules are fixed on the surface and lie flat. The dodecyl ester residue gives enough mechanical contrast to make them visible by AFM (Fig.7.4.4.8.). The physisorption of the polar **PSSE** brushes on the mica is weaker, i.e. the molecules are easily shifted by the AFM tip if the tapping force is too high. Additionally, as the **PSSE** esters are hygroscopic and become sticky during the measurement, the tip is quickly contaminated by loosened polymeric material. **PSSE** brushes are strongly aggregating, as can be seen from Fig. 7.6.3.1.. This makes the determination of the length of a single molecule practically impossible. From the morphology, it appears that **PSSE** brushes are more coiled than the **PSSD** brushes with the same grafting density. It is assumed that the **PSSD** brush molecules with low grafting densities (~30%) are stretched due to the steric repulsion of the bulky side chains. As will be discussed in chapter 7.8., the contour length of polyelectrolyte brushes obtained by saponification of such **PSSD** brushes is drastically decreased as compared to the parent ester. Thus, the different morphology of the **PSSE** brushes is not surprising, as the steric repulsion of the side chains is less for **PSSE** brushes and even smaller for the saponified brushes. In conclusion, while the **PSSE** brushes are much easier to characterize and, as we will see later, to hydrolyse than the **PSSD** brushes, they are a less rewarding object for imaging and will therefore not be considered further. However they will be used as an intermediate to obtain the corresponding polyelectrolyte brushes.

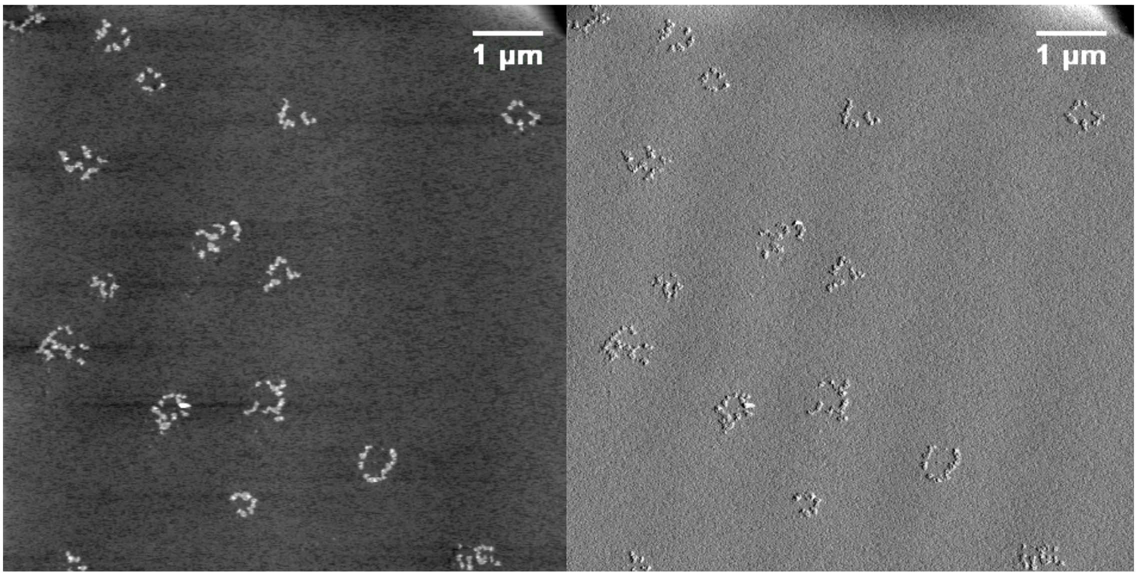

Fig. 7.6.3.1.: AFM image of sample **11-40-E4** (tapping mode, spin-coated on mica, height and phase image), contour length 269 nm, diameter 55 nm

7.7. *Polymer Brush Hydrolysis*

7.7.1. Hydrolysis of PSSD Brushes

As described by Woeste, poly(styrene sulfonate ethyl esters) can be quantitatively hydrolyzed by potassium hydroxide, potassium acetate, barium hydroxide or ammonium carbonate. In the last case, the free acid form is available, in the other cases, the salt is obtained[162]. More recent literature[166] suggests that poly(styrene sulfonate alkyl esters) can be quantitatively saponified by a transesterification with trimethylsilyl iodide, followed by hydrolysis of the resulting silylether. For the **PSSD** *brushes*, it was found that quantitative hydrolysis is very difficult and could not be obtained by either method. For sample **3-30-D1**, four different hydrolysis conditions were tested and analyzed.

- As shown in Fig. 7.7.1.1., hydrolysis with potassium hydroxide in THF/H_2O at 100℃ for 24 h led to a phase separation, followed by precipitation of the polyelectrolyte. After ion exchange with an acidic ion exchange resin, the degree of saponification of the product (**3-30-PSS1, H$^+$**) was determined by acid-base titration to be 10%.
- To avoid precipitation of the polyelectrolyte, it was attempted to conduct the reaction entirely in an organic solvent. Exploiting the alkylating properties of styrene sulfonate esters, triethylamine (at 40℃ in $CHCl_3$) was employed as a saponification agent (Fig. 7.7.1.2.). After three hours, the polyelectrolyte precipitated. After ion exchange, the product (**3-30-1, H^{++}**) was found to be 40% hydrolyzed (by acid-base titration).
- Sequential hydrolysis by triethylamine (in $CHCl_3$, 40℃, 180 min), sodium hydroxide (H_2O, 100℃, 48 h) and HCl (H_2O, 100℃, 48℃), as shown in Fig. 7.7.1.3., led to a polymer that was found to be at least 90% hydrolyzed. However, due to the severe reaction conditions applied, a large fraction of the product (**3-30-1H**) was insoluble.
- Transesterification of **3-30-D1** with trimethylsilyl iodide in CH_2Cl_2 at 40℃, followed by saponification of the silylether with NaOH at 100℃ and ion exchange (Fig. 7.7.1.4.) led to a product (**3-30-1, TMS1, H$^+$**) with at least 66% saponified groups, as determined by acid-base titration. The silylether was completely soluble in CH_2Cl_2, but due to the mild reaction conditions, complete saponification could not be obtained. The product is water soluble and not crosslinked, as shown by aqueous GPC (see below).

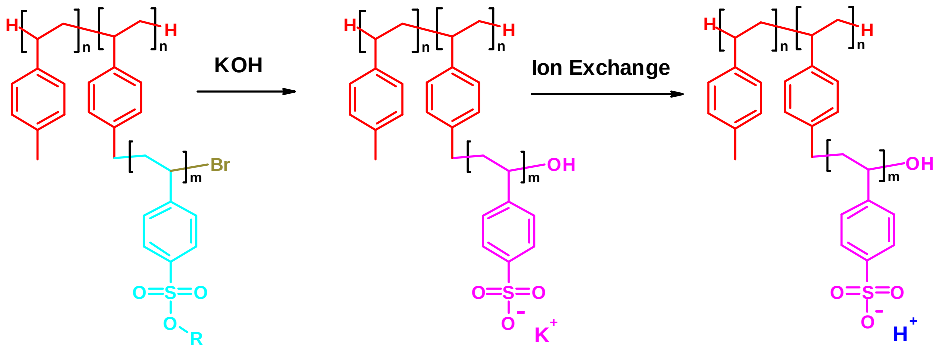

Fig. 7.7.1.1.: Synthesis of **3-30-PSS1, H$^+$**

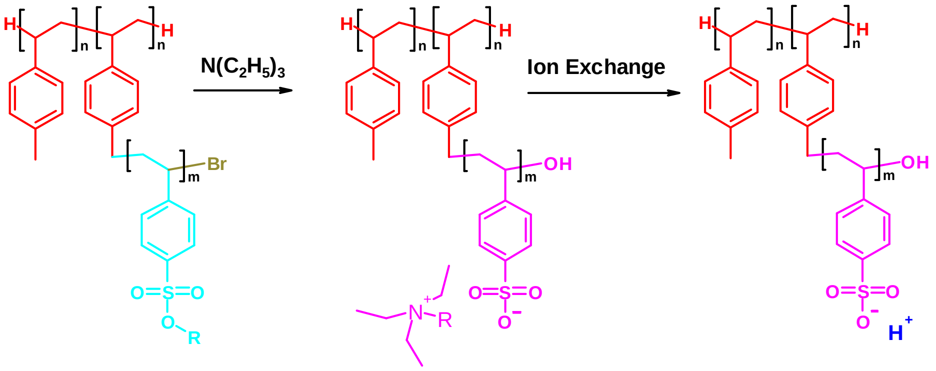

Fig. 7.7.1.2.: Synthesis of **3-30-1, H^{++}**

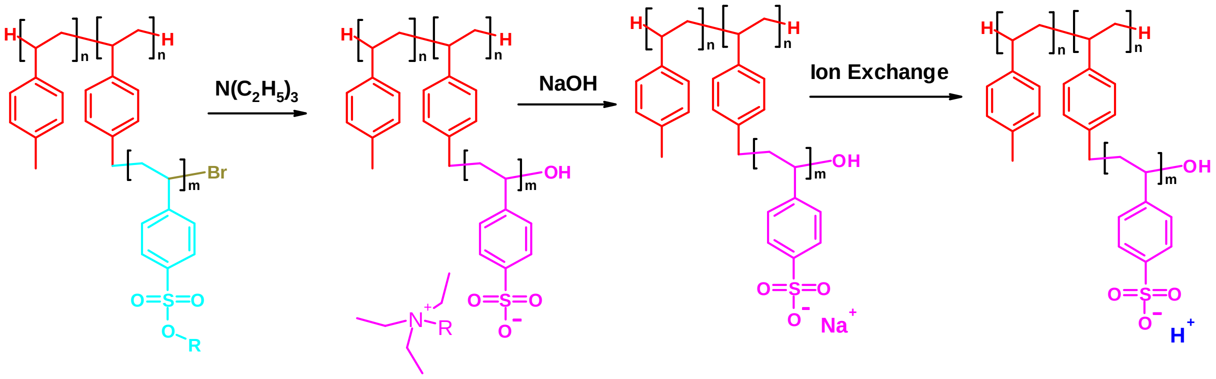

Fig. 7.7.1.3.: Synthesis of **3-30-1H**

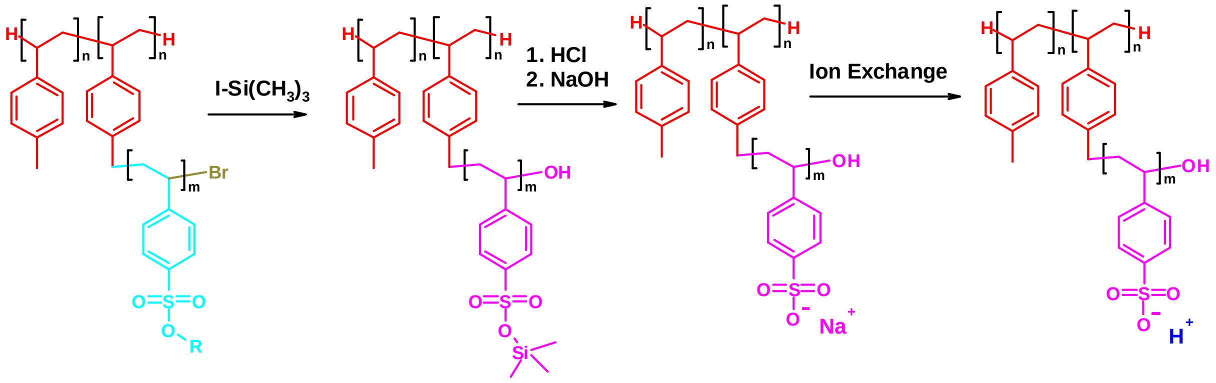

Fig. 7.7.1.4.: Synthesis of **3-30-1, TMS1**

All samples were freeze dried after ion exchange and re-dissolved in ion-free Milli-Q water (conductivity 0.1 µS) to obtain a 5% solution. After filtration, the solutions were dialyzed against 10 L Milli-Q water for two weeks. ^{1}H-NMR spectra of selected polyelectrolyte brushes are shown in Fig. 7.7.1.5.. As expected, the signals from the ester residues (at 3.8 ppm, 1.9 ppm and 1.3 ppm) are decreased in sample **3-30-1, H^{++}** as compared to sample **3-30-PSS1, H$^+$**, which is in accordance with the findings from acid-base titration. The same is found for samples **3-30-1, TMS1, H$^+$** and **3-30-1, H**.

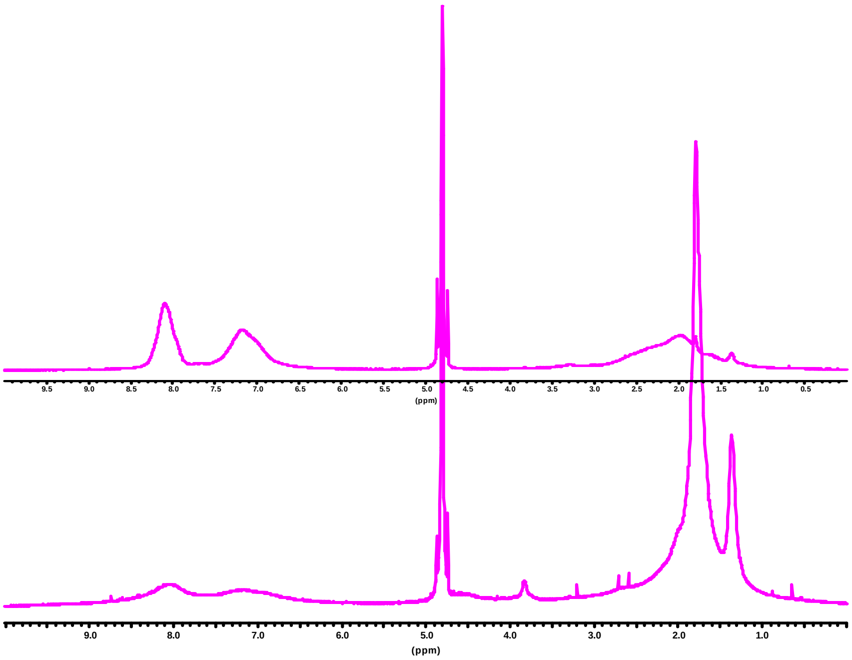

Fig. 7.7.1.5.: ^{1}H-NMR (300 MHz, D_2O, 80°C) spectra of **3-30-PSS1, H$^+$** (below) and **3-30-1, H^{++}** (above).

7.7.2. Hydrolysis of PSSE Brushes

As shown in section 7.7.1., soluble polyelectrolyte brushes with high degrees of saponification could only be obtained via saponification of the corresponding trimethylsilyl ethers. In the light of these results, the **PSSE** brushes were solely saponified by this method (Fig. 7.7.1.4. with R = C_2H_5). The reaction work-up was performed as described in section 7.7.1..

7.8. Characterization of Polyelectrolyte Brushes

7.8.1. Molar Mass Distribution – GPC and GPC-MALLS

Due to their amphiphilicity, it was difficult to find a column/eluent system in GPC which would elute the polyelectrolyte samples without tailing effects due to enthalpic interactions. Initial attempts with H_2O/acetonitrile (9:1) and H_2O/0.1 g/L $NaNO_3$ on TSK gel columns led to a peak broadening due to enthalpic interactions with the column material, as shown in Fig. 7.8.1.1. for sample **3-30-PSS1, H$^+$.** The same was found for DMF/1 g/L LiBr, DMF/H_2O and H_2O/1 g/L LiBr on Suprema columns. Switching the system to anionically charged MCX columns (H_2O/0.1 g/L $NaNO_3$) minimized the enthalpic interactions and drastically decreased the polydispersity index. After off-line measurements of the refractive index increments, the molecular weights M_w could be determined for two series of samples by GPC-MALLS, as shown in Tables 7.8.1.1. and 7.8.1.2.. The GPC elugrams for these samples are given in Figs. 7.8.1.2. and 7.8.1.3..

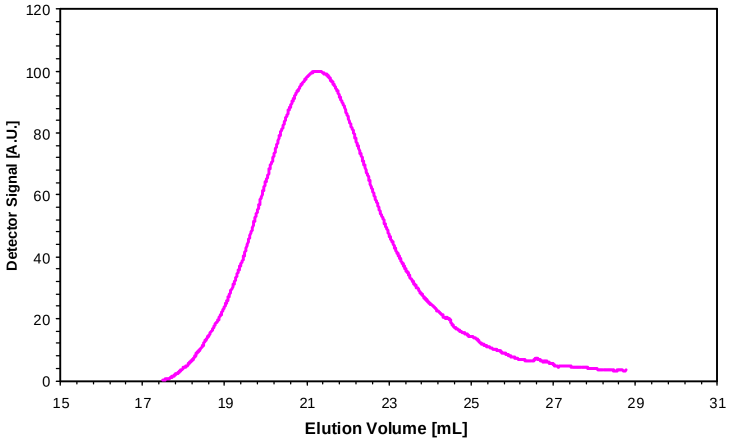

Fig. 7.8.1.1.: GPC elugram of **3-30-PSS1, K$^+$** (TSK column, H_2O/acetonitrile 9:1), M_w/M_n = 5.48

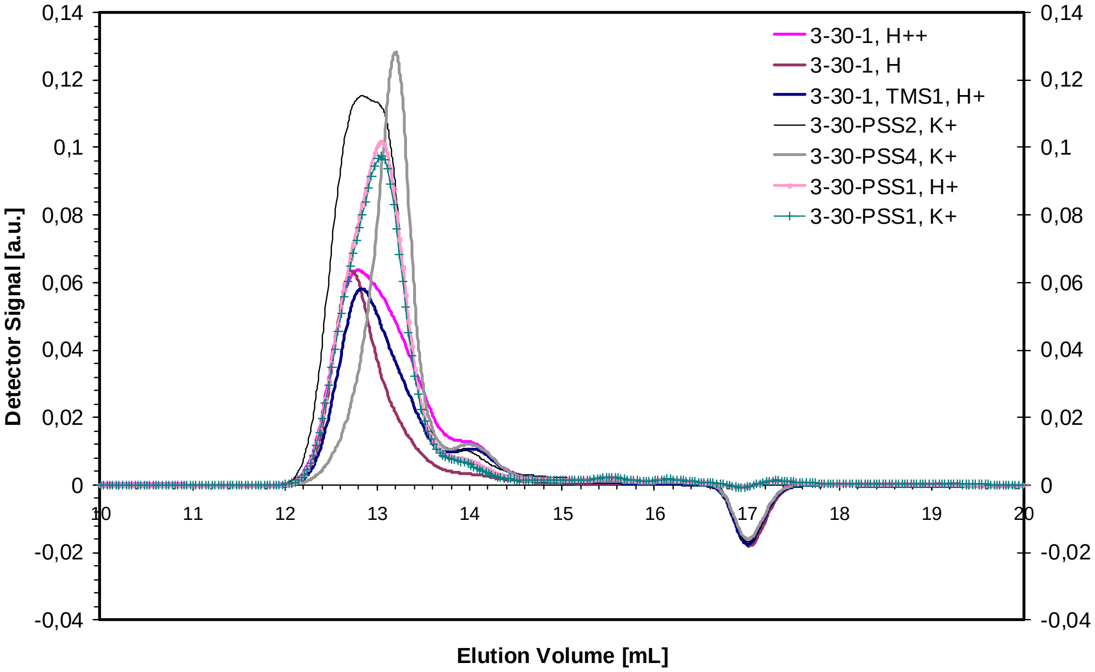

Fig. 7.8.1.2.: Polyelectrolyte brushes from the **3-series**

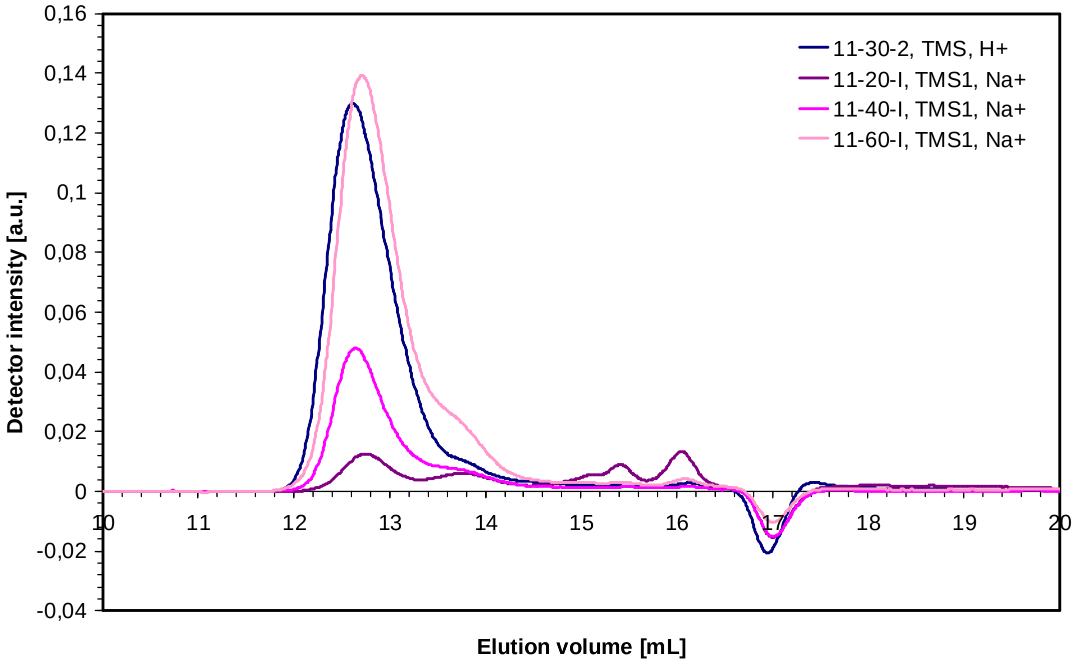

Fig. 7.8.1.3. Polyelectrolyte brushes from the **11-series**

Table 7.8.1.1. GPC-MALLS results for polyelectrolyte brush samples from the **3-series** (a = saponification with KOH, b = with NEt_3, c = with KOH/NEt_3, d = with silyl ether)

Sample	Parent Ester	*dn/dc*	M_w [g/mol]	M_w/M_n	% hydrolysis
3-30-1,PSS1, $H^{+,a}$	**3-30-D1**	0.160	1 590 000	1.25	10
3-30-1, $H^{++,b}$	**3-30-D1**	0.160	705 000	1.46	40
3-30-1, H^{c}	**3-30-D1**	0.160	920 000	1.30	90
3-30-1, TMS1, $H^{+,d}$	**3-30-D1**	0.160	850 000	1.48	66
3-30-2,PSS1, $K^{+,a}$	**3-30-D2**	0.165	1 765 000	1.19	10
3-30-4,PSS1, $K^{+,a}$	**3-30-D4**	0.165	927 000	1.43	-

As can be seen from Fig. 7.8.1.2., all samples from the **3-series** were eluted from the GPC column. The M_w values obtained for these samples (lines 1 to 4 in Table 7.8.1.1.) reflect the different degrees of saponification of each species, which is lowest for **3-30-1,PSS1,H^+** and of the same order of magnitude for **3-30-1,TMS1,H^+** and **3-30-1,H^{++}**. For **3-30-1, H**, M_w is again slightly higher due to partial crosslinking in the sample. The polydispersities vary due to their different degrees of saponification and the resulting enthalpic interactions with the column material: **3-30-1,TMS1,H^+** and

3-30-1, H^{++} with similar degrees of saponification, and two of the **PSS** samples (line 1 and 5) have about the same polydispersity index, respectively.

For the samples from the **11-series**, the elution behaviour from the GPC column is less well-behaved. Samples **11-30-2, TMS, H^{+}**, **11-40-I, TMS, Na^{+}** and **11-60-I, TMS, Na^{+}** elute with the expected (mainly) monomodal distribution with slight tailing at the low molecular flank of the elugram (Fig. 7.8.1.3.). For samples **11-20-I, TMS, Na^{+}** (Fig. 7.8.1.3.) and **11-40-I, TMS, H^{+}** (Fig. 7.8.1.4.), a series of apparently low molecular weight peaks (according to the RI detector signal) is found in addition to the high molecular weight peak.

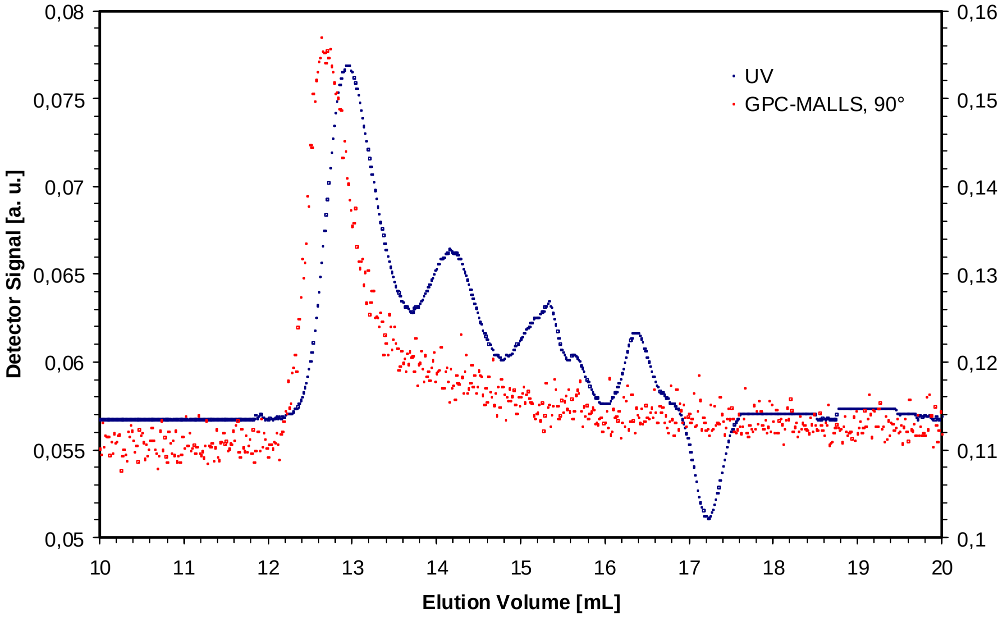

Fig. 7.8.1.4. GPC-MALLS elugram of **11-40-IV, TMS1, H^{+}**

No such peaks were found for other samples from both the **3-series** and the **11-series** which experienced the same reaction conditions. A closer analysis of these peaks by separate evaluation of the MALLS detector signal reveals that the molecules causing these peaks have similar molecular weight as those in the first maximum. Why this occurred only for these samples is unknown. The effect was reproducible for these samples and did not occur for the samples measured before and after, thus the peaks cannot be “ghost peaks”. While a retarded elution of such molecules due to entanglement of the sidechains with the column material is not unusual for highly branched molecules, it is striking that these molecules elute in discrete peaks rather than as a general ‘tail’. Therefore, the cause for delay seems to be a defined physical event during the separation process. For sample **11-40-IV, TMS1, H^{+}**, the obtained value for M_w (1 365 000 g/mol) is rather at the lower end of the expected value, considering that M_w of the starter is already 200 000 g/mol. Thus it is reasonable to assume that this value corresponds to single molecules. As will be seen in sections 7.8.2. and 7.8.5., this sample is prone to form huge well-defined aggregates. Thus the delayed elution of a series of peaks with the same M_w could be interpreted as due to the breaking of those aggregates during the separation process.

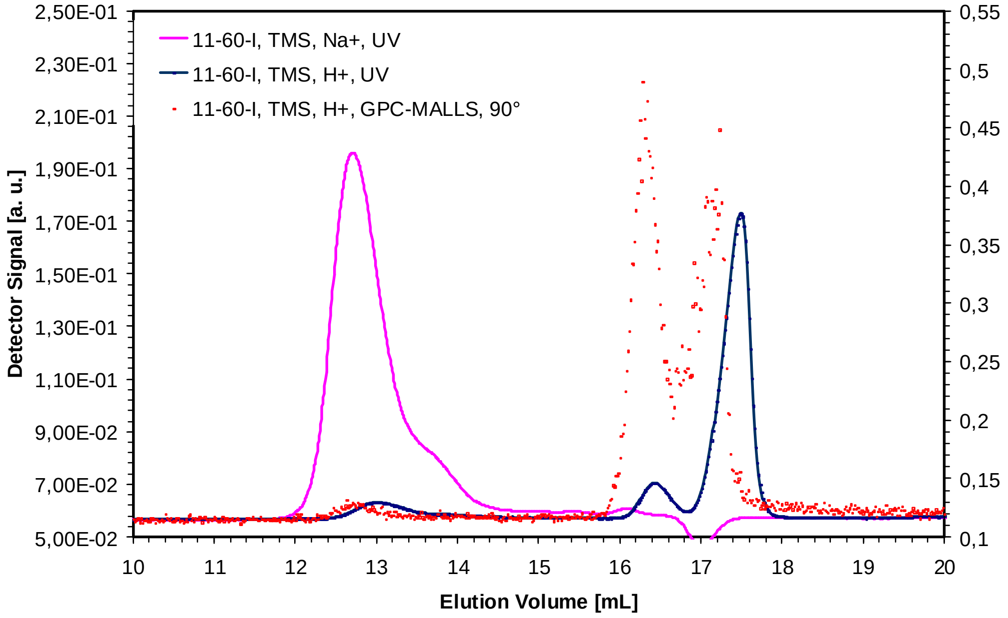

Fig. 7.8.1.4. GPC-MALLS elugram of **11-60-IV, TMS1, H$^+$**

Table 7.8.1.2.:GPC-MALLS results for polyelectrolyte brush samples from the **11-series** (saponification via silyl ether)

Sample	Parent Ester	*dn/dc*	M_w [g/mol]	M_w/M_n	side chain length (n_n)
11-30-2,TMS1, H$^+$	**11-30-D2**	0.161	1 607 000	1.17	13.3
11-40-IV, TMS1, H$^+$	**11-40-E4**	0.170	1 365 000	1.45	5.4
11-40-IV, TMS1, Na$^+$	**11-40-E4**	0.167	1 744 000	1.38	7.2
11-20-I, TMS1, Na$^+$	**11-20-E1**	0.167	2 066 000	1.78	14.3
11-60-I, TMS1, H$^+$	**11-60-E1**	0.170	1 518 000	-	5.6
11-60-I, TMS1, Na$^+$	**11-60-E1**	0.167	1 563 000	1.20	5.4

The elution behaviour of sample **11-60-I, TMS, H$^+$** is also unexpected. While only a small peak is found at the position where the high molecular height fraction would be expected (Fig. 7.8.1.4., elugram of **11-60-IV, TMS, Na$^+$** added for clarity), a strong bimodal signal is found in the lower molecular weight range. The evaluation of the light scattering signal reveals that these peaks correspond to very high molecular weight aggregates. It is known from literature that highly branched may experience a “sieving” effect[164] if the molecule size is on the same order of magnitude as the inter-particle distance of the column material. Another explanation for the delay would be enthalpic interactions with the column. Table 7.8.1.2. summarizes the GPC-MALLS results for the **11-series**, including the values for the "normally" eluted peaks for samples **11-20-I, TMS, Na$^+$**, **11-40-I, TMS, H$^+$** and **11-60-I, TMS, H$^+$** at an elution volume of 12-13 mL.

The calculated side chain length values in Table 7.8.1.2. are self-consistent, as good agreement is found for **11-60-I, TMS1, H$^+$** and **11-40-IV, TMS1, H$^+$** with their corresponding sodium salts. The deviation from the side chain lengths of the parent esters determined by GPC-MALLS (**11-60-E1**: n = 3.2, deviation 36%., **11-40-E1**: n = 9.9, deviation 38%, **11-20-I, TMS1, Na$^+$**, n = 25.8, deviation 43%) is reasonable for the cumulative experimental error of two dn/dc measurements and two GPC-MALLS measurements. As discussed previously, the side chain lengths calculated are minimum values, as 100% initiation efficiency of the macroinitiator was assumed. A sidechain length determination by ^{1}H-NMR was not attempted due to the broadness of the peaks and poor differentiation from the background even at elevated temperature (Fig. 7.7.1.5.).

7.8.2. Characterization by Static and Dynamic Light Scattering

As a second method for the determination of molecular weights, and to obtain further information on the structural properties of the polyelectrolyte brushes, selected samples were analyzed by static and dynamic light scattering. The experiments have been performed in DMF and water with lithium bromide as an additive to suppress polyelectrolyte effects. In spite of their common chemical structure (poly(p-methylstyrene) backbone and poly(styrene sulfonate) side chains), the solubility of the samples was different. For some samples, molecular disperse solutions could only be obtained in DMF but not in water, where large aggregates were formed. The results from the static light scattering measurements are presented in Fig. 7.8.2.1. and 7.8.2.2. as Zimm plots. Data analysis was performed by plotting Kc/R_θ vs q^2 for each sample concentration. Extrapolation to q = 0 yielded $Kc/R_{\theta, q=0}$. Plotting this value versus the sample concentration and extrapolation to c=0 gave $Kc/R_{\theta,\ q=0,\ c=0}$, which is the reciprocal value of M_w. The radius of gyration $\left\langle R_g \right\rangle_z$ was obtained by taking the slope of Kc/R_θ versus q^2 for each concentration and the extrapolated value $Kc/R_{\theta, q=0}$. Then, $\left\langle R_g \right\rangle_z = \sqrt{\frac{3 \cdot slope}{\mathrm{Kc/R}_{\theta,\mathrm{q=0}}}}$.

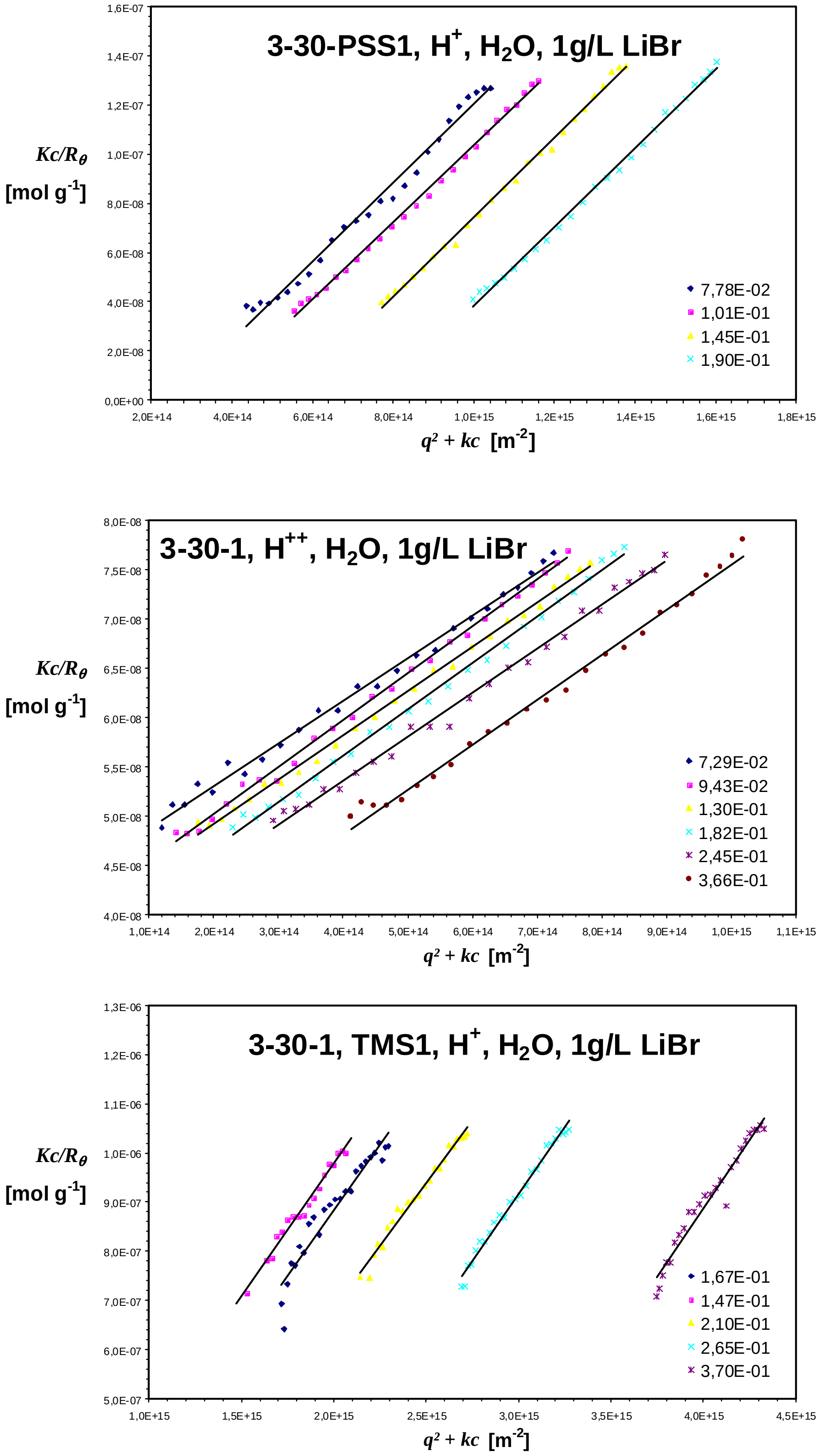

Fig. 7.8.2.1.: Zimm plots for polyelectrolyte brushes from the **3-series**, *c* in g/L

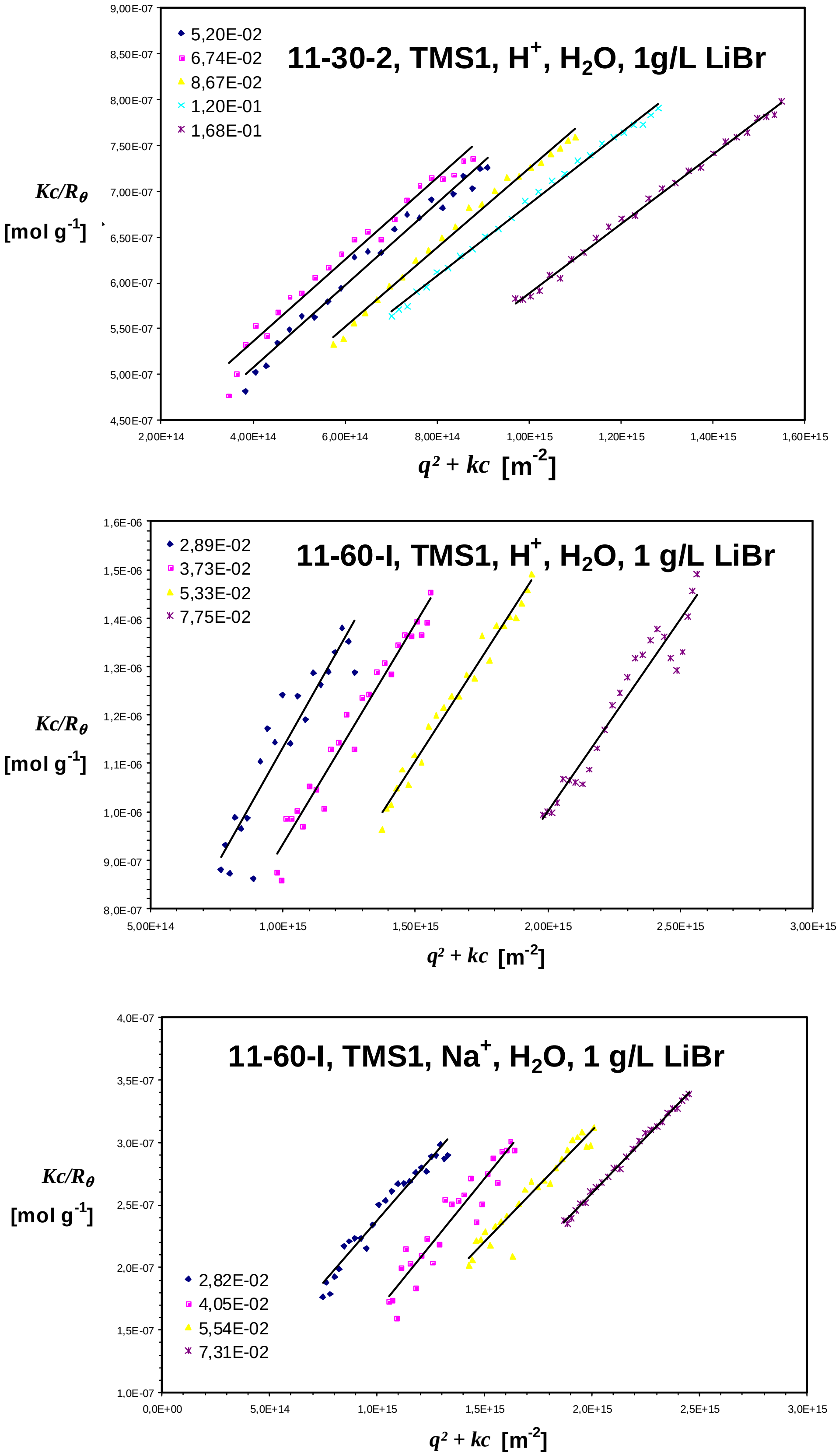

Fig. 7.8.2.2.: Zimm plots for polyelectrolyte brushes from the **11-series**, c in g/L

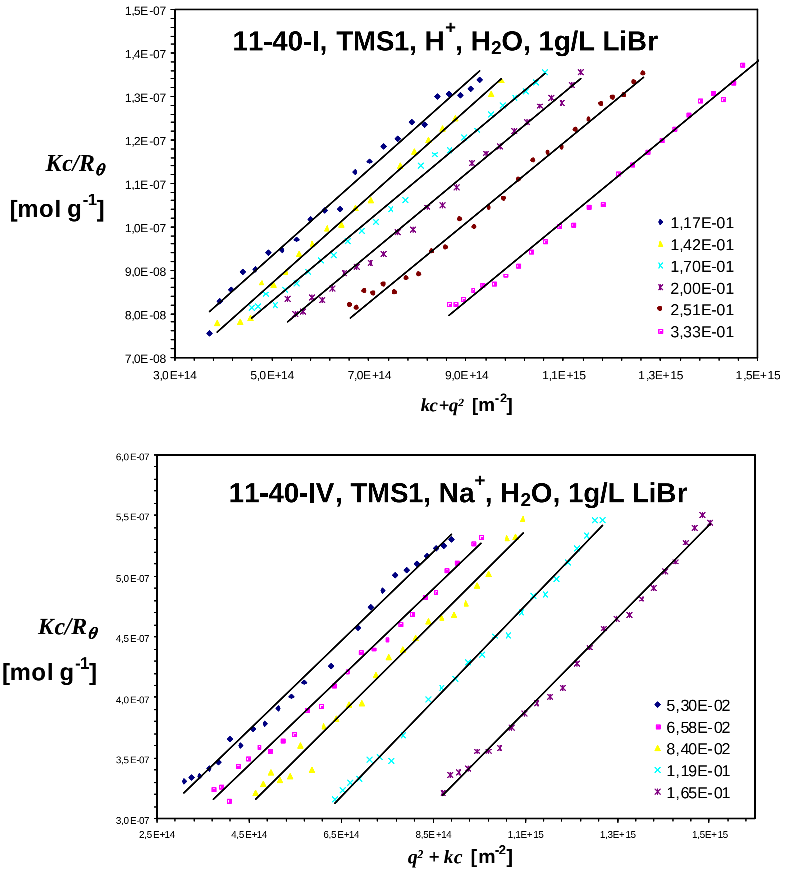

Fig. 7.8.2.2.(continued): Zimm plots for polyelectrolyte brushes from the **11-series**, *c* in g/L

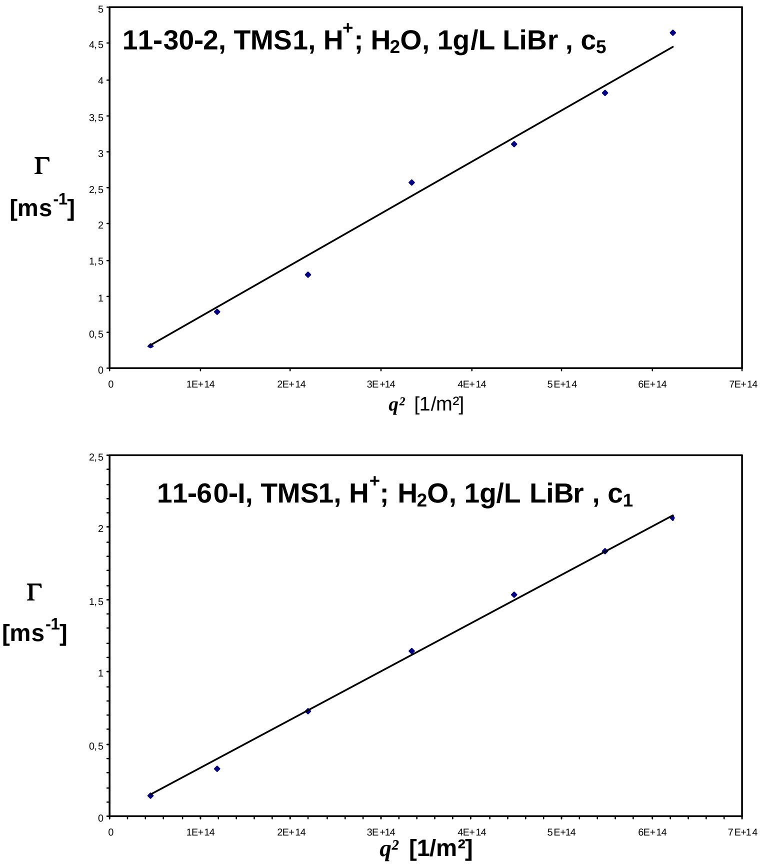

Fig. 7.8.2.3.: Plot of Γ vs q^2 for a representative sample. D_{app}. is obtained from the slope

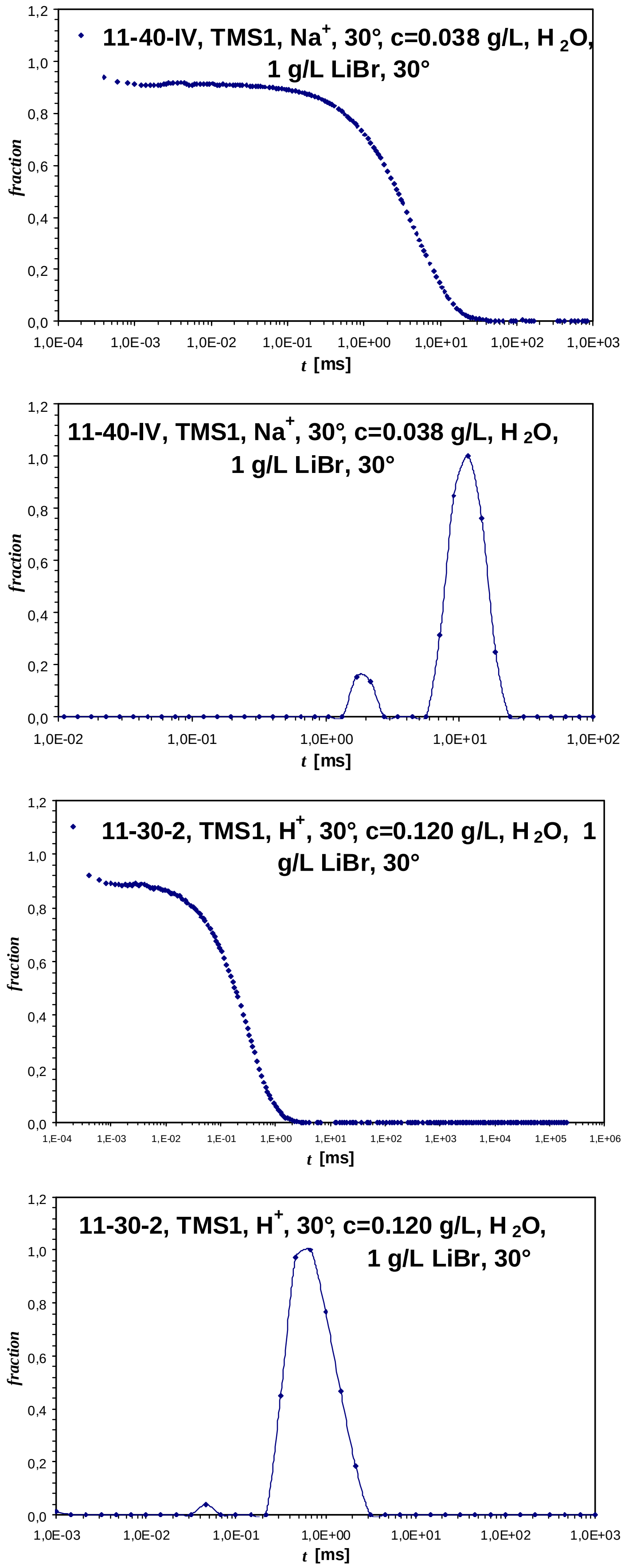

Fig. 7.8.2.4: Selected intensity correlation functions for polyelectrolyte brushes from the **11-series**, and corresponding relaxation time distributions

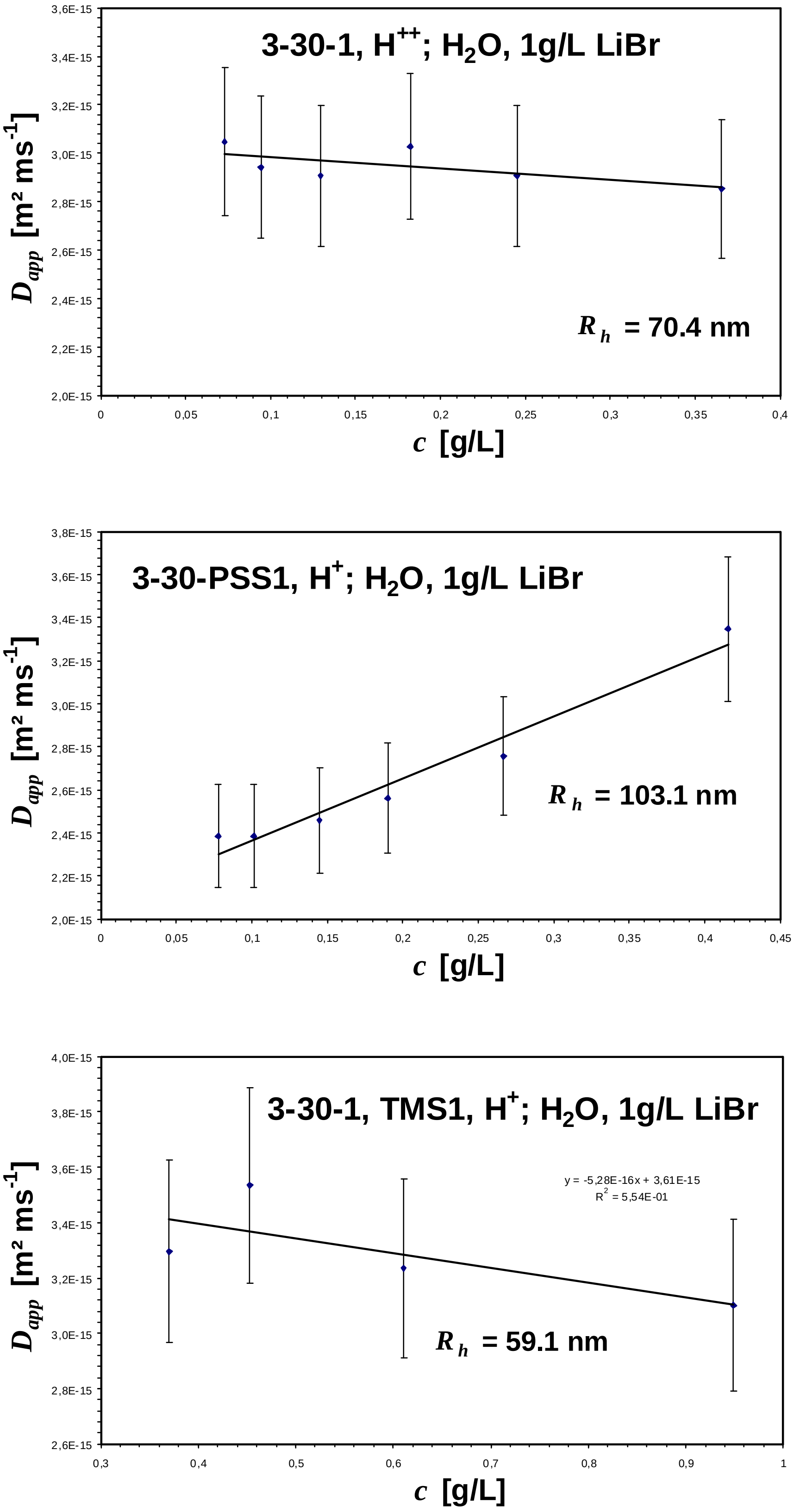

Fig. 7.8.2.5.: Hydrodynamic radii of samples from the **3-series**

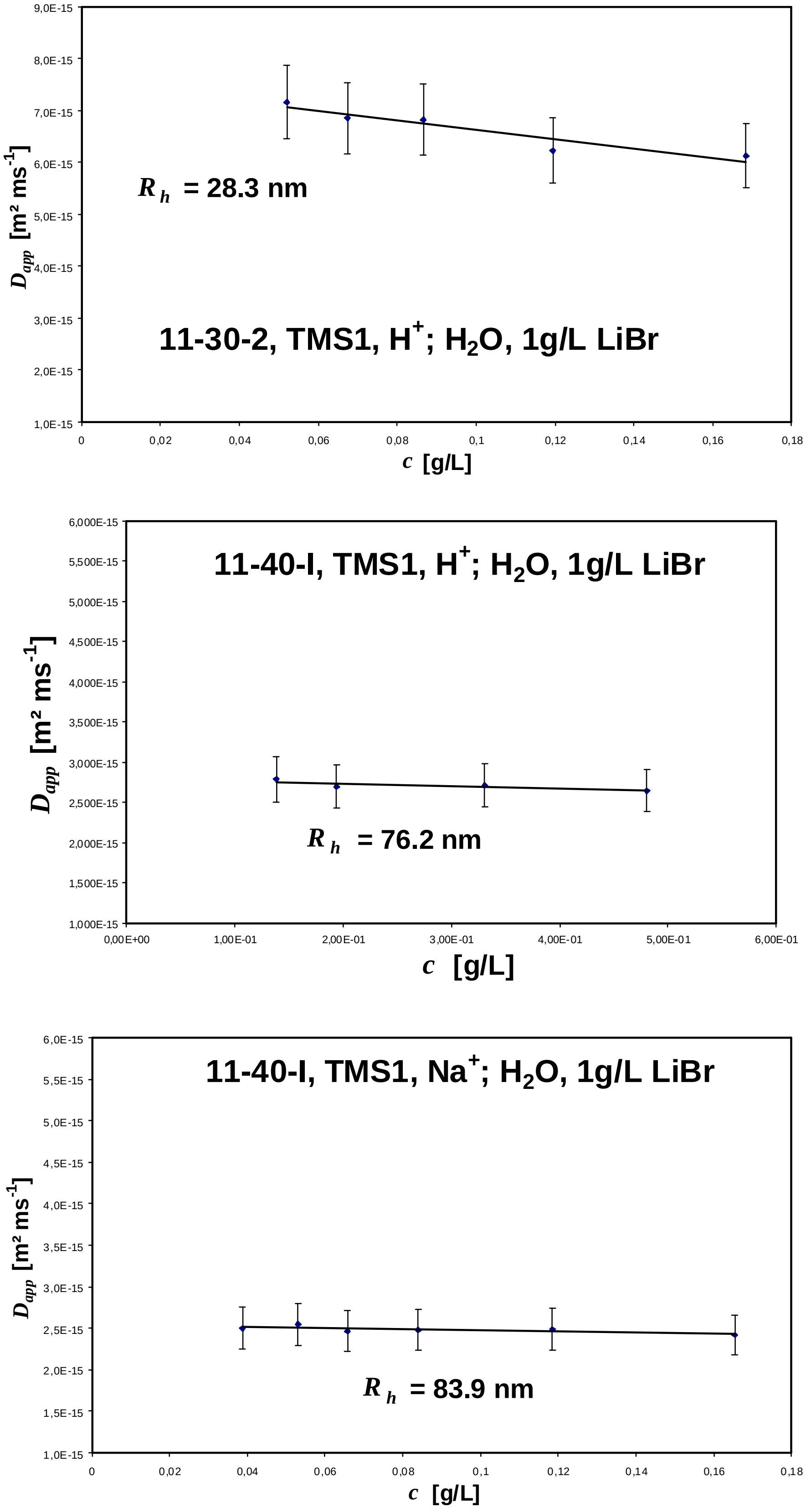

Fig. 7.8.2.6.: Hydrodynamic radii of samples from the **11-series**

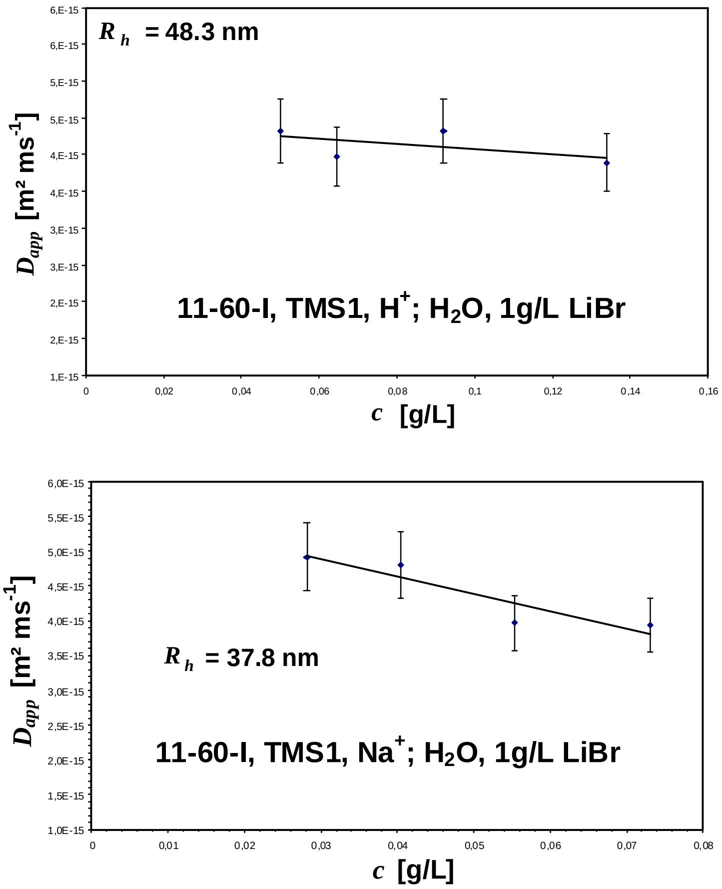

Fig. 7.8.2.6.: Hydrodynamic radii of samples from the **11-series** (continued)

Table 7.8.2.1.: Results of static and dynamic light scattering

Sample	Solvent sytem	*dn/dc*	M_w [g/mol]	A_2 [mol·L/g²]	R_g [nm]	R_h [nm]	ρ	N_{Agg}
11-30-2, TMS1, H$^+$	H_2O, LiBr	0.161	$2.6 \cdot 10^6$	$5.73 \cdot 10^{-7}$	64.3	28.3	2.27	1.6
11-40-IV, TMS1, H$^+$	H_2O, LiBr	0.170	$14.1 \cdot 10^6$	$-2.36 \cdot 10^{-7}$	58.3	76.2	0.765	10
11-40-IV, TMS1, Na$^+$	H_2O, LiBr	0.167	$13.3 \cdot 10^6$	$9.52 \cdot 10^{-9}$	62.8	83.9	0.778	7.8
11-60-I, TMS1, H$^+$	H_2O, LiBr	0.170	$1.6 \cdot 10^6$	$1.76 \cdot 10^{-7}$	61.8	48.3	1.28	1.1
11-60-I, TMS1, Na$^+$	H_2O, LiBr	0.167	$2.5 \cdot 10^6$	$5.75 \cdot 10^{-7}$	67.6	37.8	1.79	1.6
3-30-PSS1, H$^+$	H_2O, LiBr	0.160	$142 \cdot 10^6$	$1.70 \cdot 10^{-7}$	154	106	1.45	97
3-30-1, H^{++}	H_2O, LiBr	0.160	$21.7 \cdot 10^6$	$4.46 \cdot 10^{-10}$	54.3	70.4	0.771	31
3-30-1, TMS1, H$^+$	H_2O, LiBr	0.160	$1.6 \cdot 10^6$	$1.40 \cdot 10^{-7}$	49.1	59.1	0.760	1.9

The hydrodynamic radii were obtained by a CONTIN fit to the field autocorrelation function. Representative correlation functions and the corresponding CONTIN fits are given in Fig. 7.8.2.4.. For the samples forming aggregates, such as **11-40-I, TMS, Na$^+$**, two diffusive processes were found, the faster one corresponding to single molecules, the slower to aggregates. For non-aggregating samples, only one mode was found (Fig. 7.8.2.4., below). The characteristic relaxation time τ for each angle was converted into the corresponding relaxation rate Γ. Using the relation $\Gamma/q^2 = D_{app}$, a plot of Γ versus q^2 gave the apparent diffusion coefficient D_{app}. Plotting D_{app} versus the solution concentration and using the Stokes-Einstein equation gave the diffusion coefficient D and the hydrodynamic radius R_h. Representative plots of Γ versus q^2 are shown in Fig. 7.8.2.3.. The plots of D_{app} versus c curves are given in Figs. 7.8.2.5. and 7.8.2.6.. The results obtained by static and dynamic light scattering are summarized in Tab. 7.8.2.1..

The dn/dc values were obtained from the samples measured in an aqueous solution containing 1 g/L LiBr. As pointed out by Kratochvíl[167], aqueous solutions containing a low molecular weight electrolyte to suppress the polyelectrolyte effect must be considered as mixed solvents. In mixed solvents, the polymer often has a preference for one solvent component, say A, i.e. the polymer environment is enriched in component A. In the so-called microphase equilibrium model, the polymer solution is considered as a two phase system consisting of the solvent and the macromolecule swollen with solvent. In solvent mixtures, there is a partition equilibrium of solvents A and B in the two phases, i.e. the concentrations of A and B in each phase are different. Thus, the chemical potential of these components is not equal. The light scattering equations, however, are only valid for scattering in mixed solvents if the chemical potential in each phase is balanced. The light scattering equation becomes

$$R_\theta = K'\left(\frac{\partial n}{\partial c_p}\right)_\mu^2 \cdot c_p \cdot M \ ,$$

with $K' = \dfrac{2\pi^2 n^2}{\lambda^4 N_A}$ and $\left(\dfrac{\partial n}{\partial c_p}\right)_\mu^2$ as the refractive index increment in osmotic equilibrium.

Thus, the refractive index increment must be measured for a solution which is in osmotic equilibrium with the mixed solvent. If this is not done, the values determined for M, A_2 and R_g are apparent values only. Since

$$R_\theta = K'\left(\frac{\partial n}{\partial c_p}\right)_\mu^2 \cdot c_p \cdot M = K'\left(\frac{\partial n}{\partial c_p}\right)^2 \cdot c_p \cdot M_{app},$$

the effect of using a mixed solvent may be negligible if the refractive index increment in osmotic equilibrium with the solvent and that of the polymer solution in the non-dialyzed mixed solvent are similar. In the case of polyelectrolytes dissolved in water with an added low molecular weight salt, the difference in these two refractive indices may be considerable due to an exchange between the polyelectrolyte counter ions and the ions of the electrolyte.

For the free acid form of the polyelectrolyte brushes used in this work, the effect proved to be negligible, the refractive index increment for sample **11-60-I, TMS1, H^+** measured in H_2O was 0.170 mL/g, and 0.175 mL/g for the same sample measured in water with 1 g/L LiBr. The value for the dialyzed solution must be between the two extremes. The ratio of the two values squared is 0.95, i.e. the error is 5%. As the concentration determination of the dialyzed solution is difficult and prone to be erroneous by at least the same amount, the solutions were not dialyzed, but the refractive index increment value determined in 1 g/L LiBr was used.

The values in Tab. 7.8.2.1. are larger than those from GPC-MALLS. For samples **11-30-2, TMS1, H^+**, **11-60-I, TMS1, H^+**, **11-60-I, TMS1, Na^+** and **3-30-1, TMS1, H^+**, the values are on the same order of magnitude and the deviations may be attributed to the two different methods used and their respective assumptions and approximations used for data evaluation, as well as to the poor data quality for those samples in off-line static light scattering. It is therefore concluded that for these samples, monodisperse solutions were obtained and aggregation is negligible. For samples **11-40 IV, TMS1, H^+**, **11-40-IV, TMS1, Na^+** and the two other samples from the **3-series**, the values differ considerably. This is due to large aggregates, which could not be broken by stirring, heating, ultrasound and large amounts of salt addition. The shape of the Zimm plots (Fig. 7.8.2.1.) as well as the plots of the relaxation time distributions (Fig. 7.8.2.3., top right) indicate that these aggregates are relatively well defined, thus the combination of the M_w values from GPC-MALLS with the M_w values from static light scattering allows the determination of an aggregation number. The values measured for the second virial coefficient A_2 give a hint why such aggregates are only found for these samples: for **11-40-IV, TMS1, H^+**, A_2 is by two orders of magnitude smaller then for the other samples, and for the corresponding sodium salt even negative. Thus, the contact with the bad solvent is avoided by intermolecular aggregation. Two samples from the **3-series** also fit in this picture. For sample **3-30-1, H^{++}**, also with a small A_2 value, large aggregates are found; sample **3-30-1, TMS1, H^+**, with an A_2 of $1.40 \cdot 10^{-7}$ mol L g^{-2}, is molecular disperse. The comparison between those two samples is particularly interesting as they differ only slightly in the degree of hydrolysis (40% for **3-30-1, H^{++}** and 66% for **3-30-1, TMS1, H^+**). This shows the tremendous influence of the degree of hydrolysis for structure formation. Sample **3-30-PSS1, H^+**, with a low degree of hydrolysis (10%), forms huge aggregates. Yet the A_2 value determined is on the same order of magnitude as for non-aggregating samples. Also, this sample is the only one which shows a positive slope in the plot of D_{app} versus c. As the values determined for the hydrodynamic radius and the radius of gyration are about 100 nm, it is possible that this structure is so large that it is already outside the range that is observable by light scattering methods, thus the apparent values determined for A_2 and the other molecular parameters do not fit into the general picture.

The $\rho = R_g/R_h$ values, which are sensitive to the molecular shape as described in the literature[168] indicate that the polyelectrolyte samples have different solution conformations. The aggregates of **11-40-IV, TMS1, Na$^+$**, with longer side chains (n=10 according to GPC-MALLS and n=40 according to ^{1}H-NMR (both on the parent ester)) and the corresponding free acid resemble to a homogeneous sphere ($\rho_{Lit.}$[168] = 0.778). The conformation of the molecular disperse sample **11-30-2, TMS1, H$^+$** is that of a rigid rod (ρ_{Lit}[168] > 2.0). **11-60-I, TMS1, H$^+$**, with shorter side chains (n=3 according to GPC-MALLS, n=24 according to ^{1}H-NMR (both on the parent ester)) adopts a coil like conformation. For the aggregates of sample **3-30-1, H^{++}** and the single molecules of sample **3-30-1, TMS1, H$^+$**, sphere-like geometry was found. This is interesting, as light scattering for sample **3-30-1, TMS1, H$^+$** was also measured in DMF. Here, a molecular weight M_w of 720 000 g/mol was measured, with R_g = 20.6 nm and R_h = 11.6 nm, which gives a ρ ratio of 1.78. As this value is in good accordance with the M_w determined for this sample in GPC-MALLS (M_w = 850 000 g/mol), it appears that the sample avoids the aqueous solvent by forming spheres, while it is molecular disperse in DMF and here also retains its wormlike geometry. It should be mentioned that the ρ parameter, while depending on the molecular shape, is also sensitive to the solvent quality and the broadness of the distribution. Both parameters increase the ρ values.

7.8.3. Small Angle Neutron Scattering

While static light scattering allows the determination of the overall molecular weight of the polymer brushes, the range of the scattering vector q covered by small angle neutron scattering allows the determination of the form factor $P(q)$ of the polymer brushes, i.e. internal parameters such as the molecular length L, the cross-sectional radius of gyration $R_{g,c}$ and the Kuhn length l_k. From the initial slope at low q, a linear fit to the plot of log I vs log q (Fig. 7.8.3.1.) may give evidence of the particle shape. In Fig. 7.8.3.1., the plot of log I vs log q is displayed for the static light scattering data and the neutron scattering data. The static light scattering data ($I = Kc/R_\theta$ in g/mol) was used as a reference, and the neutron scattering data was multiplied by a correction factor to match this data. For samples **3-30-1, TMS1, H$^+$**, **3-30-1, H^{++}**,and **3-30-1H**, the curve shape looks reasonable. For sample **3-30-PSS1, K$^+$**, the gradients of the light scattering and the neutron scattering data do not match. In spite of identical sample preparation, this may be due to irregularities in the light scattering sample. Thus the light scattering results will be used as calibration only and will not be considered further for this sample.

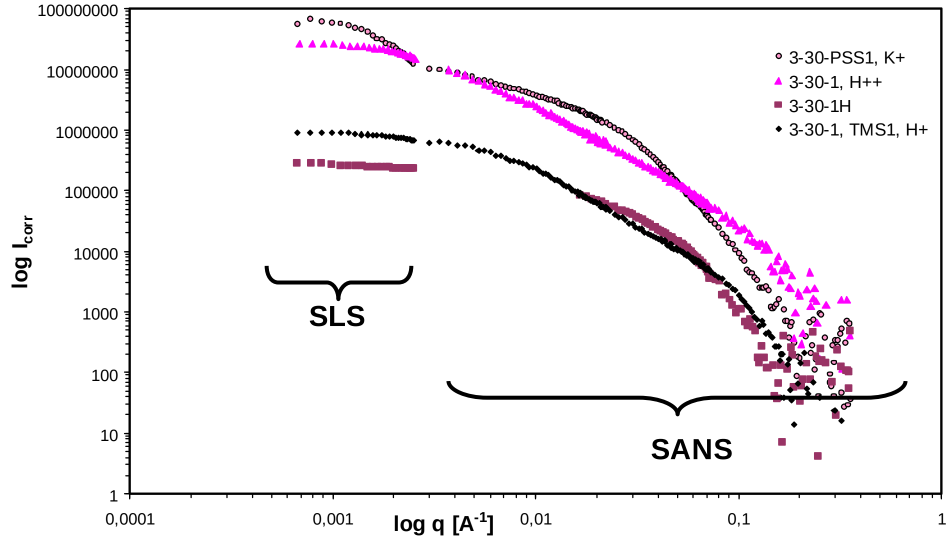

Fig. 7.8.3.1.: Small angle neutron scattering (SANS) and static light scattering (SLS) results for samples from the **3-series**, c = 2 g/L for all samples

The particle shape can be looked at further by analyzing the data with a Guinier plot (log I vs q^2) and a cross-sectional Guinier plot (log ($q \cdot I$) vs q^2). While the former yields a linear slope at low q in particular for globular samples, the latter is used for the determination of the cross-sectional radius of gyration $R_{g,c}$ of a cylindrical object by a linear fit at low q. A comparison of the two plots indicates that the curve is more linear in the low q regime in the cross-sectional Guinier plot than in the Guinier plot, thus the molecules are more rod-like than globular (Fig. 7.8.3.2.). A Kratky plot of the same data (Fig. 7.8.3.3., right) shows a maximum, typical for a branched structure, as expected. Usually, rod-like samples show a plateau in the Holtzer plot (Fig. 7.8.3.3., left) at high q range, from which the mass per unit length can be determined. In these curves, the plateau cannot be determined unambiguously. This is due to the fact that the plateau is obtained for an infinitely thin rod, while the samples are molecules with a finite diameter. Thus the cross-section influences the curve shape, and therefore this value was not calculated. The SANS results are summarized in Table 7.8.3.1..

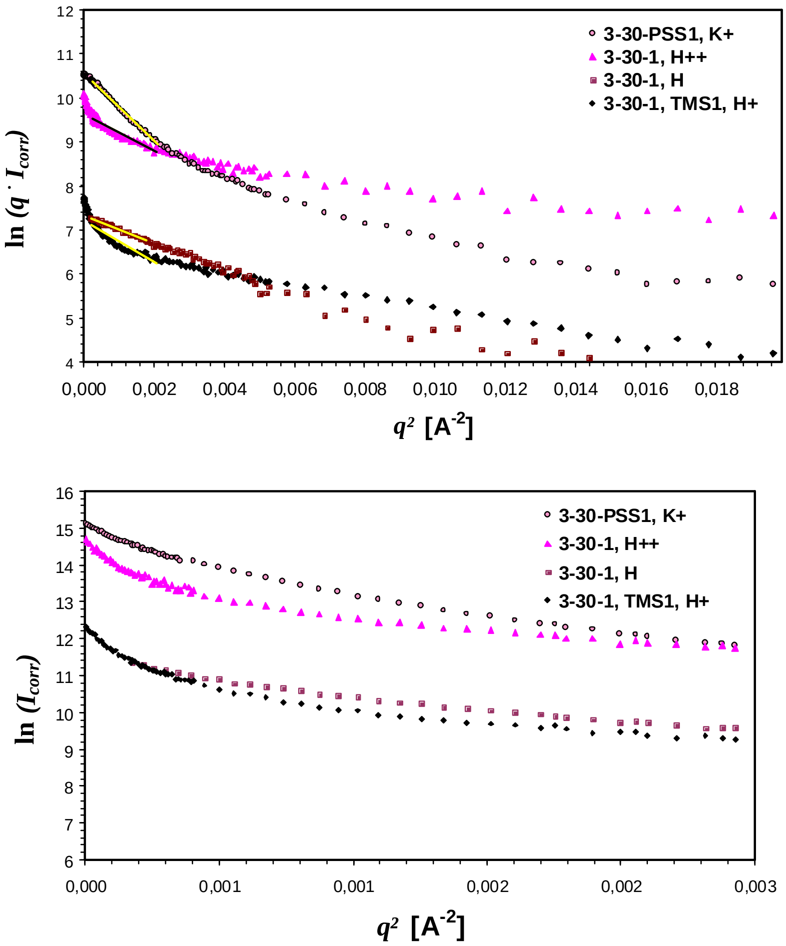

Fig. 7.8.3.2.: Cross-section Guinier plot (above) and Guinier plot (below) for samples from the **3-series**, $q \cdot R_g$ in the range of the cross-section Guinier fit = 0.25-0.75

Table 7.8.3.1.: SANS results: initial slope from double logarithmic plot, $R_{g,c}$ from cross-section Guinier plot

Sample	initial slope	$R_{g,c}$ [nm]
3-30-PSS1, K$^+$	0.9	3.9
3-30-1, H^{++}	1.3	2.9
3-30-1H	0.5	2.4
3-30-1, TMS1, H$^+$	0.2	3.1

The results can be interpreted as follows. Sample **3-30-PSS1, K$^+$**, with only 10% hydrolysis, has the highest diameter due to the voluminous residual **PSSD** side chains, the samples with medium degrees of hydrolysis (**3-30-1, H^{++}** and **3-30-1, TMS1, H$^+$**) have comparable and smaller radii, while those of the almost fully saponified samples is smallest. If there is no significant volume change between a polymer brush and its corresponding saponified polyelectrolyte analogue, the parameter $R_{g,c}$ may be used for quantification of the backbone stretching: a more stretched brush will have a smaller $R_{g,c}$ than a collapsed brush. In this case, however, this trend is counterbalanced by the large volume loss upon saponification: although AFM images (section 7.8.5.) indicate that the backbone of the saponified brushes **3-30-1, H^{++}** and **3-30-1, TMS1, H^{+}** is *more* coiled than that of the parent ester, they have a *smaller* radius than the scarcely saponified sample **3-30-PSS1, K^{+}** due to the large volume loss during saponification. In Tab. 7.8.3.1., the slopes of the log I vs log q plots at low q is included. Depending on the exact q range where this slope is determined, the values obtained vary tremendously, as can be seen from the data presented. Inclusion of a few data points more or less can lead to deviations of up to 100 % for the data presented here. Thus, this type of evaluation is not suitable for determination of the molecular shape of the samples discussed here and will not be considered further.

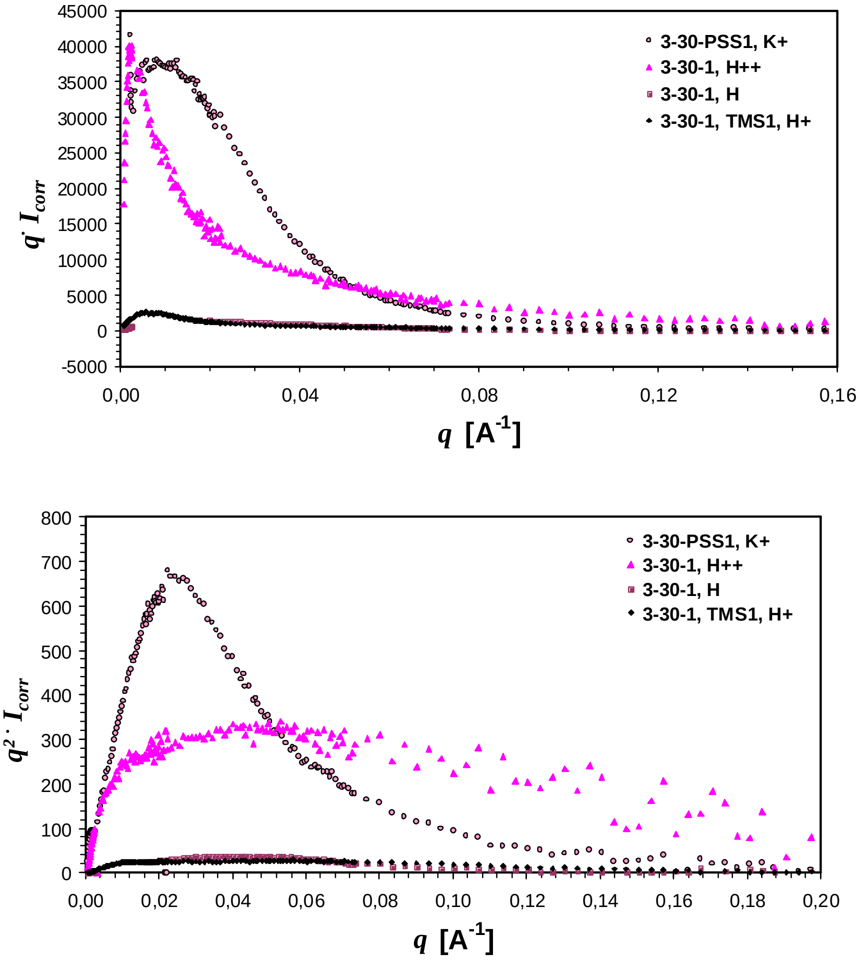

Fig. 7.8.3.3.: Holtzer (above) and Kratky plot (below) for samples from the **3-series**

7.8.4. Pedersen-Schurtenberger Wormlike Chain Fit to SANS Data

Pedersen and Schurtenberger developed a form factor model for a wormlike chain with excluded volume and finite diameter based on Monte-Carlo simulations. They defined the form factor of the wormlike chain as

$$P_{wormchain} = P^{\infty}_{wormchain} \cdot \Gamma(q, L, l_k) \cdot P_{cross\text{-}section} \, ,$$

$P_{wormchain}$ = form factor of a wormlike chain
$P^{\infty}_{wormchain}$ = form factor of an infinite semiflexible chain
Γ = overlap function
$P_{cross\text{-}section}$ = form factor of the cylinder cross-section
L = contour length
l_k = Kuhn length
χ = crossing function
P_{exvol} = form factor of an excluded volume chain
P_{rod} = form factor of a rod

and put these elements together as

$$P_{wormchain} = \left[\left(1 - \chi(q, L, l_k)\right) \cdot P_{exvol}(q, L, l_k) + \chi(q, L, l_k) \cdot P_{rod}(q, L) \right] \cdot \Gamma(q, L, l_k) \cdot P_{cross\text{-}section} \, .$$

What this expression accomplishes is that it combines the form factors of a stiff rod, an excluded volume chain and a cylinder with finite cross-section, which are - by themselves - all insufficient in describing a polymer brush. By fitting this form factor to the experimental data (minimising χ^2), a curve matching the experimental data can be obtained, from which molecular parameters such as Kuhn length, cross-sectional radius and contour length result.

The experimental data of the samples discussed in section 7.8.3. were all fitted with a software written by Petersen to test their compliance with the above stated form factor equation. The results are given in Figs. 7.8.4.1. to 7.8.4.4. and Tab. 7.8.4.4..

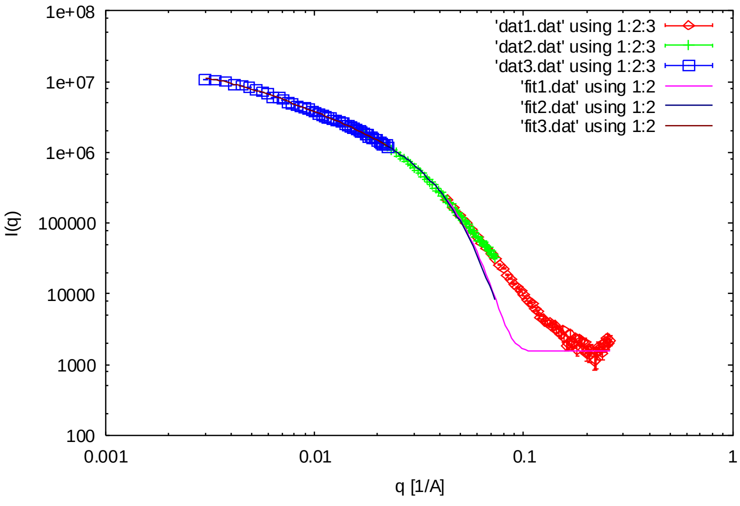

Fig. 7.8.4.1.: Pedersen fit to sample **3-30-PSS1, K$^+$**, ***R_cq*** = 0

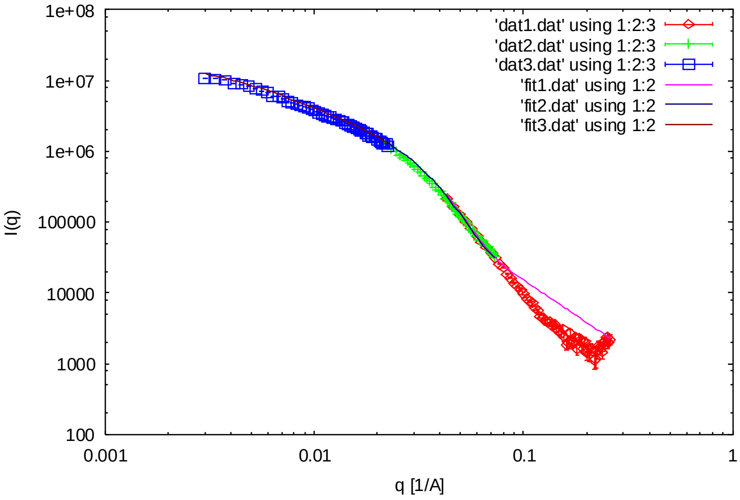

Fig. 7.8.4.1. (continued): Pedersen fit to sample **3-30-PSS1, K$^+$**, $R\_cq \neq 0$

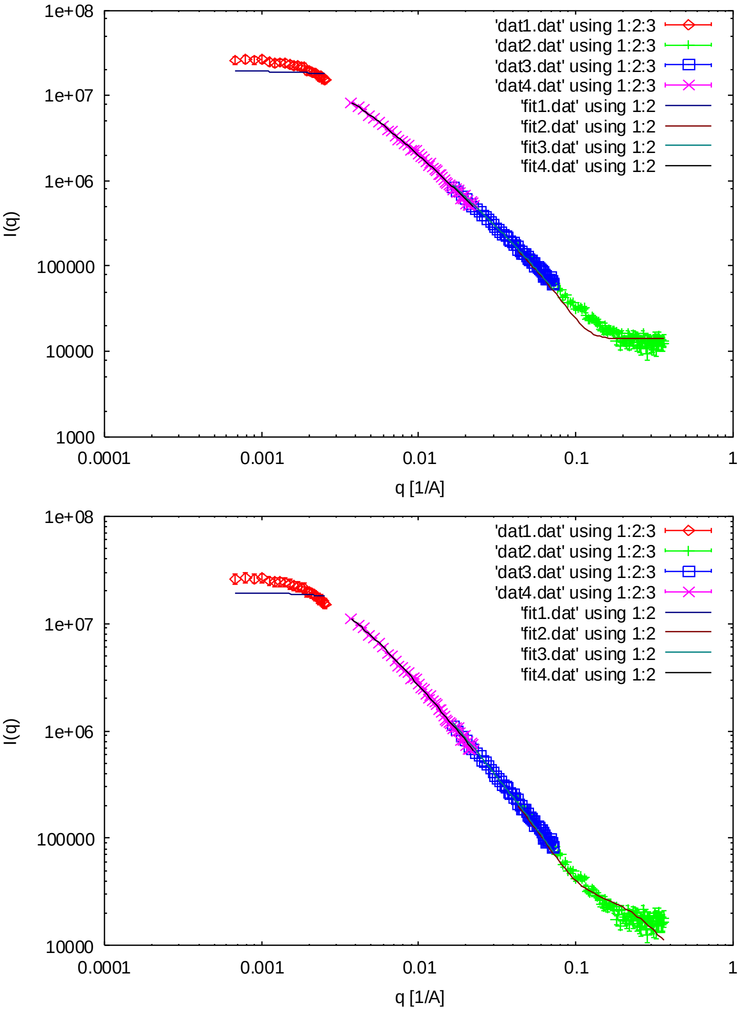

Fig. 7.8.4.2.: Pedersen fit to sample **3-30-1, H^{++}**, above: $R\_cq = 0$, below: $R\_cq \neq 0$

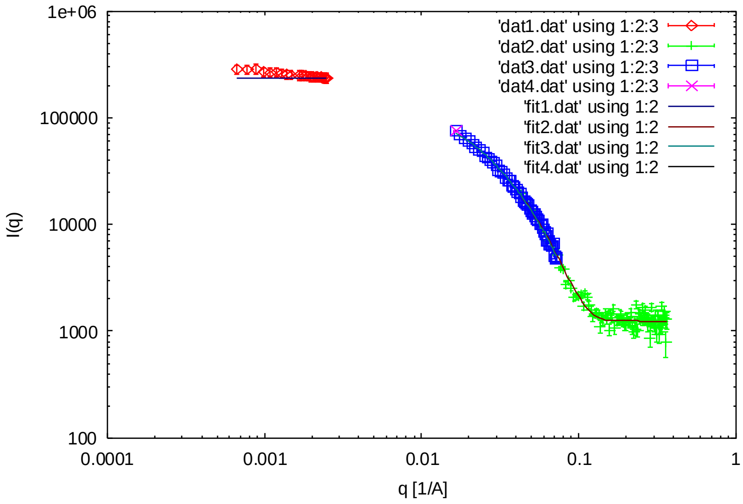

Fig. 7.8.4.3.: Pedersen fit to sample **3-30-1H**, ***R_cq*** = 0

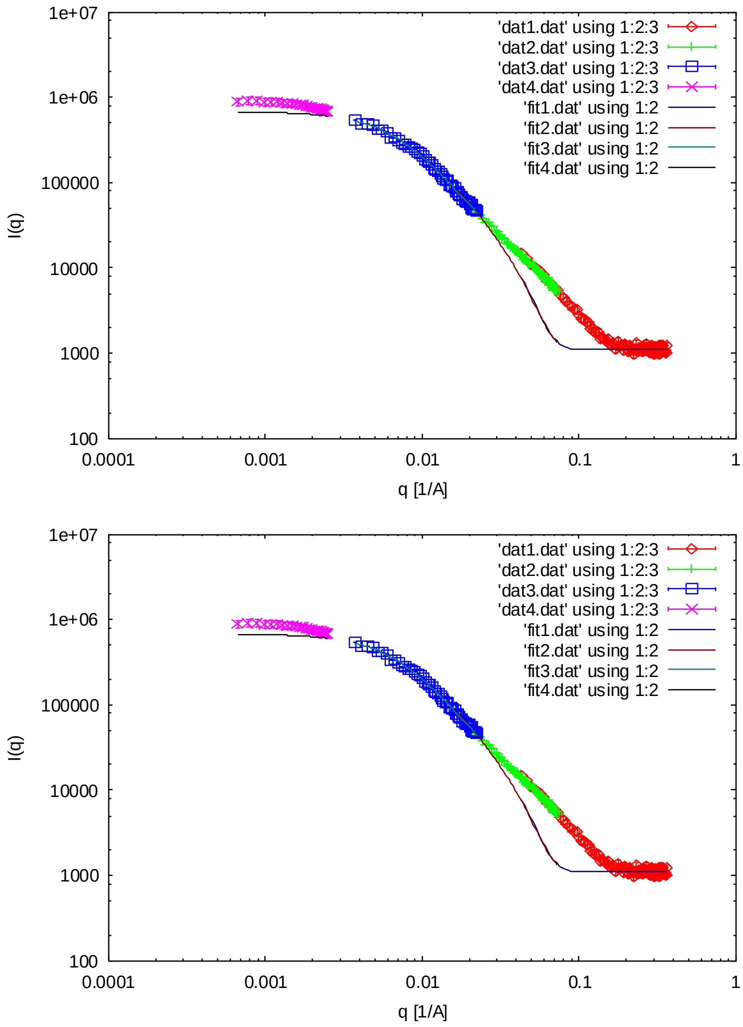

Fig. 7.8.4.4.: Pedersen fit to sample **3-30-1, TMS1, H^+**, above: ***R_cq*** = 0, below: ***R_cq*** ≠

Table 7.8.4.1.: Fit parameters

Sample/ Parameter	3-30-PSS1, K$^+$		3-30-1, H^{++}		3-30-1H	3-30-1, TMS1, H$^+$	
	R_cq =0	*R_cq* ≠0	*R_cq* =0	*R_cq* ≠0	*R_cq* ≠0	*R_cq* =0	*R_cq* ≠0
SCAL_FAK	14 220	13 670	2 263	2 980	95.5	330	330
L [Å]	222.6	260.5	3 491	3 720	539.0	1810	1818
σ_r [Å]	26.86	29.08	13.80	15.66	9.836	22.39	22.46
R_2 [Å]	23.78	24.91	47.53	2.783	1.971	31.82	31.47
SCAL_1	1	1	2.468	1.878	2.063	1	1
BACKGR	1 550	495 900	14 000	36 920	1 247	1100	1100
SCAL_3	1	1	1.031	1.037	0.987	1	1
l_k [Å]	612.1	545.6	75.53	75.53	11.9	123.5	123.4
sigl_l	2.22	2.16	1.307	1.219	1.213	0.362	0.345
R_cq	0	80.30	0	63.94	0.167	0	2.77
SCAL_4	1	1	0.980	0.988	1.026	1	1
χ^2	2780	670	671	515	1.65	1460	1460
$r_{g,c}$ [Å]	41.22		38.87		14.01		38.70

While the parameters SCAL_FAK, SCAL_1, SCAL_3, SCAL_4 and BACKGR are more "technical" - they help adjusting the individual scattering curves from SLS and SANS (at 2 m, 6 m and 18 m detector distance) and deal with background subtraction - the other parameters give evidence of the molecule shape. The χ^2 parameter, quantifying the deviation of the experimental data from the mathematical model, is extremely high for all curves except sample **3-30-1H**. As can be seen from Figs. 7.8.4.1. to 7.8.4.4., this is mainly due to the deviation of the model from the data at high q range, as well as a slight deviation at low q range, while good accordance is found in the intermediate range. At low q, the deviation might be due to aggregation of the samples. The deviations in the high q range start at 0.02 to 0.06 Å^{-1}, which corresponds to 10-31 nm in real space. In this range, the diameter of the brush is observed (Fig. 7.8.4.5.). Thus, irregularities in the brush diameter, causing an inhomogeneous brush cross-section lead to a failure of the model in that q range. The parameter *R_cq*, which takes such 'blobs' into account, is insufficient for the brushes considered here. An exception is sample **3-30-1H**. Here, almost quantitative saponification was obtained, thus the brush cross-section is more homogeneous than in the case of the other brushes, and the model fits. This assumption is backed up by the finding that the Pedersen Fit was shown to fit nicely for brushes obtained by 'grafting onto'[165] and poly(macromonomers)[170], which both have a more uniform side chain length as samples from ‘grafting from’, and thus a relatively smooth surface. The irregularities in the brush diameter were also found in AFM measurements (chapter 7.5.3.).

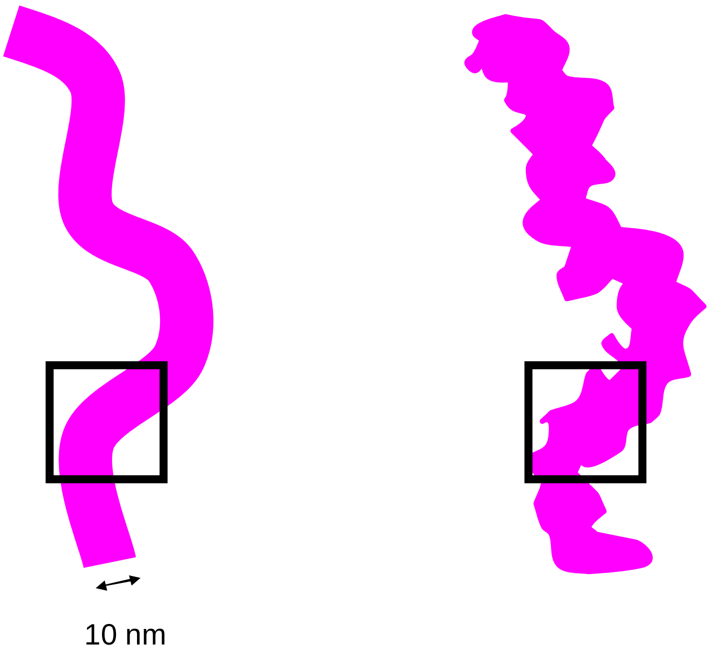

Fig. 7.8.4.5.: Polymer brush with a smooth cross-section (left) and a rough cross-section (right), the black squares indicate the size in real space corresponding to the q range where deviations from the Pedersen fit occur

For the first two samples, the fit quality improved slightly by using the additional fit parameter R_cq; for the others, it does not make much difference. Thus, the contour lengths L and the Kuhn lengths l_k obtained from these fits should be treated with care. For samples **3-30-1, H^{++}** and **3-30-1, TMS1, H^{+}**, the L values obtained are on the same order of magnitude as the ones from AFM. For samples **3-30-PSS1, K^{+}** and **3-30-1H,** the L values are much smaller than expected. The $sigl\_l$ values, quantifying the polydispersity of the contour lengths, give physically meaningful values for the first three samples, however for sample **3-30-1, TMS1, H^{+}**, the value is below one, i.e. physically meaningless. This, in combination with the behaviour of the L values, indicates that there might be a methodical problem for the determination of those parameters for these samples. Interestingly, there is a correlation between the Kuhn lengths and the degree of saponification (Fig. 7.8.4.6.). This makes sense as an increased degree of saponification leads to a shrinking of the molecules (as shown in AFM) and thus an increased flexibility of the backbone, i. e. a shorter Kuhn length.

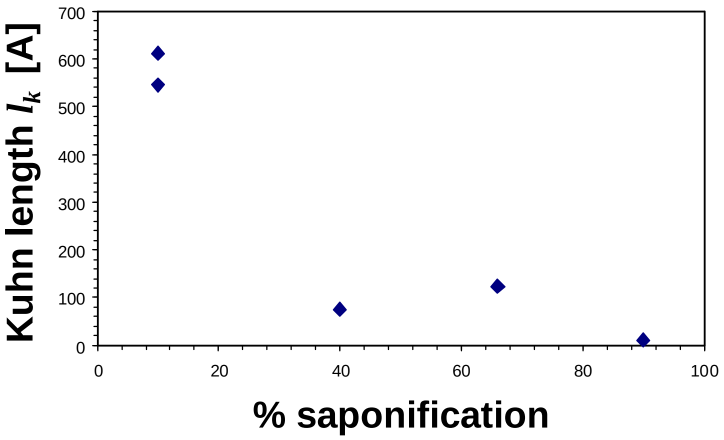

Fig. 7.8.4.6.: Correlation between Kuhn length, σ_r and degree of saponification

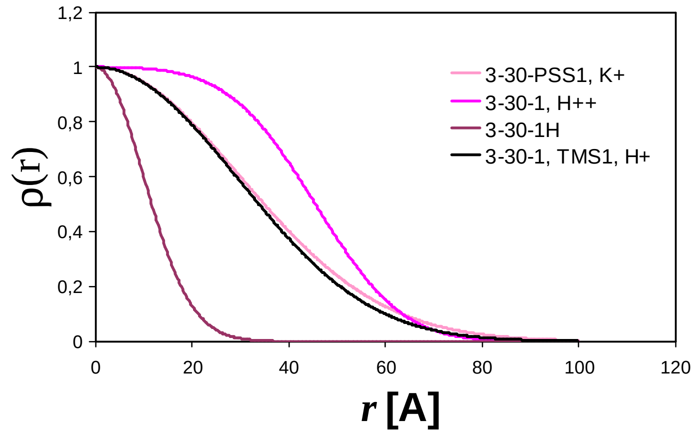

Fig. 7.8.4.7.: Radial density profile of the polymer brushes

The radial density profile was calculated from the parameters σ_r and R_2. The profiles are given in Fig. 7.8.4.7.. By evaluating the integrals $\int \rho(r)\cdot r^2 \cdot 2\pi r\, dr$ and $\int \rho(r)\cdot 2\pi r\, dr$, the cross-sectional radius of gyration is obtained as

$$r_{g,c}{}^2 = \frac{\int \rho(r)\cdot r^2 \cdot 2\pi r\, dr}{\int \rho(r)\cdot r \cdot 2\pi r\, dr}$$

The values thus calculated are included in Tab. 7.8.4.1.. Fig. 7.8.4.8. gives a graphic representation of this data, together with the $R_{g,c}$ values determined from the cross-sectional Guinier plot to the SANS data. There is a deviation of the SANS data from the fit data due to the poor fit quality, yet the trend of a decrease of $R_{g,c}$ with increasing degree of saponification is found for both data series. For sample **3-30-1H**, with the best fit quality, the value calculated is much lower than the value from the cross-sectional Guinier plot, indicating that this evaluation might be an overestimation of the 'true' value. While these qualitative trends may be extracted from the experimental data by making use of the Pedersen wormlike-chain fit, more quantitative results cannot be obtained due to the poor compliance of the data with the fit.

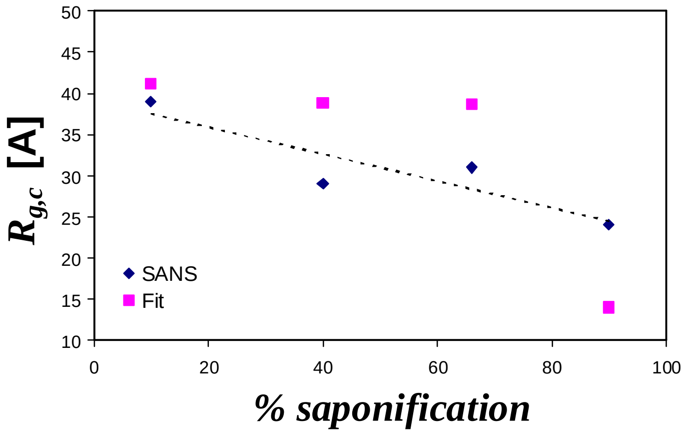

Fig. 7.8.4.8.: Cross-sectional radii of gyration from SANS data and the Pedersen fit

7.8.5. Imaging by AFM and TEM

Imaging on Surfaces

For molecular characterization by atomic force microscopy, the polyelectrolyte brushes were spin-coated from aqueous solution onto a microscopically flat surface. On silica wafers or graphite surfaces, only polymer blobs were observed. On more polar mica surfaces, single molecules could be imaged. This is in accordance with the model for polymer absorption from solution of a solid substrate, as discussed by Sheiko[169] and Zhang[170]. If the enthalpic interaction between the sample and the surface is low, i.e. absorption is weak, as for polar, charged polyelectrolytes on non-polar graphite, the polymer molecules tend to minimize the interaction with the surface and maximize their conformational entropy by forming a coil. If the absorption is stronger, as for a polyelectrolyte on a polar, charged mica surface, extended single molecules can be observed, as it requires more energy to desorb the absorbed polymer segment than can be gained by the entropy increase due to coil formation. Thus the molecules have to remain in an extended conformation.

Imaging of the polyelectrolyte brushes by AFM (tapping mode) was not as straight forward as in the case of the PSSD brushes, as the polyelectrolyte brushes were not as firmly absorbed on the mica surface as the corresponding esters. Also, due to the absence of the ester group, the mechanical contrast to the surface was worse.

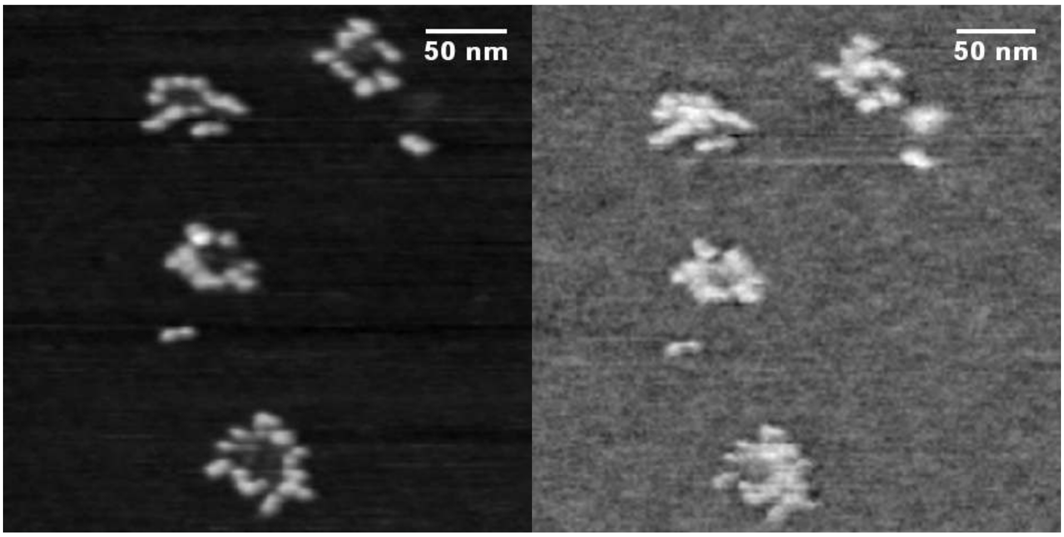

Fig. 7.8.5.1.: AFM image of **3-30-PSS1, H^+** (spincoated from H_2O on mica, tapping mode, height and phase image)

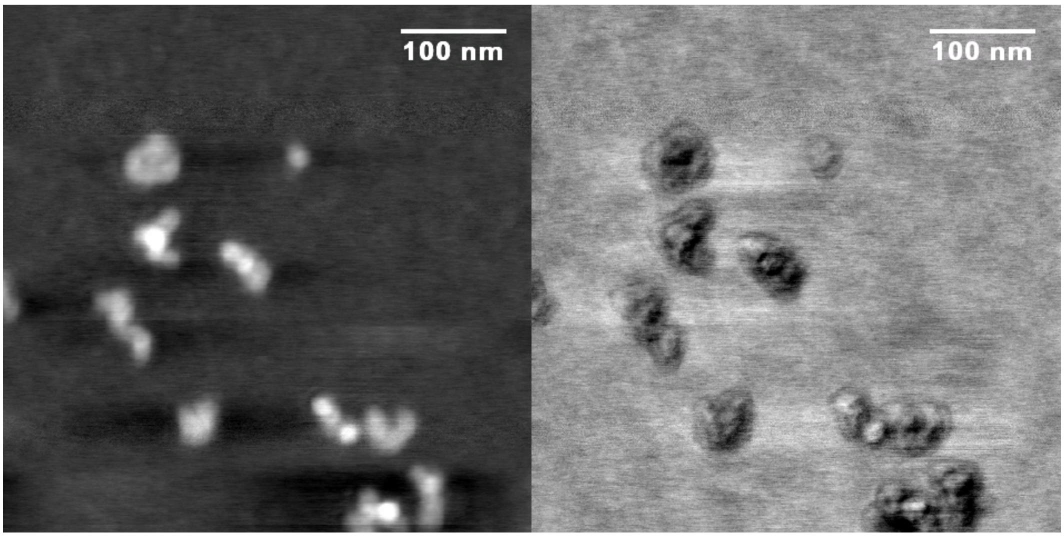

Fig. 7.8.5.2.: AFM image **of 3-30-1, NR_4^{++}** (spincoated from H_2O on mica, tapping mode, height and phase image)

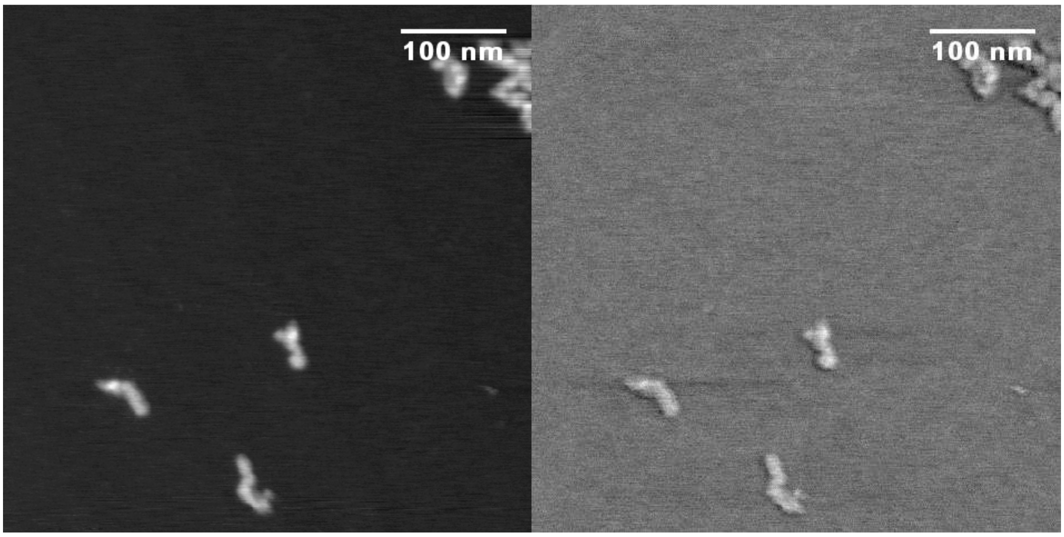

Fig. 7.8.5.3.: AFM image of **3-30-1, TMS H^+** (spincoated from H_2O on mica, tapping mode, height and phase image)

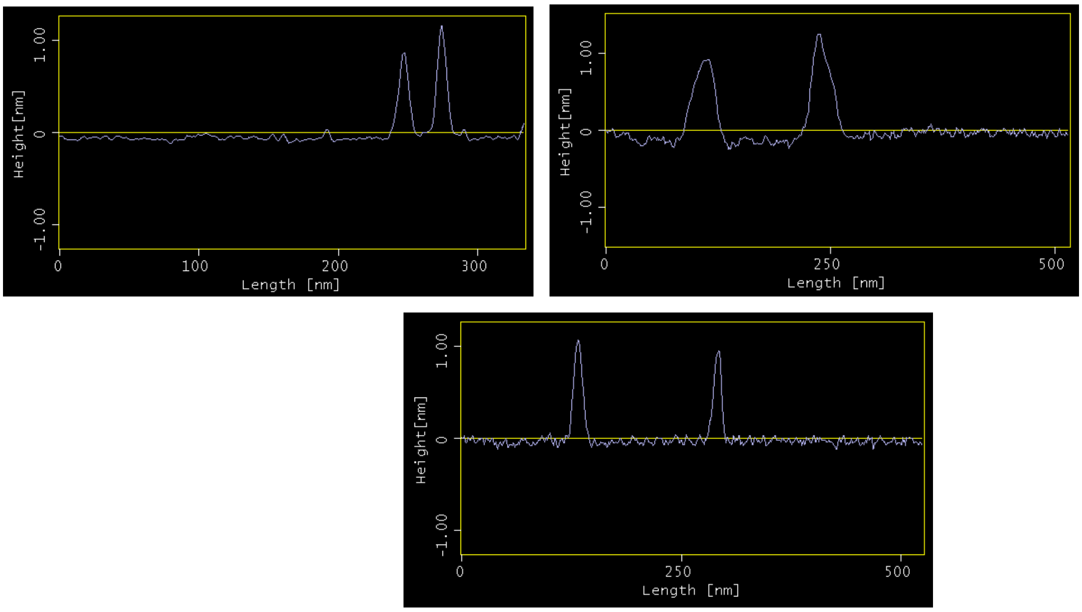

Fig. 7.8.5.4.: AFM height profiles **3-30-PSS1, H^+**, **3-30-1, NR_4^{++}** and **3-30-1, TMS1, H^+**

Table 7.8.5.1.: Contour length and diameter determination of polyelectrolyte brushes by AFM

Sample	Contour Length [nm]	Diameter [nm]	Height [nm]
3-30-PSS1, H^+	50.9±12.7	10.2±1.9	1.11±0.20
3-30-1, NR_4^{++}	65.9±9.0	20.2±2.6	1.26±0.09
3-30-1, TMS1, H^+	56.3±10.8	12.7±2.5	1.06±0.07

Figs. 7.8.5.1. to 7.8.5.3. show the AFM images for samples **3-30-PSS1, H^+**, **3-30-1, NR_4^{++}** and **3-30-1, TMS1, H^+**. From these images, it was concluded that the polyelectrolyte brushes are clustered into small groups, which is in accordance with the findings from static light scattering. It is therefore difficult to precisely determine the contour length and the molecule diameter. Table 7.8.5.1. gives best estimates for those values, as measured from the AFM images. The height profiles for all samples are given in Fig. 7.8.5.4.. These results indicate that the polyelectrolyte brushes derived from **3-30-D1** (contour length 78.5 nm, diameter 11.6 nm, height 1.04 nm) are shorter than the parent ester due to a contraction of the brush backbone in the absence of the large ester residue. Sample **3-30-1, NR_4^{++}** is slightly longer and has a significantly larger diameter than the other polyelectrolyte brushes due to its large tetraalkylammonium counter ions. Its diameter is also larger than that of the parent ester, as the alkylammonium ions are more voluminous than the ester residue of **3-30-D1**. Moreover, they are not covalently connected to the molecule, i.e. the

electrostatic attraction of the counter ions is balanced by steric repulsion, making the whole molecule larger than the parent ester.

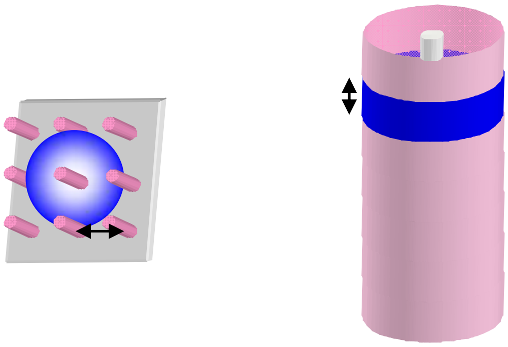

Fig. 7.8.5.5.: Model for space filling in 2D (left) and 3D polymer brushes (right). The black arrow indicates the grafting density ***r***

The coil to sphere-like geometry, as suggested by the ρ values for these samples, was not found, which is due to the differences of the solution conformation as compared to the molecules conformation on a solid substrate. The contraction of the polyelectrolyte brushes compared to their parent ester can be explained as follows: for 2D brushes (see chapter 4), Ballauf[59] stated that the radius of gyration of the side chain must be larger than the distance between the grafting points on the surface. Above that threshold value, longer chains only lead to thicker brushes. A similar argument should hold for cylindrical (3D) polymer brushes. If the backbone is to be stretched, or at least elongated compared to the coiled state, the side chains' radius of gyration must also be larger than the grafting distance. However, in the 3D polymer brush case, the situation is different, as the side chain must fill more volume than in the case of the 2D brushes. For a 2D brush with grafting density ***r***, the volume that can be filled by each chain is that of a half sphere with the radius of gyration as its radius (Fig. 7.8.5.5., left), i.e.

$$V = \frac{4}{3}\pi \cdot r^3 \cdot \frac{1}{2} = \frac{2}{3}\pi \cdot r^3 \approx 2r^3$$

For a 3D brush with a grafting density of ***r***, each chain can occupy a cylindrical volume (Fig. 7.8.5.5., right), $V = 2\pi \cdot r^2 \cdot r = 2\pi \cdot r^3 \approx 6r^3$, i.e. the threshold value for obtaining brush-like morphologies should be higher by a factor of 3 for 3D brushes as compared to 2D brushes. However, while the 2D brush side chain must first fill this volume before contributing to the brush thickness, the 3D brush side chains can avoid each other by rotation or by contributing to the brush diameter, thus the threshold value for backbone stretching is possibly even higher.

The polyelectrolyte brushes presented above, with a side chain length of $n = 18$, are below this threshold value for a 30% branched polymer brush, as the hydrolysis of the parent ester **3-30-D1**, with a contour length of 78.5 nm, led to a contour length decrease of roughly 20%.

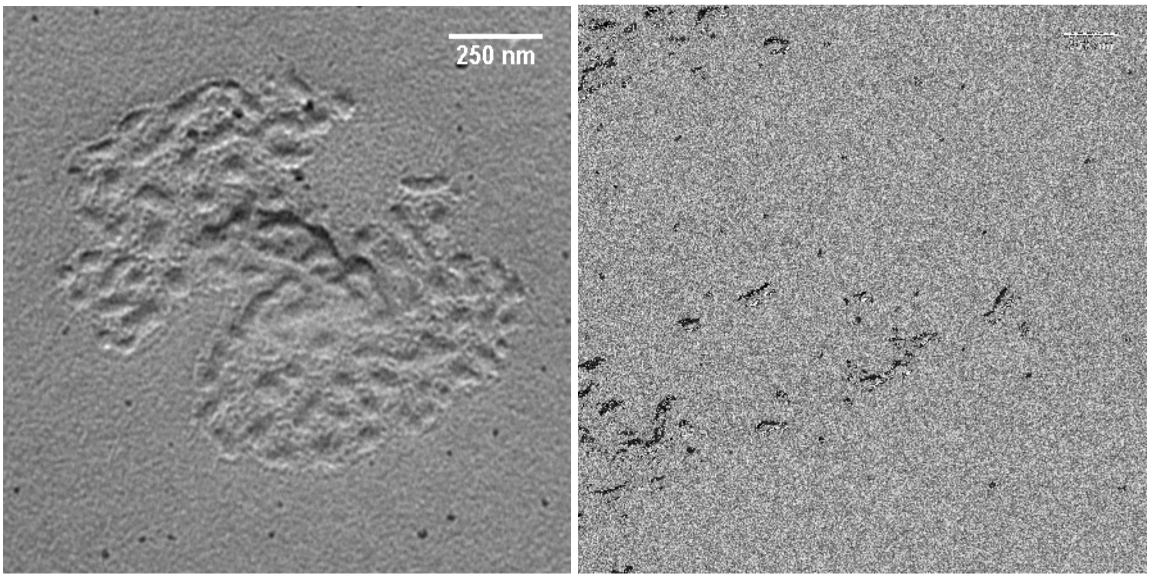

Fig. 7.8.5.6.: TEM micrographs of **3-30-TMS1, H$^+$** (shaded with W/Ta)

The aggregation of the polyelectrolyte brushes found in light scattering and AFM was also shown by TEM images. Fig. 7.8.5.6. displays a TEM micrographs of sample **3-30-1, TMS1, H$^+$**. The sample was spin-coated from solution onto a carbon-coated mica surface and shaded with W/Ta by electron beam evaporation. As can be seen from these images, the molecules are clustered into groups. The molecule dimensions measured (length: 101.3 nm ± 17.7 nm, diameter: 34.5 ± 4.6 nm) were much larger than the values determined by AFM due to the different substrates used. The aggregates are relatively well defined. Due to the hydrophobicity of the polymer backbone and the hydrophilicity of the side chains, the following structure model is suggested (Fig. 7.8.5.7.): the polyelectrolyte backbones align parallel to each other on the carbon-coated mica surface. These backbones are surrounded by a corona of polyelectrolyte side chains.

For sample **11-40-IV, TMS1, Na$^+$** from the **11-series**, with a negative second virial coefficient in aqueous solution, the clustering effect is even more pronounced. This is shown in Figs. 7.8.5.9. to 7.8.5.11. On these micrographs, long polymer strands with contour lengths of several micrometers are observed. These strands form structures that look like aerial photographs of roads with motorway junctions and interchanges. The diameters of these strands increase upon fusion of two strands at a junction.

Tab.7.8.5.2. summarizes the results measured. The single strands of the aggregates are slightly thinner than the single molecules. As a result of the backbone alignment (Fig. 7.8.5.7. and Fig. 7.8.5.8.) of the molecules, the diameter of the double and multiple strands is slightly smaller than twice or three times the diameter of the single strands, which supports the model proposed.

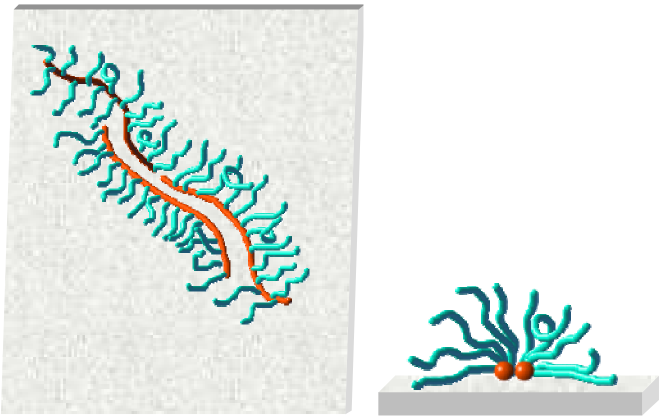

Fig. 7.8.5.7.: Model for polyelectrolyte clustering on solid supports (left: top view, right: side view)

Table 7.8.5.2.: Contour length and diameter determination for sample **11-40-IV, TMS1, Na$^+$** (single molecules and aggregates) by TEM

11-40-IV, TMS1, Na$^+$	**Contour Length [nm]**	**Diameter [nm]**
Single molecules	125.5±11.0	14.7±1.1
Single strand	several µm	13.0±2.3
Double strand		20.4±2.1
Multiple strand		27.5±2.5

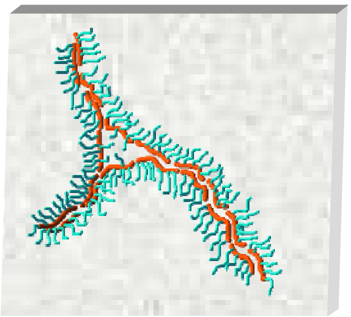

Fig. 7.8.5.8.: Model for polyelectrolyte brush aggregates in Figs. 7.8.5.9. to 7.8.5.11.

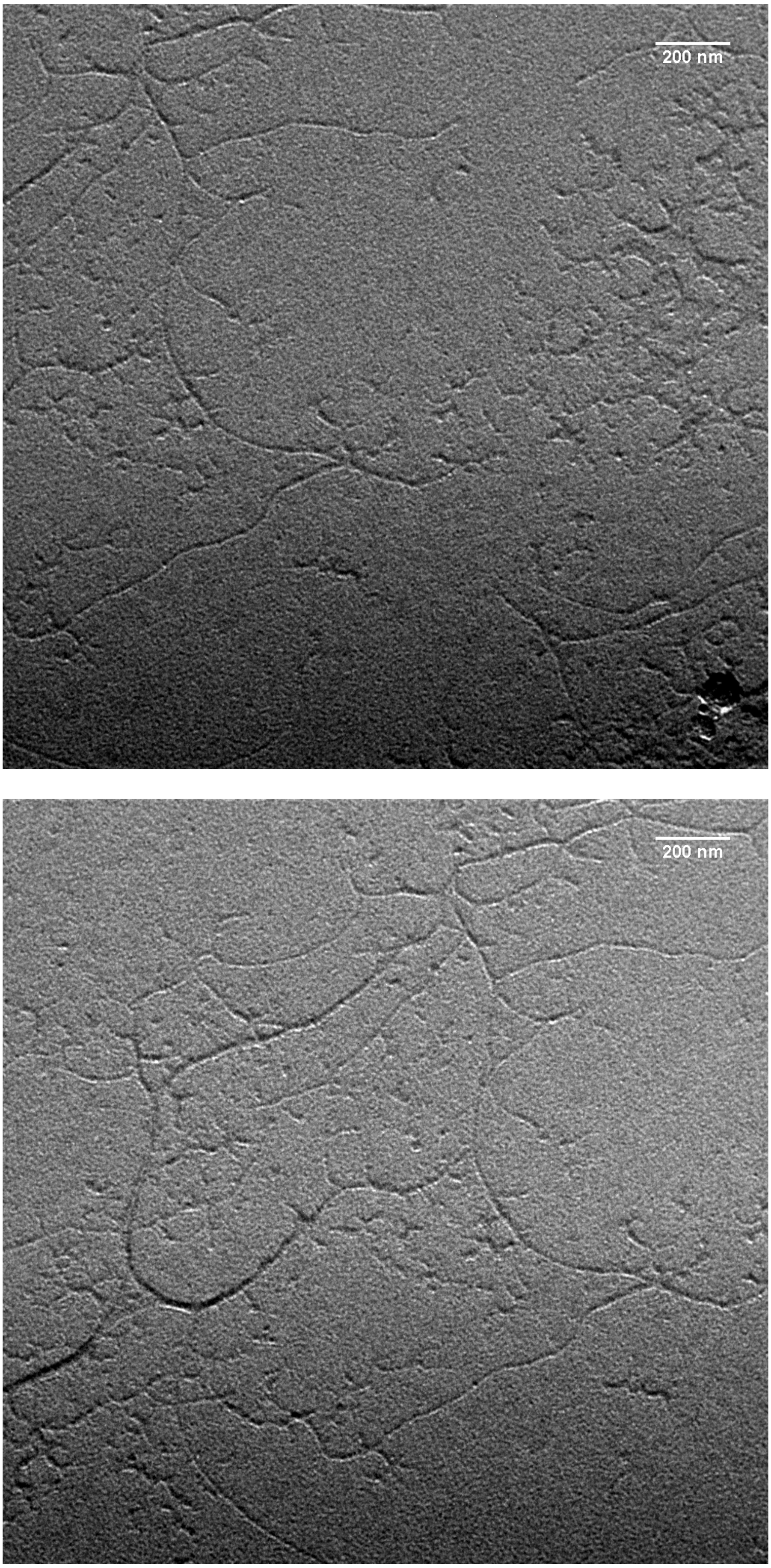

Fig. 7.8.5.9.: TEM micrographs of sample **11-40-IV, TMS1, Na$^+$**

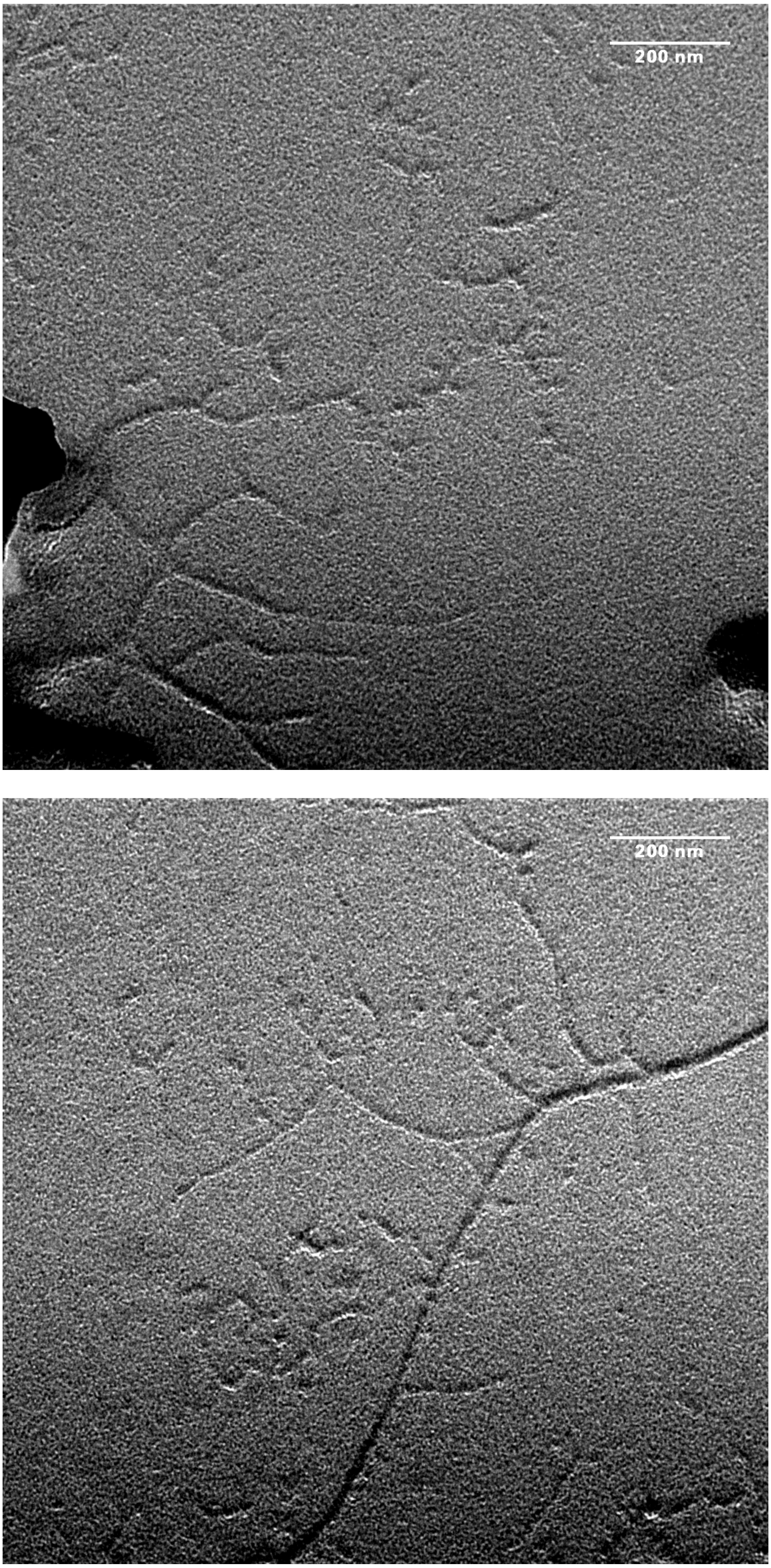

Fig. 7.8.5.10.: TEM micrographs of sample **11-40-I, TMS1, Na$^+$**

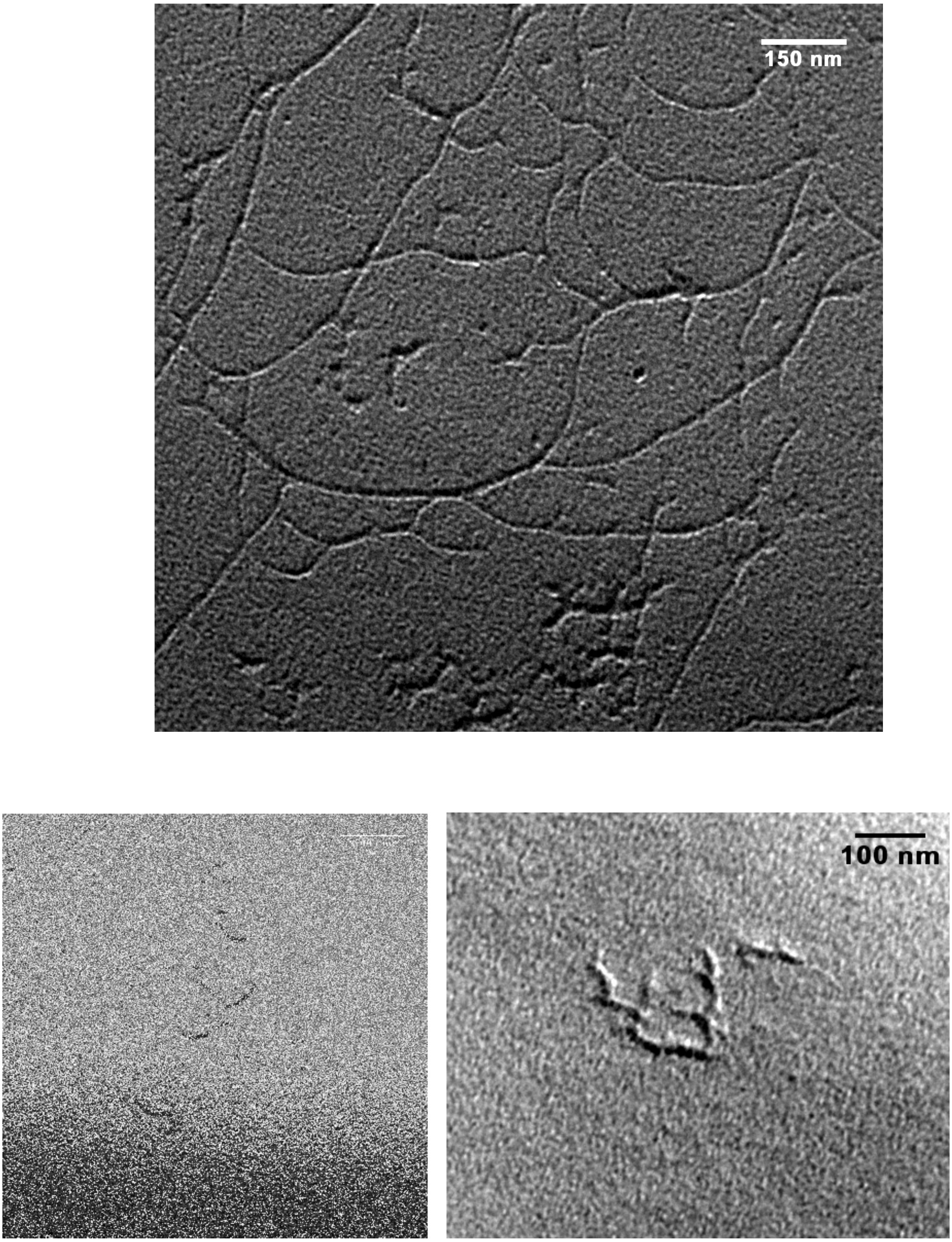

Fig. 7.8.5.11.: TEM micrographs of sample **11-40-I, TMS1, Na$^+$**

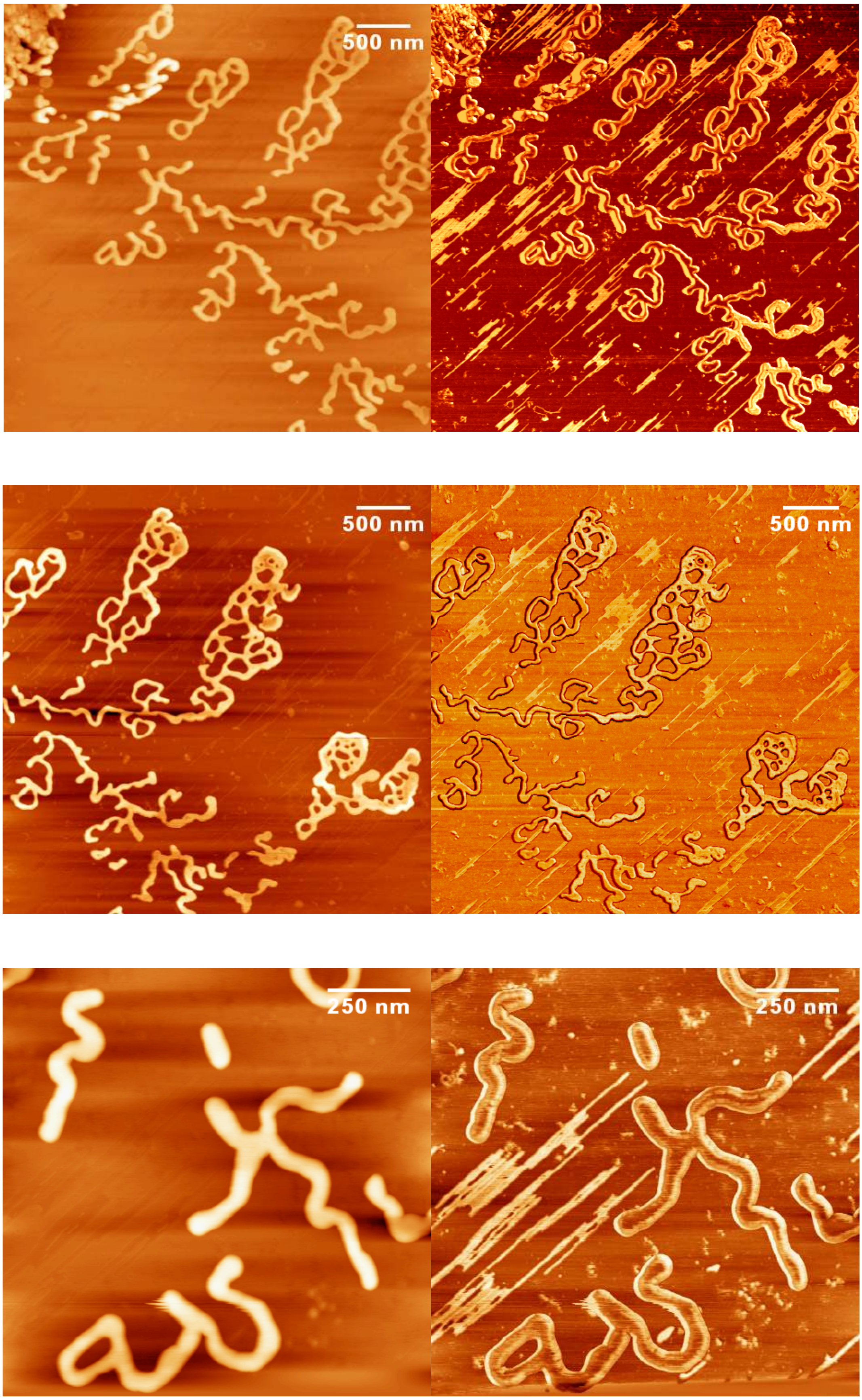

Fig. 7.8.5.12.: AFM images of **11-40-I, TMS1, H$^+$ (tapping mode, mica)**

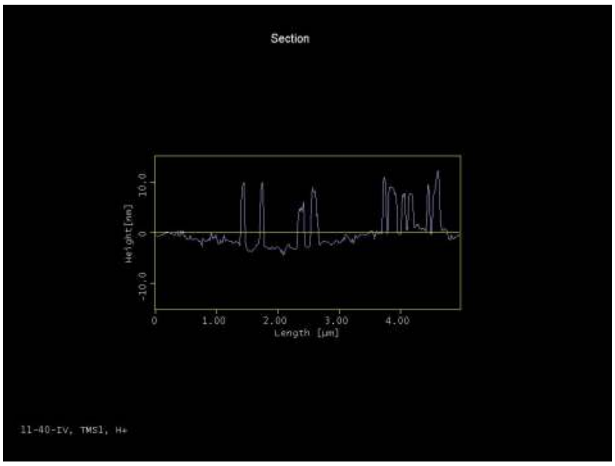

Fig. 7.8.5.13.: AFM section through sample **11-40-I, TMS1, H$^+$**

Aggregates of similar dimension, yet entirely different morphology, are found for **11-40-IV, TMS1, H$^+$**. For samples spin-coated from aqueous solution onto mica, large aggregates with diameters of 59.4 ± 5.1 nm and 11.4 ± 1.3 nm height are observed, as shown by AFM (Fig. 7.8.5.12). SEM images reveal that these structures are evenly distributed over the whole sample surface. Besides these aggregates, single molecules with 11.3 ± 1.8 nm diameter and 1.8 ± 0.5 nm height are observed.

Samples **11-40-IV, TMS1, Na$^+$** and the corresponding free acid form, according to static light scattering, have the geometry of a homogeneous sphere in solution, whereas AFM and TEM reveal that these samples (on solid support) consists of large elongated aggregates. This apparent contradiction is illustrated in Fig. 7.8.5.14. The elongated aggregate winds up in solution to form a sphere-like blob. The driving force of this transition could be minimization of solvent interactions.

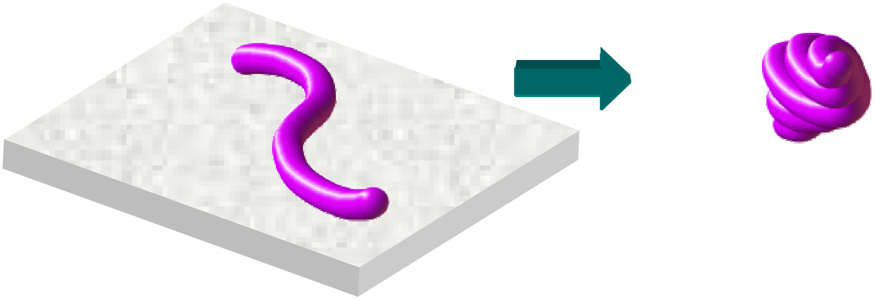

Fig. 7.8.5.14..: Samples **11-40-IV, TMS1, Na$^+$** and **H$^+$** on solid support (left) and in solution (right)

Imaging of Polyelectroyte Brushes in Solution

The AFM images and TEM micrographs presented thus far gave the possibility to image single molecules on a solid substrate. The dimensions measured from such samples have only limited relation to the actual dimensions of the sample in solution due to deformation of the single molecule on adhesion to the surface. Until now, no method for imaging undisturbed nano-scale molecules in solution is available, however a few methods exist that enable molecule imaging with closer resemblance to molecules in solution than by preparation on a solid substrate. AFM can be measured in solution, however this is difficult and not yet a routine method. Also, one measures the dimensions of a solvated species that is in contact with a solid surface, i.e. again there is a source of deformation.

TEM offers two useful alternatives for imaging “as in solution”. The first is embedding the molecule into a solid trehalose matrix: by mixing an aqueous solution of the sample with trehalose solution and spreading the solution onto a holey copper grid, the molecule conformation in solution is preserved. During drying, the sugar matrix hardens. As the process is fast, the molecule is not able to change its conformation[171]. This method is frequently applied for TEM imaging of biological structures. TEM micrographs thus obtained for samples **3-30-PSS2, K$^+$**, **3-30-PSS1, K$^+$**, **3-30-PSS1, H$^+$** and **3-30-1, NR$_4^+$** are shown in the following section. Another alternative for solution-like TEM imaging is cryo-TEM. For this method, the sample solutions are frozen in liquid butane and then imaged with TEM in a cooled sample holder at very low temperatures. This is shown below for samples **11-40-I, TMS1, H$^+$** and **11-60-IV, TMS1, H$^+$**.

Fig. 7.8.5.11. shows a TEM image of **3-30-PSS2, K$^+$** (from aqueous solution) in a trehalose matrix, contrasted with uranyl acetate. Thus the polyelectrolyte brushes appear as bright shapes on a dark, uranyl stained background. Collapsed brushes (dots) next to stretched brushes (lines) are observed. The average diameter of the extended brushes is 11.7±1.6 nm. The brushes tend to align end-to-end to form small networks, thus the contour length cannot be determined. The collapsed brushes have a relatively uniform size distribution. Large aggregates are not observed.

Fig. 7.8.5.12. presents the TEM micrographs of **3-30-PSS1, H$^+$** in a trehalose matrix without staining. As can be seen, the contrast between the sample and the matrix is quite weak. However, the uranyl ions may have an influence on the molecular shape of

the polyelectrolyte, thus the unstained sample gives a more realistic impression of the state of the polymer in solution. The average brush diameter is 18.1±2.6 nm. This is in the in excellent agreement with the cross-sectional radius of gyration $\boldsymbol{R_{g,c}}$ determined for **3-30-PSS1, K$^+$** from the SANS measurements (chapter 7.8.4.) which was determined to be as 3.9 nm. For a cylinder, the geometrical relation between $\boldsymbol{R}$ and $\boldsymbol{R_g}$ is $\left\langle {R_g}^2 \right\rangle = \frac{1}{3} R^2$, and $2\left\langle {R_{g,c}}^2 \right\rangle = \left\langle {R_g}^2 \right\rangle$, thus $R = \sqrt{6} \cdot \left\langle R_{g,c} \right\rangle$. The geometrical radius $\boldsymbol{R}$ calculated from the SANS data is 9.6 nm, i.e. the diameter is about 19.1 nm, which is close to the 18.1 nm determined from TEM. In addition to single brushes, large stiff aggregates with a diameter of about 70 nm and a length of 430 nm are observed. This corresponds to the findings from light scattering for this sample.

Aggregates of similar dimensions are found for sample **3-30-1, NR$_4$$^{++}$**, as shown in Fig. 7.8.5.13. Here, the single molecules have a diameter of 12.1±2.4 nm. The value calculated from small angle neutron scattering is for sample **3-30-1, H^{++}**, the corresponding free acid, is 14.2 nm.

The images obtained by cryo-TEM show an even weaker contrast as compared to the trehalose images. Sample **11-60-I, TMS1, H$^+$** was stained by the addition of CsOH, which did not result in much contrast enhancement (Fig. 7.8.5.14.). The brushes imaged had a diameter of 6.1 nm. Sample **11-40-IV, TMS1, H$^+$** was stained with CsCl and bovine serum albumin (BSA) as described for spherical polyelectrolyte brushes by Talmon and Ballauff[59]. BSA is a natural protein that has a good contrast in electron microscopy and was shown to migrate into polyelectrolyte brushes, thus making them visible in cryo-TEM. Fig. 7.8.5.15. and 7.8.5.16. show the cryo-TEM images thus obtained from sample **11-40-IV, TMS1, H$^+$**. The images show a mesh-like structure that look like a superposition of the strand-like structure from sample **11-40-IV, TMS1, Na$^+$** in Figs. 7.8.5.8. to 7.8.5.10.. This makes sense as Figs. 7.8.5.8. show images obtained from a sample coated with W-Ta, i.e. only the sample surface is visible. The cryo-TEM samples have a finite thickness, and the image thus obtained is a projection of all elements in this ‘slice’ onto a 2D image or screen. Thus, the molecule strands with highway junction-like shape put on top of each other will resemble a network like entity. The diameter of the strands making up the image in Fig. 7.8.5.15. is much smaller than expected (3.1 nm compared to the 13 nm single strands from Fig. 7.8.5.8.). This could be another effect of the weak contrast, or the staining only affects the polymer backbone.

Table 7.8.5.3. summarizes the results obtained for the polyelectrolyte brush diameters from the **3-series** obtained by different methods.

Table 7.8.5.3.: Diameters of polyelectrolyte brushes

Sample	Diameter (SANS) [nm]	Diameter AFM [nm]	Diameter TEM [nm]
3-30-PSS1, K^+	19.1	10.2±1.9	18.1±2.6
3-30-1, NR_4^{++}	-	20.2±2.6	12.1±2.4
3-30-1, H^{++}	14.2	-	-
3-30-1, TMS1, H^+	15.1	12.7±2.5	-
3-30-PSS2, K^+	-	-	11.7±1.6
3-30-1H	11.8	-	-
11-60-I, TMS1, Cs^+	-	-	6.1±1.0
11-40-IV, TMS1, H^+	-	-	3.1±0.6

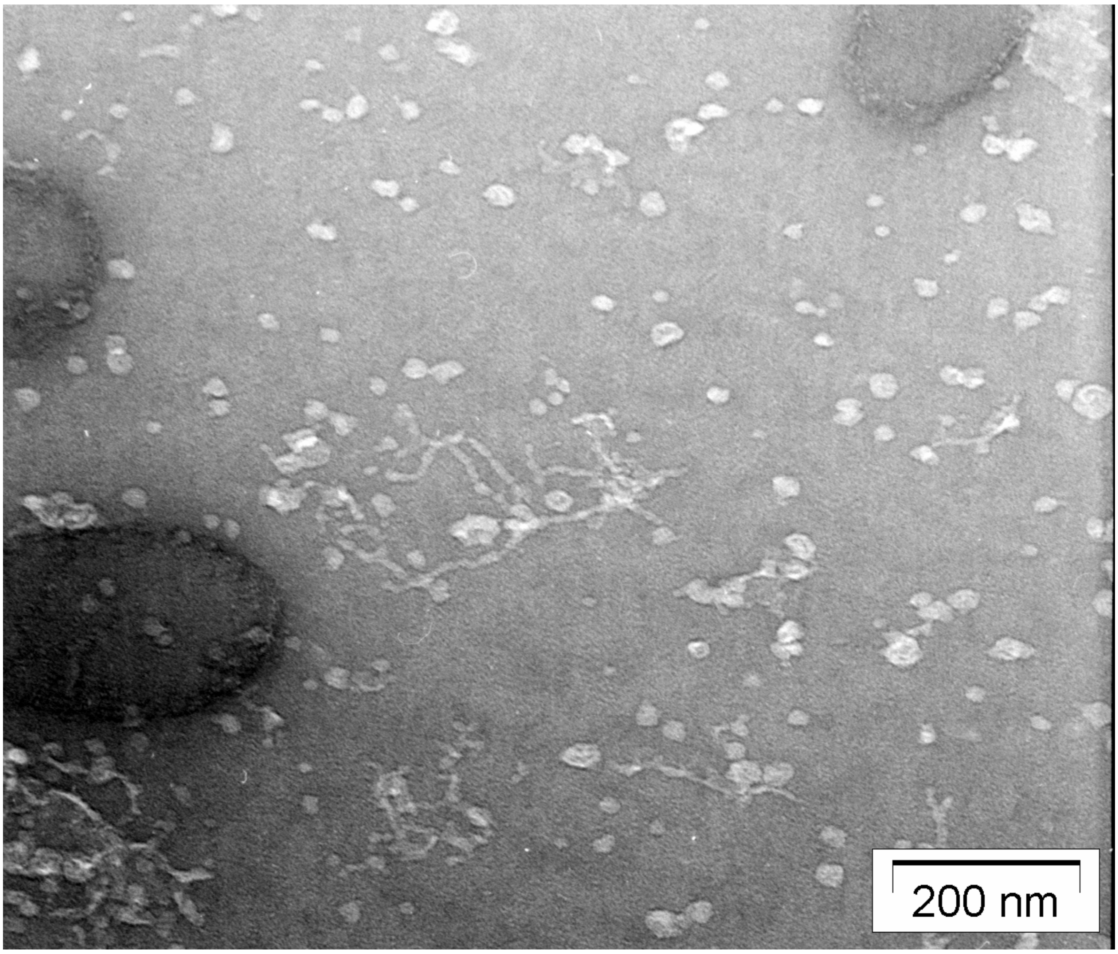

Fig. 7.8.5.11.: TEM micrograph of sample **3-30-PSS2, K^+** in trehalose matrix, contrasted with uranyl acetate

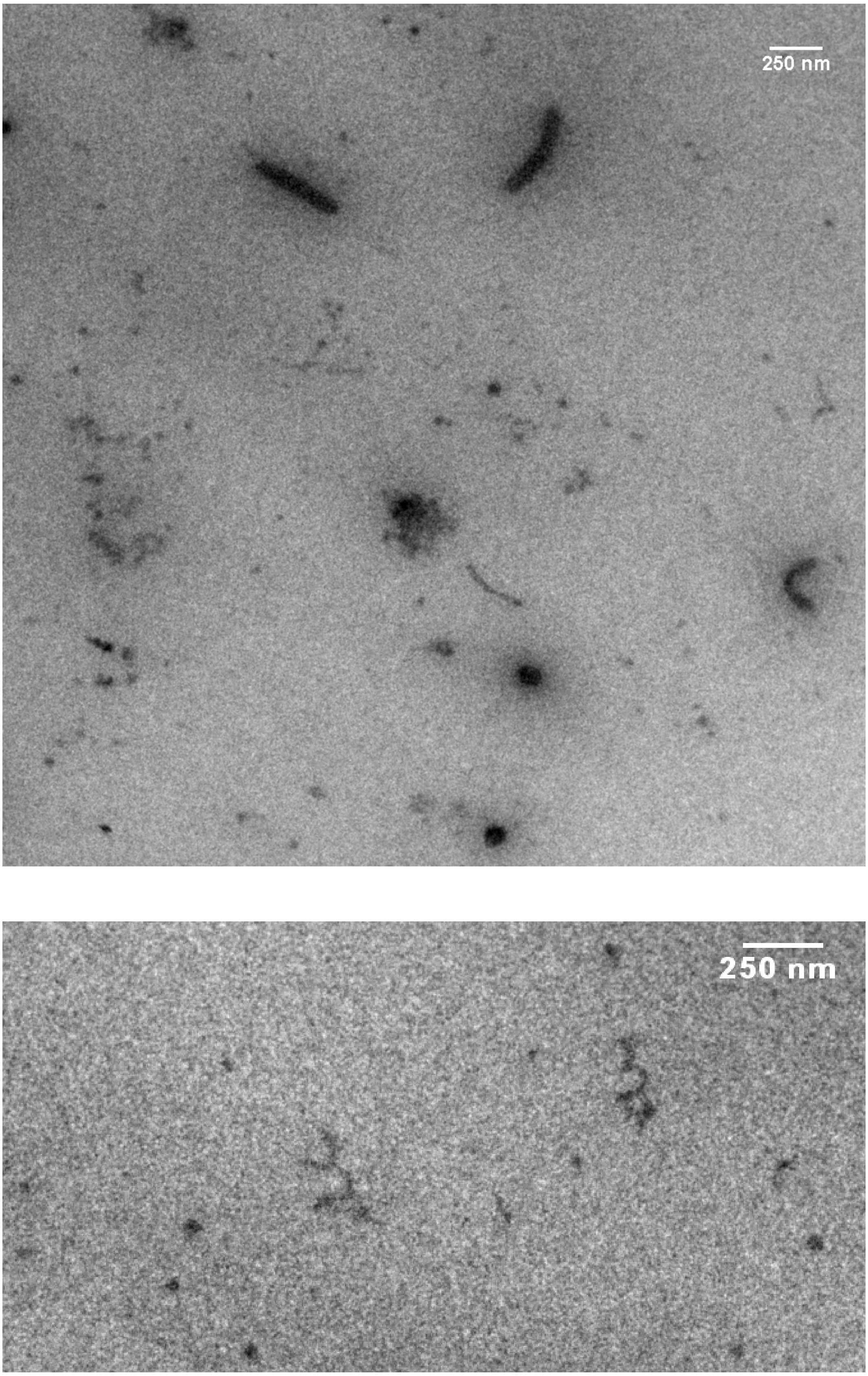

Fig. 7.8.5.12.: TEM micrograph of sample **3-30-PSS1, H$^+$**, unstained, in trehalose matrix

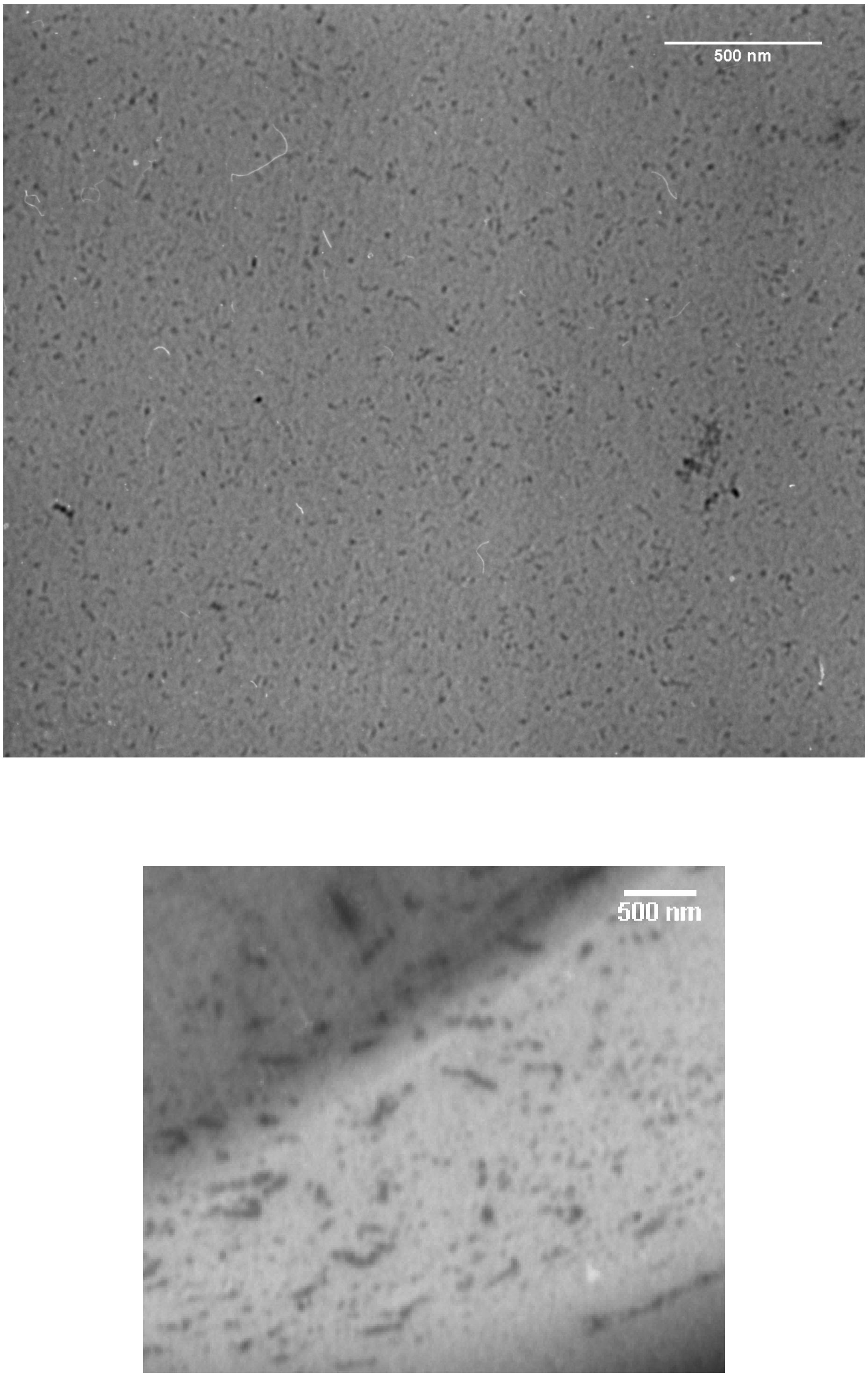

Fig. 7.8.5.13.: TEM micrograph of sample **3-30-1, NR_4^{++}**, unstained, in trehalose matrix; top: single molecules (underfocussed), bottom: aggregates

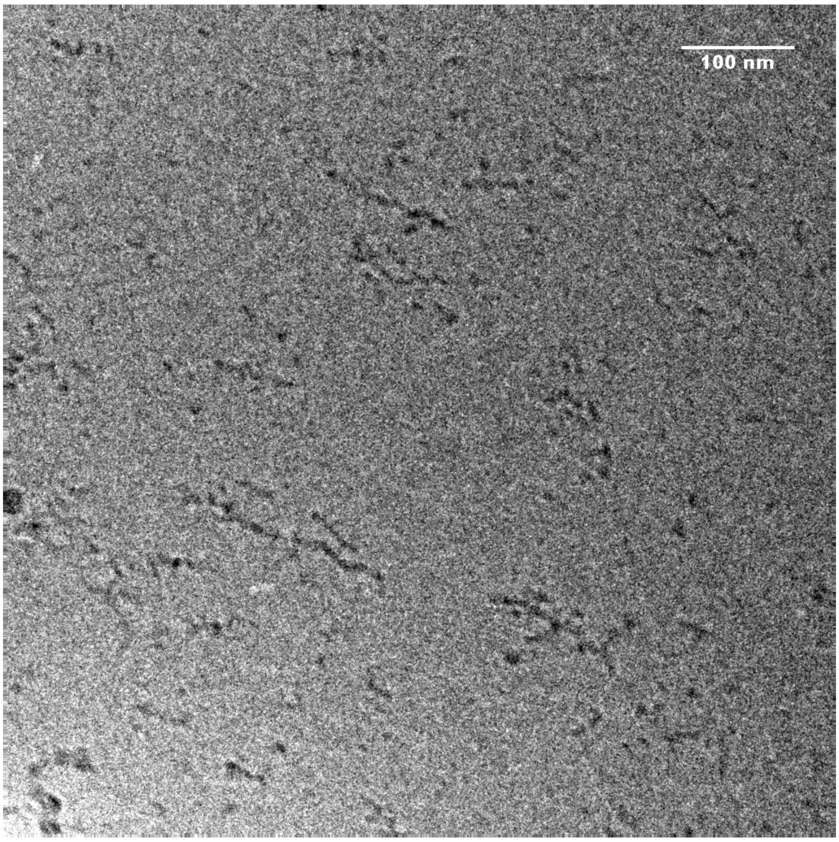

Fig. 7.8.5.14. Cryo-TEM micrograph of **11-60-I, TMS1, Cs$^+$**

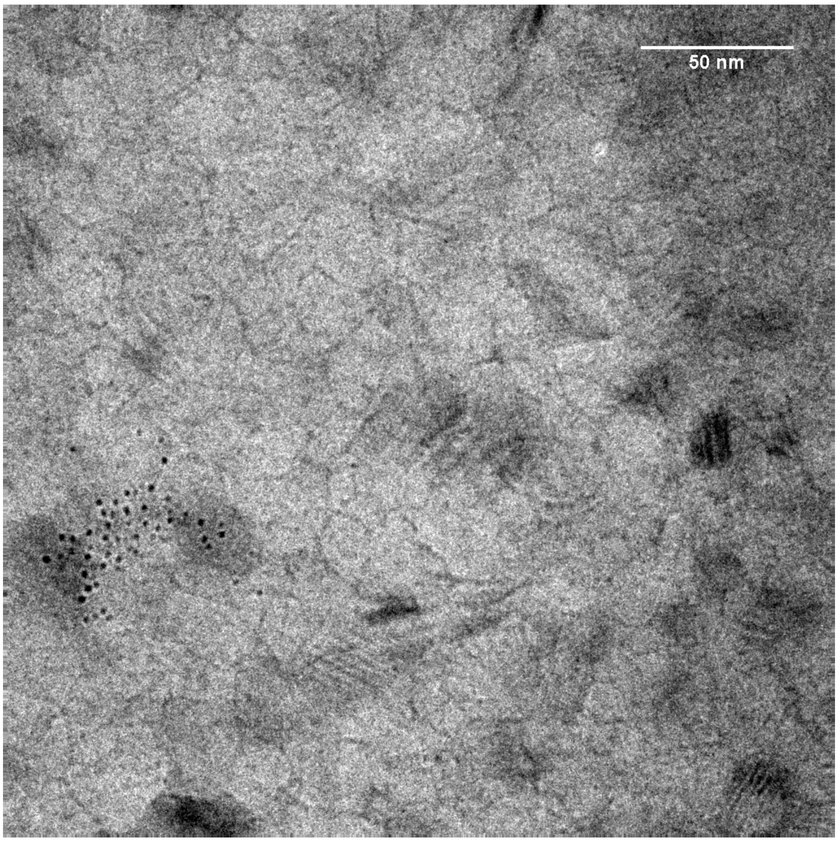

Fig. 7.8.5.15. Cryo-TEM micrograph of **11-40-IV, TMS1, Cs$^+$/BSA**

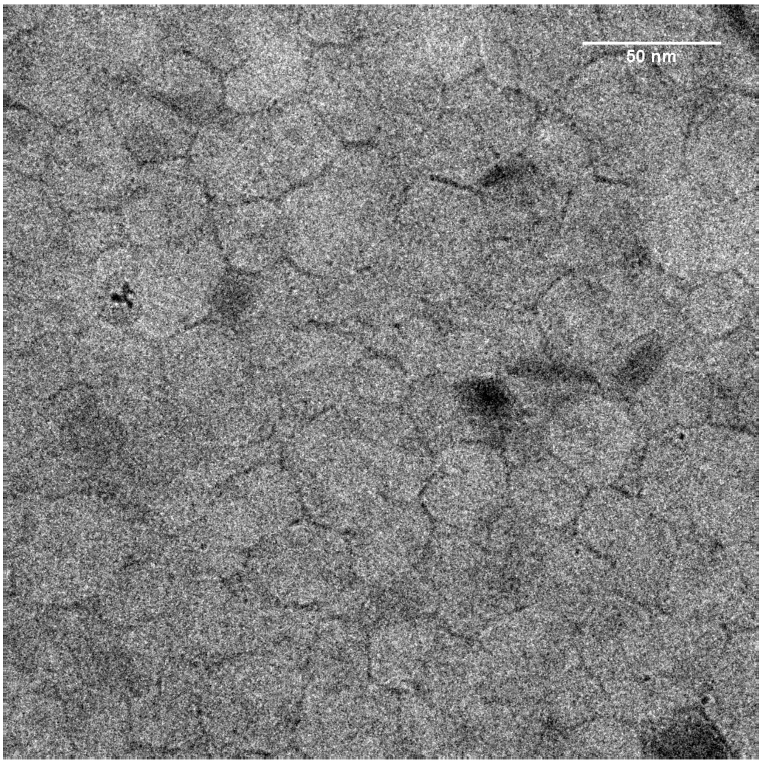

Fig. 7.8.5.16. Cryo-TEM micrograph of **11-40-IV, TMS1, Cs^+/BSA**

The idea of cluster formation of the polyelectrolyte brushes due to hydrophobic interactions is further supported by the following experiment: 4-dimethylamino-2-methylazobenzene (Fig. 7.8.5.17.), which is insoluble in water and NaOH, but soluble in HCl due to protonation, is a classical dye for fat[172]. 1 mg of 4-dimethylamino-2-methylazobenzene have been added to: 2 ml H2O, 2 ml NaOH, 2 ml HCl, 2 ml H_2O with 5 mg **3-30-PSS4, H^+** and 2 ml NaOH with 5 mg **3-30-PSS4, H^+**. The results are shown in Fig. 7.8.5.17. As expected, the dye is insoluble in water and NaOH. In HCl, it forms a pink-red solution. In water with the polyelectrolyte brush, the solution is orange. To exclude the possibility that this solubilization is due to protonation of the primary amine of the dye, the experiment is repeated with NaOH and polyelectrolyte brush. Here, the solution is yellow, and the dye is completely dissolved. As the same amount of dye is used in all experiments, it can be concluded that the different colors are not due to concentration effects. The interpretation is that in the case of HCl, solubilization is due to protonation, causing a red shift of the dye absorption. In the case of the polymer in NaOH, the dye is solubilized within the hydrophobic part of the polyelectrolyte brush near the backbone, causing a yellow color. In H_2O with polyelectrolyte, both mechanisms are active, which can be seen from the orange color. The comparison of the experiments with NaOH alone and NaOH with the polyelectrolyte proves that the polyelectrolyte addition causes the dye solubilization.

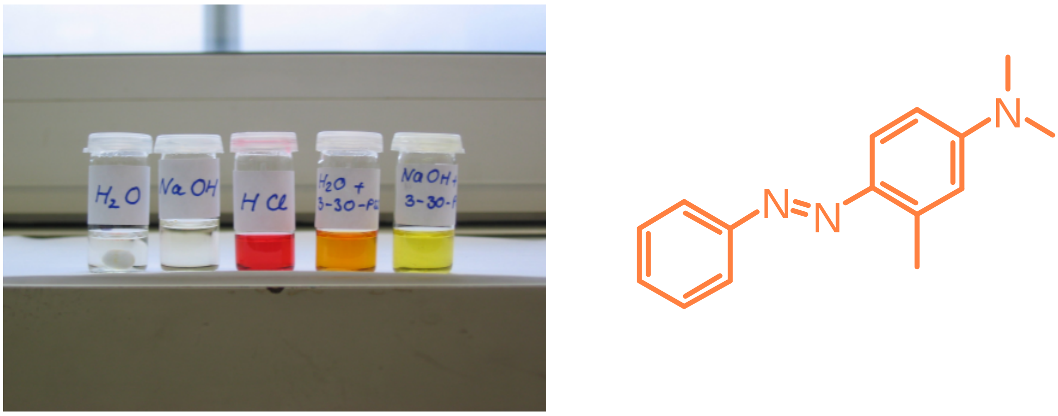

Fig. 7.8.5.17.: Dye solubilization – structure of 4-dimethylamino-2-methylazobenzene (right), experimental results (left)

7.9. *Conclusive Remarks*

With the macroinitiator approach, polymer and polyelectrolyte brushes with varying degree of branching and different degrees of hydrolysis were obtained. For the **PSSD** brushes, the average side chain length was determined by ^{1}H-MNR. For the **PSSE** brushes, additional data from GPC-MALLS was available. The branched structure was confirmed by AFM and TEM. The resulting polyelectrolyte brushes with different degrees of hydrolysis were analyzed by GPC-MALLS, static and dynamic light scattering, neutron scattering, ^{1}H-NMR and acid-base titration, as well as imaging methods, as discussed in chapters 7.1. to 7.8.. The main issues investigated in this work, besides the synthetic aspects, were the difficulties arising during saponification of the polymer brushes, and the aggregation behavior of the resulting polyelectrolyte brushes in aqueous solution.

Saponification

As can be seen from the titration results and the ^{1}H-NMR results, quantitative hydrolysis of the polymer brushes could not be obtained. This is in contrast to findings by Woeste[162] and others[173, 166] on the saponification of linear **PSSD** and **PSSE** homopolymers. For those systems, quantitative hydrolysis is claimed. This discrepancy may be attributed to the more complicated polymer architecture. On a semi-quantitative basis, the following interpretation is suggested: For quantitative hydrolysis, the free enthalpy ΔG of the overall reaction must be negative. As $\Delta G = \Delta H - T\Delta S$, the contributions to each of these parameters must be investigated. T is positive by definition, thus the second term of the equation only becomes negative if the entropy of the system increases upon saponification. Relevant contributions to the entropy parameter are:

- change of entropy due to a change in the number of particles during the reaction,
- increase of translational, rotational and conformational entropy of the hydrolyzed ester groups and
- change of conformational entropy of the brush side chains and backbone.

For the enthalpy parameter, the following factors need to be considered:

- reaction enthalpy of the elementary reaction step,
- interactions between the hydrophobic polymer brush and the hydrophilic saponification reagent and
- increase of the osmotic pressure of the polyelectrolyte brush with increasing conversion.

In the following section, these parameters will discussed for each reaction:

a) n K^+ + n OH^- + Polymer brush → n R-OH + Polyelectrolyte brush

As a large fraction of the counterions will be condensed to the polyelectrolyte brush, the number of particles decrease by n. The rotational and conformational entropy of the n hydrolyzed ester groups increases, as they are freed from the confined environment of the polymer brush. The change in conformational entropy of the side chains and the backbone should be negligible, as experimental evidence in the literature[114] has shown that the molecule dimensions do not change when going from a neutral precursor to a charged polyelectrolyte brush. As the polymer brush is highly non-polar, the polar, charged hydroxide anion should experience a severe hydrophobic repulsion, which would decrease with progressive hydrolysis. The osmotic pressure exerted by the condensed counterions will increase with increasing degree of saponification, making it continuously more difficult for the saponification agent to penetrate the molecule. The influence of the reaction enthalpy of the elementary reaction should be negligible; it is approximated by the value found in literature for the saponification of benzyl sulfonate phenyl ester (ΔH = 72.5 kJ/mol)[174].

b) n NEt_3 + Polymer brush → Polyelectrolyte brush

Due to counterion condensation and formation of an ammonium salt, the number of particles decrease by n. As before, the rotational and conformational entropy of the n hydrolyzed ester groups increases, while the change in conformational entropy of the side chains and the backbone should be negligible. The hydrophobic repulsion of triethylamine by the non-polar polymer brush should be less as compared to the hydroxide anion in a), and it should not increase with increasing degree of hydrolysis.

The osmotic pressure exerted by the condensed counterions will increase with increasing degree of saponification.

c) In combined saponification by first triethylamine and, secondly, KOH, the number of particles decreases by ***n***. As before, the rotational and conformational entropy of the ***n*** hydrolyzed ester groups increases, while the change in conformational entropy of the side chains and the backbone should be negligible. In the first step, the hydrophobic repulsion of triethylamine is very little, as discussed above, and in the second step, in aqueous medium, the hydroxide ion should not experience much hydrophobic interaction with the partially saponified brush. The osmotic pressure exerted by the condensed counterions will increase with increasing degree of saponification.

d) ***n*** **TMS-I + Polymer brush →** ***n*** **R-I + Polymer brush →**
n **Na-OTMS +** ***n*** **R-I + Polyelectrolyte brush**

In both steps of the reaction, the number of particles is balanced. As before, the rotational and conformational entropy of the ***n*** hydrolyzed ester groups increases, while the change in conformational entropy of the side chains and the backbone should be negligible. In the first step, the hydrophobic interaction of the brush and TMS-I should be small; in the second step, the hydrophobic repulsion of the polar, charged hydroxide anion should be quite strong, however it would decrease with progressive hydrolysis. In any case, the osmotic pressure exerted by the condensed counterions will increase with increasing degree of saponification. A further driving force of the reaction is the formation of a TMS-O bond in the first reaction step, as well as the facilitated hydrolysis of the R'-OTMS compared to R'-OR, $OTMS^-$ being a much better leaving group than the alcoholate.

Table 7.9.1.: Parameters influencing the polymer brush hydrolysis

Reaction	% hydrolysis	particle number	entropy ester groups	entropy brush	interactions	osmotic pressure
a)	10	- ***n***	+	0	+	+
b)	40	- ***n***	+	0	0	++
c)	90	- ***n***	+	0	0	+++
d)	66	0	+	0	+	++

The enthalpic and entropic effects of reactions **a)** to **d)** are summarized in Tab. 7.9.1. With this information, the different yields of the hydrolysis reactions, and, more importantly, the question why the reactions work quantitatively for linear polymers, but not for brushes, can be discussed in more detail. As can be seen from the compilation in Tab. 7.9.1., the entropy gain of the ester group as well as the entropy change of the total brush is the same for all four reactions. The different yields obtained thus should be explainable with arguments based on the remaining parameters.

The low yield in reaction **a)** is most probably due to the strong hydrophobic interactions. These also play a role in reaction **d)**, yet due to the high reaction enthalpy this is compensated. The counterion condensation is certainly enhanced in the polyelectrolyte brush as compared to its linear analogue, as has been shown in the literature (see chapter 4). This influences the entropy parameter, as the number of particles on the right side of the reaction equation decreases stronger for the brush due to a higher fraction of the counterions being condensed to the polyelectrolyte. Due to the counterion condensation, the osmotic pressure in the brush is high, i.e. it is increasingly difficult for any saponification agent to penetrate it. Also, the hydrophobic repulsion should be more pronounced in the case of the brush due to its branched architecture. These parameters make the reaction more unfavorable for the brush compared to the linear analogue. On the other hand, the gain of conformational and rotational entropy of the hydrolyzed ester residues is more pronounced in the case of the brush, as it has a much more confining environment than in a linear poly(styrene sulfonate ester). However, the experimental data shows that this effect cannot compensate the joint effect of the hydrophobic repulsion and the osmotic pressure, i.e. the degree of hydrolysis stays low. The previous considerations lead to the following model for saponification: the saponification agent acts first in the molecule periphery, as it is more approachable than the ester groups near the core and the hydrophobic interactions are less pronounced. This decreases the hydrophobicity of the whole molecule. At the same time, the progressive saponification leads to an increased osmotic pressure due to counterion condensation. At a point depending on the specific reaction conditions (nature of the saponification agent, reaction enthalpy, temperature etc. as discussed above), the conversion of the hydrolysis in not increased further as the effect of the osmotic pressure does not allow the saponification agent to enter the molecule. The result is a polyelectrolyte molecule with an internal hydrophobicity gradient: it is hydrophobic inside near the backbone and hydrophilic in the periphery. The gradient assumption is supported by the following experimental findings:

- Polyelectrolyte brushes with different sidechain lengths and different sidechain-backbone length ratios show remarkable difference in their solution and aggregation behavior in water (chapter 7.8.2.).

- As has been shown in chapter 7.8.5, the polyelectrolyte brushes tend to align the backbones to form high molecular weight aggregates. The driving force of this aggregation are hydrophobic interactions, which are minimized by aligning the hydrophobic parts and exposing the hydrophilic parts to the surrounding water. This also explains why single molecules are found in DMF while aggregates are formed in water.
- As shown before, the polyelectrolyte brushes are able to solubilize a hydrophobic dye in aqueous solution, which is otherwise water-insoluble.

As is not possible to obtain quantitatively saponified polyelectrolytes from the reactions described above, solvent free reactions such as pyrolysis may be considered as an alternative. As this is a solid state reaction, the factors influencing the reaction conversion discussed above do not play a role. It was shown by Corey[175] that for sulfonate esters with alkyl substitution in the para-position, the yield for this reaction is only 56% at 150℃. At this temperature, the structural integrity of the polymer backbone might also suffer. A very recent paper[176] suggests that poly(styrene sulfonate neopentyl ester) may be thermolyzed quantitatively without loss of the structural integrity of the sample. Thus, switching to this monomer may solve the encountered difficulties.

Aggregation

With the concept of a gradient within the polyelectrolyte brush, its solution and aggregation behavior can be understood. The fact whether a specific sample dissolves as a single molecule or as an aggregate depends on the degree of saponification and the sidechain length, which both influence the A_2 value. The higher the degree of hydrolysis, the smaller the aggregates, as demonstrated for polyelectrolyte samples derived from the parent ester **3-30-D1**. The size and shape of the aggregates seems to be is influenced by the sidechain-backbone length ratio: for longer backbones, larger and more complex aggregate shapes were observed, as shown for samples **11-40-IV, TMS1**. For more quantitative statements, more samples would be necessary. The samples discussed in this chapter were obtained in the process of establishing and optimizing a complicated synthetic procedure with many reaction parameters. Thus the products obtained, though being well-defined, do not feature the systematic variation of side chain length, backbone length and grafting density that might be wished for to obtain a more complete picture. Now that the synthesis of such molecules is established, and some striking and unexpected structural features were found, samples with systematically varied molecular parameters should be synthesized for a complete understanding of their influence of the molecular shape and aggregation behavior.

8. Synthesis of End-functionalized Polymer Brushes

8.1. Introduction

As a model for the proteoglycan, anionic polymer brushes from poly(styrene sulfonic acid) with a positively charged head group were synthesized (Fig. 8.1.1.).

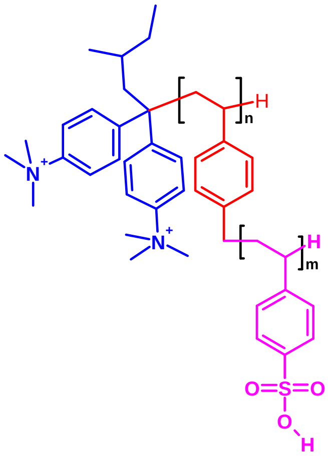

Fig. 8.1.1.: Functionalized polyelectrolyte brush

As a first approach to model the link protein that connects proteoglycans with hyaluronic acid in nature (chapter 5.2.), the structure was simplified as much as possible. The complex structure of the link protein was entirely ignored and replaced in the synthetic model by a head group containing merely two positive charges. Again, the macroinitiator approach was chosen for the synthesis of this structure, and a functionalized macroinitiator for ATRP of styrene sulfonate esters was designed.

8.2. Synthesis of a Functionalized Macroinitiator

Functionalized polymers with one head group can be obtained by different synthetic strategies. The most common ones are end-capping of a living polymer with a reagent carrying a functional group or initiation of a living polymerization with an initiator carrying a functional group. For this work, anionic polymerization has been chosen, as it yields polymers with narrow polydispersity and is well-established for the polymerization of styrenes and methylstyrenes. As end-capping of a living anionic polymer always includes the danger of unwanted side reactions due to intrusion of water or oxygen, yielding only partially functionalized polymer samples, functionalization by initiation was chosen. For this purpose, 1,1-di(4-dimethylamino-phenyl)ethylene) (**NN-DPE**) was synthesized and applied as an initiator. An analogous anionic polymerization with the mono-aminosubstituted DPE derivative was published by Quirk[178]. The initiator **NN-DPE** was synthesized after modified procedures by Wittig[177] for the ylid formation, combined with a procedure by Quirk[178] for the mono-amino substituted compound (Fig. 8.2.1.).

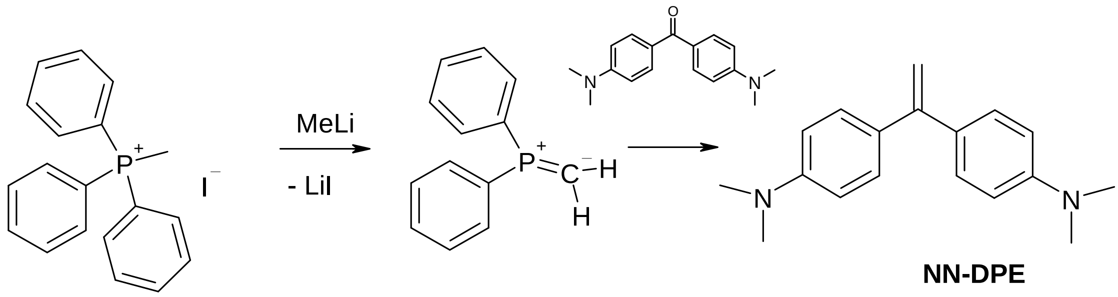

Fig. 8.2.1.: Synthesis of the functionalized initiator

Using 1 equivalent of *sec*-butyl lithium on an excess of **NN-DPE** yielded an active initiator for methylstyrene polymerization. Applying standard procedures for the anionic polymerization of styrenic monomers (chapter 12), a functionalized macroinitiator precursor was obtained (Fig. 8.2.2.).

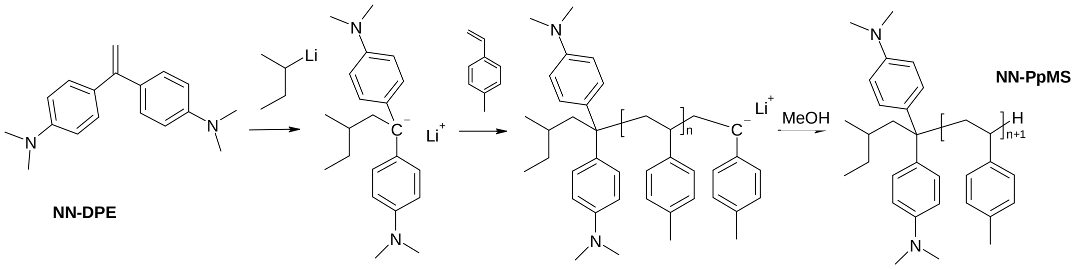

Fig. 8.2.2.: Synthesis of the macroinitiator precursor.

For the synthesis of proteoglycane models, high molecular weight was aimed at, however to be able to demonstrate the success of the functionalization, a low molecular weight model compound was also synthesized. The analytical results of both compounds are summarized in Table 8.2.1. Fig. 8.2.3. shows the GPC elugram of **NN-PpMS1**.

Table 8.2.1.: Analytical results for NN-poly(methylstyrene) (**NN-PpMS**)

Sample	$M_{n,\,theory}$ **[g/mol]**	$M_{w,\,GPC\text{-}MALLS}$ **[g/mol]**	$M_{n,\,GPC\text{-}MALLS}$ **[g/mol]**	M_w/M_n
NN-PpMS1	200 000	212 000	196 000	1.10
Me-NN-PpMS1	200 000	209 000	195 000	1.10
NN-PpMS2	7 000	8 200	7 900	1.04
Me-NN-PpMS2	7 000	9 200	8 700	1.05

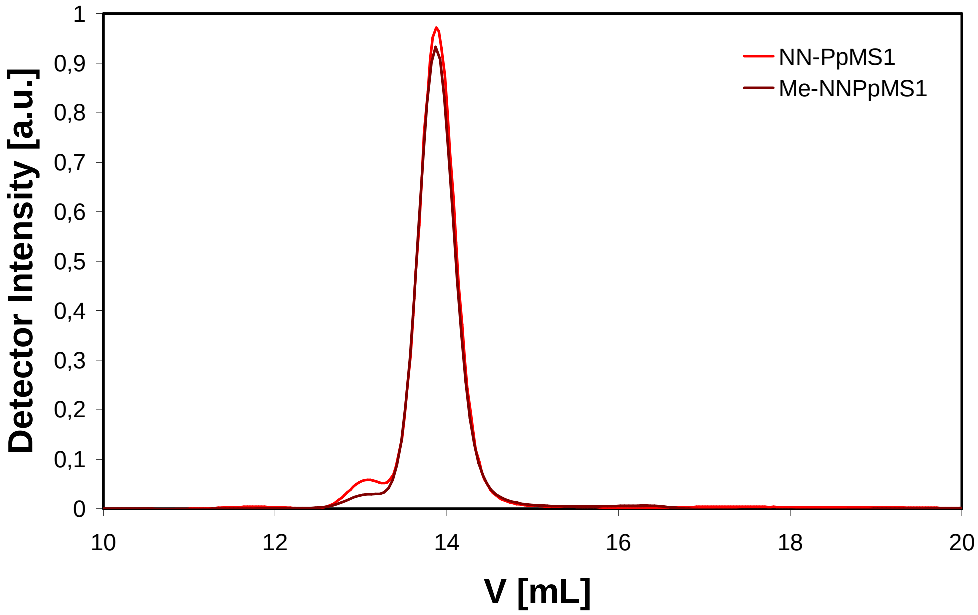

Fig. 8.2.3.: GPC Elugram of Samples **NN-PpMS1** and **Me-NN-PpMS1**

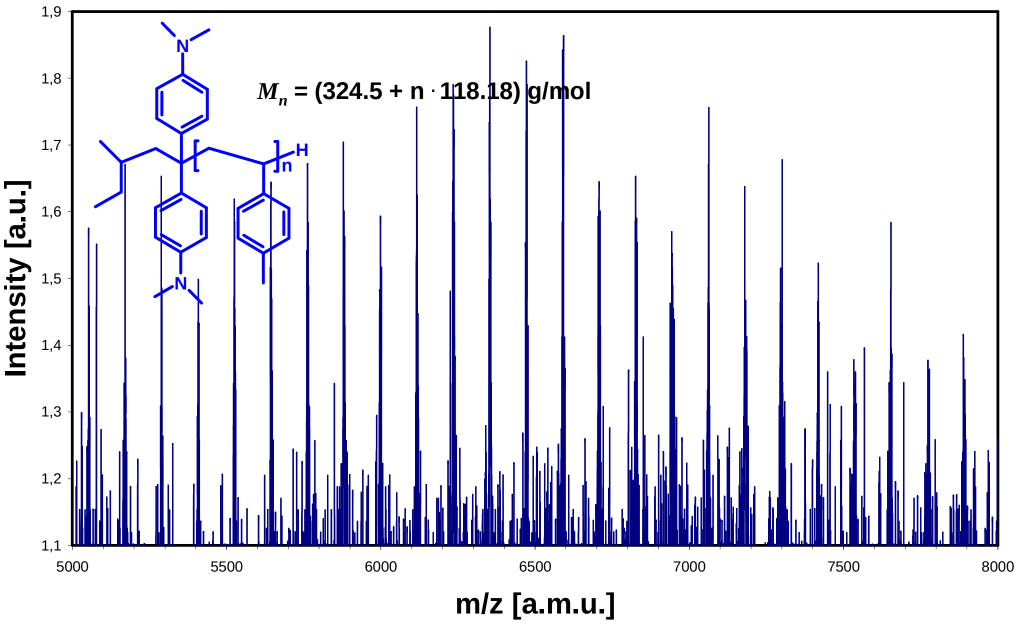

Fig. 8.2.4.: MALDI-TOF MS of **NN-PpMS2**

The molar mass distribution of sample **NN-PpMS1** is reasonably narrow to use it as a macroinitiator precursor. The success of the functionalization was demonstrated with model compound **NN-PpMS2** by In MALDI-TOF mass spectrometry. For sample **NN-PpMS1**, this was not possible due to its high molecular weight. To avoid interpretation difficulties, the compound was measured without any salt added, although this naturally leads to a loss in the spectrum quality. The spectrum obtained is shown in Fig. 8.2.4.. A comparison between the peaks calculated and the peaks measured (Tab. 8.2.2.) clearly demonstrates that the desired functionalized polymer was obtained. Subtraction of the first peak listed from the last one and division by eight yields 118.4 g/mol, which matches the mass of the poly(methylstyrene) repeat unit. The ^{1}H-NMR resonances of the head group are covered by the signals from the polymer and could not even be resolved on the 700 MHz machine. Thus ^{1}H-NMR gives no additional prove of the compound structure.

Table 8.2.2.: MALDI-TOF MS peaks of **NN-PpMS2** and **Me-NN-PpMS2**

NN-PpMS2		**Me-NN-PpMS2**	
$M_{n,\ theory}$ **[g/mol]**	$M_{n,\ MALDI}$ **[g/mol]**	$M_{n,\ theory}$ **[g/mol]**	$M_{n,\ MALDI}$ **[g/mol]**
5878	5879	5893	5897
5997	5999	6012	6015
6115	6116	6130	6134
6233	6234	6248	6252
6351	6353	6366	6369
6469	6472	6484	6487
6588	6592	6608	6605
6506	6707	6521	6724
6824	6826	6839	6842

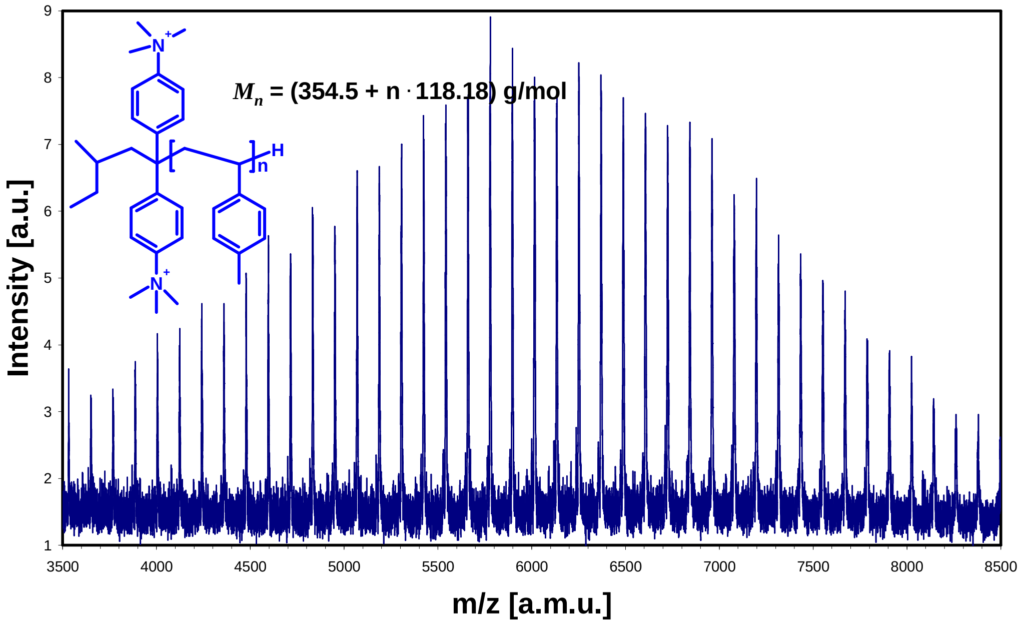

Fig. 8.2.5.: MALDI-TOF MS of **Me-NN-PpMS2**

As the macroinitiator is designed for ATRP, and amines act as ligands for the copper complex used in ATRP, the positive charge had to be introduced prior to the ATRP reaction step. Consequently, the **NN-PpMS** samples were reacted with methyl iodide, yielding the desired quarternized ammonium functionality (**Me-NN-PpMS**). Again, the functionalization was checked with model compound **Me-NN-PpMS2** by MALDI-TOF MS. The peak list for this compound is included in table 8.2.2.. The corresponding mass spectrum is displayed in Fig. 8.2.5.. As can be seen from the peak list, the relative shift of the mass spectrum of **Me-NN-PpMS2** compared to the non-quarternized compound is approximately 15 a.m.u., matching with the molecular weight of an additional methyl group. The fact that the spectrum is shifted by 15 a.m.u. and not 30 a.m.u. (two nitrogen atoms are quarternized) is due to plotting m/z. As z = 2 in this case, $\frac{M+30}{2} = M'+15$. Besides this characteristic shift, the spectrum intensity, which went up by a factor of ten as compared to the non-quarternized spectrum, is a further indication of successful quarternization. Further analytical results for the **Me-NN-PpMS** samples are included in Table 8.2.1.. The GPC elugram of **Me-NN-PpMS1** is included in Fig. 8.2.3..

To obtain the desired macroinitiator, the quarternized precursor was reacted with N-bromosuccinimide (Fig. 8.2.5.), according to the procedures discussed in chapter 7. The success of this reaction was confirmed by the peak from 4.2 to 4.5 ppm in the ^{1}H-NMR spectrum of the macroinitiator. Integration of this peak versus the aromatic signals (6.0 to 7.1 ppm), as discussed in chapter 7, indicates a degree of bromination of 51 %.

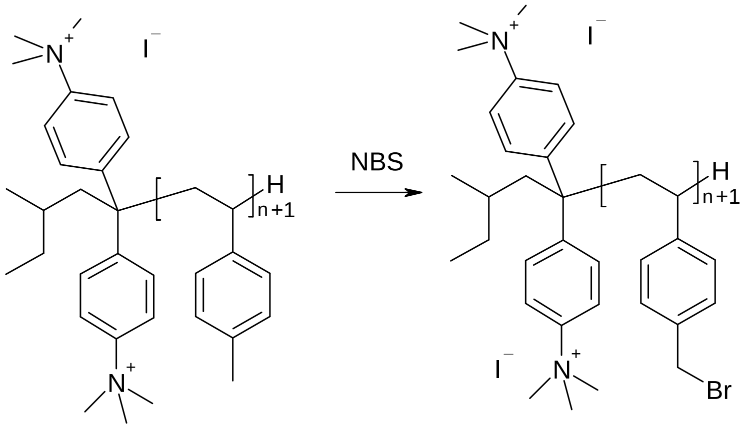

Me-NN-PpMS **Me-NN-PpMS-Br**

Fig. 8.2.6 .: Synthesis of the functionalized macroinitiator

8.3. *Synthesis of Functionalized Polymer Brushes*

Following the procedures used for unfunctionalized polymer brushes (chapter 7), the macroinitiator **Me-NN-PpMS1-Br** was used for the synthesis of functionalized polymer brushes from styrene sulfonate dodecyl ester (Fig. 8.3.1.). As expected, the ATRP reaction of this functionalized product did not pose any further synthetic problems as the functional head group was inactive during the reaction. The reaction medium was homogeneous and no gel formation was observed. The substance was freed from copper, the ligand and the unconsumed monomer by repeated precipitation into methanol and re-dissolving in THF. It was then passed over an ion exchange resin for quantitative copper removal. The ^{1}H-NMR spectrum of the substance obtained is presented in Fig. 8.3.2..

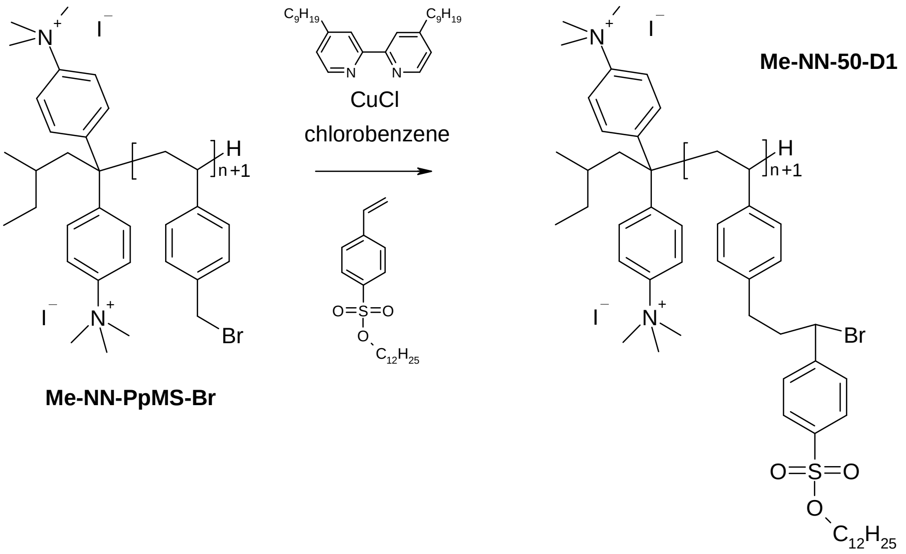

Fig. 8.3.1.: Synthesis of functionalized polymer brushes from styrene sulfonate dodecyl ester

The signal group from 6.0 to 8.0 ppm corresponds to the sum of all aromatic protons, the signal at 3.8 to 4.2 ppm originates from the α-CH_2 group from the $C_{12}H_{25}$ side chain. The absence of a peak from 4.2 to 4.5 ppm suggests that all initiating sites of the macroinitiator were consumed. Thus a functionalized polymer brush with 50% branching density (**Me-NN-50-D1**) was obtained. The peak group from 0.5 to 2.5 ppm corresponds to the aliphatic backbone and the side chains (see chapter 12). By the same method as outlined in chapter 7.3., the side chain length was determined as $n_n = 9$.

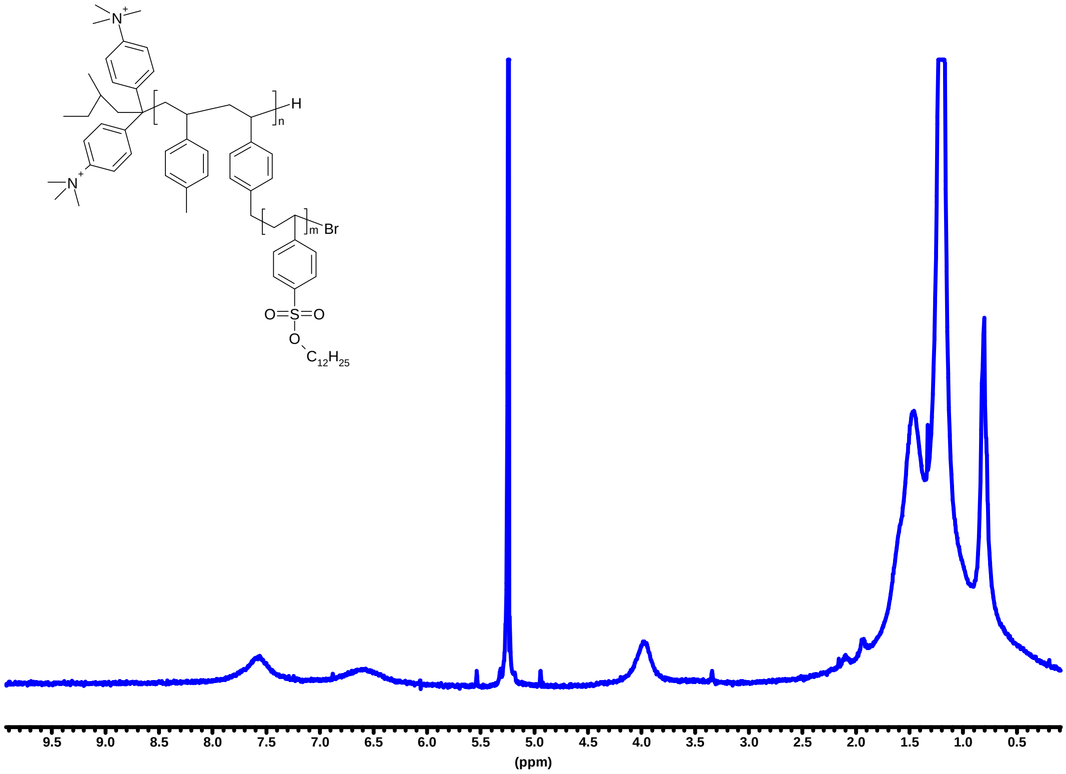

Fig. 8.3.2.: ^{1}H-NMR of the functionalized PSSD polymer brush (**Me-NN-50-D1**)

The solubility of the polymer brush **Me-NN-50-D1** in THF and CH_2Cl_2, compared to the unfunctionalized **PSSD** polymer brush, was unexpectedly low. Rather than dissolving properly, the substance swelled with solvent, leaving a gel-like precipitate. It only dissolved completely after increasing the solvent amount by a factor of 20. The solubility improved upon addition of lithium bromide. This is a clear indication that, already at the pre-polyelectrolyte level, there is intermolecular complexation. This could be due to the loss of a few dodecyl ester groups during the reaction or during work up. The resulting negative charge finds the positive head group, forming a polyelectrolyte complex with low solubility. If the complexation was merely intramolecular, this would not have such a drastic effect on the solubility. Shielding of these electrostatic interactions by salt addition then increases the solubility again. This effect was unexpected and makes it difficult to further pursue the path of model compound formation with the ‘neutral’ polymer brushes. To really investigate the difference in mechanical behavior of a single brush compared to a ‘brush of brushes’ before introducing negative charges to the brushes, a system with no interaction of the individual brushes must be obtained. Yet the complexation found is a clear indication why nature, being an efficient designer, uses such a complicated linker to connect the anionic polyelectrolyte brushes with hyaluronic acid. In this claw-shaped linker molecule, the positive charges are pointing to the inside of the claw and are surrounded by a non-charged periphery. Thus, self-complexation or inter-brush complexation is avoided. From this point of view, the aggregation between proteoglycans and hyaluronic acid is not only an example of ionic self-assembly, but also of the host-guest principle.

8.4. Synthesis of Functionalized Polyelectrolyte Brushes

The desired polyelectrolyte brush structure was obtained by hydrolysis of the poly(styrene sulfonate dodecyl ester) with trimethylsilyl iodide as discussed in chapter 7 (Fig. 8.4.1.).

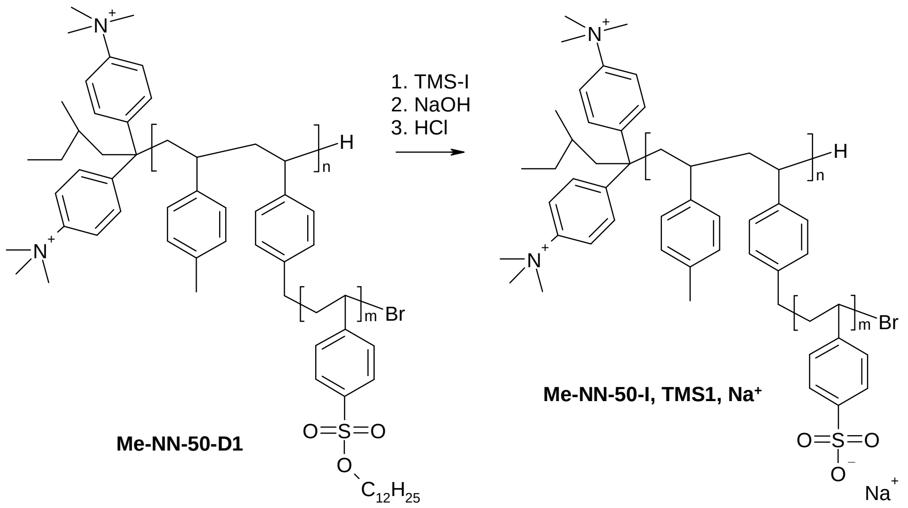

Fig. 8.4.1.: Synthesis of functionalized polyelectrolyte brushes (**Me-NN-50-I, TMS 1, Na$^+$**)

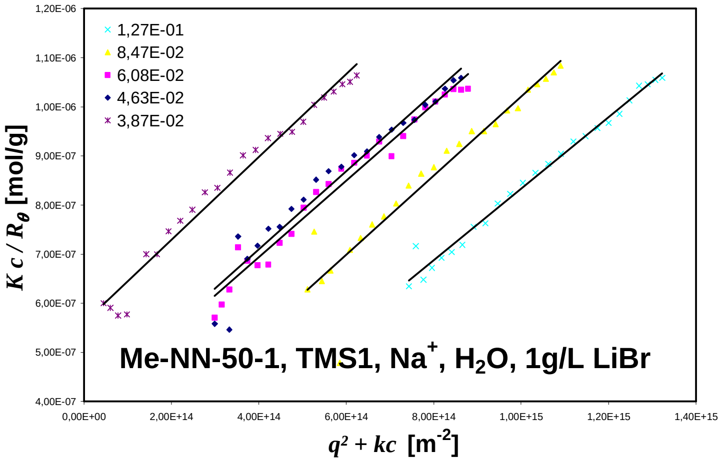

Fig. 8.4.2.: Static light scattering results (Zimm plot)

The sample was analyzed by static and dynamic light scattering and TEM. The light scattering results are displayed in Figs. 8.4.2. and 8.4.3.. M_w was determined to be 1 880 000 g/mol, $R_{g,z}$ = 68.1 nm, R_h = 46.8 nm and ρ = 1.45. This is in line with the findings for single molecules from the **11-series** (chapter 7).

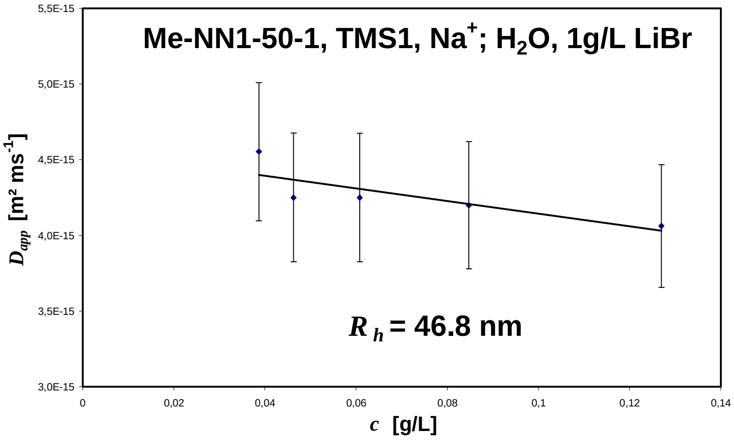

Fig. 8.4.3.: Dynamic light scattering results

The GPC-MALLS results are shown in Fig. 8.4.4.. The first peak in the elugram corresponds to the sample, the second to the solvent. The delayed elution of the sample may be explained by interaction between the positively charged end groups and the negatively charged column material. M_w was determined as 2 400 000 to 3 400 000 g/mol, depending on the evaluation parameters, as the values scatter significantly for low θ values. The polydispersity was 1.47 to 2.29. These values are also biased by the RI signal of the solvent peak, which did not allow a correct baseline subtraction. Yet the elugram shows that a monomodal distribution was obtained.

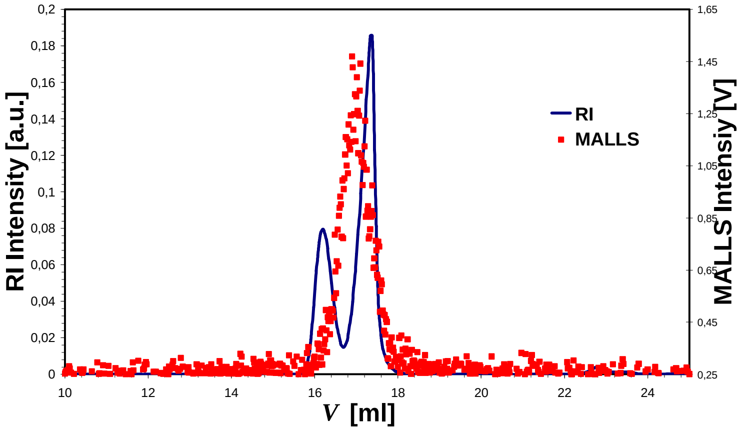

Fig. 8.4.4.: GPC-MALLS elugram and light scattering signal (θ = 90°)

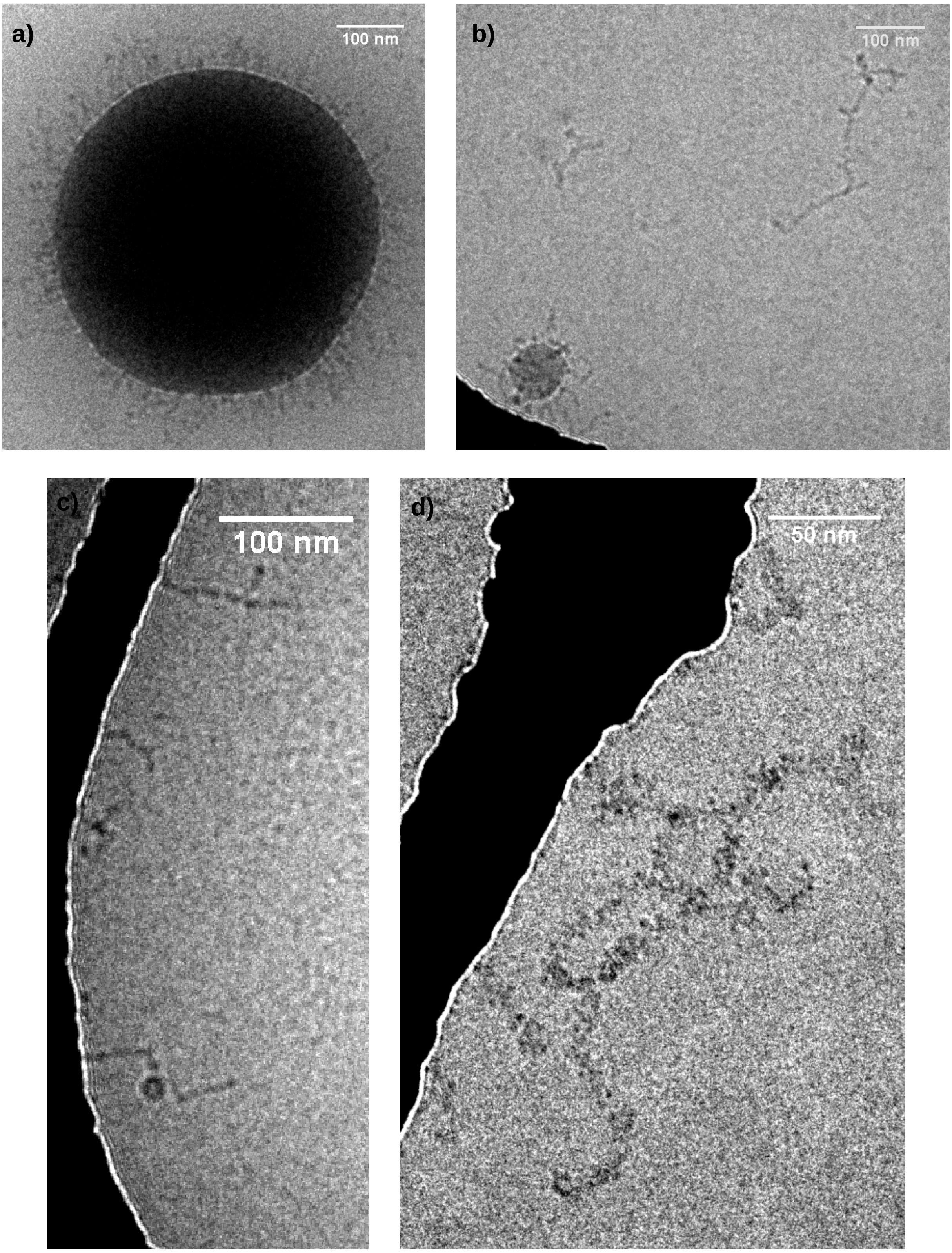

Fig. 8.4.5.: Cryo-TEM images of **Me-NN-50-I, TMS 1, Na$^+$**

In the cryo-TEM images (Fig. 8.4.5. and 8.4.6.), long wormlike shapes are found. These have a diameter of 9.1 ± 3.7 nm, which is on the same order of magnitude as for the non-functionalized brushes. One striking feature of these brushes, as compared to the non-functionalized brushes, is that they tend to attach end-on to all kinds of heterogeneities of the sample, from drop-like impurities of various diameters (Fig. 8.4.5., a) and b)) to the pore edges of the holey carbon films on the gold grid that hold the cryo-TEM sample (Fig. 8.4.5., c) and d), Fig. 8.4.6.). They also stick to each other, thus the precise determination of the contour length is not possible. This is a strong indication that complex formation with this simple model compound with only two positive charges as a linker molecule is possible.

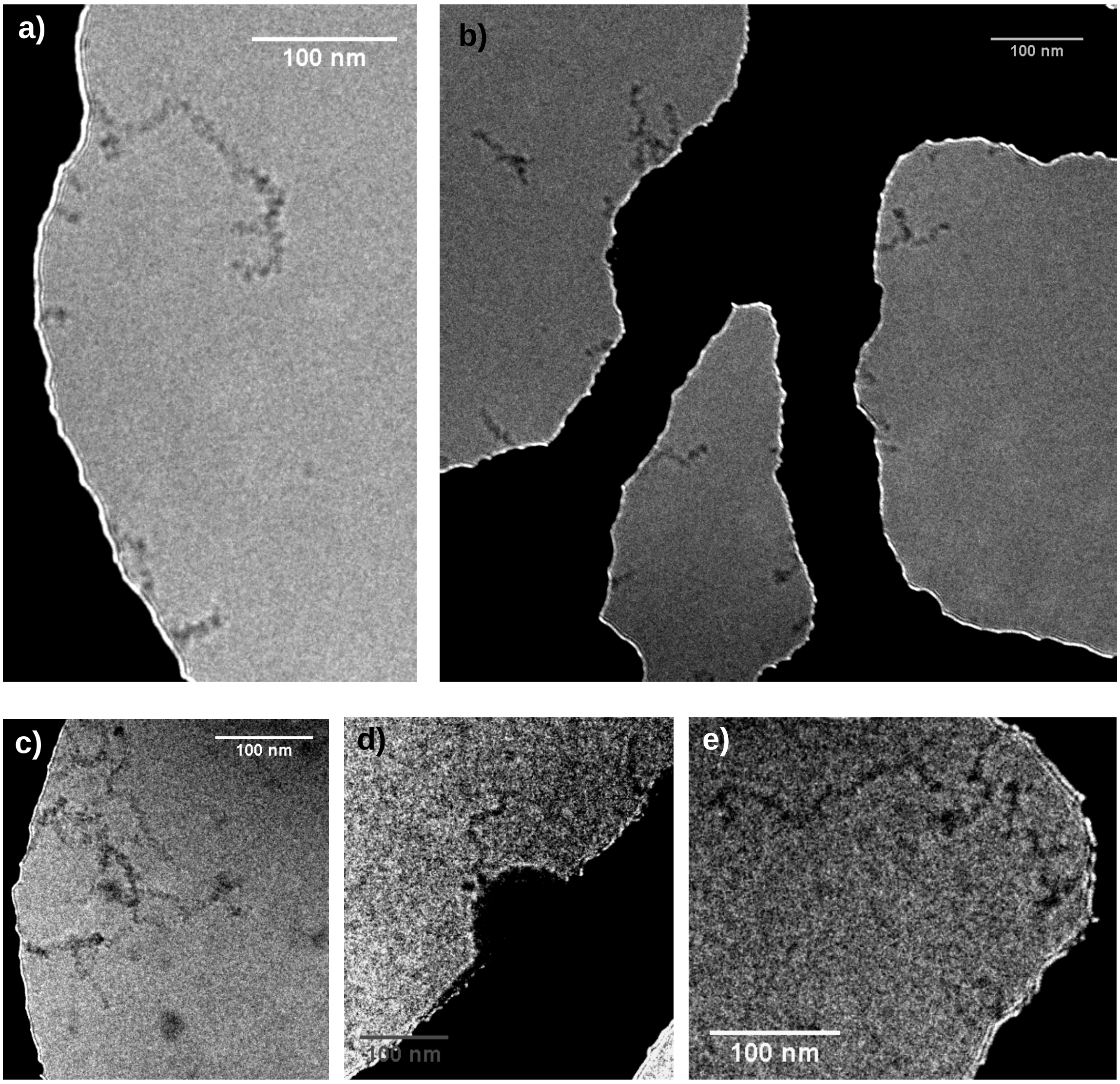

Fig. 8.4.6.: Cryo-TEM images of **Me-NN-50-I, TMS 1, Na$^+$**

8.5. Complexation Experiments

To further test the ability of the above described functionalized polyelectrolyte brushes to interact with negatively charge species, an aqueous solution of

Me-NN-50-I, TMS 1, Na$^+$ (c = 0.1 g/L, 3 ml, pH adjusted to 9 with 0.1 M NaOH) was mixed with 1 µL of a negatively charged spherical Latex particle[1] solution (c= 0.1 g/L). First, the components (brush and latex) were characterized separately by dynamic light scattering. The results are given in Fig. 8.5.1.. The hydrodynamic radius of the brush was determined as 46.0 nm with a relatively broad distribution (relative peak width ± 0.51), while the latex particle had an R_h of 37.4 nm, with a sharper distribution (relative peak width ± 0.19). Directly after mixing, a broad peak corresponding to a particle with R_h = 55.0 nm was found (Fig. 8.5.2., left), while two diffusion processes corresponding to particles with R_h = 52.8 nm and R_h = 139 nm were found after 24 h (Fig. 8.5.2., right). As a control experiment, the same mixture was investigated at pH 2, where the carboxylic acid groups of the latex particle were not dissociated. Here, no aggregation was found.

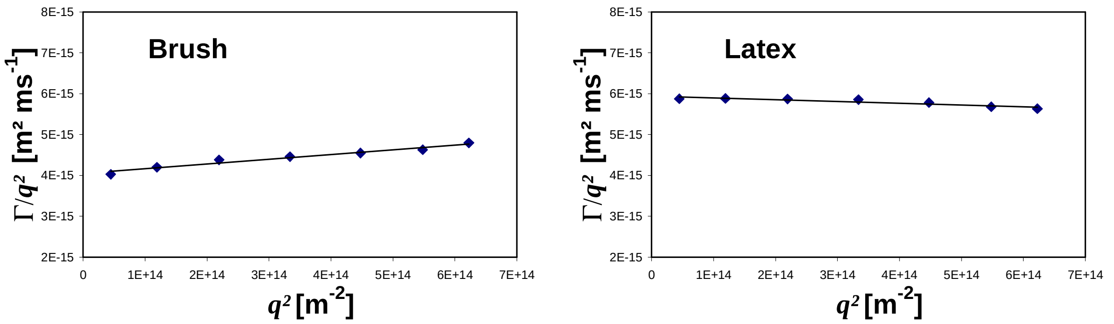

Fig.: 8.5.1.: DLS results for the polyelectrolyte brush (left) and the Latex particle

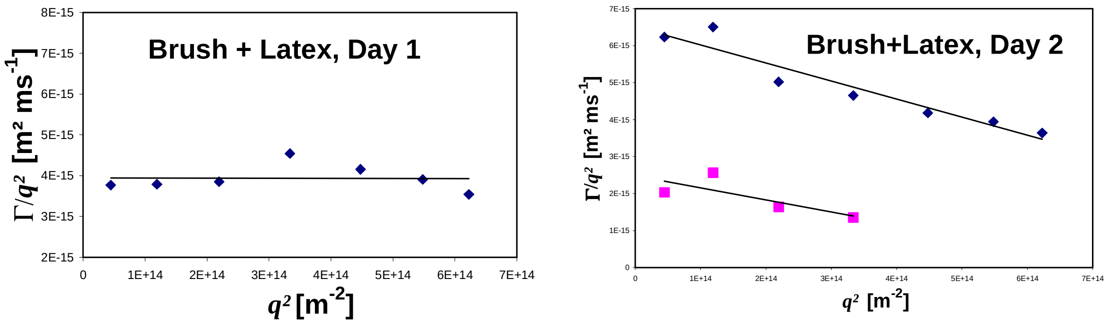

Fig.: 8.5.2.: DLS results for the polyelectrolyte brush-latex particle complex

These results lead to the following interpretation: As the measurement of the polyelectrolyte brushes in water indicates, these molecules are not significantly self-aggregating. Directly after mixing, there is barely any interaction between latex and brush, as the values of R_h measured for the individual particles are on the same order of magnitude as the R_h value determined for the mixture. After 24 hours, large

---

[1] poly(styrene-acrylic acid) latex particle with 4 % acrylic acid, negative surface charge; generously supplied by Dr. Rafael Munoz-Espi; MPI-P Mainz

aggregates are formed, which are almost out of the light scattering regime. The particle size roughly corresponds to the value expected for a central particle with 37 nm radius, surrounded by a layer of polyelectrolyte brushes with a hydrodynamic radius of 46 nm (Fig. 8.5.3.).

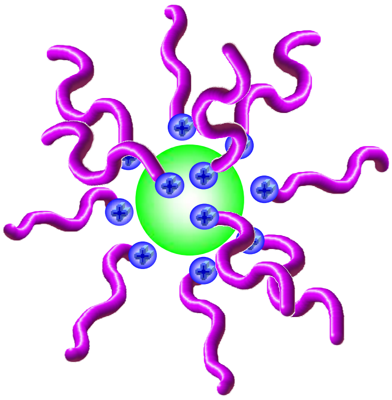

Fig. 8.5.3.: Cartoon representation of the polyelectrolyte brush-latex complex

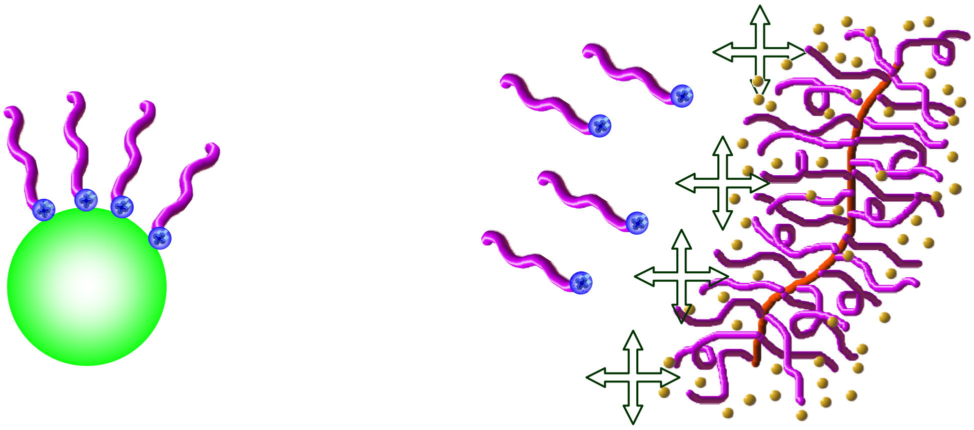

Fig. 8.5.4.: Interaction of the polyelectrolyte brushes with a smooth, ‘static’ surface (left) and an inhomogeneous, ‘dynamic’ surface (with arrows indicating the chain motion)

As an answer to the question why these functionalized brushes do not form aggregates with themselves, the following explanation is suggested (Fig. 8.5.4.): the driving force for ionic self-assembly is the electrostatic attraction of the oppositely charge species. However, the charged particles have, depending on their size, a certain thermal diffusivity. For the negatively charged latex particle the diffusivity is low, and the charged TEM grids do not diffuse at all. Thus, these surfaces may be considered as ‘static’. The negatively charged side chains of the functionalized brush, on the other hand, are more mobile. In addition to the diffusion of the whole brush through the solution, the side chains can adopt a large number of conformations, i.e. they are moving continuously. Thus, the polymer brush has a ‘dynamic’ surface. This thermal motion of the side chains counteracts the electrostatic attraction between the side chains and the end groups – they are hustled away all the time. Consequently, the end groups attach preferentially to the ‘static’ latex particles or the TEM grids.

8.6. Conclusion

It has been demonstrated in the previous sub-chapters that our simplified model polyelectrolyte brushes are able to mimic the proteoglycane molecules and thus are a suitable components for a ‘first approximation’ model of the proteogylcane-hyaluronic acid aggregate.

For further synthetic attempts to model the proteoglycan-hyaluronic acid complex, the following strategies are possible:

- With the present system, complexation experiments with linear, negatively charged poly(para-phenylene micellles) particles could further prove the ability of these molecules to attach to negatively charged entities. With this model complex, rheological investigations could be carried out to examine the difference of the mechanical properties of simple brushes and the model complex.
- More emphasis can be put on the synthesis of the linker molecule. Like the natural archetype, such a molecule must have an inner and an outer side. The outer side further prevents unwanted aggregation, while the inner side carries the desired positive charges.
- Even though the proteoglycan-hyaluronic acid complex is a polyelectrolyte complex, the structure could be modeled by first building up a ‘brush of brushes’ from a less complicated monomer, e.g. styrene, using the above used linker for complexation to an anionically charged polymer. Once the ‘brush of brushes’ architecture has been established, and the relevance of this special architecture for the mechanical properties is investigated, the additional complication of a more complex linker and a charged monomer could be tackled. By careful polymer analogous sulfonation, the desired polyelectrolyte structures could be obtained.

Due to time limitations, this cannot be attempted in this work.

9. Macromonomer Approach

9.1. Macromonomers – General Synthetic Strategies

Macromonomers, an abbreviation for 'macromolecular monomers', are polymeric or oligomeric compounds that contain a polymerizable group at one chain end. Their molecular weight usually ranges from 1000 to 10 000 g/mol. Polymerization of a macromonomer yields polymer brushes with predetermined branching densities[179]. The first macromonomer was synthesized by ICI researchers in the 1960s by end functionalization of poly(lauryl methacrylate) with glycidyl methacrylate[180]. Commercially available macromonomers, sold under the trade name of 'macromer', were introduced by Milkovich et al., who produced poly(styrenes) and poly(isoprenes) via anionic polymerization[181]. These were end functionalized by quenching the living anion, giving macromonomers with vinylic, hydroxyl or vinylbenzyl end groups.

Macromonomers can be obtained by different synthetic strategies. The most common ones are (**I**) end-capping of a living polymer with a reagent carrying a functional group or (**II**) initiation of a living polymerization with an initiator carrying a functional group. The introduced functional groups can also be modified by polymer analogous reactions after the polymerization to introduce the desired polymerizable unit. The obtained end-functionalized macromonomers can be converted into polymer brushes via free radical polymerization[182,183], anionic polymerization[184], or by polyaddition and polycondensation reactions. The first macromonomers carrying a functional group that could be polymerized by Suzuki polycondensation were introduced by Cianga and Yagci[185,186,187,188]. These macromonomers carried an aromatic unit with either two bromine atoms or two boronic ester groups. Stoichiometric combination of these two macromonomers under Suzuki polycondensation conditions resulted in a polymer brush with a conjugated backbone.

9.2. Styrene Sulfonate Esters

9.2.1. Polymerization of Styrene Sulfonate Esters

The chosen monomers for this work, styrene sulfonate ethyl ester (polar) and dodecyl ester (non-polar), cannot be polymerized by anionic polymerization. It has been reported by Whicher and Brash[189] that various styrene sulfonic esters do not homopolymerize well by anionic polymerization. For the n-propyl ester, M_n was up to 7 000 g/mol (GPC, THF, calibrated with polystyrene) for polymers with decent polydispersities (1.06-1.25). Higher molecular weights (up to 20 000 g/mol) could be obtained at the expense of broad polydispersities (up to 2.9). In all cases, the conversion was low (typically 10%). The authors attribute the difference in polymerization behavior of these monomers as compared to styrene to the complexation of the living anion to neighboring sulfonate ester groups, yielding a dormant anionic species. Therefore, anionic polymerization cannot be applied to obtain macromonomers via end-capping. It is also not desirable for macromonomers functionalized by initiation due to restrictions in the attainable chain length and conversion.

Woeste[190] reports that homo- and copolymers from poly(styrene sulfonate ethyl ester) can be obtained via free radical polymerization. Further works by Rühe confirm this finding[191]. However, this polymerization method leads to broad polydispersities. As yet, there are no reports in literature on the controlled radical polymerization of styrene sulfonate esters[1].

9.2.2. Monomer Synthesis

The most elegant – yet not the most cost-effective - method to obtain styrene sulfonate esters (**SSE**) is a two step synthesis via the silver salt[190] (Fig. 9.2.2.1.). The monomer could only be obtained in small quantities. Literature procedures yield approximately 5 g, up-scaling to 15 g was possible. Further up-scaling to 25 g batches led to drastic decreases in the reaction yield. Since 2005, the monomer is commercially available.[192] Styrene sulfonate dodecyl ester can be obtained via the same synthetic procedure.

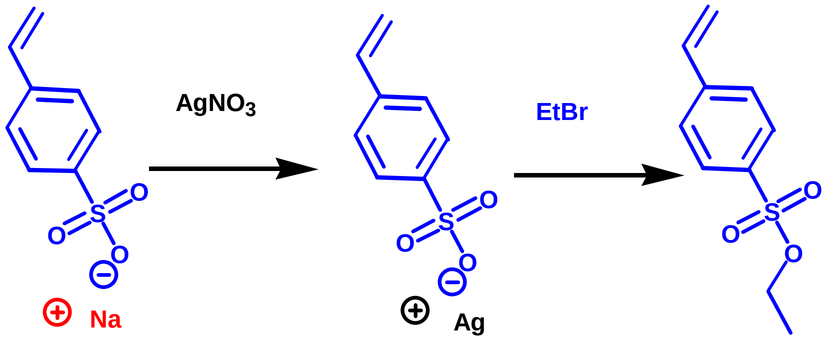

Fig. 9.2.2.1.: **SSE** monomer synthesis

---

[1] A very recent paper describes the polymerization of styrene sulfonate neopentyl ester – see reference 176)

9.2.3. Macromonomers from Styrene Sulfonate Ethyl Ester

The aim was to obtain relatively monodisperse macromonomer samples. To obtain this with the methods available for styrene sulfonate esters, free radical polymerization cannot be used, but anionic polymerization and controlled radical polymerization generally fulfill this requirement. As anionic polymerization is leads only to the formation of oligomers for this monomer, controlled radical polymerization will be attempted. This rules out the option of functionalization by termination. To obtain polymer chains with definitely one and only one functional group per chain, functionalization by initiation was employed. From the three general methods that are available (SFRP, ATRP and RAFT), ATRP seemed to be the most promising one, as there are a wide variety of copper(I) salts and ligands commercially available. By this, a good tuning of the reactivity of the system can be achieved. Also, ATRP reactions proceed at milder temperatures than the corresponding SFRP reactions. For ATRP, the initiator has to fulfill the following requirements: (**I**) the compound must carry a functional group that, when cleaved homolytically, looks very similar to the monomer radical and (**II**) the decomposition of this functional group must occur at the desired reaction temperature to ensure efficient and quantitative initiation, and (**III**) the cleavage must be reversible, such that the dormant Initiator-Cu(I)-Br complex can be formed, which allows good control over the reaction kinetics. Furthermore, to obtain a macromonomer, the initiator must carry a functional group that is polymerizable, leading to the desired polymer brushes. Yet this functional group must be stable at the given polymerization conditions. This excludes any functional group containing a C-C double bond (vinylic, acrylic etc.). Therefore, an initiator has been chosen that will yield a macromonomer that can undergo Suzuki polycondensation, as the functional group needed for this reaction (an aromatic bromine atom) is inert at the given ATRP reaction conditions. For Suzuki polycondensation, a halogen atom at an sp^2 hybridized reaction site and a boronic acid ester (also at a sp^2 hybridized carbon atom) are necessary. They can be either on the same molecule (AB-monomer), giving a macromonomer that can be homopolymerized, or two each on two different monomers (AA-monomer and BB-monomer) that can be copolymerized. These synthesis of two suitable initiators is described in section 9.3..

9.3. ATRP Initiator Synthesis

Figure 9.3.1. shows the synthesis of the initiator for the AA-macromonomer according to literature procedures[193]: The target molecule, 2,5-dibromo-1,4-(bromomethyl)benzene, carries two benzylic bromine functionalities for ATRP initiation and

two aromatic bromine functionalities for Suzuki polycondensation. It was obtained by bromination of commercially available 2,5-dibromo-p-xylene with N-bromosuccinimide.

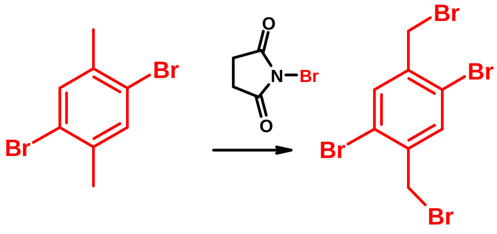

Fig. 9.3.1.: Synthesis of the AA macroinitiator

The corresponding starter for the AB-macromonomer with two benzylic bromine functionalities for ATRP initiation, one aromatic bromine functionality and one aromatic boronic acid ester for Suzuki polycondensation was synthesized from 2,5-dibromo-p-xylene in a two step reaction (Fig. 9.3.2.). In the first step, 2,5-dibromo-p-xylene was reacted with *n*-butyl lithium (halogen-metal exchange). Upon addition of 2-isopropoxy-4,4,5,5-tetramethyl-1,3,2-dioxaborolane, the desired boronic ester was formed[194]. In the second step, the ester was brominated with N-bromosuccinimide (as above).

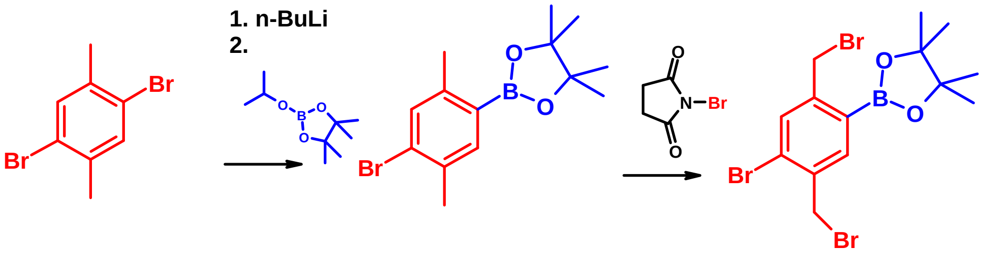

Fig. 9.3.2.: Synthesis of the AB macroiniator

9.4. *Synthesis of the AA-Macromonomer via ATRP*

9.4.1. AA Macromonomer Synthesis and Characterization

Cianga and Yagci[184] used the above described AA-initiator (1,4-dibromo-2,5-bromomethylbenzene) for the polymerization of styrene (Fig. 9.4.1.1.). This could be reproduced (narrow molecular weight distribution, M_n = 5 000 g/mol). The polymerization was carried out at 110°C in bulk, with copper(I) bromide and N-N'-bipyridine as catalyst system. The initiator could be successfully removed by precipitation into methanol, followed by repeated filtration through SiO_2 (in THF) to remove the remaining copper.

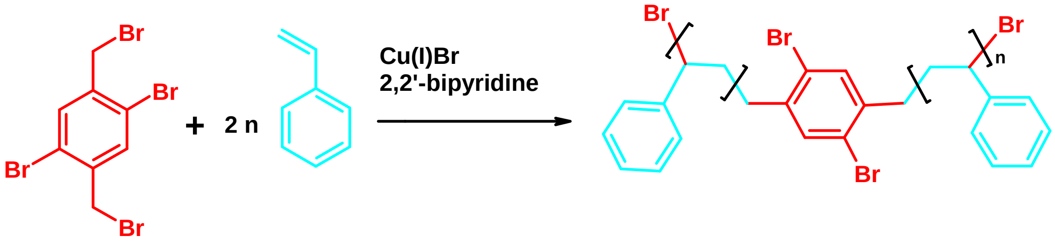

Fig. 9.4.1.1.: Styrene AA macromonomer

The same procedure was applied to obtain styrene sulfonate ethyl ester macromonomers (**PSSE** macromonomers, Fig. 9.4.1.2.). The ratio of the reagents (Starter : CuBr : bipyridine) was 1 : 2 : 4. At 110℃, the polymerization was very rapid and exothermic, yielding a hard, brittle polymer that was insoluble in any solvent. As styrene sulfonate ethyl ester is usually soluble in acetone, acetonitrile, N,N'-dimethylformamide and dichloromethane, this indicates that the reaction was poorly controlled due to the high reaction temperature and a cross linked product was formed. At lower temperature (60℃), styrene sulfonate ethyl ester could be polymerized with a unimodal and relatively narrow molecular weight distribution. The resulting polymer was soluble in DMF. Analysis by GPC (GRAM column, DMF, calibrated with poly(styrene)) indicated that no homopolymer was formed. However, the molecular weight range aimed at (M_n = 2 000 g/mol, n $\approx$ 9) was not obtained. The polymer was larger by a factor of approx. 4. The reaction medium was inhomogeneous – the monomer added was scarcely enough to wet all of the solid components of the reaction mixture (initiator and catalyst complex). Therefore, solution polymerization was attempted.

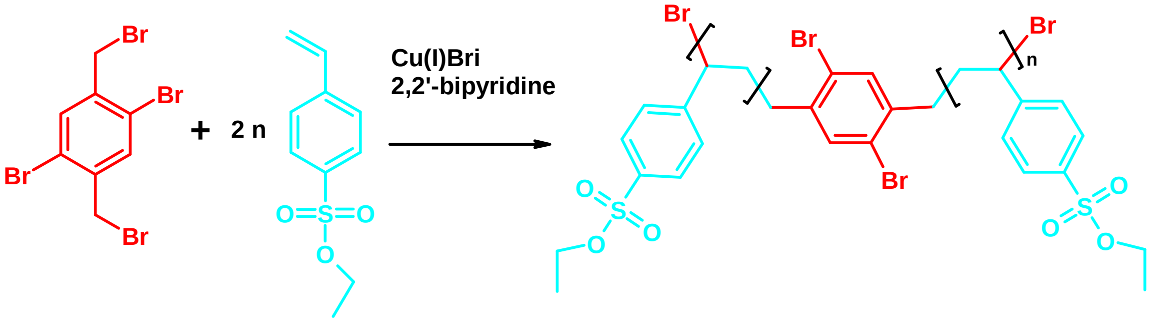

Fig. 9.4.1.2.: **PSSE** AA Macromonomer Synthesis

The solvents used were benzene, acetonitrile and N,N-dimethylformamide. Polymerization occurred in all there solvents, however the molar mass distribution was broadened, and the yield was low in benzene and acetonitrile (ca. 30 %). Also, the polymerization system was not homogeneous (phase separation). The GPC curve was not monomodal for the polymerizations in acetonitrile and benzene, indicating the formation of homopolymer. Therefore, solution polymerization had no advantage over bulk polymerization. Table. 9.4.1. summarizes the reaction conditions and the results obtained. $M_{n,\ theory}$ was calculated assuming 100 % initiation efficiency and 100 % conversion. $M_{n,\ GPC\text{-}MALLS}$ was calculated from $M_{w,\ GPC\text{-}MALLS}$ and M_w/M_n. For the four bulk polymerizations with similar reaction conditions but different monomer amounts (**PSSE4** to **PSSE7**), the molecular weights obtained from GPC-MALLS were larger by a factor of two than the molecular weights aimed at. Consequently, either initiation was incomplete or Br functionalities were lost during reaction.

Table 9.4.1.: **PSSE** AA-macromonomers

Sample	$M_{n,\ GPC\text{-}MALLS}$ [g/mol]	M_w/M_n	**Solvent**
ATRP 4	-	1.50	-
ATRP 6	-	1.18	-
PSSE1	-	1.43	C_6H_6
PSSE2	17 400	1.51	CH_3CN
PSSE3	17 700	1.84	DMF
PSSE4	13 800	1.38	-
PSSE5	24 400	1.25	-
PSSE6	31 400	1.32	-
PSSE7	36 800	1.29	-

During reaction and work-up, some of the sulfonate ethyl ester groups were hydrolysed. This was observed by ^{1}H-NMR spectroscopy – a second set of vinylic signals from the hydrolyzed monomer, and a signal at approx. 9 ppm from an OH group, appeared (see Fig. 9.4.1.4.). Literature reports that styrene sulfonate alkyl esters are stable to acids, but somewhat labile to basic conditions[195]. The basic contaminations (amines) in DMF, which was used during work-up, were assumed to be the cause for hydrolysis. ^{1}H-NMR (Fig. 9.4.1.4.) confirms the chemical structure of the macromonomer. Peaks assignment is included in Fig. 9.4.1.4.. The triplet at 1.15 ppm and the quartet at 3.42 ppm and 2.7 ppm (blue circles) originate from ethanol impurities, which could not be removed even after several days of drying in vacuum (10^{-3} mbar). The additional peaks at 1.94 ppm and 2.5 ppm correspond to the solvent (acetonitrile) and water. The peaks of the initiator are not visible due to the relatively high molecular weight of the macromonomer.

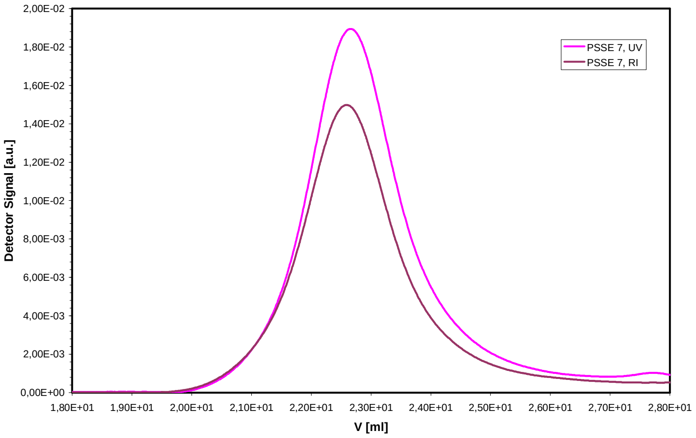

Fig. 9.4.1.3: GPC elugrams (UV and RI signal) of **PSSE 7**

Fig. 9.4.1.3. presents a typical GPC elugram (UV and RI signal) of AA-macromonomer 7. The curve has the shape of a Poisson distribution. It is monomodal, with a M_w/M_n of 1.29.

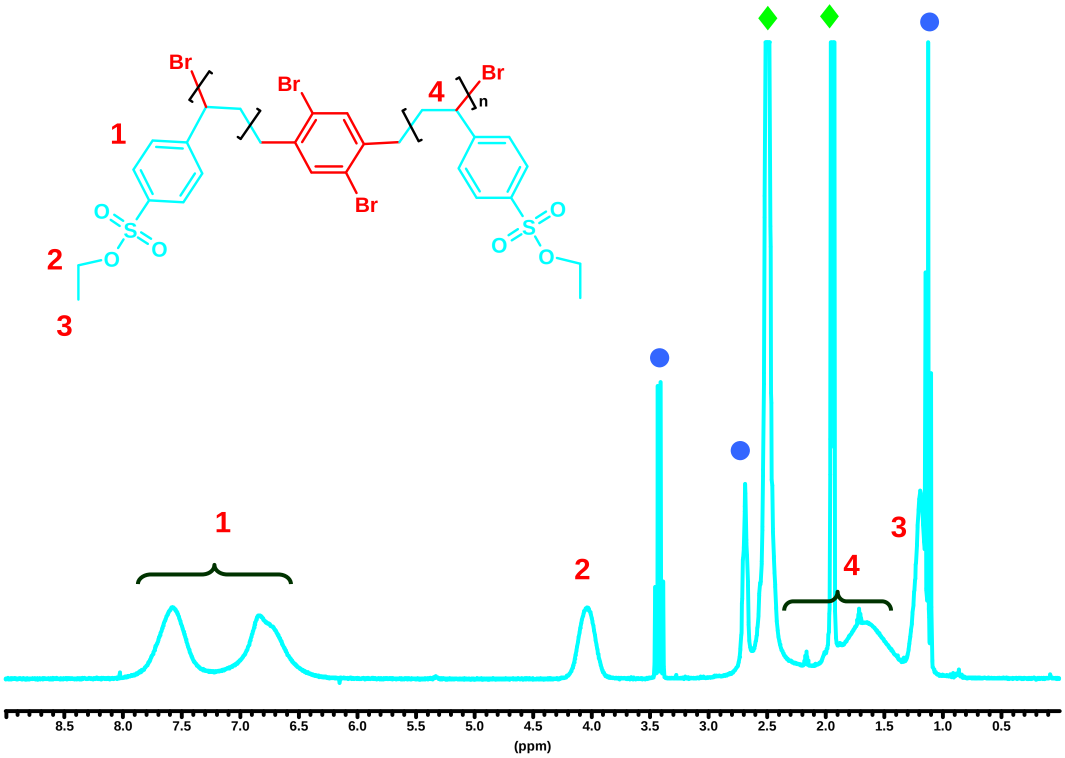

Fig. 9.4.1.4.: ^{1}H-NMR spectrum of macromonomer **PSSE 6**

9.4.2. Bulk Polymerization followed by *In situ* ^{1}H-NMR in solution

To identify the origin of the hydrolysis (reaction or work-up), and to describe the reaction kinetics of macromonomer formation, the reaction was followed by *in situ* ^{1}H-NMR. For that purpose, a mixture of starter : CuBr : bipyridine : monomer = 1 : 2 : 4 : 50 was prepared. The reaction mixture was polymerized in an NMR tube at 60℃. In defined intervals, ^{1}H-NMR spectra were recorded. The monomer conversion was determined by integration and stoichiometric weighting of the vinylic signals versus the signal of the CH_2 group of both monomer and polymer, which was used as a reference constant. Figure 9.4.2.1. shows a plot of styrene sulfonate ethyl ester conversion (in %) vs. time. The curve indicates an exponential consumption of the monomer. From kinetic investigations on the mechanism of ATRP, first order kinetics with respect to monomer concentration are expected[196].

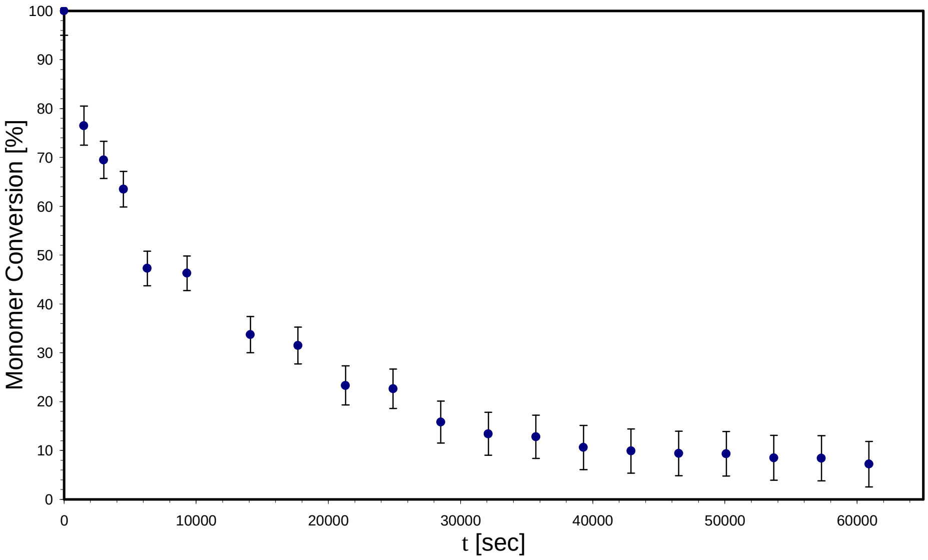

Fig. 9.4.2.1.: **SSE** Monomer conversion versus time (in DMF)

When plotting $\ln \frac{c_t}{c_{t=0}}$ vs t (Figure 9.4.2.3.), a linear dependence is observed at low conversions, while a deviation from linearity is found at higher conversions. A closer look on the individual ^{1}H-NMR spectra reveals the origin of that deviation. In Fig. 9.4.2.2., the spectrum of the initial reaction mixture (t = 0, top) and of the reaction mixture at the end of the reaction (t = 61 000 sec, bottom) are shown. In the second spectrum, a second set of vinylic protons appears (red arrows), as well as an acidic proton at 9 ppm (green rhomb). Also, a triplet and a quartet of the hydrolysis product, ethanol, appear (blue circles). This indicates that the monomer decomposes during solution polymerization in DMF. From the gradient of the curve fit in Fig. 9.3.2.3., the first order rate constant for the polymerization of styrene sulfonate ethyl ester was determined as 5.5 · 10^{-5} s^{-1}.

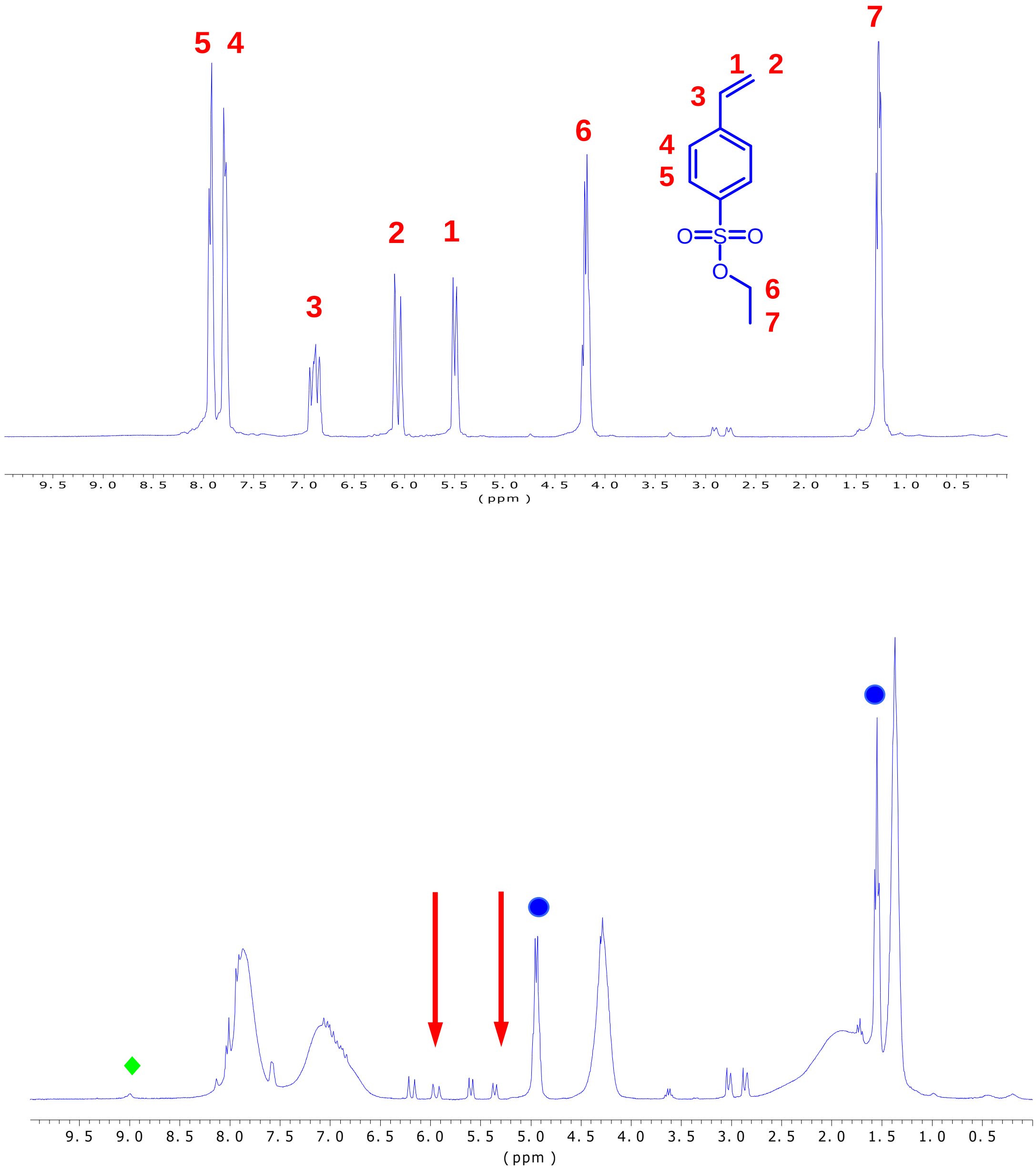

Fig. 9.4.2.2.: **SSE** polymerization in DMF, ***t*** = 0 (top), ***t*** = 61 000 s (bottom)

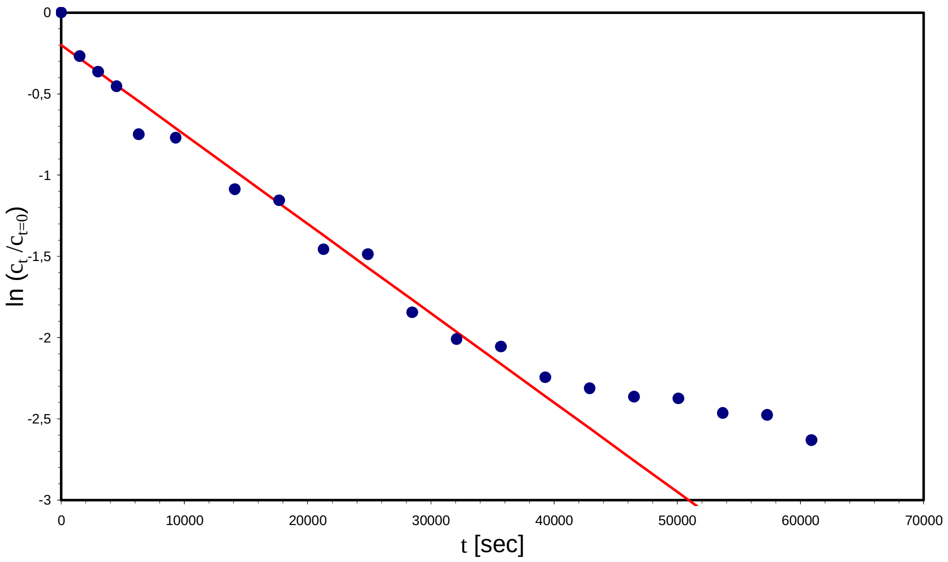

Fig. 9.4.2.3.: Plot of ln (c_t/c_0) versus time, fit (red) to the linear part of the curve

9.4.3. Bulk Polymerization followed by *In situ* solid state ^{1}H-NMR

As described above, polymerization in solution gives results inferior to bulk polymerization. The kinetics of the bulk polymerizaton could not be followed by *in situ* solution NMR, as the reaction medium became too viscous, making proton relaxation too slow on the timescale of the experiment. Therefore, the reaciton kinetics of the bulk polymerization was followed by solid state ^{1}H-NMR. The reagents (starter : CuBr : ligand : monomer = 1 : 2 : 4 : 5 - 100) were put into a TiO_2 rotor and frozen until use. Spectra were recorded in intervals of 5 minutes. In a test experiment with low monomer concentraton (5 eq, T = 60℃; Fig. 9.4.3.1.), the consumption of the initiator was demonstrated: the peak at 4.5 ppm in Fig. 9.4.3.1. at t = 0 (red arrow) corresponds to the benzylic protons of the initiator. This peak is not present in the following spectra (Fig. 9.4.3.2., 2D contour plot of all spectra plotted versus time). It can be therefore concluded that the initiation step is quick and quantitative. Also, there is no indication of a second set of vinylic protons in the spectra – therefore, no monomer decomposition occurs in bulk polymerization. The experiment was repeated with higher monomer concentration (Starter : CuBr : Ligand : Monomer = 1 : 2 : 4 : 100). With this reaction mixture, the polymerization was monitored at three different temperatures (T = 45℃, 60℃, 75℃). The results of these experiments are p lotted in Fig. 9.4.3.3.-9.4.3.4. (for each temperature, individual ^{1}H-NMR spectra at different reaction times).

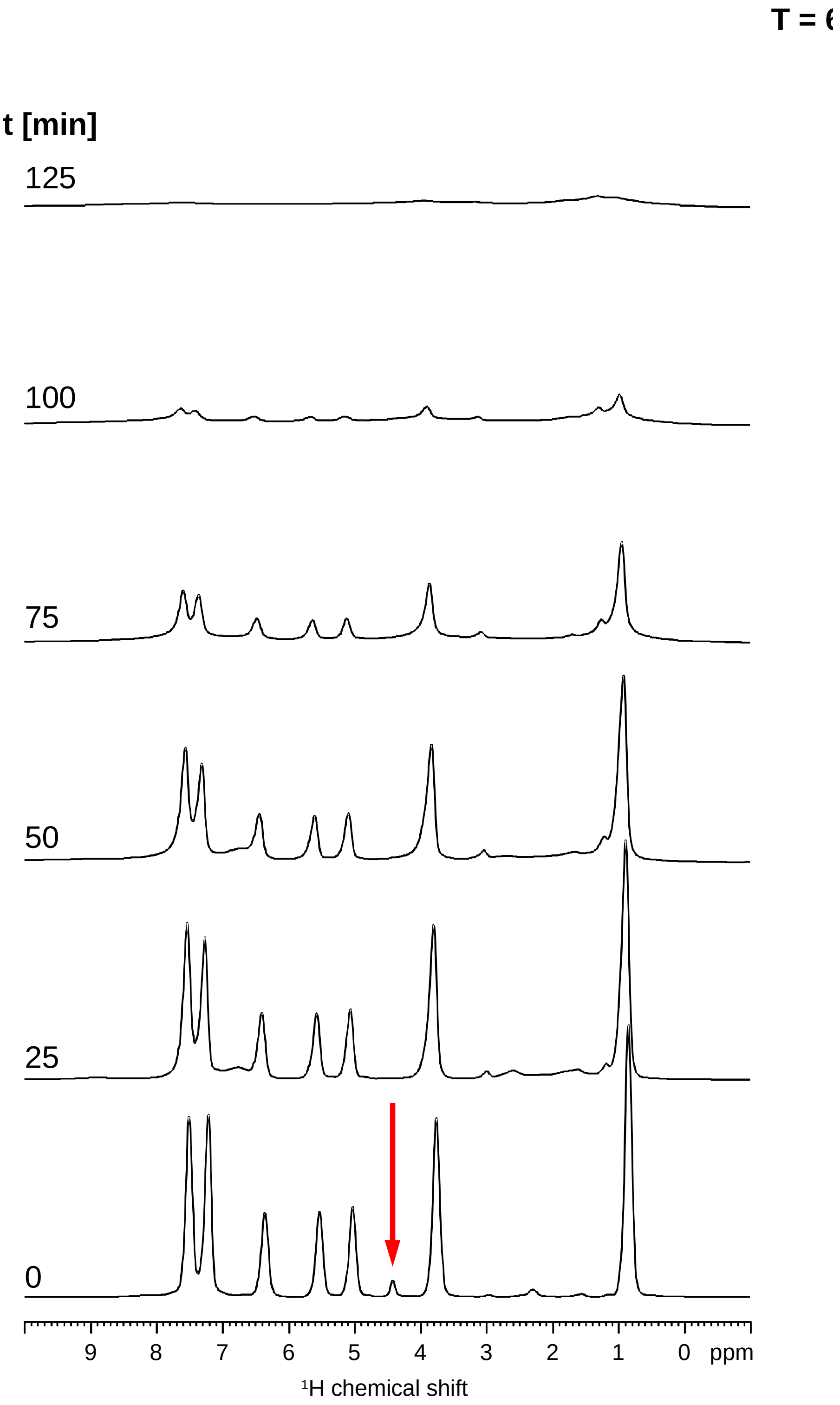

Fig. 9.4.3.1.: **SSE** polymerization in bulk

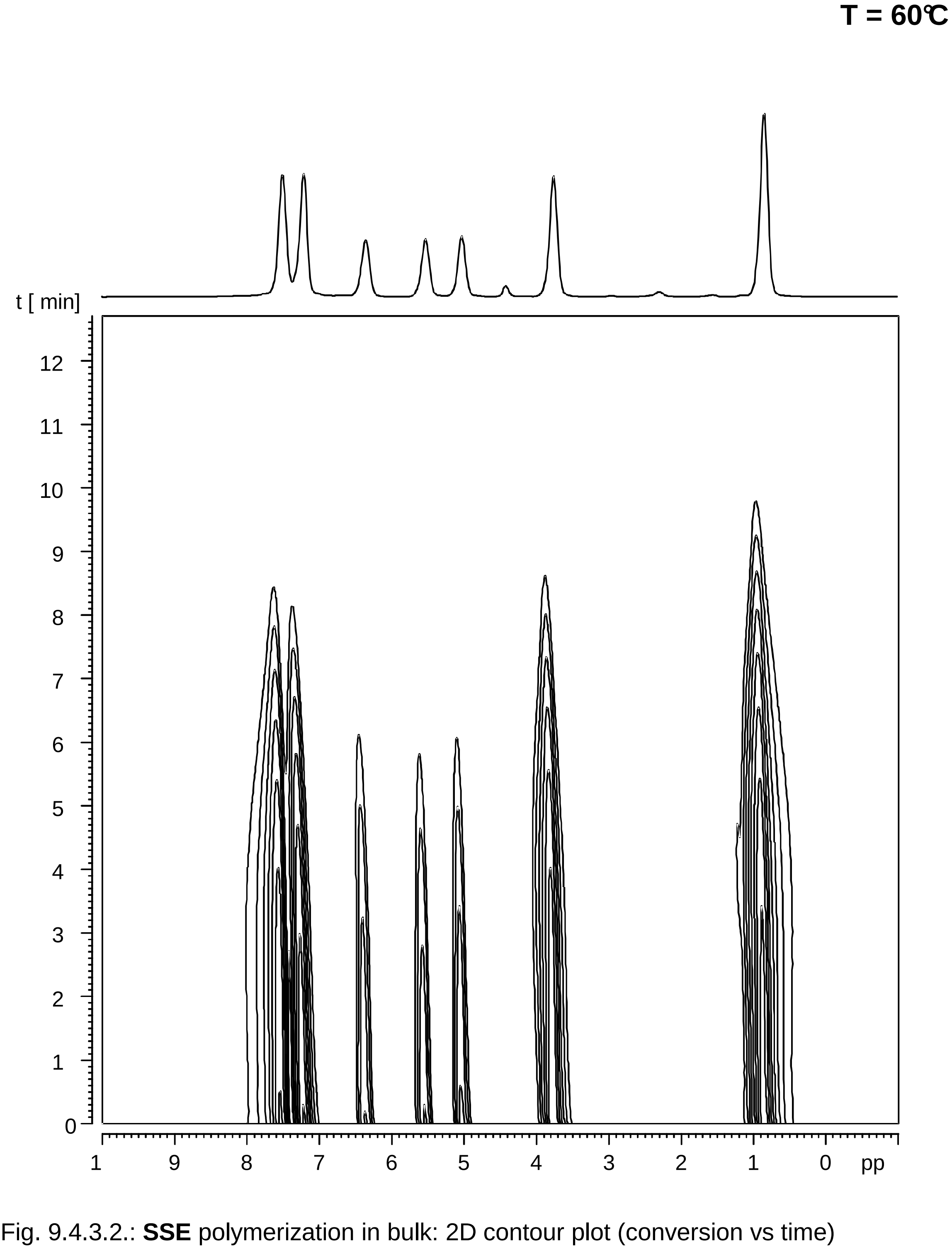

Fig. 9.4.3.2.: **SSE** polymerization in bulk: 2D contour plot (conversion vs time)

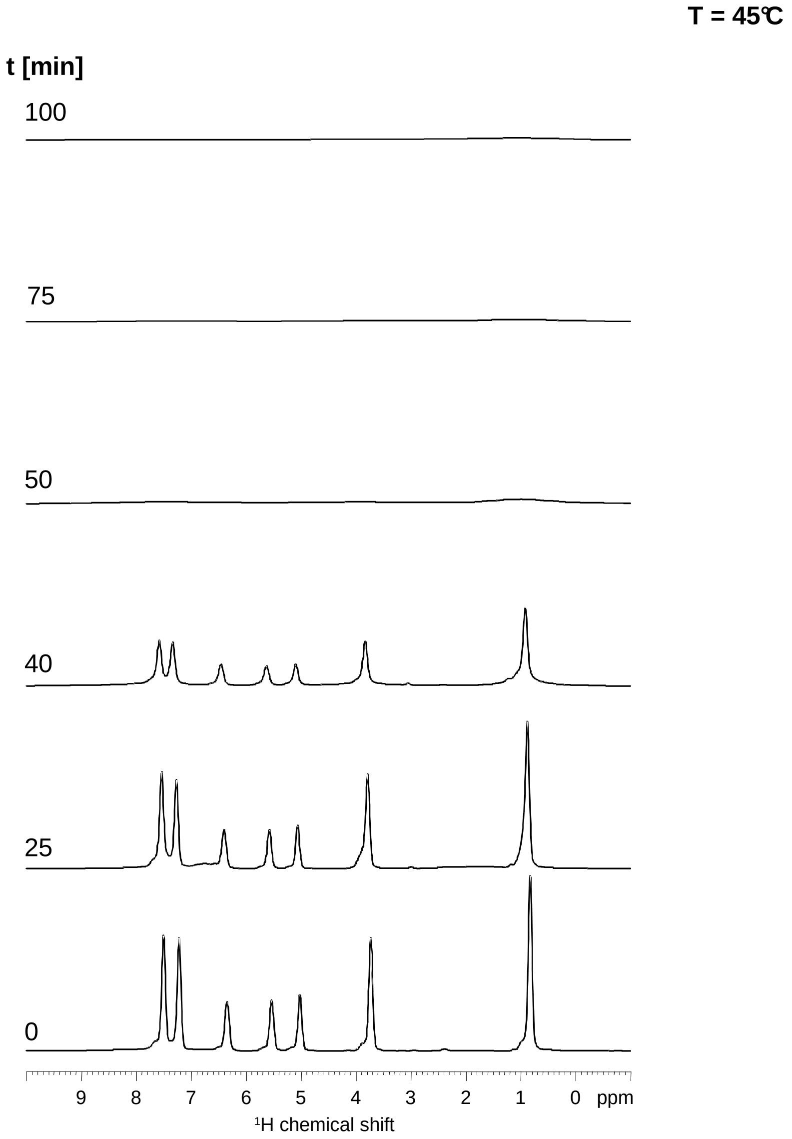

Fig. 9.4.3.3.: **SSE** polymerization in bulk: 45℃

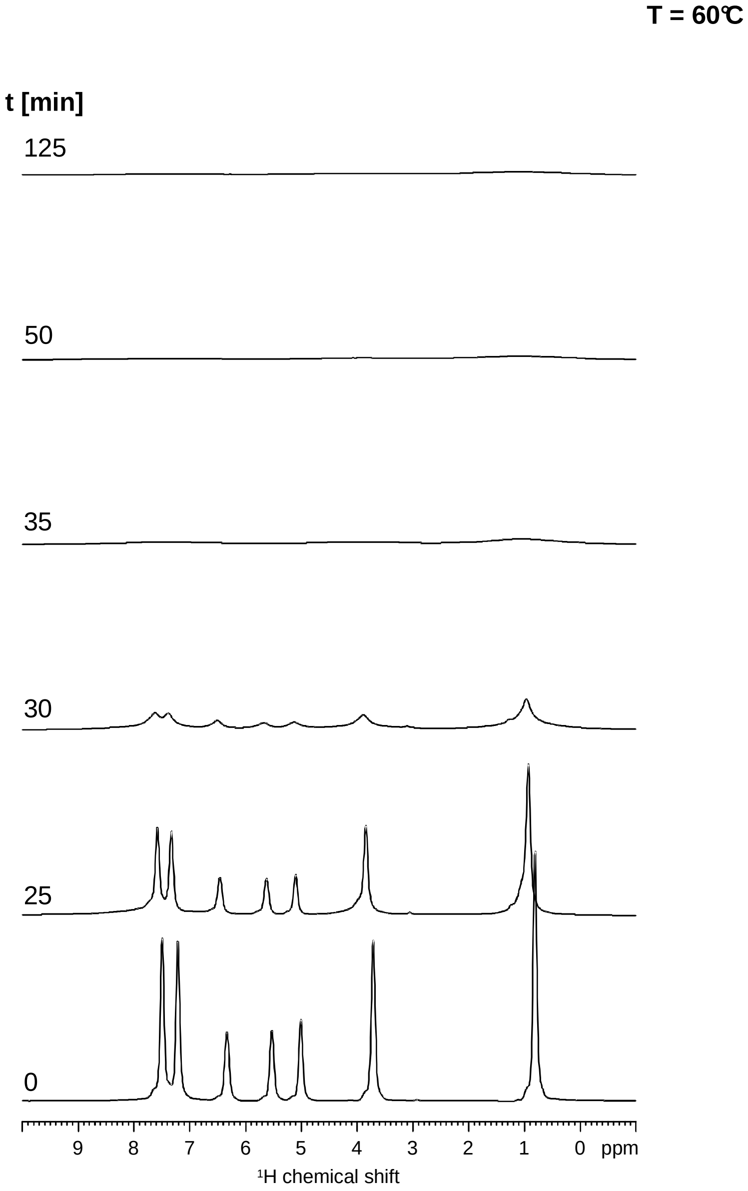

Fig. 9.4.3.4.: **SSE** polymerization in bulk: 60℃

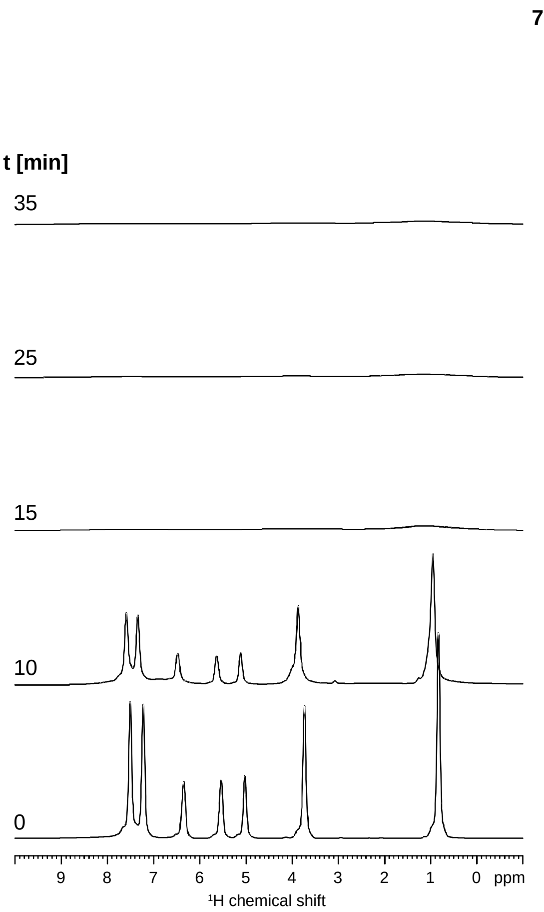

Fig. 9.4.3.5.: **SSE** polymerization in bulk: 75℃

As in the pervious experiment, the monomer conversion was determined by integration and stoichiometric weighting of the vinylic signals vs the signal of the CH$_2$ group of both monomer and polymer. In Fig. 9.4.3.6., the normalized monomer concentration (c_t/c_0) at three temperatures is plotted versus time. From these curves, it can be seen that there are two regimes: after a – roughly – linear part, the monomer concentration decreases exponentially, as has been observed for solution polymerization. It is striking that the transiton between these two regimes occurs at similar conversions (56 – 66 % conversion). One possible explanation for this finding is that, due to the lack of stirring in the NMR rotor, monomer cannot diffuse sufficiently fast to the reactive sites - the reaction is diffusion controlled in the first regime. At a certain conversion, the reactive sites are better approachable, and the reaction proceeds with its expected first order kinetics. In Fig. 9.4.3.7.-9.4.3.9., the second part of the curves are fitted with an exponential function. In all curves, there is a systematic deviation from the exponential fit at high conversions. This is attributed to instrumental deficiencies: as the signal peaks become broader at higher converions, it becomes increasingly difficult to discriminate between the background noise and actual peak signals. Therefore, the measured values were larger than expected at high conversions.

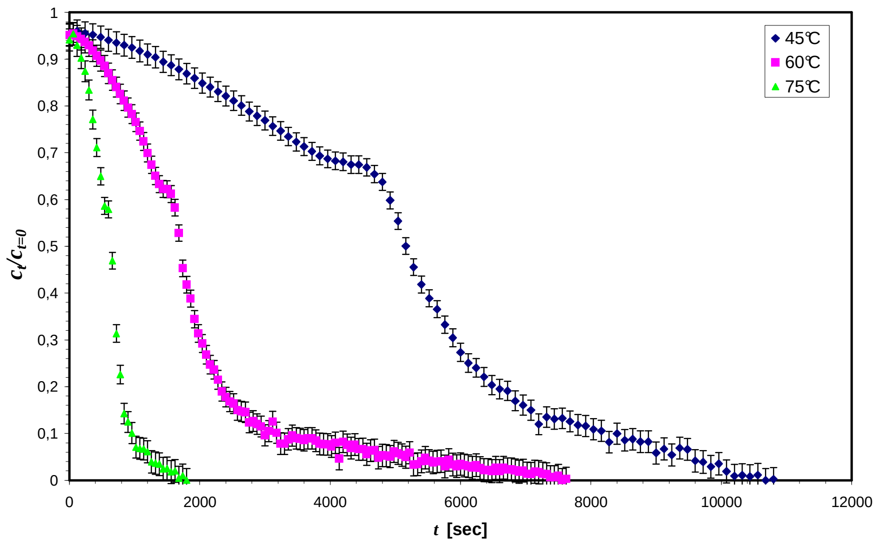

Fig. 9.4.3.6.: Plot of the normalized monomer conversion versus time

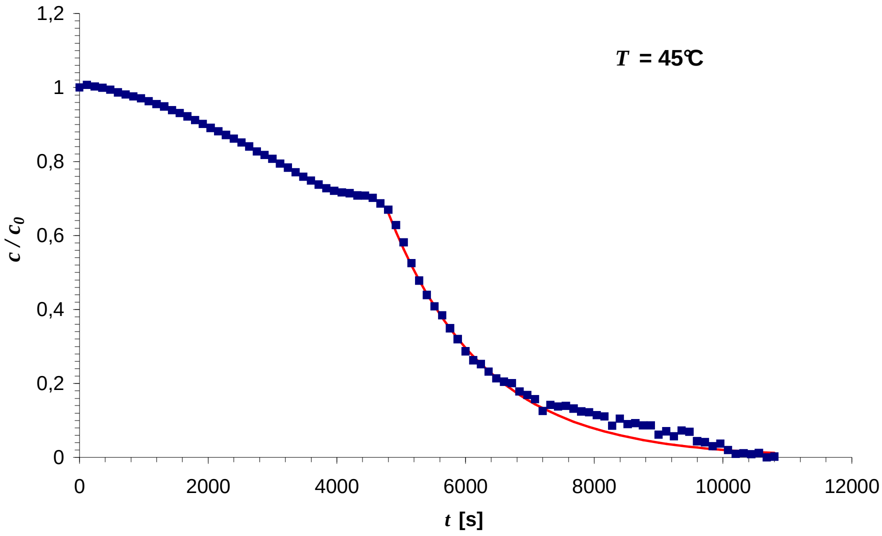

Fig. 9.4.3.7: Monomer consumption at ***T*** = 45℃

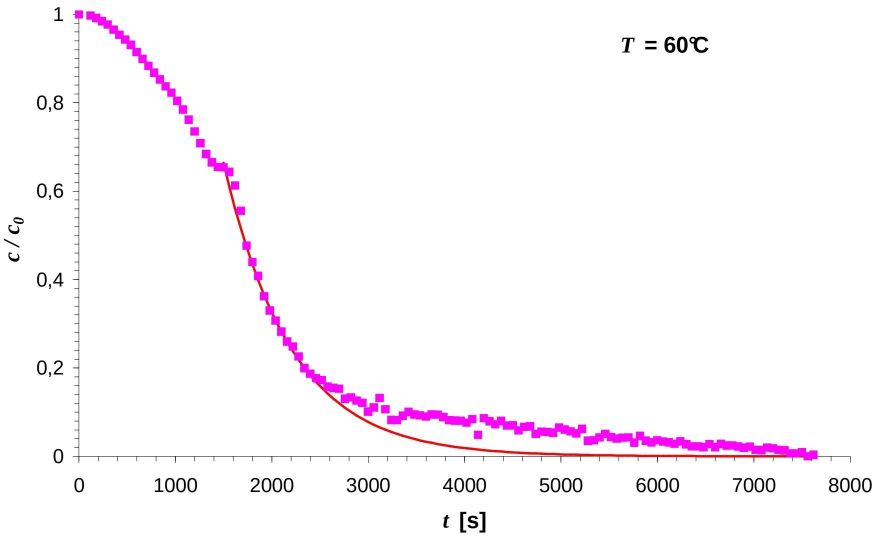

Fig. 9.4.3.8: Monomer consumption at ***T*** = 60℃

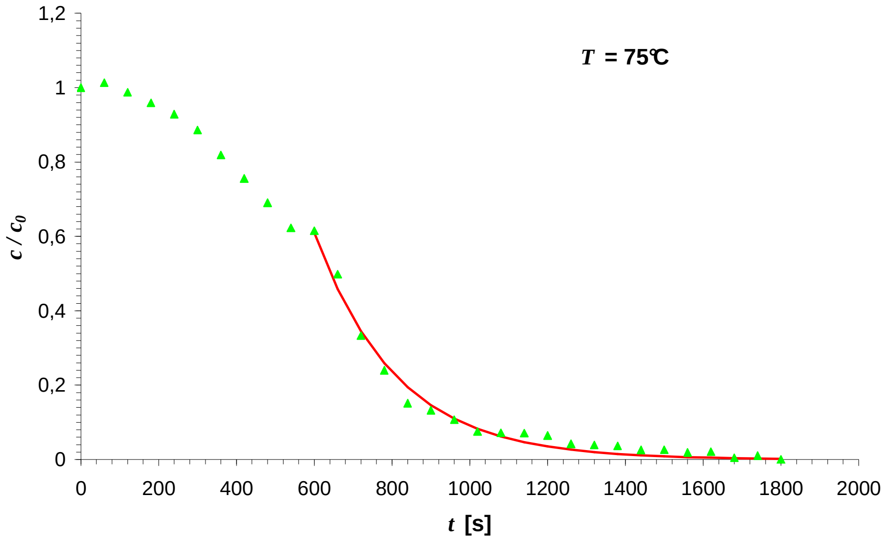

Fig. 9.4.3.9: Monomer consumption at T = 75℃

Fig 9.4.3.10 summarizes the reaction rates determined from Fig. 9.4.3.7.-9.4.3.9. From an Arrhenius plot, the activation energy of the reaction was determined as 60.1 kJ/mol.

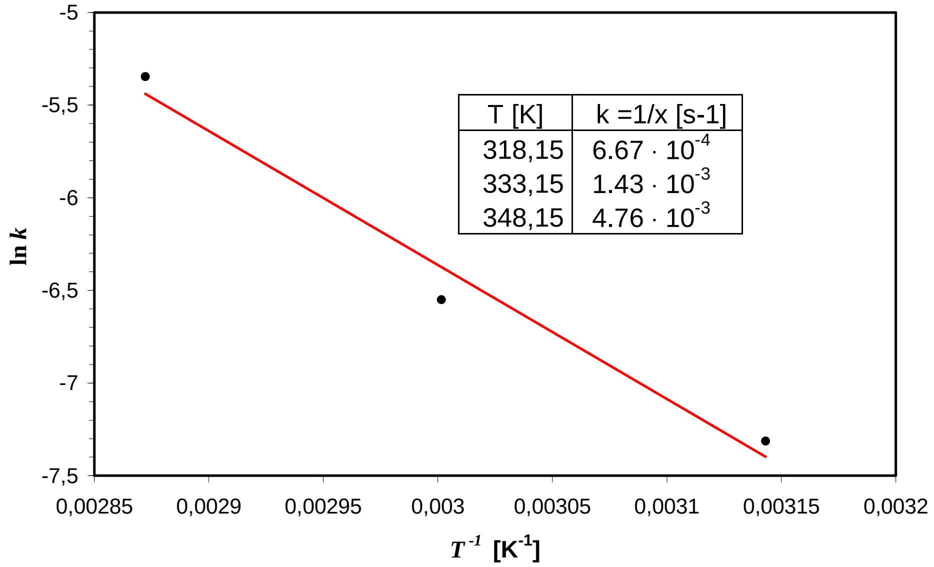

T [K]	k =1/x [s-1]
318,15	$6.67 \cdot 10^{-4}$
333,15	$1.43 \cdot 10^{-3}$
348,15	$4.76 \cdot 10^{-3}$

Fig. 9.4.3.10.: Activation energy of styrene sulfonate ethyl ester polymerization: Arrhenius Plot

9.4.4. Reaction work-up and Copper removal

After the reaction, the AA macromonomers were contaminated by the dark brown catalyst-ligand system. As discussed in the literature[197], copper removal from ATRP systems with polar monomers and polar solvents is not trivial. The reaction mixture, a brown-green viscous substance, was only soluble in acetone, DMF and acetonitrile. Purification was attempted by column chromatography first on neutral Al_2O_3, then on SiO_2, with DMF and acetonitrile as an eluent. In both solvents, a certain amount of the Cu species was not held back by the column material due to the solvents' strong ligand properties. A greenish brown solution was obtained. To remove cooper completely, the solution was passed over an ion exchange column. However, many ion exchange column materials disintegrate upon treatment with organic solvents, therefore the material must be carefully conditioned with the desired solvent – otherwise, the sample will be contaminated with the column material, which can be observed as a high molecular weight peak in GPC-MALLS analysis that was not present prior to the ion exchange. The mildest solvent with respect to the column material is acetone, which is also the weakest ligand for copper. Therefore, acetone was used as an eluent for ion exchange. Suitable column materials were Amberlyst 15 (Fluka) and DOWEX MSC-1 (Fluka).

9.5. Synthesis of the AB-Macromonomer via ATRP

The same procedure as for the AA-Macromonomer was applied for the polymerization of styrene sulfonate ethyl ester with an AB starter (Fig. 9.5.1.). At a reagent ratio of initiator : CuBr : bipyridine = 1 : 2 : 4 and 60℃, the monomer could be polymerized with narrow molecular weight distribution (see Table 9.5.1.). Again, the molecular masses obtained were much higher than the molecular masses aimed at.

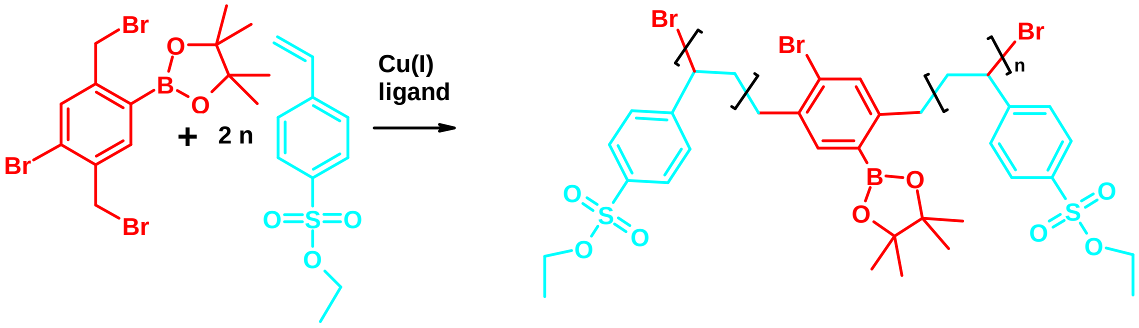

Fig. 9.5.1.: Synthesis of the AB-macromonomer

Table 9.5.1.: **PSSE** AB-macromonomers

Sample	$M_{n,\ theory}$ [g/mol]	$M_{n,\ GPC}$ [g/mol]	$M_{n,\ GPC\text{-}MALLS}$ [g/mol]	M_w/M_n
PSSEAB 1	8640	15100	16 500	1.61
PSSEAB 5	5550	11 900	-	1.26
PSSEAB 6	3010	9 800	7 700	1.48
PSSEAB 7	1320	11 000	16 000	1.31

9.6. Macromonomer Hydrolysis

Before polymerization, the AA- and AB-Macromonomers were hydrolyzed in DMF with a large excess (10 eq) of aqueous KOH. After dialysis to remove the excess salt, the samples were freeze-dried from water. However, as already mentioned by Woeste[190], traces of DMF remained in the samples that could not be completely removed, not even by repeated freeze-drying.

Fig. 9.6.1. shows ^{1}H-NMR spectra (300 MHz, D_2O) of the purified hydrolysed macromonomers. In the top spectrum (AA macromonomer), the two peaks from 8.0 – 6.0 ppm can be assigned to the protons of the aromatics in styrene sulfonate, whereas the peak between 2.4 and 0.5 ppm is from the aliphatic protons of the polymer backbone. The sharp signal at 2.5 ppm is assigned to the four benzylic protons of the initiating unit. This proves that the AA-starter was incorporated into the polymer, as the signal of these benzylic protons (next to Br) at 4.45 ppm vanished completely. Consequently, the polymer obtained did not form by spontaneous polymerization, but by ATRP initiation. In the spectrum of the AB macromonomer (Fig. 9.6.1., bottom), the polymeric peaks are also present and are assigned analogously. As can be seen in the enlargement of the spectrum there are two peaks of equal intensity at 2.83 ppm and 2.68 ppm. These values are close to the position of the aromatic CH_3 group in the non-brominated AB-starter precursor (see centre molecule in Fig. 9.3.2.) at 2.2 ppm and 2.4 ppm and are therefore assigned to be the two different benzylic protons (next to bromine and the boronic acid, respectively) of the initiating group. Additional peaks at 0.7 ppm (triplet) and 2.9 ppm (quartet) are due to impurities from ethanol that was cleaved off during the ethyl ester hydrolysis. The peak of the methyl groups form the boronic ester of the initiating unit (see Fig. 9.5.1.) could not be assigned. It is likely that this group did not survive the hydrolysis, i.e. boronic acid was formed. Both spectra clearly prove that – within the analytical limit of the method – the ester hydrolysis was complete. Table 9.6.1. summarizes the GPC results for the hydrolyzed AA- and AB

macromonomers. In all cases, the polydispersities found are bigger than the polydispersities measured for the neutral precursor molecules. This indicates that, besides the size-exclusion based separation of the molecules, some enthalpic interactions with the column material occurred, leading to a broadening of the molar mass distribution.

For the hydrolyzed macromonomers, the GPC results are in much better agreement with the predicted molecular weights that for the styrene sulfonate ethyl ester macromonomers. This is due to the fact that for the PSS macromonomers (K^+ form), the standard used for calibration was the sodium salt of styrene sulfonate, which does not differ much in hydrodynamic volume from the actual potassium salt. For the **PSSE** macromonomers, the standard used was poly(styrene), which can be expected to have very different hydrodynamic properties that poly(styrene sulfonate ethyl ester).

Table 9.6.1.: GPC results of the hydrolyzed macromonomers (TSK column, PSSNa calibration, H_2O, 10 % acetonitrile)

Sample	T [℃]	$M_{n,\,\mathrm{theory}}$ [g/mol]	$M_{n,\,GPC}$ [g/mol]	M_w/M_n
PSSAB 1	80	7 540	7 000	1.87
PSSAB 2	80	1 530	1 700	1.33
PSSAB 3	80	3 440	3 300	1.67
PSSAB 4	80	3 740	3 200	1.85
PSSAB 5	80	4 850	3 800	1.56
PSSAB 6	80	2 630	2 000	1.38
PSSAB 7	80	1 150	2 800	2.16
PSS 1	80	1 330	-	-
PSS 2	80	2 280	1 300	1.61
PSS 3	80	2 280	540	4.85
PSS 4	80	5 430	4 300	1.71
PSS 5	80	10 480	7 500	2.07
PSS 6	80	19 730	14 300	1.87
PSS 7	80	16 850	12 000	1.75

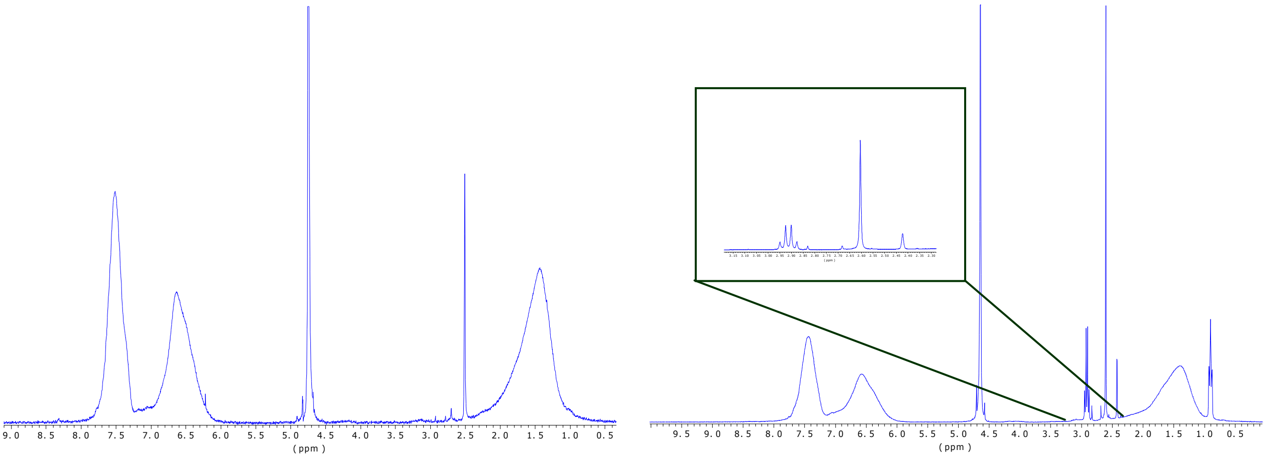

Fig. 9.6.1.: AA-macromonomer PSS 7 (above) and AB-macromonomer PSSAB1 (below)

9.7. *Further Macromonomer Characterization*

For the **PSSE** macromonomers as well as the PSS (K^+ form) macromonomers, MALDI-TOF Mass Spectrometry was attempted. Literature procedures[198] for linear, non-functionalized sodium styrene sulfonate oligomers were applied to the PSS (K^+ form) samples. However, good quality spectra could not be obtained. This is could be due to the sample polydispersities, which were not narrow enough for MALDI-TOF MS, as well as the presence of bromine groups in the molecule, which could lead to halogen loss in the flight phase.

9.8. *Macromonomer Polymerization Attempts*

As Suzuki polymerization takes place in the presence of a base (e.g. K_2CO_3), the **PSSE** and **PSSEAB** macromonomers, which are base labile, cannot be polymerized directly. Instead, polymerization was attempted with the saponified PSS and PSSAB macromonomers. However, there analysis of the reaction products by GPC indicated that no polymerization occurred. Several reasons for this finding are plausible. If traces of copper ions from the ATRP reaction step were still present in the sample, these might interact in the catalytic process, thus impairing polymerization. According to atom absorption spectra, the amount of copper ions in the sample was smaller than 0.5 mass percent. The macromonomers that were successfully polymerized by this method (as described in the literature[185]) were of much lower molecular weight, which, by statistical considerations, makes it more probable that the reactive centres find each other and undergo coupling. Also, these macromonomers were made from poly(styrene), which is non-polar. If the polar sulfonate groups of poly(styrene sulfonate) act as competing ligands for the palladium catalyst, this might also impair the reaction.

9.9. Conclusion

As has been discussed in the previous sections of this chapter, macromonomers from poly (styrene sulfonate ethyl ester) and poly(styrene sulfonate) were obtained, however they could not be polymerized via Suzuki polycondensation. At this point, two alternatives were considered: (**I**) polymerization by a different metal-catalyzed reaction, e.g. by Ullmann coupling or (**II**) synthesis of polyelectrolyte brushes via the macroinitiator approach. The reasons that were suggested in section 9.8. as having prevented Suzuki polycondensation would also affect other metal-catalysed reactions. Additionally, harsh reaction conditions such as those used for Ullmann coupling might lead to polymer decomposition or chain crosslinking, thus yielding structurally imperfect products. From these considerations, the second alternative, the macroinitiator route, was followed to obtain the desired polyelectrolyte brushes. This was described in chapter 7.

10. Conclusion and Outlook

On the pathway to functionalized polyelectrolyte brushes from styrene sulfonate as a synthetic model compound for the proteoglycan-hyaluronic acid complex, the following was achieved:

- ATRP was first applied to the polymerization of styrene sulfonate ethyl ester and styrene sulfonate dodecyl ester. Kinetic parameters of this polymerization reaction were estimated by ^{1}H-NMR.
- New poly(styrene sulfonate ester) and poly(styrene sulfonate) macromonomers were synthesized, however their polymerization was not successful.
- Macroinitiators for the ATRP of styrene sulfonate esters with different chain lengths and initiation site densities from 10 % to 100 % were synthesized.
- Polymer brushes from styrene sulfonate ethyl ester and styrene sulfonate dodecyl ester with varying grafting density, backbone length and side chain length were synthesized and characterized by ^{1}H-NMR, AUC, AFM, TEM, and in the case of the ethyl esters, GPC-MALLS.
- Polyelectrolyte brushes from styrene sulfonate were synthesized from the corresponding esters. These brushes were characterized in solution (GPC-MALLS, static and dynamic light scattering, SANS and ^{1}H-NMR) and on solid interfaces (AFM and TEM). It was shown that these brushes may form huge aggregates in solution. The aggregation behavior and the shape and size of the aggregates depend on the side chain length and the degree of saponification.
- A functionalized ATRP macroinitiator with a positively charged head group was synthesized and employed for the synthesis of functionalized styrene sulfonate polyelectrolyte brushes. These brushes were found to form complexes with negatively charged latex particles and are thus suitable as proteoglycan models in the proteoglycan-hyaluronic acid complex.

Thus, the target structures, both functionalized and unfunctionalized, were obtained and characterized. First conclusions about the influence of molecular parameters such as side chain length and degree of hydrolysis on the molecular shape in solution, as well as the aggregation behavior, were obtained. For more detailed information, a project dedicated solely to the elucidation of this problem would be necessary. Other parameters, such as the influence of grafting density and backbone length, should also be investigated.

The result of the present investigation with respect to the purpose of modeling cartilage may be summarized as follows:

- Poly(styrene sulfonate) brushes derived from poly(styrene sulfonate ester) brushes can only be used as model compounds for proteoglycans if care is taken that the degree of saponification is high (min. 66%) and the side chains are short enough to avoid the building-up of a gradient in the molecule after saponification, as this leads to aggregation due to hydrophobic interactions.
- The functionalized *polymer* brushes were strongly self-aggregating on the pre-polyelectrolyte level due to loss of a few ester groups, forming a solvent-swollen gel. Although this was a major drawback for the formation of well-defined ‘brush of brushes’-like aggregates with the polymer brushes, it yet shows that we are on the right track – this gel-like material, while having only a slightly different chemical structure as compared to the unfunctionalized brushes, shows entirely different mechanical and solution properties.
- The functionalized *polyelectrolyte* brushes have the desired property of attaching to negatively charged entities. All that is left to do is to direct this aggregation tendency towards more organized structures and characterize the resulting materials. Yet this aim, due to the complexity of synthesizing a more suitable linker, is probably another Ph.D.’s work away. For possible applications as cartilage substitutes, care should be taken at a more advanced stage of the project that all materials used are bio-compatible and non-biodegradable.

Some ‘side products’ of this project might be of further interest: the extended and complicated aggregates of the unfunctionalized brushes may be used as templates for the production of nanowires. The gradient brushes, which have been shown to be able to solubilize a water-insoluble organic dye, may be used for delivery of such molecules into hydrophilic, water-containing compartments, i.e. in organisms, for drug delivery. It would be interesting to investigate whether it is possible to trigger the release of such molecules by external stimuli.

11. Summary

Macroinitiators for the ATRP of styrene sulfonate esters with different chain lengths and initiation site densities from 10 % to 100 % were synthesized. Polymer brushes from styrene sulfonate ethyl ester and styrene sulfonate dodecyl ester with varying grafting density, backbone length and side chain length were synthesized and characterized by ^{1}H-NMR, AUC, AFM, TEM, and in the case of the ethyl esters, GPC-MALLS. Polyelectrolyte brushes from styrene sulfonate were synthesized from the corresponding esters. These brushes were characterized in solution (GPC-MALLS, static and dynamic light scattering, SANS, ^{1}H-NMR) and on solid interfaces (AFM and TEM). It was shown that these brushes may form extended aggregates in solution. The aggregation behavior and the size and shape of the aggregates depend on the side chain length and the degree of saponification. For samples with identical backbone and side chain length, but varying degrees of ester hydrolysis, marked differences in the aggregation behavior were observed. A functionalized ATRP macroinitiator with a positively charged head group was synthesized and employed for the synthesis of a functionalized polyelectrolyte brush. These brushes were found to form complexes with negatively charged latex particles and are thus suitable as proteoglycan models in the proteoglycan-hyaluronic acid complex.

12. Experimental Part

12.1. Synthesis

12.1.1. Monomer synthesis:

Styrene sulfonate silver salt, styrene sulfonate ethyl ester and styrene sulfonate dodecylic ester were synthesized as described elsewhere[199].

12.1.2. Macromonomer initiator synthesis:

AA-Macroinitiator (1,4-dibromo-2,5-(α,α'-bromomethyl)benzene; $C_8H_6Br_4$))

The AA-macroinitiator (1,4-dibromo-2,5-(α,α'-bromomethyl)benzene; $C_8H_6Br_4$)) was synthesized after literature procedures[200].

AB-Macroinitiator (1-Bromo-2,5-dimethyl-4-(4,4,5,5-tetramethyl-1,3.2-dioxaboro-lan2yl)benzene; $C_{14}H_{20}BBrO_3$)

The AB-macroinitiator (1-bromo-2,5-dimethyl-4-(4,4,5,5-tetramethyl-1,3.2-dioxaborolan-2-yl)benzene) was synthesized in a two step procedure analogously to a literature procedure for fluorene derivatives[201].

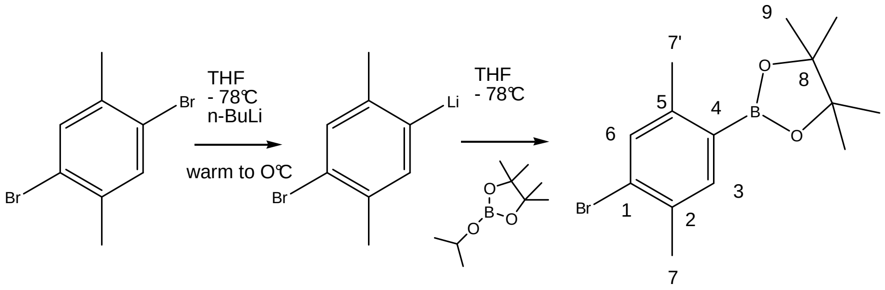

Fig. 12.1.2.1.: AB-macroinitiator synthesis, step 1

1. Step (Fig. 12.1.2.1.): In a three neck flask with septum, reflux condenser and thermometer, 2 g (7.58 mmol, 1 eq) 1,4-bromo-2,4-dimetylbenzene were dissolved in 50 ml THF under argon atmosphere. The solution was cooled to – 78°C and 4.75 ml n-butyllithium (1.6 M in cyclohexane, 7.58 mmol, 1 eq) were slowly added. Upon warming to 0°C, the lithiated species formed. After cooling down to – 78°C, 3.90 ml (3.52 g, 18.95 mmol, 2.5 eq) 2-isopropoxy-4,4,5,5-tetramethyl-1,3,2-dioxaborolane were added. The reaction mixture was warmed to room temperature and stirred over night. It was then poured into water and three times extracted with diethyl ether. After washing the organic extract with brine, it was dried with $MgSO_4$. The solvent was removed under reduced pressure and the crude product was purified by flash column chromatography (silica gel, hexane:CH_2Cl_2 10:1). A colourless liquid was obtained.

Yield:	31 %
^{1}H-NMR ($CDCl_3$, 300 MHz):	7.59 (s, 1H, H at C6), 7.35 (s, 1H, H at C3), 2.46 (s, 3H, H at C7), 2.35 (s, 3H, H at C7’), 1.34 (s, 12 H, H at C9)
^{13}C-NMR ($CDCl_3$, 300 MHz):	144.03 (s, C1), 137.95 (s, C6), 133.95 (s, C2), 133.46 (s, C3), 128.00 (s, C5), 83.57 (s, C8), 24.87 (s, C9), 22.01 (s, C7), 21.31 (s, C7’)
M.S. [a.m.u.]:	309-312:M*, 295-298: M-CH_3, 249-252: M - 4 CH_3, 209-212 M – $C_6H_{12}O$, 192 M – $C_6H_{12}O_2$ (* B-isotopes: ^{10}B,^{11}B, Br-isotopes: ^{79}Br,^{81}Br)

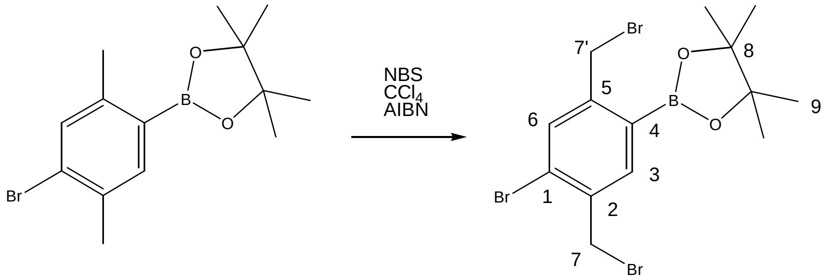

Fig. 12.1.2.2.: AB-macroinitiator synthesis, step 2

2. Step (Fig. 12.1.2.2.): In a three neck flask reflux condenser and thermometer, 500 mg (1.61 mmol, 1 eq) 1-bromo-2,5-dimethyl-4-(4,4,5,5-tetramethyl-1,3.2-dioxaborolan-2-yl)benzene were dissolved in 20 ml CCl_4 under argon atmosphere. 398 mg (4.02 mmol, 2.5 eq) N-bromosuccinimide (NBS) were added. To facilitate radical formation, 6.6 mg (0.04 mmol, 0.03 eq) azoisobutyricacid nitrile (AIBN) were added. Upon refluxing at 90℃, NBS was consumed. The reaction was finished after 4 h, as indicated by the resulting succinimid floating at the CCl_4 sulface. After cooling, succinimid was removed by filtration. The solvent was removed under reduced pressure and the crude product was purified by flash column chromatography (silica gel, hexane:CH_2Cl_2 20:1-8:1). A colourless solid was obtained.

Yield:	70 %
^{1}H-NMR ($CDCl_3$, 300 MHz):	7.86 (s, 1H), 7.61 (s, 1H), 4.81 (s, 3 H), 4.58 (s, 3H), 1.37 (s, 12 H)
^{13}C-NMR ($CDCl_3$, 300 MHz):	146.29 (s, C1), 139.01 (s, C6), 136.33 (s, C2), 134.79 (s, C3), 127.70 (s, C5), 84.31 (s, C8), 32.70 (s, C7) , 31.78 (s, C7’), 24.85 (s, C9)

M.S. [a.m.u.]:	465-472 M*, 386-392 M-Br, 453 M-CH_3, 365-372 M – $C_6H_{12}O$, 307-312 M – 2 Br (* B-isotopes: ^{10}B,^{11}B, Br-isotopes: ^{79}Br,^{81}Br)

12.1.3. Poly(styrene sulfonate ethyl ester) Macromonomer Synthesis and Hydrolysis

AA-Macromonomer Synthesis

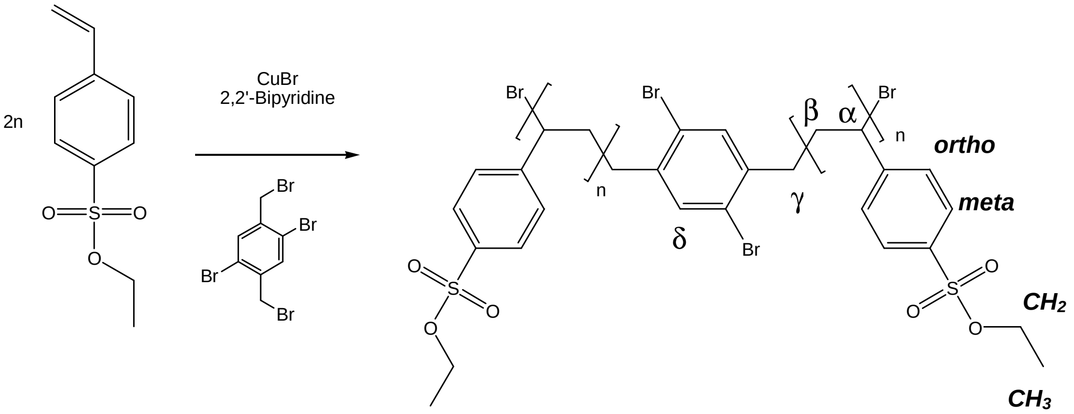

Fig. 12.1.3.1.: AA-macromonomer synthesis

The radical starter, CuBr and the bipyridine ligand were put into a Schlenk tube (ratio 1:2:4) under inert gas atmosphere. The monomer was added through a septum with a syringe. The Schlenk tube was placed in a pre-heated oil bath at 60℃ and left to react for 5 hours. After cooling, the dark brown solid was dissolved in Acetonitrile. The catalyst was removed by ion exchange (Dowex MSC-1, CH_2Cl_2). After filtration, the solvent was removed under vacuum. The polymer was redissolved in acetonitrile and purified by repeated precipitation into methanol. After three precipitations, a colourless powder was obtained.

^{1}H-NMR ($CDCl_3$, 300 MHz):	7.5-8.0 H_{meta}, 6.5-7.5 H_{ortho}, 3.9-4.3 *CH_2*, 2.7 H_γ, 1.4-2.6 (H_α + H_β), 1.3 *CH_3*
MALDI-TOF MS:	molecule could not be ionized and desorbed

GPC and GPC-MALLS (DMF):

Sample	*n* [mmol]				*T* [℃]	$M_{n,\ theory}$ [g/mol]	$M_{n,\ GPC\ RI}$ [g/mol]	$M_{n,\ GPC\text{-}MALLS}$ [g/mol]	M_w/M_n	Solvent
	PSSE	Starter	CuBr	Ligand						
ATRP 4	7.07	0.685	5.06	3.19	110	2 590	41 700	-	1.50	-
ATRP 6	7.74	0.737	3.39	3.20	60	2 650	9 000	-	1.18	-
PSSE1	5.16	1.00	1.39	2.56	60	1 520	4 400	-	1.43	C_6H_6
PSSE2	10.3	1.00	1.05	1.92	60	2 610	2 800	17 400	1.51	CH_3CN
PSSE3	10.3	1.00	1.32	2.43	60	2 610	5 000	17 700	1.84	DMF
PSSE4	13.6	0.498	0.488	0.999	60	6 220	13 800	13 800	1.38	-
PSSE5	13.6	0.249	0.265	0.512	60	12 000	12 200	24 400	1.25	-
PSSE6	13.6	0.130	0.132	0.256	60	22 600	45 300	31 400	1.32	-
PSSE7	11.0	0.124	0.139	0.256	60	19 300	29 300	36 800	1.29	-

AA-Macromonomer Hydrolysis

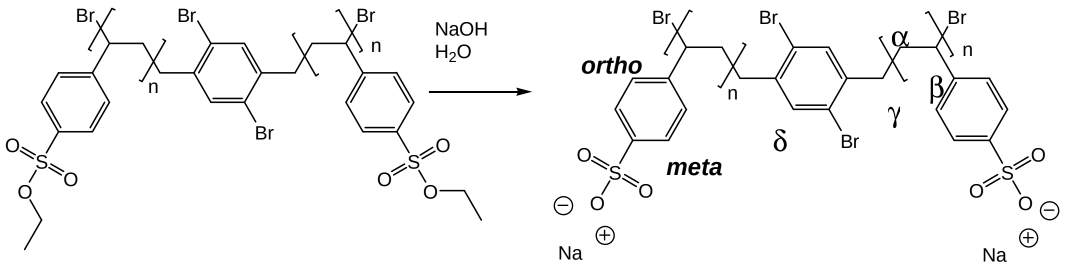

Fig. 12.1.3.2.: AA-macromonomer hydrolysis

Poly(styrene sulfonic acid ethyl ester) macromonomers were dissolved in a minimum amount of DMF. 100 ml NaOH (1 mol/L) was added. The emulsion was stirred at 80℃ for 3 hours and then freeze-dryed. The resulting material was dissolved in 50 ml H_2O and dialyzed versus 10 L MilliQ water, which was exchanged every 24h, until the conductivity of the water dropped to 0.1 µS after 12 h (membrane pore size 1 000 g/mol, water exchange every day). Freeze-drying yielded the desired product.

^{1}H-NMR (D_2O, 300 MHz, 80℃): 7.0-7.9 H_{meta}, 6.1-7.1 H_{ortho}, 2.5 H_γ, 0.6-2.6 (H_α + H_β)

MALDI-TOF MS: molecule could not be ionized and desorbed

GPC (H_2O, 0.1 M $NaNO_3$, poly(styrene sulfonate sodium salt standard):

Sample	T [℃]	$M_{n,\ theory}$ [g/mol]	$M_{n,\ GPC\ RI}$ [g/mol]	M_w/M_n
PSS 2	80	2 280	1 300	1.61
PSS 3	80	2 280	540	4.85
PSS 4	80	5 430	4 300	1.71
PSS 5	80	10 480	7 500	2.07
PSS 6	80	19 730	14 300	1.87
PSS 7	80	16 850	12 000	1.75

AB-Macromonomer Synthesis

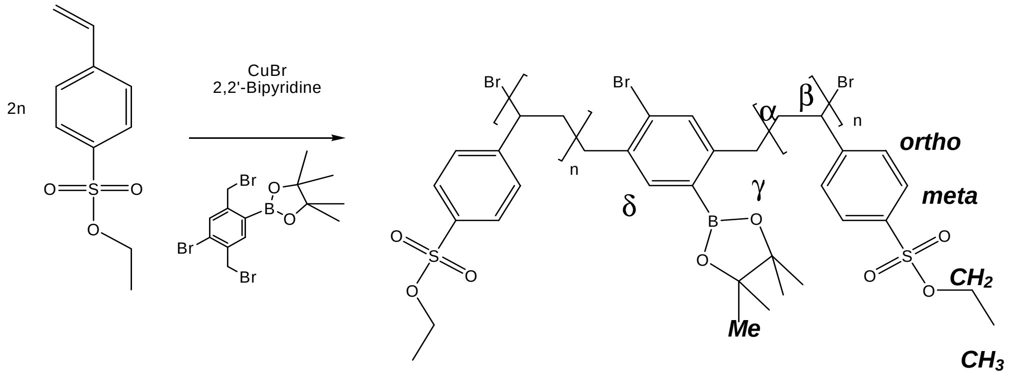

Fig. 12.1.3.3.: AB-macromonomer synthesis

The radical starter, CuBr and the bipyridine ligand were put into a Schlenk tube (ratio 1:2:4) under inert gas atmosphere. The monomer was added through a septum with a syringe. The Schlenk tube was placed in a pre-heated oil bath at 60℃ and left to react for 5 hours. After cooling, the dark brown solid was dissolved in Acetonitrile. The catalyst was removed by ion exchange (Dowex MSC-1, CH_2Cl_2). After filtration, the solvent was removed under vacuum. The polymer was redissolved in acetonitrile and purified by repeated precipitation into methanol. After three precipitations, a colourless powder was obtained.

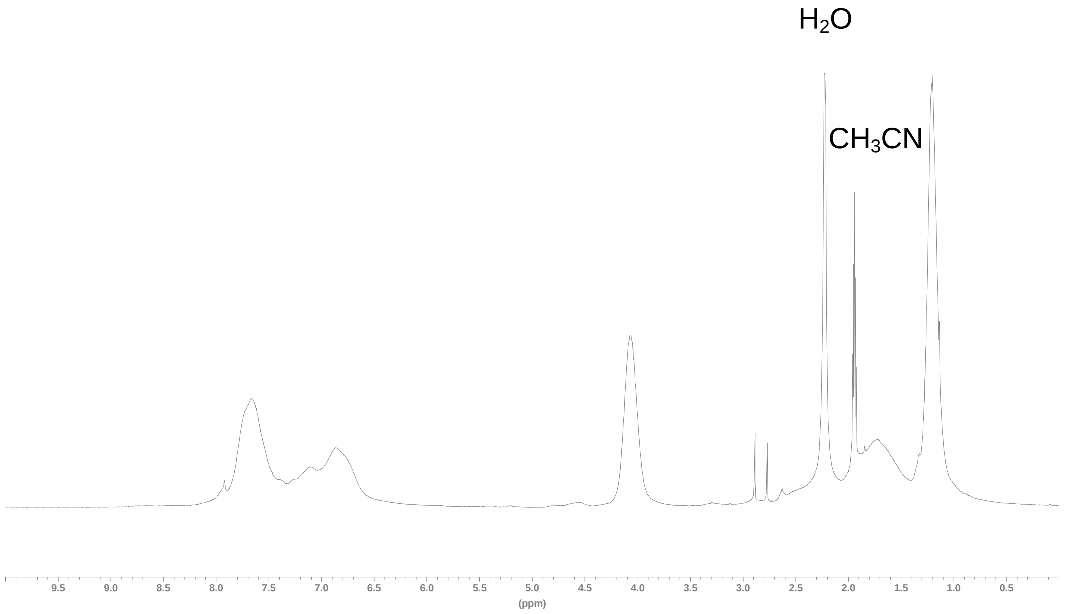

Fig. 12.1.3.4.: ^{1}H-NMR spectrum of sample **PSSEAB** 1

^{1}H-NMR (DMF, 300 MHz):	7.4-8.0 H_{meta}, 6.4-7.5 H_{ortho}, 3.9-4.3 CH_2, 2.7 H_γ, 2.9 $H_{\gamma'}$, 1.4-2.5 ($H_\alpha + H_\beta$), 1.3 *Me*, 1.25 CH_3,
MALDI-TOF MS:	molecule could not be ionized and desorbed

GPC and GPC-MALLS (DMF):

Sample	*n* [mmol]				T [℃]	$M_{n,\ theory}$ [g/mol]	$M_{n,\ GPC}$ [g/mol]	$M_{n,\ GPC\text{-}MALLS}$ [g/mol]	M_w/M_n
	PSSE	Starter	CuBr	Ligand					
PSSEAB 1	16.3	0.422	0.848	0.875	60	8640	15100	16 500	1.61
PSSEAB 5	10.37	0.433	0.854	1.71	60	5550	11 900	-	1.26
PSSEAB 6	9.19	0.766	1.530	3.07	60	3010	9 800	7 700	1.48
PSSEAB 7	7.25	1.810	3.630	7.25	60	1320	11 000	16 000	1.31

AB-Macromonomer Hydrolysis

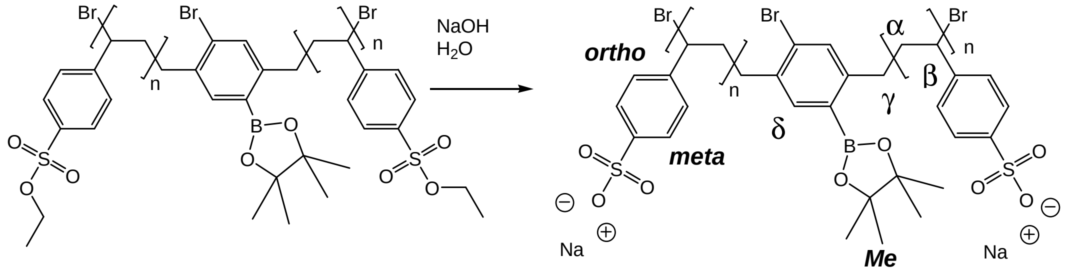

Fig. 12.1.3.5.: AB-macromonomer hydrolysis

Poly(styrene sulfonic acid ethyl ester) macromonomers (150 mg) were dissolved in a minimum amount of DMF (approx. 3 ml). 100 ml of NaOH (1 mol/l) were added. The emulsion was stirred at 80℃ for 3 hours and then freeze-dryed. The resulting material was dissolved in 50 ml H_2O and dialyzed versus 10 L MilliQ water, which was exchanged every 24h, until the conductivity of the water dropped to 0.1 µS after 12 h (membrane pore size 1 000 g/mol, water exchange every day). Freeze-drying yielded the desired product.

^{1}H-NMR (D_2O, 300 MHz, 80℃): 7.2-7.9 H_{meta}, 6.2-6.9 H_{ortho}, 2.5 H_γ, 0.9-2.2 (H_α + H_β), 1.0 *Me*

MALDI-TOF MS: molecule could not be ionized and desorbed

GPC (H_2O, 0.1 M $NaNO_3$, poly(styrene sulfonate sodium salt standard):

Sample	T [℃]	$M_{n,\text{ theory}}$ [g/mol]	$M_{n,\text{ GPC}}$ [g/mol]	M_w/M_n
PSSAB 1	80	7 540	7 000	1.87
PSSAB 2	80	1 530	1 700	1.33
PSSAB 3	80	3 440	3 300	1.67
PSSAB 4	80	3 740	3 200	1.85
PSSAB 5	80	4 850	3 800	1.56
PSSAB 6	80	2 630	2 000	1.38
PSSAB 7	80	1 150	2 800	2.16

Macromonomer Polymerization Attempts

Poly(styrene sulfonic acid sodium salt) macromonomers (150 mg, 0.01 mmol, 1 eq) were dissolved in 3 ml H_2O. THF (2 ml) was added, together with 25.2 mg (0.3 mmol, 30 eq) of $NaHCO_3$. The solution was degassed three times via freeze-thaw cycles. 0.2 mg ($3\cdot10^{-4}$ mmol, $3\cdot10^{-2}$ eq) $Pd(PPh_3)_4$ catayst were added, followed by three more freeze-thaw cycles. The solution was stirred at 80°C for 10 days. After evaporation of the solvent, the resulting material was dissolved in 50 ml H_2O and dialyzed versus 10 L distilled water MilliQ water, which was exchanged every 24h, until the conductivity of the water dropped to 0.1 µS after 12 h (membrane pore size 3 000 g/mol, water exchange every day). Freeze-drying yielded the reaction product.

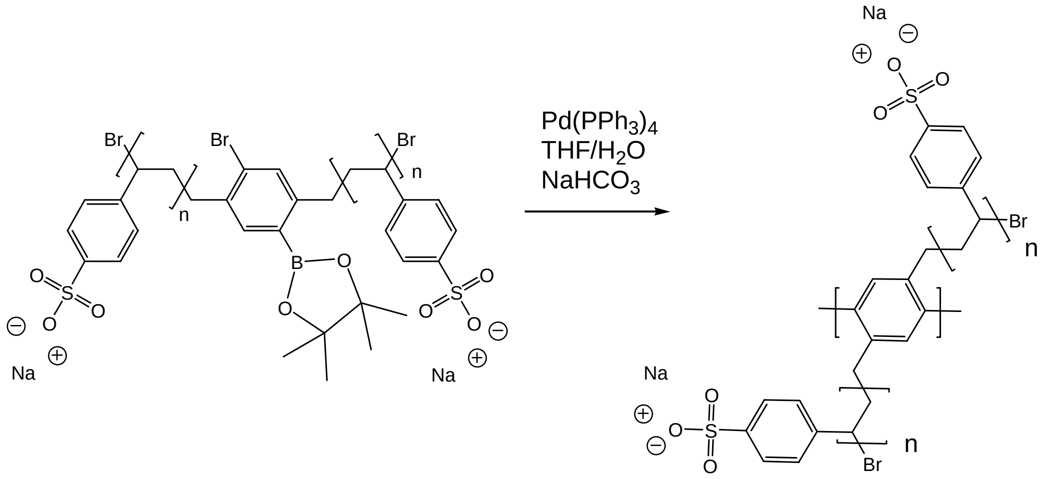

Fig. 12.1.3.6.: AB-macromonomer polymerization

^{1}H-NMR (D_2O, 300 MHz, 80℃): 7.2-7.9 H$_{meta}$, 6.2-6.9 H$_{ortho}$, 2.5 H$_\gamma$, 0.9-2.2 (H$_\alpha$ + H$_\beta$), 1.0 *Me*

GPC (H_2O, 0.1 M $NaNO_3$, poly(styrene sulfonate sodium salt standard):

Sample	Monomer	T [℃]	$M_{n,\ GPC,\ PSSNa}$ [g/mol]	M_w/M_n
PPP1	**PSSAB01**	80	4 200	2.15
PPP2	**PSSAB04**	80	4 300	1.86
PPP3	**PSSAB04**	80	4 000	1.46
PPP4	**PSSAB03**	80	3 400	1.64

12.1.4. Macroinitiator Synthesis

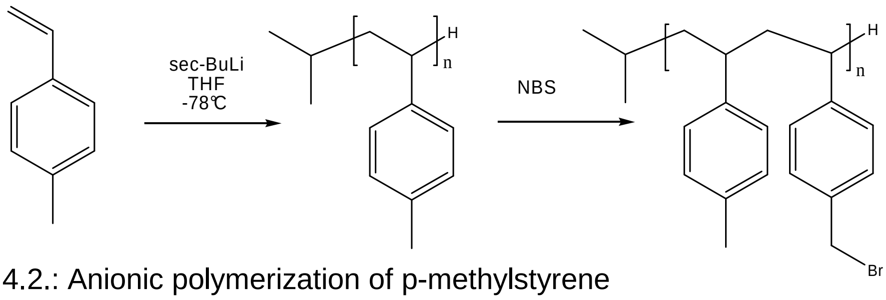

Fig. 12.1.4.2.: Anionic polymerization of p-methylstyrene

Fig. 12.1.4.3.: High vacuum anionic polymerization line with solvent reservoirs (left arrow, reactor (middle arrow) and vacuum distillation setup (right arrow).

Poly(p-methylstyrene-*co*-vinylbenzylbromide macroinitiators were synthesized in a two step procedure following procedures by Janata et al.[202].

1. Step: A high-vaccum line with an oil-diffusion pump (10^{-6} mbar) and Schlenk technique was used for all manipulations (Fig. 12.1.4.3.). Following standard procedures anionic polymerization[203], 1 g (6.02 mmol) fluorine was dissolved in 50 ml THF and reacted with 3 ml (c= 1.3 g/L, 3.90 mmol) n-butyllithium. The solvent was evaporated. 15 g (127 mm) p-methylstyrene was added to the bright orange solid and purified by high-vacuum distillation into a Schlenk tube (Fig. 12.1.4.4., left). The tube was sealed and cooled until further use. THF was titrated with diphenyl ethylene and n-butyl lithium until a deep red color was observed. The initiator, sec-butyl lithium, is used as received. A one liter glass reactor with one main Teflon valve with a NS 19 ground neck and six small Teflon valves with NS 14 ground necks (Fig. 12.1.4.4., right) was used. The main valve was connected to the anionic polymerization line for vacuum and inert gas supply. Reagents were added via the small valves using standard Schlenk techniques. Under high vacuum, the reactor was heated with a hot air gun to 400℃ and allowed to cool to room temperature. The procedure was repeated twice. THF (200 ml) was distilled directly into the reactor from the reservoir in the polymerization line (Fig. 12.1.4.3.). The desired amount of initiator was added via Schlenck technique as shown in Fig. 12.1.4.4., left. The reactor was cooled to – 78℃ with dry ice/iso-propanol. P-methylstyrene was added via Schlenck technique. The reaction was allowed to complete over night. The product was precipitated by pouring the reaction mixture into methanol (800 ml). It was re-dissolved in THF and precipitated twice into methanol.

Fig. 12.1.4.4.: Monomer distillation (left), reagent addition to anionic polymerization reactor via Schlenk technique (right)

^{1}H-NMR ($CDCl_3$, 300 MHz): 6.5-6.9 H_{meta}, 6.1-6.5 H_{ortho}, 1.9-2.2 $H_{p\text{-}CH3}$, 0.9-1.9 $H_{backbone}$

GPC-MALLS and GPC (THF, PS standard):

Sample	*n* [mmol]		T [℃]	$M_{n, theory}$ [g/mol]	$M_{n, GPC}$ [g/mol]	$M_{n, GPC\text{-}MALLS}$ [g/mol]	M_w/M_n
	p-methyl-styrene	**BuLi**					
PpMS3	144	0.65	-78℃	25 000	57 700	67 700	1.04
PpMS7	107	1.30	-78℃	10 000	25 500	23 400	1.07
PpMS11	144	0.20	-78℃	85 000	163 000	189 700	1.07

2. Step: The reaction product of the first step was dissolved in 200 ml freshly distilled ($CaCl_2$) CCl_4 under argon. Vacuum-dried n-bromosuccinimide (NBS) was added. To facilitate radical formation, 0.03 mol% azoisobutyricacid nitrile (AIBN) were added.

Upon refluxing at 90℃, NBS was consumed. The reaction was finished after 4 h, as indicated by the resulting succinimid floating at the CCl_4 sulface. After cooling to room temperature, succinimid was removed by filtration. The solvent was removed under reduced pressure. The product was re-dissolved in THF and precipitated into methanol (400 ml). This was repeated twice. After drying in vacuum, a colourless solid was obtained.

^{1}H-NMR ($CDCl_3$, 300 MHz): 6.6-7.0 H_{meta}, 6.1-6.5 H_{ortho}, 4.2-4.4 $H_{benzylic}$, 2.0-2.3 $H_{p\text{-}CH3}$, 1.0-1.9 $H_{backbone}$

GPC-MALLS (THF):

Sample	***n*** **[mmol]**			$M_{w,\ GPC\text{-}MALLS}$ **[g/mol]**	M_w/M_n	***% Br***		
	PpMS X	**NBS**	**AIBN**			**^{1}H-NMR**	**Elemental Analysis**	**GPC-MALLS**
3-10%Br	18.2	1.82	0.02	69 800	1.04	9	-	-
3-20%Br	18.2	3.64	0.04	71 600	1.04	17	-	-
3-30%Br	18.2	5.46	0.06	74 600	1.04	23	-	-
7-20%Br	18.2	3.64	0.04	30 700	1.04	17	-	-
7-40%Br	18.2	7.28	0.08	34 200	1.04	35	-	-
7-60%Br	18.2	10.9	0.12	37 100	1.05	52	-	-
7-80%Br	18.2	14.3	0.14	40 100	1.05	64	-	-
11-10%Br	18.2	1.82	0.02	206 000	1.07	9	10.6	15
11-20%Br	18.2	3.64	0.04	211 400	1.07	18	20.6	19
11-30%Br	18.2	5.46	0.06	227 000	1.08	25	29.1	31
11-40%Br	18.2	7.28	0.08	221 300	1.11	34	45.1	26
11-50%Br	18.2	9.10	0.10	257 000	1.12	40	49.6	52
11-60%Br	18.2	10.9	0.12	220 300	1.27	50	62.7	26
11-80%Br	18.2	14.3	0.14	269 300	1.24	65	77.5	62
11-100%Br	18.2	18.2	0.16	329 200	1.45	68	96.4	107

12.1.5. Polymer Brush Synthesis

Preliminary Experiments – Synthesis Optimization

In a 25 ml Schlenk tube with argon atmosphere, the indicated amount of catalyst, solid ligand and starter polymer was added. The system was subject to three freeze-thaw cycles. Liquid ligand (PMDETA) and solvents were freshly distilled before use and added via a syringe. Monomers were dissolved in CH_2Cl_2 in a Schlenck flask. The solvent was removed with an oil pump over night to yield an oxygen-free monomer. The reaction components were combined in the order solids – liquids – monomer and stirred until a homogeneous, brown solution was obtained. They were then put into a preheated oil bath at 60℃. The product was recovered by precipitation into 500 ml methanol, filtration and drying. The exact amounts of each component and analytical results are given in Tab. 12.1.5.1..

Table 12.1.5.1.: Synthesis optimization: variation of ligand, copper species, solution conditions, and monomer

Sample	Starter eq. / [mmol] Monomer eq./ [mmol]	Catalyst eq./ [mmol]	Ligand	Ligand eq./ [mmol]	Solvent	$M_{n, GPC}$ [g/mol], M_w/M_n	t [min]	homo-geneous	T [℃]
PpMS1-Br-PSSE1	1 / 2.88 11.4 / 8.95	CuBr 0.944 / 2.72	PMDETA	0.944 / 2.72	MEK	not soluble	5	no	60
PpMS1-Br-PSSE2	1 / 2.88 1.96 / 5.65	CuBr 0.508 / 1.46	PMDETA	0.962 / 2.77	MEK	not soluble	5	no	60
PpMS1-Br-PSSE3	1 / 2.88 3.96 / 11.4	CuBr 1.96/ 5.66	bpy	0.948 / 2.73	-	not soluble	60	no	60
PpMS1-Br-PSSE4	1 / 2.88 3.96 / 11.4	CuBr 0.944 / 2.72	PMDETA	0.948 / 2.73	-	not soluble	120	no	60
PpMS3-Br-PSSD2	1 / 1.49 5.71/ 8.51	CuCl 0.488 / 0.727	dNbpy	0.933 / 1.39	Chloro-benzene	cannot filter	210	yes	60
PpMS3-Br-PSSE5	1 / 1.50 10.7 / 24.0	CuCl 0.673 / 1.01	dNbpy	0.930 / 1.39	-	cannot filter	10	no	60
PpMS3-Br-PSSE6	1 / 1.48 15.5 / 23.0	CuBr 0.471 / 0.698	dNbpy	0.939 / 1.39	-	cannot filter	10	no	60

Synthesis of Poly(styrene sulfonate dodecylic ester) Brushes

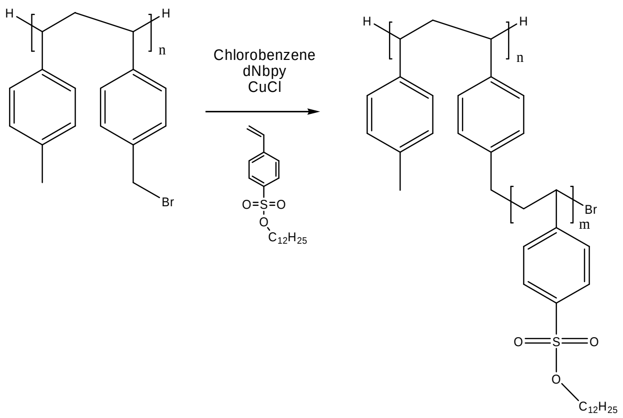

Fig. 12.1.5.1.: Synthesis of poly(styrene sulfonate dodecylic ester) brushes

The exact amount of each reagent is given in Tab. 12.1.5.2.. Chlorobenzene was freshly distilled to exclude oxygen. Copper chloride and 4,4’-dinonyl-2,2’-bipyridyl were subject to three freeze-thaw cycle in a 25 ml Schlenk tube and dissolved in half the indicated solvent amount under argon, resulting in a brown suspension. In another 25 ml Schlenk tube, the macroinitiator was subject to three freeze-thaw cycles and dissolved in the other half of the solvent under argon. Styrene sulfonate dodecylic ester was dissolved in chlorobenzene in a 50 ml Schlenk flask. The solvent was removed with an oil pump, resulting in a solidification of the monomer. The solid monomer was molten at 40℃ under argon and added to the dark brown copper-ligand complex with a syringe. After 5 min stirring, the macroinitiator solution was added with a syringe. The Schlenk tube was placed into a preheated oil bath at 60℃ for 48 h. The reaction mixture was allowed to cool to room temperature and dissolved in a small amount of THF and precipitated into 500 ml methanol. After stirring until the suspension turned green, the solid was filtrated with a Büchner funnel. After drying in vacuum, the green solid was dissolved in THF. The remaining copper was removed by passing the solution three times over an ion exchange column (Amberlyst 15, Fluka). The resulting polymer solution was concentrated at the rotary evaporator until a marked viscosity was observed. In was then precipitated into 300 ml cold methanol (4℃) and filtrated. This was repeated twice. After drying in vacuum, a colourless solid was obtained.

Table 12.1.5.2.: **PSSD** brush synthesis

Sample	Starter	Starter [mmol]	SSD [mmol]	CuCl [mmol]	dNbpy [mmol]	Chlorobenzene [ml]	Reaction time [h]
3-10-D2	3-10%Br	0,40	1,78	0,40	0,73	1	-
3-10-D3	3-10%Br	0,40	3,79	0,40	0,73	1	-
3-10-D4	3-10%Br	0,40	7,17	0,40	0,73	1	-
3-20-D1	3-20%Br	0,60	0,10	0,53	1,03	1	-
3-20-D3	3-20%Br	0,60	2,46	0,53	1,03	1	-
3-20-D3	3-20%Br	0,60	5,06	0,53	1,03	1,5	-
3-20-D4	3-20%Br	0,60	11,40	0,53	1,03	1	47
3-30-D1	3-30%Br	0,86	21,19	0,68	1,37	3	72
3-30-D2	3-30%Br	0,86	11,97	0,68	1,37	3	72
3-30-D4	3-30%Br	0,85	37,73	0,71	1,38	3	72
7-40-D1	7-40%Br	0,54	24,68	0,48	0,98	3	-
7-60-D1	7-60%Br	0,73	33,10	0,65	1,31	3	-
7-80-D1	7-80%Br	0,96	22,83	0,77	1,54	3	-
7-80-D2	7-80%Br	0,96	31,49	0,77	1,54	2	-
7-80-D3	7-80%Br	0,96	32,34	0,77	1,54	3	-
11-10-D1	11-10%Br	0,16	11,35	0,18	0,32	5	-
11-20-D1	11-20%Br	0,30	12,10	0,31	0,61	5	5
11-20-D2	11-20%Br	0,30	12,23	0,31	0,61	10	5
11-30-D1	11-30%Br	0,52	12,20	0,25	0,61	5	-
11-30-D2	11-30%Br	0,52	12,20	0,29	0,61	10	-
11-40-D1	11-40%Br	0,53	17,02	0,48	0,98	5	6
11-80-D1	11-80%Br	0,22	14,18	0,24	0,50	2,5	4
11-100-D1	11-100%Br	0,25	19,86	0,31	0,64	2,5	4

^{1}H-NMR (side chain length) and AUC:

Sample	Side Chain Length	M_n, calc [g/mol]	Maxima $s(S)$
3-20-D4	13	585 000	11.5
3-30-D1	18	1 008 000	13.6
3-30-D3	55	3 079 000	21.2
11-10-D1	37	2 565 000	16.2
11-20-D1	26	3 215 000	18.2
11-30-D1	15	2 620 000	25.8
11-30-D2	-	-	11.1
11-40-D1	24	6 493 000	32.3

^{1}H-NMR (Acetone, 300 MHz): 6.2-7.9 H_{arom}, 3.8-4.1 $H_{\alpha\text{-}CH2\ ester}$, 1.9-2.2 $H_{p\text{-}CH3}$, 1.0-1.3 $H_{ß\text{-}\omega CH2}$, 0.9-1.9 $H_{backbone}$, 0.7-0.8, $H_{CH3\ ester}$

Synthesis of Poly(styrene sulfonate ethyl ester) Brushes

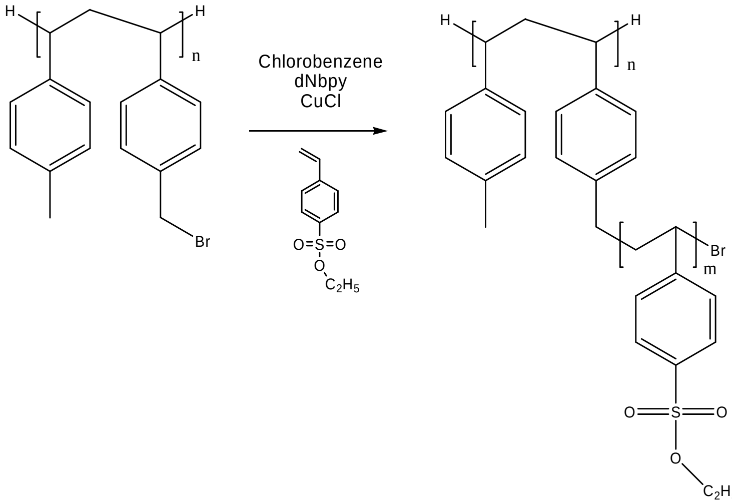

Fig. 12.1.5.2.: Synthesis of poly(styrene sulfonate dodecylic ester) brushes

Poly(styrene sulfonate ethyl ester) brushes (Fig. 12.1.5.2.) were synthesized according to the same method as described for poly(styrene sulfonate dodecylic ester) brushes, with a few alterations. The reaction was conducted in a mixture of chlorobenzene and acetone. The reaction temperature was 45℃. The reaction mixture was dissolved in CH_2Cl_2, which was also used for the ion exchange (Amberlyst 15, Fluka). Precipitation from acetonitrile into methanol yielded the desired product, which was obtained as a colourless solid. The complete reaction parameters are given in Tab. 12.1.5.3..

Table 12.1.5.3.: **PSSE** brush synthesis

Sample	Starter	Starter [mmol]	SSE [mmol]	CuCl [mmol]	dNbpy [mmol]	Chloro-benzene [ml]	Acetone [ml]	Reaction time [h]	T [℃]
11-40-E1	11-40%Br	0,03	9,43	0,07	0,15	1	1	24	25
11-40-E2	11-40%Br	0,13	20,60	0,35	0,74	2	1	3	45
11-40-E3	11-40%Br	0,13	54,37	0,35	0,74	2	1	2	60
11-40-E4	11-40%Br	0,13	35,75	0,36	0,84	2	2	3	45
11-40-E5	11-40%Br	0,26	67,90	0,72	1,49	4	4	4	45
11-10-E1	11-10%Br	0,05	17,45	0,08	0,16	2	2	7	45
11-20-E1	11-20%Br	0,15	29,90	0,16	0,35	2	2	7	45
11-30-E2	11-30%Br	0,21	42,34	0,23	0,49	2	2	3	45
11-50-E1	11-50%Br	0,32	63,49	0,35	0,73	2	2	3	45
11-60-E1	11-60%Br	0,36	72,55	0,40	0,84	2	2	3	45
11-80-E1	11-80%Br	0,44	88,30	0,49	1,02	2	2	2	45
11-100-E1	11-100%Br	0,51	101,52	0,56	1,17	2	2	2	45

^{1}H-NMR (CD_2Cl_2, 300 MHz): 7.2-7.9 H_{meta}, 6.3-6.9 H_{ortho}, 3.8-4.2 $H_{CH2\ ester}$, 1.1-1.3, $H_{CH3\ ester}$, 0.9-2.4 $H_{backbone}$

GPC-MALLS (DMF, 1 g/L LiBr):

Sample	M_w [g/mol]	M_n [g/mol]	M_w/M_n
11-10-E1	637 000	461 600	1.38
11-20-E1	2 739 000	2 123 500	1.29
11-30-E2	2 736 000	2 104 600	1.30
11-40-E4	3 127 000	1 807 500	1.73
11-50-E1	2 664 000	1 944 500	1.37
11-60-E1	1 577 000	922 200	1.71
11-80-E1	7 261 000	4 523 100	1.60
11-100-E1	22 260 000	12 793 000	1.74

12.1.6. Polyelectrolyte Brush Synthesis

Hydrolysis of Poly(styrene sulfonate dodecylic ester) Brushes

a) Hydrolysis with KOH

100 mg (0.29 mmol **SSD**) polymer was dissolved in a minimum amount of THF. 96 mg (2.9 mmol) KOH (85%) were dissolved in Milli-Q H_2O and added to this solution. The reaction mixture was kept at 60℃ for three days. It was then dialyzed versus 10 L Milli-Q water, which was exchanged every 24h, until the conductivity of the water dropped to 0.1 µS after 12 h (membrane pore size 10 000 g/mol, water exchange every day). Freeze-drying yielded the desired polyelectrolyte as the potassium salt (Fig. 12.1.6.1.).

^{1}H-NMR (D_2O, 300 MHz, 80℃): 7.8-8.5 H_{meta}, 7.5-6.7 H_{ortho}, 4.3-5.5 $H_{CH2\ ester}$, 1.1-1.4, $H_{CH3\ ester}$, 1.4-1.9, $H_{ß\text{-}\omega\ CH2\ ester}$, 0.9-3.0 $H_{backbone}$

Characterization: see below

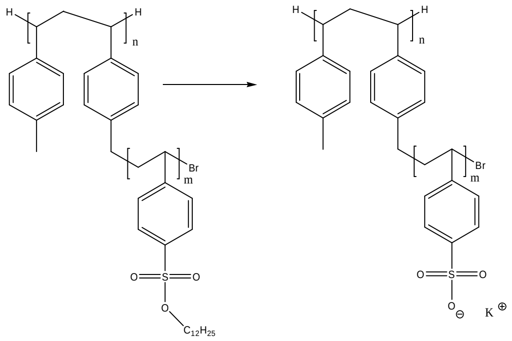

Fig. 12.1.6.1.: **PSSD** hydrolysis with KOH

b) Hydrolysis with triethylamine

250 mg (0.71 mmol **SSD**) were dissolved in 20 ml $CHCl_3$. 1 ml (7.10 mmol) triethylamine was added. The reaction mixture was refluxed for 12 h and cooled to room temperature. The solvent was removed by vacuum evaporation. The reaction product was dissolved in 50 ml Milli-Q H_2O. It was then dialyzed versus 10 L Milli-Q water, which was exchanged every 24h, until the conductivity of the water dropped to 0.1 µS after 12 h (membrane pore size 10 000 g/mol, water exchange every day). Freeze-drying yielded the desired polyelectrolyte (Fig. 12.1.6.2.).

^{1}H-NMR (D_2O, 300 MHz, 80℃):7.8-8.5 H *meta*, 7.5-6.7 H*ortho*, 1.4-1.9, 0.9-3.0 H*backbone*
Characterization: see below

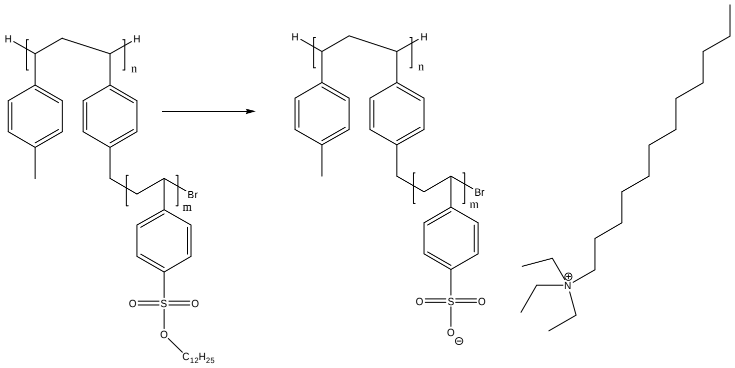

Fig. 12.1.6.2.: **PSSD** hydrolysis with triethylamine

c) Hydrolysis with triethylamine and KOH

250 mg (0.71 mmol **SSD**) were dissolved in 20 ml $CHCl_3$. 1 ml (7.10 mmol) triethylamine was added. The reaction mixture was refluxed for 3 h and cooled to room temperature. The solvent was removed by vacuum evaporation. The reaction product was dissolved in 50 ml Milli-Q H_2O. 240 mg (7.10 mmol) KOH (85%) was added. The

reaction was refluxed for 48 h. It was then brought to pH = 1 with HCl and refluxed for 48 h. The solution was cooled to room temperature and dialyzed versus 10 L Milli-Q water, which was exchanged every 24h, until the conductivity of the water dropped to 0.1 µS after 12 h (membrane pore size 10 000 g/mol, water exchange every day). Freeze-drying yielded the desired polyelectrolyte.

^{1}H-NMR (D_2O, 300 MHz, 80℃): 7.8-8.5 H_{meta}, 7.5-6.7 H_{ortho}, 1.4-1.9, 0.9-3.0 $H_{backbone}$
Characterization: see below

d) Hydrolysis with trimethylsilyl iodide

150 mg (0.43 mmol **SSD**) were dissolved in 20 ml CH_2Cl_2. 856 mg (4.30 mmol) trimethylsilyl iodide was added. The reaction mixture was refluxed for 4 h and cooled to room temperature. The solvent was removed by vacuum evaporation. The reaction product was dissolved in 50 ml Milli-Q H_2O. 100 ml 2 M NaOH was added. The reaction was stirred for 4 h. It was then dialyzed versus 10 L Milli-Q water, which was exchanged every 24h, until the conductivity of the water dropped to 0.1 µS after 12 h (membrane pore size 10 000 g/mol, water exchange every day). Freeze-drying yielded the desired polyelectrolyte sodium salt.

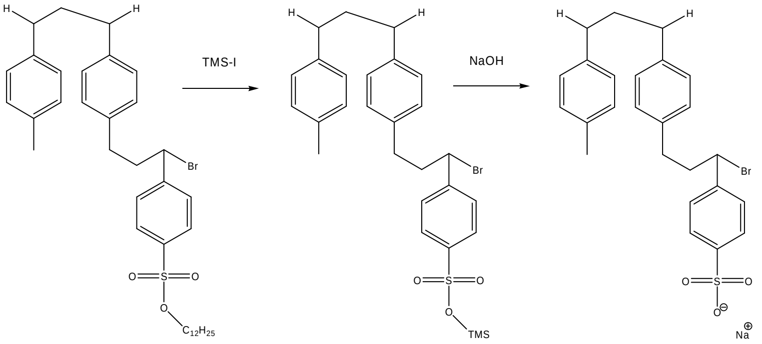

Fig. 12.1.6.3.: **PSSD** Hydrolysis with TMS-I/NaOH

^{1}H-NMR (D_2O, 300 MHz, 80℃): 7.8-8.5 H_{meta}, 7.5-6.7 H_{ortho}, 1.4-1.9, 0.9-3.0 $H_{backbone}$
Characterization: see below

Hydrolysis of Poly(styrene sulfonate ethyl ester) Brushes

50 mg (0.24 mmol **SSE**) were dissolved in 20 ml CH_2Cl_2. 960 mg (2.40 mmol) trimethylsilyl iodide was added. The reaction mixture was refluxed for 24 h and cooled to room temperature. The solvent was removed by vacuum evaporation. The reaction product was dissolved in 50 ml Milli-Q H_2O. 100 ml 2 M NaOH was added. The reaction was stirred for 4 h and then dialyzed versus 10 L Milli-Q water, which was exchanged

every 24h, until the conductivity of the water dropped to 0.1 µS after 12 h (membrane pore size 10 000 g/mol, water exchange every day). Freeze-drying yielded the desired polyelectrolyte sodium salt.

^{1}H-NMR (D_2O, 300 MHz, 80℃):7.8-8.5 H_{meta}, 7.5-6.7 H_{ortho}, 1.4-1.9, 0.9-3.0 $H_{backbone}$
Characterization: see below

Poly(styrene sulfonic acid) Brushes from Poly(styrene sulfonate salt) Brushes

100 mg of the polyelectrolyte brush salt was dissolved in 100 ml Milli-Q H_2O and passed slowly (1 drop/min) over an ion exchange resin (Amberlyte IR-120($^+$)). The solution was then dialyzed versus 10 L Milli-Q water, which was exchanged every 24h, until the conductivity of the water dropped to 0.1 µS after 12 h (membrane pore size 10 000 g/mol, water exchange every day). Freeze-drying yielded the desired poly(styrene sulfonic acid) brushes.

All saponification and ion exchange reactions are summarized in Tab. 12.1.6.1.. The results of the polyelectrolyte brush characterization are summarized in Tabs. 12.1.6.2. and 12.1.6.3..

Table 12.1.6.1.: Hydrolysis of poly(styrene sulfonate ester) brushes

Sample	Parent Ester	Reagent	Ester [mmol]	Reagent [mmol]	Reaction time [h]	T [℃]	Free Acid Form
3-30-PSS1, K+	3-30-D1	KOH	0,2	20,0	24	100	**3-30-PSS1, H+**
3-30-PSS2, K+	3-30-D2	KOH	0,2	20,0	24	100	**3-30-PSS2, H+**
3-30-PSS4, K+	3-30-D4	KOH	0,2	20,0	24	100	**3-30-PSS4, H+**
11-30-PSS1, Na+	11-30-D1	NaOH	0,2	20,0	24	100	**11-30-PSS1, H+**
3-30-1, NR4+	3-30-D1	EtN3	0,2	2,0	12	50	**3-30-1, H++**
3-30-1, Na	3-30-D1	EtN3/NaOH	0,2	2,0	101	50/100	**3-30-1, H**
11-30-1, Na	11-30-D1	EtN3/NaOH	0,2	2,0	101	50/100	**11-30-1, H**
3-30-1, TMS1	3-30-D1	TMS-I	0,2	2,0	4	50	**3-30-1, TMS1, H+**
3-30-1, TMS2	3-30-D1	TMS-I	0,2	2,0	4	50	**3-30-1, TMS2, H+**
11-30-1, TMS1	11-30-D1	TMS-I	0,2	2,0	4	50	**11-30-1, TMS1, H+**
11-30-2, TMS1	11-30-D2	TMS-I	0,2	2,0	4	50	**11-30-2, TMS1, H+**
11-20-I, TMS1	11-20-E1	TMS-I	0,2	2,0	4	50	**11-20-I, TMS1, H+**
11-40-IV, TMS1	11-20-E4	TMS-I	0,2	2,0	4	50	**11-40-IV, TMS1, H+**
11-60-I, TMS1	11-60-E1	TMS-I	0,2	2,0	4	50	**11-60-I, TMS1, H+**

Table 12.1.6.2.: Poly(styrene sulfonate ester) from the **3-series**: characterization

Sample	**Parent Ester**	*dn/dc*	M_w **[g/mol] (GPC-MALLS)**	M_w/M_n	**% hydrolysis (titration)**
3-30-1,PSS1, H$^{+,}$	3-30-D1	0.160	1 590 000	1.25	10
3-30-1, H$^{++,}$	3-30-D1	0.160	705 000	1.46	40
3-30-1, H	3-30-D1	0.160	920 000	1.30	90
3-30-1, TMS1, H^{+}	3-30-D1	0.160	850 000	1.48	66
3-30-2,PSS1, K^{+}	3-30-D2	0.160	1 765 000	1.19	10
3-30-4,PSS1, K^{+}	3-30-D4	0.160	927 000	1.43	-

Table 12.1.6.3.: Poly(styrene sulfonate ester) from the **11-series**: characterization

Sample	**Parent Ester**	*dn/dc*	M_w **[g/mol] (GPC-MALLS)**	M_w/M_n	side chain length
11-30-2,TMS1, H^{+}	**11-30-D2**	0.161	1 607 000	1.17	12.8
11-40-IV, TMS1, H^{+}	**11-40-E4**	0.170	1 365 000	1.45	4.1
11-60-I, TMS1, H^{+}	**11-60-E1**	0.170	1 518 000	-	5.4
11-20-I, TMS1, Na^{+}	**11-20-E1**	0.167	2 066 000	1.78	13.3
11-40-IV, TMS1, Na^{+}	**11-40-E4**	0.167	1 744 000	1.38	6.7
11-60-I, TMS1, Na^{+}	**11-60-E1**	0.167	1 563 000	1.20	5.0

12.1.7. Synthesis of End-functionalized Polyelectrolyte Brushes

Synthesis of the Functionalized Initiator (1,1-di(4-dimethylaminophenyl)-ethylene) (NN-DPE)

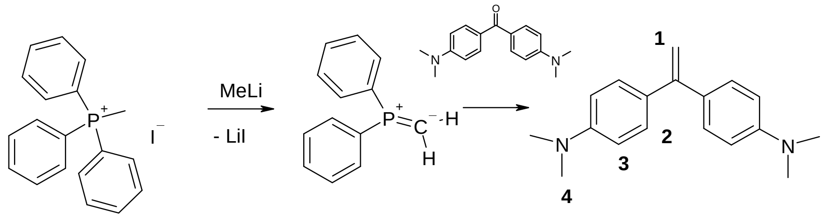

Fig. 12.1.7.1.: Synthesis of the functionalized initiator

The functionalized initiator was synthesized by combination of a procedure by Wittig[204] for the ylid formation with a modified procedure (for the formation of the mono-substituted compound) by Quirk[205]. 8.36 g (20.6 mmol) triphenylphosphonium iodide was dissolved in 100 ml dry diethyl ether under argon atmosphere. 16.1 ml (20.6 mmol) methyl lithium was slowly added at room temperature. After an intense gas development, a colourless precipitate of lithium iodide appeared. The solution was stirred for 4 hours and then filtered with a reverse frit under argon. The yellow solution was cooled to 0℃. 5.00 g (18.7 mmol) 4,4'-bis-(dimetylamino)benzophenone was suspended in 100 ml dry THF under argon atmosphere. The blue suspension was added drop wise to the cooled ylid solution with a steel transfer needle. The reaction mixture was allowed to warm to room temperature over night. In was then quenched with 30 ml methanol and 10 ml water. After the gas development stopped, the solution was filtered and the solvent was evaporated. The remaining solid was three times recrystallized from methanol and dried in vacuum. A white solid was obtained.

^{1}H-NMR ($CDCl_3$, 300 MHz):	7.25 (d, 4H, H2), 6.65 (d, 4H, H3), 5.15 (s, 2H, H1), 2.90 (s, 12 H, H4)
MS:	266.6 (M^+), 267.6 ($M+H^+$), 268.5 ($M+2H^+$), 530.9 (dimer)
Elemental Analysis (%):	C: 81.16 /81.05, H: 8.32/8.36, N: 10.52/10.55 (calc./found)

Synthesis of the Functionalized Macroinitiator Precursor (NN-PpMS)

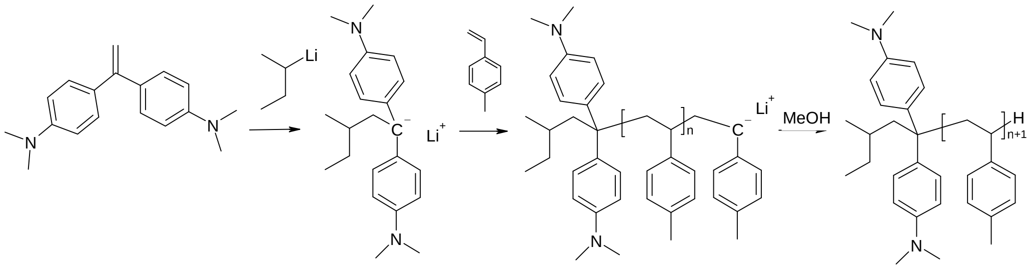

Fig. 12.1.7.2.: Functionalized macroinitiator precursor by anionic polymerization

A high-vaccum line with an oil-diffusion pump (10^{-6} mbar) and Schlenk technique was used for all manipulations (Fig. 12.1.4.3.). Following standard procedures anionic polymerization[206], 1 g (6.02 mmol) fluorine was dissolved in 50 ml THF and reacted with 3 ml (c= 1.3 g/L, 3.90 mmol) n-butyllithium. The solvent was evaporated. 15 g (127 mm) p-methylstyrene was added to the bright orange solid and purified by high-vacuum distillation into a Schlenk tube (Fig. 12.1.4.4., left). The tube was sealed and cooled until further use. THF was titrated with diphenyl ethylene and n-butyl lithium until a deep red color was observed. The initiator, sec-butyl lithium, was used as received. A one liter glass reactor with one main Teflon valve with a NS 19 ground neck and six small Teflon valves with NS 14 ground necks (Fig. 12.1.4.4., right) was used. The main valve was connected to the anionic polymerization line for vacuum and inert gas supply. Reagents were added via the small valves using standard Schlenk techniques. Under high vacuum, the reactor was heated with a hot air gun to 400℃ and allowed to cool to room temperature. The procedure was repeated twice. THF (200 ml) was distilled directly into the reactor from the reservoir in the polymerization line (Fig. 12.1.4.3.). 10 eq 1,1-di(4-dimethylaminophenyl)ethylene) were put into a Schlenk tube and connected to the polymerization line. It was evacuated and purged with argon three times. 10 ml THF were distilled into this tube on the line. The solution was added to the reactor using Schlenk technique as shown in Fig. 12.1.4.4., left.. 1 eq of *sec-*

butyl lithium was added via Schlenk technique. A deep red solution was obtained The reactor was cooled to – 78℃ with dry ice/iso-propanol. P-methylstyrene was added via Schlenk technique, resulting in an yellow-orange solution. The reaction was allowed to complete in 3 hours. It was quenched with methanol before further reaction with 1,1-di(4-dimethylaminophenyl)ethylene) could happen. The product was precipitated by pouring the reaction mixture into methanol (800 ml). It was re-dissolved in THF and precipitated twice into methanol.

^{1}H-NMR ($CDCl_3$, 300 MHz):	6.5-6.9 H_2, 6.6-6.7 H_7, 6.1-6.5 H_3, 6.1-6.2 H_6, 1.9-2.2 H_1, 1.4 H_8,0.9-1.9 $H_{4,5}$
MALDI-TOF MS:	see chapter 8
Elemental Analysis:	C: 91.45 /91.47, H: 8.53/8.64, N: 0.01/<0.1 (% calc./found):
GPC-MALLS (THF):	

Sample	$M_{n,\ theory}$ [g/mol]	$M_{w,\ GPC\text{-}MALLS}$ [g/mol]	$M_{n,\ GPC\text{-}MALLS}$ [g/mol]	M_w/M_n
NN-PpMS1	200 000	212 000	196 000	1.10
NN-PpMS2	7 000	8 200	7 900	1.04

Quarternization of the Functionalized Macroinitiator Precursor (Me-NN-PpMS)

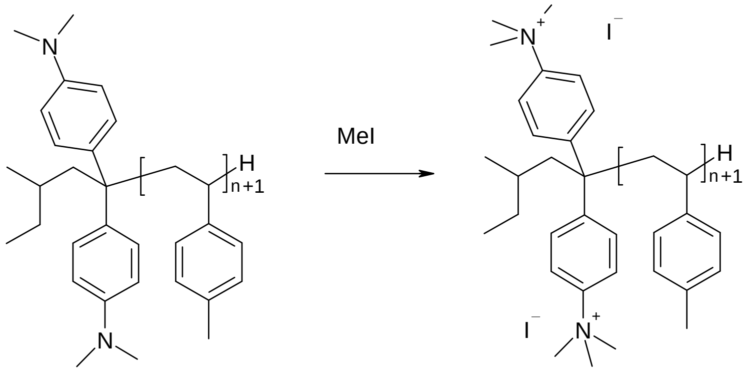

Fig. 12.1.7.3.: Quarternized macroinitiator precursor

500 mg (4.23 mmol) of the functionalized macroinitiator precursor (**N-PpMSX**) were dissolved in 50 ml dry CH_2Cl_2 under argon. 6.00 g (42.3 mmol) methyl iodide were added. The reaction was stirred for 4 h at room temperature. The solvent was removed by vacuum evaporation and the product was redissolved in THF. It was precipitated three times into 200 ml methanol. The product was recovered by filtration and dried in vacuum.

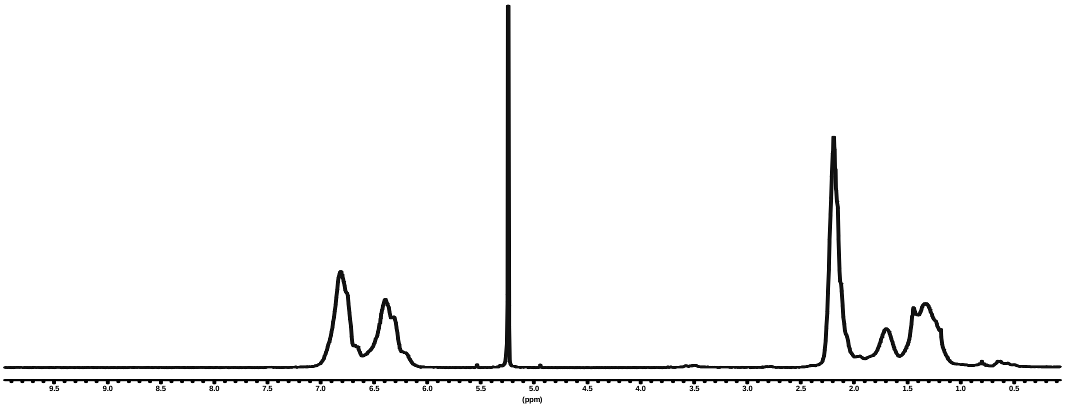

Fig. 12.1.7.4.: ^{1}H-NMR spectrum of **MeN-PpMS2**

^{1}H-NMR (CD_2Cl_2, 300 MHz): 6.6-7.1 H_{meta}, 6.1-6.6 H_{ortho}, 2.0-2.3 $H_{p\text{-}CH_3}$, 1.4 H_{N+CH_3}, 1.0-1.8 $H_{backbone}$

MALDI-TOF MS: see chapter 8

Elemental Analysis: C: 91.45 /91.49, H: 8.53/8.52, N: 0.01/<0.1 (% calc./found):

GPC-MALLS (THF):

Sample	$M_{n,\ theory}$ [g/mol]	$M_{w,\ GPC\text{-}MALLS}$ [g/mol]	$M_{n,\ GPC\text{-}MALLS}$ [g/mol]	M_w/M_n
Me-NN-PpMS1	200 000	209 000	195 000	1.10
Me-NN-PpMS2	7 000	9 200	8 700	1.05

Synthesis of the Functionalized Macroinitiator (Me-NN-PpMS-Br)

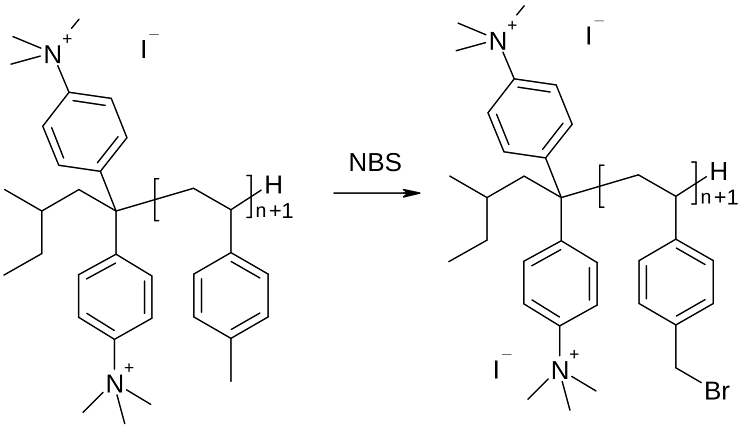

Fig. 12.1.7.5.: Synthesis of the functionalized macroinitiator

200 mg (1.69 mmol) **MeN-PpMSX** was dissolved in 100 ml freshly distilled ($CaCl_2$) CCl_4 under argon. 83.8 mg (0.846 mmol) vacuum-dried n-bromosuccinimide (NBS) was added. To facilitate radical formation, 0.03 mol% azoisobutyricacid nitrile (AIBN) were

added. Upon refluxing at 90℃, NBS was consumed. The reaction was finished after 4 h, as indicated by the resulting succinimid floating at the CCl_4 sulface. After cooling to room temperature, succinimid was removed by filtration. The solvent was removed under reduced pressure. The product was re-dissolved in THF and precipitated into methanol (50 ml). This was repeated twice. After drying in vacuum, a colourless solid was obtained.

^{1}H-NMR (CD_2Cl_2, 300 MHz): 6.6-7.0 H_2, 6.1-6.5 H_3, 4.2-4.4 H_1, 2.0-2.3 $H_{1\ (unbromiert)}$, 1.4 H_8, 1.0-1.9 $H_{4,5}$

Elemental Analysis: C: 65.82 /65.30, H: 5.99/5.48, Br: 26.19/26.19 (% calc./found)

Synthesis of End-Functionalized Polymer Brushes from Styrene Sulfonate Dodecylic Ester (MeN-X-YY-DZ)

Chlorobenzene was freshly distilled to exclude oxygen. 31.4 mg (0.318 mmol) copper chloride and 260 mg (0.644 mmol) 4,4'-dinonyl-2,2'-bipyridyl were subject to three freeze-thaw cycle in a 25 ml Schlenk tube and dissolved in 3.5 ml chlorobenzene under argon, resulting in a brown suspension. In another 25 ml Schlenk tube, 50 mg (0.318 mmol) **MeN-PpMS2-Br** was subject to three freeze-thaw cycles and dissolved in 3.5 ml chlorobenzene under argon. 5.00 g (14.2 mmol) styrene sulfonate dodecylic ester was dissolved in acetone in a 25 ml Schlenk flask. The solvent was removed with an oil pump, resulting in a solidification of the monomer. The solid monomer was molten at 40℃ under argon and added to the dark brown copper-ligand complex with a syringe. After 5 min stirring, the macroinitiator solution was added with a syringe. The Schlenk tube was placed into a preheated oil bath at 60℃ for 48 h. The reaction mixture was allowed to cool to room temperature and dissolved in a small amount of THF and precipitated into 100 ml methanol. After stirring until the suspension turned green, the solid was filtrated with a Büchner funnel. After drying in vacuum, the green solid was dissolved in THF. The remaining copper was removed by passing the solution three times over an ion exchange column (Amberlyst 15, Fluka). The resulting polymer solution was concentrated at the rotary evaporator until a marked viscosity was observed. In was then precipitated into 50 ml cold methanol (4℃) and filtrated. This was repeated twice. After drying in vacuum, a colourless solid was obtained.

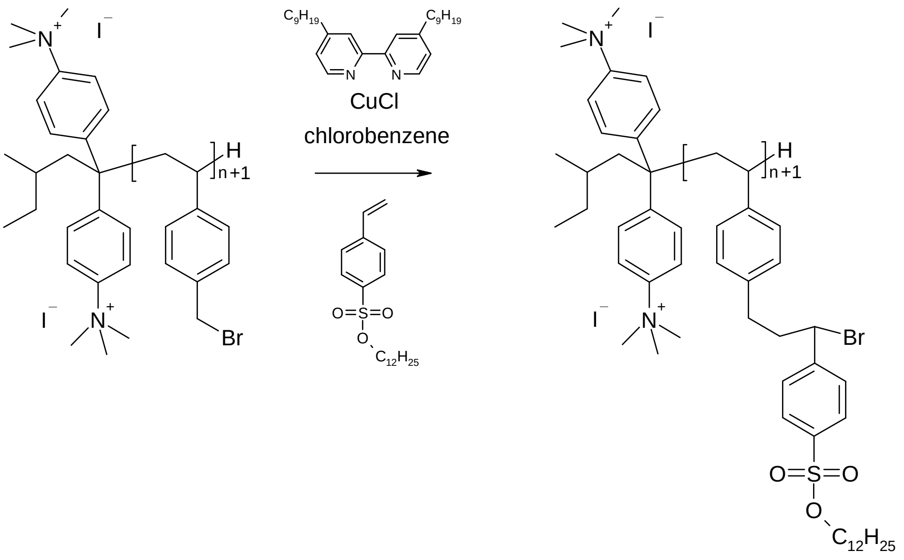

Fig. 12.1.7.7.: Synthesis of the functionalized polymer brushes

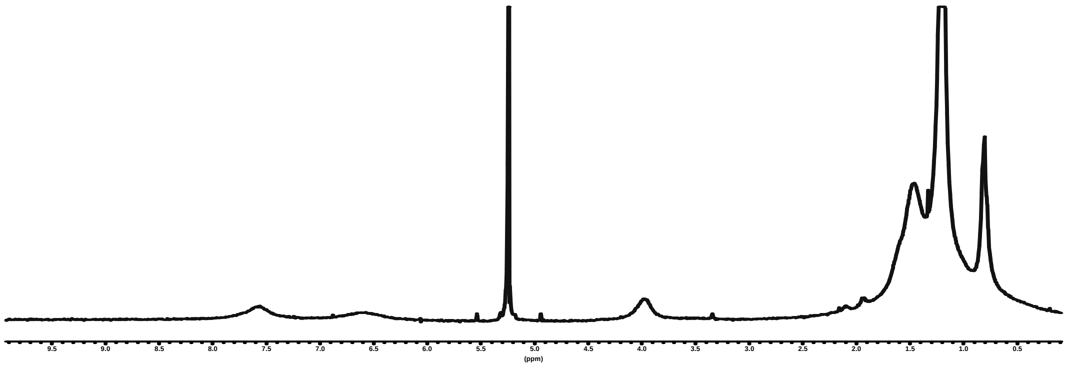

Fig. 12.1.7.8.: ^{1}H-NMR spectrum of **MeN-1-50-D1**

^{1}H-NMR (CD_2Cl_2, 300 MHz): 6.5-8.5 H_{arom}, 4.0-4.5 $H_{\alpha\text{-}CH2\ ester}$, 1.9-2.2 $H_{p\text{-}CH3}$, 1.2-1.6 $H_{ß\text{-}\omega\ CH2}$, 0.9-1.9 $H_{backbone}$, 0.8-1.2, $H_{CH3\ ester}$

Elemental Analysis: C: 68.11 /67.61, H: 8.90/9.23, S: 8.37/8.90, O: 12.53/12.77, Br: 2.09/0.39 (% calc./found)

Hydrolysis of End-Functionalized Polyelectrolyte Brushes

150 mg (0.43 mmol **SSD**) of **MeN-1-50-D1** were dissolved in 100 ml CH_2Cl_2. 1.71 g (8.60 mmol) trimethylsilyl iodide was added. The reaction mixture was refluxed for 4 h and cooled to room temperature. The solvent was removed by vacuum evaporation. The reaction product was dissolved in 50 ml Milli-Q H_2O and freeze-dried. It was re-dissolved in 100 ml 2 M NaOH. The reaction was stirred for 12 h and then dialyzed versus 10 L Milli-Q water, which was exchanged every 24h, until the conductivity of the water dropped to 0.1 µS after 12 h (membrane pore size

10 000 g/mol, water exchange every day). Freeze-drying yielded the desired polyelectrolyte sodium salt.

^{1}H-NMR (D_2O, 300 MHz, 80°C): 7.8-8.5 H_{meta}, 7.5-6.7 H_{ortho}, 1.4-1.9, 0.9-3.0 $H_{backbone}$
SLS, DLS, GPC-MALLS: see chapter 8

12.2. Light Scattering Methods

The static and dynamic light scattering measurements were performed on a light scattering line with an ALV 5000 correlator (ALV, Langen), an ALV-SP81 goniometer, an avalanche photodiode and a krypton ion laser (647.1 nm).

The samples vessels were cleaned in dichloromethane/ultrasound and Milli-Q water/ultrasound. Dried samples (vacuum chamber, 10^{-3} mbar) were weighed out (analytic balance, precision 0.01 mg) and dissolved in the specified solvent (HPLC quality for organic solvents or Milli-Q water (Ultrafiltration unit, Millipore, Bedford) with a conductivity of 0.1 µS). In the closed vessel, the solutions were stirred and heated to the solvent's boiling point for 2 h. After cooling to room temperature and stirring over night, the samples were diluted, filtered with a 0.2 µm Millex™ cellulose membrane filter (Millipore, Bedford) into dust free light scattering cells (∅ 20 mm, Hellmanex), which were cleaned with an acetone fountain (according to a procedure by Thurmont[207]) and measured. By measuring UV absorption spectra and gravimetrical analysis, the sample amount lost during filtration was determined and corrected for the data analysis. For Zimm plots, samples were diluted in one light scattering cell to obtain different concentrations. Static light scattering measurements were performed from 30° to 150° in 5° steps, dynamic light scattering was measured from 30° to 150° in intervals of 20°.

12.3. Small Angle Neutron Scattering (SANS)

The dried samples (vacuum chamber, 10^{-3} mbar) were weighed out (analytic balance, precision 0.01 mg) and dissolved in the specified deuterated solvent. In the closed vessel, the solutions were stirred and heated to the solvent's boiling point for 2 h. After cooling to room temperature and stirring over night, the samples were filtered with a 0.2 µm Millex™ cellulose membrane filter (Millipore, Bedford) into SANS cells and measured. By measuring UV absorption spectra and gravimetrical analysis, the sample amount lost during filtration was determined and corrected for the data analysis. The samples were measured by F. Gröhn and K. Klein at the Paul-Scherrer-Institut, Villigen, Switzerland. Detector-sample distances of 2 m, 6 m and 18 m were used.

12.4. Gel Permeation Chromatography (GPC) and GPC-MALLS

GPC measuring units with a Waters-515 pump, Waters autosampler, column oven, column set (precolumn, two GPC columns as indicated below), Soma S 3702 UV detector (GPC) or Wyatt Dawn Eos detector (MALLS), ERC RI-101 detector and PSS GPC software were used. The column material and the measurement conditions were adjusted to the specific analytical problem. Typically, the following parameters were used:

- THF: room temperature, SDV column (PSS, Mainz), flow rate 1mL/min
- DMF: T =60-80°C, GRAL column (PSS, Mainz), flow rate 1mL/min
- Water: 60°C, 0.1 g/L $NaNO_3$, TSK column (TOSOH, Japan), flow rate 0.5-1 ml/min

The samples were weighed out (analytic balance, precision 0.01 mg) in the specified solvent and dissolved while stirring. The aqueous samples were filtered with 0.45 µm Millex™ Celluloseester membrane filters (Millipore, Bedford) before injection, the samples in organic solvent were filtered with a 0.45 µm Durapore™ membrane filter (Millipore, Bedford).

12.5. Measurement of the Refractive Index Increment

The refractive index increment was measured by C. Rosenauer on a Michelson scanning interferometer[208].

12.6. Analytical Ultracentrifugation (AUC)

The samples were measured by A. Völkel, Golm with an Optima XL-I analytical ultracentrifuge (Beckman-Coulter, Palo Alto) with online Rayleigh interference and scanning UV-VIS absorption optic. Concentrations of 1 g/L were used. Sedimentation occurred below 60 000 rpm.

12.7. Transmission Electron Microscopy

Samples were measured on a Zeiss EM902, LEO EM 912 with 1k CCD camera or FEI Tecnai F20 with 4k CCD camera (cryo TEM samples). Samples were prepared with one of the following methods as specified above:

- Coal film: thin coal films were prepared by thermal evaporation of coal in high vacuum (10^{-6} mbar) onto glass substrates. The films were immediately floated off on a water surface and collected on 300 mesh square copper grids. The sample solution was applied by drop-casting. The surplus solution was removed with a filter paper. The grids were allowed to dry at ambient conditions.

- Trehalose matrix: 20 µL sample solution (0.01 g/L to 1 g/L) was placed on a freshly opened piece of parafilm. 20 µL trehalose solution (1 w% in MQ-H_2O) were placed next to the sample drop. For stained samples, 10µL uranyl acetate (4 w% in MQ-H_2O) or 10 µL cesium chloride (0.1 g/L in MQ-H_2O) were added to the sample drop. The sample drop was mixed with the trehalose drop with an Eppendorff pipette and put onto a copper grid (10-25 µm round holes). Samples were extremely sensitive and imaged immediately after preparation and drying for ~ 15 min.
- Tungsten-tantalum coating: on a thin coal film on a mica substrate (prepared by electron beam evaporation, Balzers evaporation equipment), sample solutions (10^{-3} g/L to 1 g/L) were applied by spin-coating. The samples were shaded at an angle of ~ 30° with an electron beam evaporated tungsten-tantalum layer. The coal film was floated off on a water surface and collected on 300 mesh square copper grids. The films were allowed to dry at ambient conditions.
- Cryo TEM: Cryo TEM samples were prepared and imaged by Dr. I. Lieberwirth by freezing of the aqueous solution in liquid propane with a Vitrobot preparation unit on holey carbon films.

12.8. Scanning Electron Microscopy (SEM)

All images were measured by G. Glasser on a LEO Gemini 1530. Samples were prepared by spin-coating of the polymer solution on a mica substrate.

12.9. Atomic Force Microscopy (AFM)

All AFM images were measured on a NanoScope IIIa (Veeco Inc., Santa Barbara) using Nanoscope Software V. 5.12r. An E scanner with a scan size of 12 µm x 12 µm was used. Most images were recorded in the tapping mode™ with Olympus OMCL-AC160TN-W2 cantilevers. The “supercantilever” used was a DP15 (MikroMasch, Talin) with a force constant of 20-75 N/m. Sample solutions (10^{-7} g/L to 1 g/L) were spin-coated on freshly cleaved mica surfaces (1000-2000 rpm, 60-120 sec).

12.10. MALDI-TOF Mass Spectrometry

MALDI-TOF mass spectra were measured by S. Türk and A. Rohanipour on a Bruker Time-of-flight Reflex III mass spectrometer. The matix used was dithranol. Ag was added to uncharged samples. Matrix, sample and cationizing agent were mixed by suspension in THF and applied onto a sample grid.

12.11. ^{1}H-NMR Measurements in Solution

All ^{1}H-NMR solution spectra were measured by Petra Kindervater on a Bruker 300 MHz Avance NMR Spectrometer. The samples (1-100 mg) were dissolved in the specified deuterated solvent (0.6 mL) and put into NMR tubes with 5 mm diameter. The samples were measured at room temperature unless otherwise specified.

12.12. ^{1}H-NMR Measurements (Solid State)

All ^{1}H-NMR solid state spectra were measured by Dr. Ingo Schnell on a Bruker 500 MHz Avance NMR Spectrometer. Sample mixtures for the kinetics series were prepared under argon atmosphere and filled into a TiO_2 rotor with 2 mm diameter. Samples were measured at 45-75°C.

12.13. Elemental Analysis

Elemental analyses were measured by Analytische Laboratorien Prof. Dr. H. Malissa und G. Reuter GmbH, Lindlar.

12.14. Chemicals

All chemicals used, unless otherwise indicated, were purchased from Fluka, Acros or Aldrich in p.a. quality (reagents) or HPLC quality (solvents) and used as received.

13. References

1. L. Lehninger, D. Nelson, M. M. Cox, *Principles of Biochemistry*, Worth Publishers, New York, **1993**
2. B. Alberts, *Molecular Biology of the Cell*, Francis & Tailor, New York, **2002**
3. J. M. G. Cowie, *Chemie und Physik der synthetischen Polymeren*, Vieweg Verlag, Braunschweig, **1997**
4. M. Sawamoto, M. Kamigaito, *Living Radical Polymerization*, in A. D. Schlüter [Ed.], *Polymer Synthesis*, Wiley-WCH, Weinheim, **1999**
5. V. Percec, D. A. Tirrell, *J. Polym. Sci., Polym. Chem.*, **2000**, *38*, 1705
6. K. M. Georges, R. P. N. Veregin, P. M. Kazmaier, G. K. Hamer, *Macromolecules*, **1993**, *26*, 2987
7. J. Hawker, A. W. Bosnan, E. Harth, *Chem. Rev.*, **2001**, *101*, 3661
8. J. Hawker, *Nitroxide-Mediated Living Radical Polymerizations*, in K. Matyjaszewski, T. Davis [Ed.], *Handbook of Radical Polymerizations*, Wiley-Interscience, New York, **2002**
9. P. Curran, *Synthesis*, **1988**, 489
10. K. Matyjaszewski, T. Davis, *Handbook of Radical Polymerizations*, Wiley-Interscience, New York, **2002**
11. M. Kato, M. Kamigaito, M. Sawamoto, T. Higashimura *Macromolecules*, **1995**, *28*, 1721 J. S. Wang, K. Matyjaszewski, *J. Am. Chem. Soc.*, **1995**, *117*, 5614
12. adapted for styrene polymerization from: K. Matyjaszewski, *Fundamentals of Atom Transfer Radical Polymerization*, in K. Matyjaszewski, T. Davis [Ed.], *Handbook of Radical Polymerizations*, Wiley-Interscience, New York, **2002**
13. J. Ciefari, Y. K. Chong, F. Ercole, J. Krstina, J. Jeffery, T. P.T. Le, R. T. A. Mayadunne, G. F. Meijs, C. L. Moad, G. Moad, E. Rizzardo, S. H. Thang, *Macromol. Symp.*, **1999**, *143*, 291
14. T. P. Le, G. Moad, E. Rizzardo, S. H. Thang, *Int. Patent Appl.* WO 9801478
15. G. Moad, R. T. A. Mayadunne, E. Rizzardo, M. Skidmoore, S. H. Thang, *Macromol. Symp:*, **2003**, *192*, 1
16. B. Y. K. Chong, T. P. T. Le, G. Moad, E. Rizzardo, S. H. Thang, *Macromolecules*, **1999**, *32*, 2071
17. M. Szwarc, *Nature*, **1956**, *178*, 1168
18. H. Morawetz, *Polymers: the Origins and Growth of a Science*, Wiley, New York, **1985**
19. M. Szwarc, M. Levy, R. Milkovich, *J. Am. Chem. Soc.*, **1956**, *78*, 2656
20. M. D. Lechner, K. Gehrke, E.H. Nordmeier, *Makromolekulare Chemie*, Birkhäuser-Verlag, Basel, **1996**
21. M. Szwarc, *Adv. Polym. Sci.*, **1983**, *49*, 108
22. Baskaran, *Prog. Polym. Sci.*, **2003**, *28*, 521
23. P. Teyssié, P. Bayard, R. Jeromé, S. K. Varshney, J.-S. Wang, *Makromol. Chem. Macromol. Symp.*, **1995**, *98*, 171-183
24. B. Bingöl, *personal communication*
25. S. J. Whicher, J. L. Brash, *J. Polym. Sci., Polym. Chem.*, **1981**, *19*, 1995
26. H. Cramail, A. Deffieux, *Cationic Polymerization*, in A. D. Schlüter [Ed.], *Polymer Synthesis*, Wiley-WCH, Weinheim, **1999**
27. A. Suzuki, *Chem. Commun.*, **2005**, 4759
28. O. Aliprantis, J. W. Canary, *J. Am. Chem. Soc.*, **1994**, *116*, 6985
29. H. G. Kuivila, J.F. Reuwer, J. A. Margravite, *Can. J. Chem.*, **1963**, *41*, 3081
30. W. Heitz, *Macromol. Chem. Phys.*, **1997**, *198*, 1531
31. L. Chenard, *J. Org. Chem.*, **1995**, *60*, 12
32. A. D. Schlüter, *J. Polym. Sci., Polym. Chem.*, **2001**, *39*, 1533

33. P. Lindner, T. Zemb, *Neutrons, x-rays and light: Scattering Methods Applied to Soft Condensed Matter*, North-Holland, **2002**
34. Gröhn, *Scattering Methods for the Characterization of Polymers and Nanostructures*, University of Mainz, **2003**
35. J. Hunt, S. R. Holding [Ed.], *Size exclusion chromatography*, Blackie & Son Ltd, Glasgow, **1989**
36. W. W. Yau, J. J. Kirkland, D. D. Bly, *Modern Size-Exclusion Liquid Chromatography*, Wiley, New York, **1979**
37. Drawing taken from P. Wittmeyer, *Diplomarbeit,* Universität Darmstadt*,* **2000**
38. Z. Grubisic, P. Rempp, and H. Benoit, *J. Polym. Sci. B: Polym. Lett.*, **1967**, *5*, 753
39. M. Wintermantel, M. Schmidt, A. Becker, R. Dorn, A. Kühn, R. Lösch, *Nachr. Chem . Technol. Lab.*, **1992**, *40*, 331
40. P. J. Wyatt, *Anal. Chim. Acta.*, **1993**, *272*, 1
41. W. W. Yau, *Chemtracts, Macromol. Lab.*, **1992**, *40*, 331
42. W. Radke, A.H.E. Müller, *Macromolecules*, **2005**, *38*, 3949
43. M. Gerle, K. Fischer, S. Roos, A. H. E. Müller, M. Schmidt, S. S. Sheiko, S. Prokhorova, M. Möller, *Macromolecules*, **1999**, *32*, 2629-2637
44. M. D. Lechner, K. Gehrke, E. H. Nordmeier, *Makromolekulare Chemie*, Birkhäuser Verlag, Basel, **1996**
45. T. M. Schuster, T. M. Laue, *Modern Analytical Ultracentrifugation*, Birkhäuser, Boston, **1994**
46. S. E. Harding, A. J. Rowe, J. C. Horton [Ed.], *Analytical Ultracentrifugation in Biochemistry and Polymer Science*, The Royal Society of Chemistry, Cambridge, **1992**
47. A. Putnis, *Introduction to Mineral Science*, Cambridge University Press, **1993**
48. http://cryoem.berkeley.edu/~nieder/em_for_dummies/background.html
49. Digital Instruments SPM Training Notebook, Version 3.0, DI, **2000**
50. C. Binning, H. Rohrer, Ch. Gerber, E. Weibel, *Phys. Rev. Lett.*, **1982**, *49*, 57
51. T. R. Albrecht, M. M. Dovek, C. A. Lang, P. Gruetter, C. R. Quate, S. N. J. Kuan, C. W. Frank, R. F. W. Pease, *J. Appl. Phys.*, **1988**, *64*, 117
52. S. N. Magonov, in R. A. Meyers [Ed.], *Encyclopedia of Analytical Chemistry*, John Wiley & Sons Ltd., Chichester, **2000**
53. http://www3.physik.uni-greifswald.de/method/afm/eafm.htm
54. Digital Instruments User Manual, Veeco, 2000
55. G. Montaudo, M. S. Montaudo, C. Pulgisi, F. Samperti, *Rapid Commun. Mass Spectrom.*, **1995**, *9*, 453
56. A. Zhang, L. Shu, Z. Bo, A. D. Schlüter, *Macromol. Chem. Phys.*, **2003**, *204*, 328
57. M. Zhang, A. H. E. Müller, *J. Polym. Sci. Part A: Polym. Chem.*, **2005**, *43*, 3461
58. R. C. Advincula, W. J. Brittain, K. C. Caster, J. Rühe, *Polymer Brushes*, Wiley-VCH, Weinheim, **2004**
59. A. Wittemann, M. Drechsler, Y. Talmon, M. Ballauff, *J. Am. Chem. Soc.*, **2005**, *127*, 9688
60. M. Wintermantel, M. Gerle, K. Fischer, M. Schmidt, I. Wataoka, H. Urakawa, K. Kajiwara, Y. Tsukahara, *Macromolecules*, **1996**, *29*, 978
61. B. Zhang, *Dissertation*, Universität Mainz, **2004**
62. C. Wahnes, *Dissertation*, Universität Mainz, **2005**
63. M. Wintermantel, M. Schmidt, Y. Tsukahara, K. Kajiwara, S. Kohjiya, *Macromol. Rapid Commun*, **1994**, *15*, 279
64. M. Zhang, T. Breiner, H. Mori, A. H. E. Müller, *Polymer*, **2003**, *44*, 1449
65. K. Fischer, M. Gerle, M. Schmidt, *Proc. ACS, PMSE Anaheim*, **1999**, *30*, 133
66. K. Fischer, M. Schmidt, *Macromol. Rapid Commun.*, **2001**, *22*, 787
67. S. S. Sheiko, M. Gerle, K. Fischer, M. Schmidt, M. Möller, *Langmuir*, **1997**, *13*, 5368

68. M. Wintermantel, K. Fischer, M. Gerle, R. Ries, M. Schmidt, K. Kajiwara, H. Urakawa, I. Wataoka, *Angew. Chem. Int. Ed.,* **1995**, *34*, 1472
69. Y. Tsukahara, Y. Ohta, K. Senoo, *Polymer*, **2000**, *11*, 210
70. Y. Tsukahara, J. Inoue, Y. Ohta, S. Kohiya, *Polymer*, **1994**, *35*, 5785
71. S. S. Sheiko, M. Gerle, M. Möller, *Langmuir*, **1997**, *13*, 5368
72. S. Namba, Y. Tsukahara, K. Kaeriyama, K. Okamoto, M. Takahashi, *Polymer*, **2000**, *41*, 5165
73. Y. Tsukahara, S. Namba, J. Isawa, Y. Nakano, K. Kaeriyama, M. Takahashi, *Macromolecules*, **2001**, *34*, 2624
74. A. Deffieux, M. Schappacher, *Macromolecules*, **1999**, *32*, 1797
75. M. Schappacher, C. Billaud, C. Paulo, A. Deffieux, *Macrom. Chem. Phys.*, **1999**, *200*, 1377
76. M. Schappacher, J. Bernard, A. Deffieux, *Macrom. Chem. Phys.*, **2003**, *204*, 762
77. W. Radke, A. H. E. Müller, *Macromolecules*, **2005**, *38*, 3949
78. K. L. Beers, S. G. Gaynor, K. Matyjaszewski, S. S. Sheiko, M. Möller, *Macromolecules*, **1998**, *31*, 9413
79. H. G. Börner, K. Beers, K. Matyjaszewski, S. S. Sheiko, M Möller, *Macromolecules*, **2001**, *34*, 4375
80. G. Cheng. A. Böker, M. Zhang. G. Krausch, A. H. E. Müller, *Macromolecules*, **2001**, *34*, 6683
81. M. Zhang, T. Breitner, H. Mori, A. H. E. Müller, *Polymer*, **2003**, *44*, 1449
82. B. Zhang, K. Fischer, M. Schmidt, *Macromol. Chem. Phys.*, **2005**, *206*, 157
83. S. Muthukrishnan, M. Zhang, M. Burkhardt, M. Drechsler, H. Mori, A. H. E. Müller, *Macromolecules*, **2005**, *38*, 7926
84. D. Neugebauer, B. S. Sumerlin, K. Matyjaszewski, B. Goodhart, S. S. Sheiko, *Polymer*, **2004**, *45*, 8173
85. Y. Tsukahara, K. Mizuno, A. Segawa, Y. Yamashita *Macromolecules*, **1989**, *22*, 154
86. Y. Tsukahara, K. Tsutsumi, Y. Yamashita, S. Shimada, *Macromolecules*, **1990**, *23*, 5201
87. M. Wintermantel, M. Gerle, K. Fischer, M. Schmidt, I. Wataoka, H. Urakawa, K. Kajiwara, Y. Tsukahara, *Macromolecules*; **1996**, *29*, 978
88. M. Wintermantel, M. Schmidt, Y. Tsukahara, K. Kajiwara, S. Kohjiya, *Macromol. Rapid Commun*, **1994**,*15*, 279
89. P. Dziezko, S. S. Sheiko, K. Fischer, M. Schmidt, M. Möller, *Angew. Chem. Int. Ed.*, **1997**, *36*, 2812
90. M. Gerle, K. Fischer, S. Roos, A. H. E. Müller, M. Schmidt, S. S. Sheiko, S. Prokhorova, M. Möller, *Macromolecules*, **1999**, *32*, 2629
91. Y. Tsukahara, J. Inoue, Y. Ohta, S. Kohjiya, Y. Okamoto, *Polymer J.*, **1994**, *26*, 1013

    D. Pantazis, I. Chalari, N. Hadjichristidis, *Macromolecules*, **2003**, *36*, 3783
92. V. Heroguez, Y. Gnanou, M. Fontanille, *Macromolecules*, **1997**, *30*, 4791
93. W. J. Feast, V. C. Gibson, A. F. Johnson, E. Khosravi, A. M. Mohsin, *Polymer*, **1994**, *35*, 3542
94. R. Djalali, S. Y. Li, M. Schmidt, *Macromolecules*; **2002**, *35*, 4282
95. K. Ishizu, K. Tsubaki, S. Uchida, *Macromolecules*; **2002**, *35*, 10193
96. M. Zhang, M. Drechsler, A. H. E. Müller, *Chem. Mater.*, **2004**, *16*, 537
97. M. Zhang, C. Estournes, W. Biertsch, A. H. E. Müller, *Adv. Funct. Mater.*, **2004**, *14*, 871
98. J. Widmer, *Dissertation*, Universität Mainz, **2004**
99. C. Li, N. Gunari, K. Fischer, A. Janshoff, M. Schmidt., *Angew. Chem. Int. Ed.*, **2004**, *1101*
100. M. O. Gallamov, B. Tartsch, A. R. Khokhlov, S. S. Sheiko, H. G. Börner, K. Matyjaszewski, M. Möller, *Macromol. Rapid Commun*, **2004**, *25*, 1703
101. C. Wahnes, *Dissertation*, Universität Mainz, **2005**

102. C. Böttcher, B. Schade, C. Ecker, J. P. Rabe, L. Shu, A. D. Schlüter, *Chem. Eur. J.*, **2005**, *11*, 2923
103. M. Groß, *Diplomarbeit*, Universität Mainz, **2003**
104. M. Schwägler, *Disseration*, Universität Mainz, *in progress*
105. M. Mandel: *Polyelectrolytes*, in: F.H. Mark, N. M. Bikales, C. G. Overberger, G. Menges, *Encyclopedia of Polymer Science and Engineering*, Wiley, New York, **1988**, *11*, 739
106. G. S. Manning, *Ann. Rev. Phys. Chem.*, **1967**, *1*, 56
107. F. G. Donnan, *Z. Elektochem.*, **1911**, *49*, 1049
108. A. Vrij, T. Overbeek, *J. Colloid Sci.*, **1962**, *17*, 570
109. F. Gröhn, M. Antonietti, *Macromolecules*, **2000**, *33*, 5938
110. S. Förster, M. Schmidt, *Adv. Polym. Sci*, **1995**, *120*, 50
111. S. Förster, *Dissertation*, Universität Mainz, **1992**
112. S. Förster, M. Schmidt, M. Antonietti, *Polymer*, **1990**, *31*, 781
113. M. Beer, M. Schmidt, M. Muthukumar, *Macromolecules*, **1997**, *30*, 8375
114. J. Rühe, M. Ballauf, M. Biesalski, P. Dziezok, F. Gröhn, D. Johannsmann, N. Houbenov, N.Hugenberg, R. Konradi, S. Minko, M. Motornov, R. R. Netz, M. Schmidt, C. Seidel, M. Stamm,T. Stephan, D. Usov, H. Zhang, *Adv. Polym. Sci.*, **2004**, *165*, 79
115. P. Dziezok, *Dissertation*, Universität Mainz, **1999**
116. N. Hugenberg, *Dissertation*, Universität Mainz, **2000**
117. D. A. Tomalia, Z. G. Wang, M. Tirrell, **1999**, *Curr. Opin. Colloid Interf. Sci.*, *4*, 3
118. J. M. Lehn, *Polym. Int.*, **2002**, *51*, 825
119. C. F. J. Faul, M. Antonietti, *Adv. Mater.*, **2003**, *15(9)*, 673
120. A. F. Thünemann, D. Ruppelt, C. Burger, K. Müllen, *J. Mater. Chem.*, **2000**, *201*, 31
121. F. Gröhn, *Annual Report of the MPIP*, Mainz, April **2002**
122. A. J. Day, G. D. Prestwich, *J. Biol. Chem.*, **2002**, *277(7)*, 4585
123. http://medweb.uni-muenster.de/institute/pcpb/mitarbeiter/buddeck/research.html
124. L. Ng, A. J. Grodzinsky, P. Patwari, J. Sandy, A. Plaas, C. Ortiz, *J. Struct. Biol.*, **2003**, *143*, 242
125. J. A. Buckwalter, L. C. Rosenberg, *J. Biol. Chem.*, **1982**, *257(16)*, 9830
126. B. P. Toole, *J. Clin. Invest.*, **2000**, *106*, 335
127. C. B. Knudson, W. Knudson, *Semin. Cell. Dev. Biol.*, **2001**, *12*, 69
128. J. D. Kahmann, R. O'Brien, J. M. Werner, D.Heinegård, J. E. Ladbury, I. D. Campbell, A. J. Day*, Structure*, **2000**, *8*, 763
129. C. D. Blundell, J. D. Kahmann, A. Perczel, D. J: Mahoney, M. R. Cordell, P. Teriete, I.D. Campbell, J. A. Day, In: J. F. Kennedy, *Hyaluronan*, Woodhead Publishing Ltd., Cambridge, **2001**
130. Z. C. Li, Y. Z. Liang, G. Q. Chen, F. M. Li, *Macromol. Rapid Commun*, **2000**, *21*, 375
131. Y. Z. Liang, Z. C. Li, G. Q. Chen, F. M. Li, *Polymer Int.*, **1999**, *48*, 739
132. M. Ejaz, K. Ohno, Y. Tsujii, T. Fukada, *Macromolecules*, **2000**, *33*, 2870
133. S. Muthukrishnan, G. Jutz, X. André, H. Mori, A. H. E. Müller, *Macromolecules*, **2005**, *38*, 9
134. S. Muthukrishnan, H. Mori, A. H. E. Müller, *Macromolecules*, **2005**, *38*, 3108
135. Y. Tran, P. Auroy, *J. Am. Chem. Soc.*, **2001**, *123(16)*, 3644
136. Y. Mir, Pl Auroy, L. Auvray, *Phys. Rev. Lett.*, **1995**, *75*, 2863
137. Y. Tran, P. Auroy, L.-T. Lee, M. Stamm, *Physical Review E*, **1999**, *60*, 6984
138. Y. Tran, P. Auroy, L.-T. Lee, *Macromolecules*, **1999**, *32*, 8952
139. N. Hugenberg, *Dissertation*, Universität Mainz, **2000**
140. J. Ding, C. Chuy, S. Holdcroft, *Macromolecules*, **2002**, *35*, 1348
141. S. J. Whicher, J. L. Brash, *J. Polym. Sci., Polym. Chem.*, **1981**, *19*, 1995
142. B. Keoshkerian, M. K. Georges, D. Boils-Boissier, *Macromolecules*, **1995**, *28*, 6381
143. M. Nowakowska, S. Zapotoczny, A. Karewicz, *Macromolecules*, **2000**, *33*, 7345

144. M. Bouix, J. Gouzi, B. Charleux, J.-P. Vairon, P. Guinot., *Macromol. Rapid Commun.*, **1998**, *19*, 209
145. J.-S. Wang, K. Matyjaszewski, *Macromolecules*, **1995**, *28*, 7901
146. X.-S. Wang, R. A. Jackson, S. P. Armes, *Macromolecules*, **2000**, *33*, 255
147. S. Coca, C. B. Janieszek, K. L. Beers, K. Matyjaszewski, *J. Polym. Sci., Polym. Chem.*, **1998**, *36*, 1417
148. X.-S. Wang, S. F. Lascelles, R. A. Jackson, S. P. Armes, *Chem. Commun.*, **1999**, *18*, 1817
149. A. B. Lowe, C. L. MacCormick, *Austr. J. Chem.*, **2002**, *55*, 367
150. J. Chiefari, Y. K. Chong, F. Ercole, J. Krstina, J. Jeffery, T. P. T. Le, R. T. A. Mayadunne, G. F. Meijs, C. L. Moad, G. Moad, E. Rizzardo, S. H. Thang, *Macromolecules*, **1998**, *31*, 5559
151. G. Woeste, *Dissertation*, Universität Mainz, **1993**
152. B. Masař, M. Janata, P. Vlček, L. Toman, D. Kurková, *J. Appl. Polym. Sci.* **2002**, *86*, 2930
153. K. L. Beers, S. G. Gaynor, K. Matyjaszewski, S. S. Sheiko, M. Möller, *Macromolecules*, **1998**, *31*, 9413
154. G. Cheng, A. Böker, M. Zhang, G. Krausch, A. H. E. Müller, *Macromolecules*, **2001**, *34*, 6888
155. B. Masař, M. Janata, P. Vlček, L. Toman, D. Kurková, *J. Appl. Polym. Sci.*; **2002**; *86*; 2930
156. S. H. Hong, T. Pakula, K. Matyjaszewski, *Macromol. Chem. Phys.*, **2001**, *202*, 3392
157. U. Wendler, J. Bohrisch, W. Jaeger, G. Rother, H. Dautzenberg, *Macromol. Rapid Commun.*, **1998**,*19*, 185
158. P. Moschogianni, S. Pispas, N. Hadjichristidis, *J. Polym. Sci. Polym. Chem.,* **2001**, *39*, 650
159. K. Ishizu, H. Kakinuma, *J. Polym. Sci. Polym. Chem.*, **2005**, *43*, 63
160. D. R. Lide, *Handbook of Chemistry and Physics*, CRC Press, New York, **1995**
161. M. E. Honigfort, S. Liou, J. Rademacher, D. Malaba, T. Bosanac, C. S. Wilcox, W. J. Brittain, *ACS Symposium Series*, **2003**, *854*, 250
162. G. Woeste, *Dissertation*, Universität Mainz, **1993**
163. W. Radke, A. H. E. Müller, *Macromolecules,* **2005**, *38*, 3949,
164. M. Gerle, *Dissertation*, Universität Mainz, **1998**
165. C. Wahnes, *Dissertation*, Universität Mainz, **2005**
166. H. Okamura, Y. Takatori, M. Tsunooka, M Shirai, *Polymer*, **2002**, *43*, 3155
167. P. Kratchovil, *Classical light scattering from polymer solutions*, Elsevier, Amsterdam, **1987**, 145
168. W. Burchard in W. Brown [Ed.], *Light Scattering, Principles and Development*, Claredon Press, Oxford, **1996**
169. S. S. Sheiko, S. A. Prokhorova, K. L. Beers, K. Matyjaszewski, I.I. Potemkin, A. R. Khokhlov, M. Moeller, *Macromolecules*; **2001**; *34*; 8354
170. B. Zhang, *Dissertation*, Universität Mainz, **2004**, 60
171. J. R. Harris, D. Scheffler, *Micron*, **2002**, *33*, 461
172. F. Green, *The Sigma-Aldrich Handbook of stains, dyes & indicatiors*, Aldrich Chemical Company, Milwaukee, **1991**, 263
173. K. Matsumoto, H. Hasegawa, H. Matsuoka, Hideki, *Tetrahedron*, **2004**, *60*, 7197
174. A. Laleh, R. Ranson, J. G. Tillett, *J. Chem. Soc., Perkin Trans. 2*, **1980**, *4*, 610
175. E. J. Corey, G. H. Posner, R. F. Atkinson, A. K. Wingard, D. J. Halloran, D. M. Radzik, J.J. Nash, *J. Org. Chem.*, **1989**, *54*, 389
176. K. Y. Baek, N. P. Balsara, *PMSE Preprints*, **2005**, *92*, 7
177. G. Wittig, U. Schöllkopf, *Chem. Ber.*, **1954**, *87*, 1318
178. R. Quirk, *British Polymer J.*, **1990**, *23*, 47
179. K. Ito, *Prog. Polym. Sci.*, **1998**, *23*, 581
180. M. W. Thompson, F. A. Waite, BP 1,096,912, **1967**

181. G. O. Schulz, R. Milkovich, *J. Polym. Scil, Polym. Chem. Ed*, **1984**, *22*, 1633
182. M. Wintermantel, S. Schmidt, Y. Tsukahara, K. Kajiwara, S. Kohjiya, *Macromol. Rapid Commun*, **1994**, *15*, 279
183. M. Wintermantel, K. Fischer, M. Gerle, R. Ries, M. Schmidt, K. Kajiwara, H. Urakawa, I. Wataoka, *Angew. Chem. Int. Ed.,* **1995**, *34*, 1472
184. D. Pantazis, I. Chalari, N. Hadjichristidis, *Macromolecules*, **2003**, *36*, 3783
185. I. Cianga, Y. Yagci, *Polymer Bull.*, **2001**, *47*, 17
186. I. Cianga, Y. Yagci, *Europ. Polym. J.*, **2002**, *38*, 695
187. I. Cianga, Y. Hepuzer, Y.Yagci, *Macromol. Symp.*, **2002**, *183*, 145
188. I. Cianga, Y. Hepuzer, Y. Yagci, *Polymer*, **2002**, *43*, 2141
189. S. J. Whicher, J. L. Brash, *J. Polym. Sci., Polym Chem.*, **1981**, *19*, 1995
190. G. Woeste, *Dissertation*, Universität Mainz, **1993**
191. M. Biesalski, J. Rühe, *Macromolecules*, **2003**, *32*, 1222
192. TOSOH, Japan
193. J. Blum, M. Zimmermann, *Tetrahedron*, **1972**, *28*, 275
194. adapted from M. Ranger, D. Rondeau, M. Leclerc, *Macromolecules*, **1997**, *30*, 7668
195. T. .W. Green, P. G. M. Wuts, *Protective Groups in Organic Synthesis*, John Wiley & Sons, New York, **1999**
196. K. Matyjaszewski, T. P. Davis, *Handbook of Radical Polymerization*, Wiley-Interscience, New York, **2002**, *409*
197. X. S. Wang, S. P. Armes, *Macromolecules*, **2000**, *33*, 6640
198. H. Pasch, W. Schrepp (ed.), *MALDI-TOF-Mass Spectrometry of Synthetic Polymers*, Springer Verlag, Berlin, **2003**
199. G. Woeste, *Dissertation*, Universität Mainz, **1993**
200. J. Blum, M. Zimmermann, *Tetrahedron*, **1972**, *28*, 275
201. M. Ranger, D. Rondeau, M. Leclerc, *Macromolecules*, **1997**, *30*, 7686
202. M. Janata, *Reactive & Functional Polymers*, **2001**, *50*, 67
203. D. Uhrig, J. W. Mays, *J. Polym. Sci., Polym. Chem.*, **2005**, *43*, 6179
204. G. Wittig, U. Schöllkopf, *Chem. Ber.*, **1954**, *97*, 1318
205. R. Quirk, *British Polymer J.*, **1990**, *23*, 47
206. D. Uhrig, J. W. Mays, *J. Polym. Sci., Polym. Chem.*, **2005**, *43*, 6179
207. D. Thurmont, *J.Polym. Sci.,* **1952**, *8*, 607
208. A. Becker, W. Köhler, B. Müller, *Ber. Bunsenges. Phys. Chem.*, **1995**, *99*, 600

14. List of Abbreviations

α	polarizability
Γ	relaxation rate
δ	chemical shift (NMR)
δV	volume increment
ΔE	energy loss
ΔG	free enthalpy
Δh	enthalpy per unit volume
ΔH	enthalpy
ΔU	internal energy
ΔS	entropy
ε_0	dielectric constant in vacuo
ε_r	dielectric constant of the solvent
η	viscosity
$[\eta]$	Intrinsic viscosity
λ	radiation wavelength
μ	chemical potential
τ	relaxation time
θ	scattering angle
ρ	density
ρ-*ratio*	R_g/R_h, particle shape specific ratio
Π	osmotic pressure
ϕ_i	volume fraction of component *i*
υ	partial specific volume
ω	angular frequency
a.m.u.	atomic mass units
a.u.	arbitrary units
A_2	second virial coefficient
A_3	third virial coefficient
Ac	CH_2COO
AFM	atomic force microscopy
AIBN	azoisobutyricacid nitrile
ATRA	atom transfer radical addition
ATRP	atom transfer radical polymerization
AUC	analytical ultracentrifugation
bpy	N,N'-bipyridyl
BuLi	butyl lithium
c	concentraton
C	conversion
c_2	concentration of the dissolved species
c_p	polymer concentration
c_s	salt concentration
D	diffusion coefficient
d	intermolecular distance
DBPO	dibenzoyl beroxide
DLS	dynamic light scattering
DMF	N,N'-dimethylformamid
$\frac{\mathrm{d}n}{\mathrm{d}c_2}$	refractive index increment
DNA	deoxyribonucleic acid
dNbpy	4,4'(dinonyl)bipyridine
$\mathrm{d}r/\mathrm{d}t$	sedimentation velocity
DSC	differential scanning calorimetry
e	elementary charge of the electron
E_0	electric field strength
EELS	electron energy loss spectrometry
eq.	equivalent
f	Initiator efficiency
f'	frictional coefficient
F_b	buoyant force
F_c	centrifugal force
F_f	frictional force
FT-IR	fourier-transformed infrared spectroscopy
$g_1(\tau)$	amplitude autocorrelation function
$g_2(\tau)$	intensity autocorrelation function
GPC	gel permeation chromatography (=SEC)
GPC-MALLS	GPC coupled with multi-angle laser light scattering
I	initiator concentration
I_θ	scattering intensity
$I(q,t)$	intensity as a function of scattering vector and time
I_0	initial intensity
IR	Infrared
k	wave vector, $k = 2\pi/\lambda$
K	optical constant
k_B	Boltzmann constant
K_i	equilibrium constant for reaction i
k_p	rate constant of polymerization

L	rod length
l_B	Bjerrum length
l_k	Kuhn statistical segment length
M	monomer concentration
M	molar mass
M_2	particle mass
MALDI-TOF MS	matrix-assisted laser desorption and ionization time-of-flight mass spectrometry
MEK	methylethyl ketone
M_n	number average molecular weight
MS	mass spectrometry
M_w	weight average molecular weight
M_w/M_n	polydispersity index
n	refractive index
N	number of repeat units per polymer chain
N	number of scattering centres
N_A	Avogadro’s number
$n_{Br,calc}$	calculated number of bromine atoms per molecule
n_{calc}	calculated number of repeat units
NMP	nitroxide-mediated polymerization
NMR	nuclear magnetic resonance spectroscopy
p	pressure
$P(q)$	form factor
p^*	reaction conversion
p.a.	pro analysis
PBIEM	2-(2-bromoisobutyryloxy)ethyl methacrylated
p_{ind}	induced dipole moment
PMDETA	N,N,N’,N’,N’’pentametyldiethylentriamine
ppm	parts per million
PS	poly(styrene)
PSSD	poly(styrene sulfonate dodecylic ester)
PSSE	poly(styrene sulfonate ethyl ester)
q	scattering vector
R	universal gas constant
r	radius
R_θ	Rayleigh ratio
r.t.	room temperature
R^2	coefficient of determination
RAFT	reversible addition-fragmentation chain transfer polymerization
R_G	hydrodynamic radius
$R_{g,c}$	Cross-sectional radius of gyration
R_h	Hydrodynamic Radius
RI	refractive index
r_i	rate of reaction i
RNA	ribonucleic acid
ROMP	ring-opening metathesis polymerization
s	sedimentation coefficient
$S(q)$	structure factor
s'	flight path
SANS	small angle neutron scattering
SAXS	small angle x-ray scattering
SEC	size exclusion chromatography (=GPC)
SEM	scanning electron microscopy
SFRP	stable free radical polymerization
SLS	static light scattering
S_N2	bimolecular nucleophilic substitution
SSD	styrene sulfonate dodecylic ester
SSE	styrene sulfonate ethyl ester
t	time
T	temperature
TEM	transmission electron microscopy
TEMPO	2,2,6,6-tetramethyl piperidine-1-oxyl
TEMPO	2,2,6,6-tetramethyl piperidine-1-oxyl
THF	tetrahydrofuran
TLC	thin Layer Chromatography
U	voltage
UV	ultra violet
v	kinetic chain length
V	volume
V_0	interstitial volume
V_1	solvent volume
V_e	elution volume
V_h	hydrodynamic volume
v_i	rate of reaction i
x_n	number average degree of polymerization
z	number of scattering centers per particle
z'	molecule charge

15. Appendix

15.1. Sample Nomenclature

The samples nomenclature is systematic and includes a number for each polymer and its precursors. Thus the sample history can be followed more easily. Examples are given below.

15.1.1. Non-functionalized Brushes

- Macroinitiator precursors:

PpMS3	Poly(p-methylstyrene) No. **3**

- Macroinitiators:

3-30%Br	Poly(p-methylstyrene-co-(p-bromometylstyrene)) from **PpMS3** with 10% of bromination

- Polymer Brushes:

3-30-D1	Poly(styrene sulfonic acid **dodecyl** ester) from **3-30%Br**,No. **1**
11-40-E4	Poly(styrene sulfonic acid **ethyl** ester) from **11-40%Br** No. **4**

- Polyelectrolyte Brushes

3-30-PSS1, X^+	Poly(styrene sulfonate) from **3-30-D1**, saponified with NaOH, **X** as counter ion
3-30-1, X^{++}	Poly(styrene sulfonate) from **3-30-D1**, saponified with Et_3N, **X** as counter ion
3-30-1X	Poly(styrene sulfonate) from **3-30-D1**, saponified with NaOH, Et_3N and HCl, **X** as counter ion
3-30-1, TMS1, X^+	Poly(styrene sulfonate) from **3-30-*D*1**, saponified with TMS-I, **X** as counter ion
11-40-IV, TMS1, X^+	Poly(styrene sulfonate) from **11-40-*E*4**, saponified with TMS-I, **X** as counter ion

15.1.2. Functionalized Brushes

- Macroinitiator precursors:

NN-PpMS1	Poly(p-methylstyrene) No. **1** with end group
Me-NN-PpMS1	Poly(p-methylstyrene) No. **1** with quarternized end group

- Macroinitiators:

Me-NN-PpMS1-Br	Poly(p-methylstyrene-co-(p-bromometylstyrene)) from **Me-NN-PpMS1** with quarternized end group

- Polymer Brush:

Me-NN-50-D1	Poly(styrene sulfonic acid **dodecyl** ester) from **Me-NN-PpMS1-Br**

- Polyelectrolyte Brush

Me-NN-50-I, TMS 1, Na$^+$	Poly(styrene sulfonate) from **Me-NN-50-D1**, saponified with TMS-I, Na as counter ion

15.2. GPC-MALLS Results: Angular Dependence

As supporting information, the $\sin^2(\theta/2)$ dependence of all GPC-MALLS measurements is given in the following section.

15.2.1. Macroinitiators

For the macroinitiators from the **11-series**, a plot of Kc/R_θ versus $\sin^2(\theta/2)$ is given for a representative slice from near the peak maximum (Fig. 15.2.1.1.). A linear dependence is found for all other slices throughout the peak, except at the very edges of the elugram where the accuracy of the RI detector (high molar mass edge) or the MALLS detector (low molar mass edge) is limited. For the other macroinitiator series, the same linear dependence was observed.

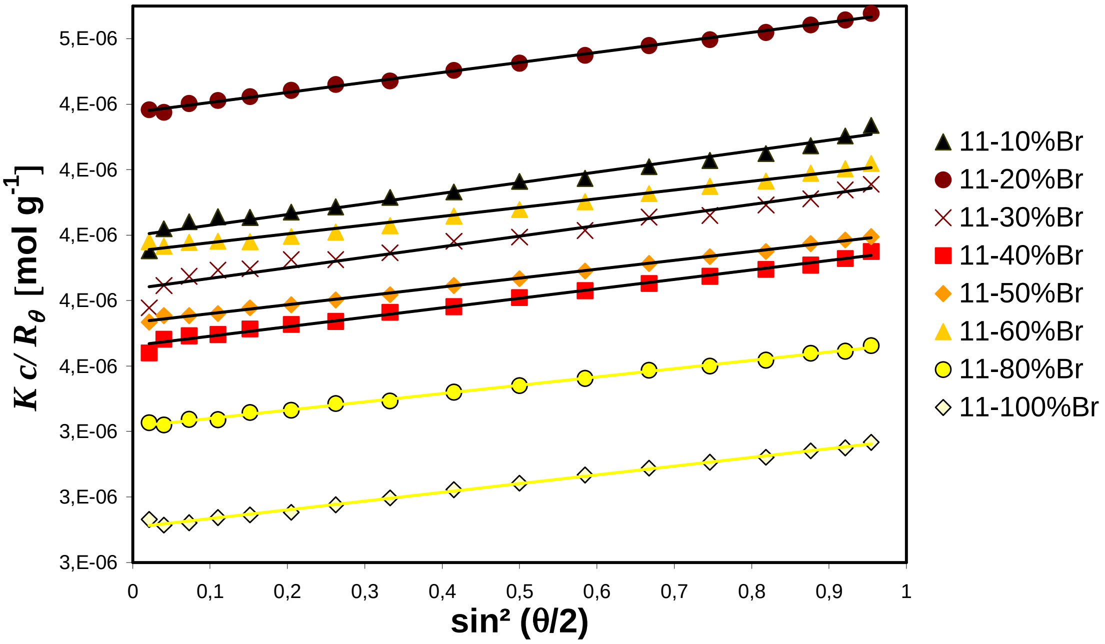

Fig. 15.2.1.1.: $K\,c/R_\theta$ versus q^2 plot for a central slice from the GPC-MALLS elugram for starters from the **11-series**; all measurements in THF

15.2.2. Poly(styrene sulfonate ethyl ester) Brushes

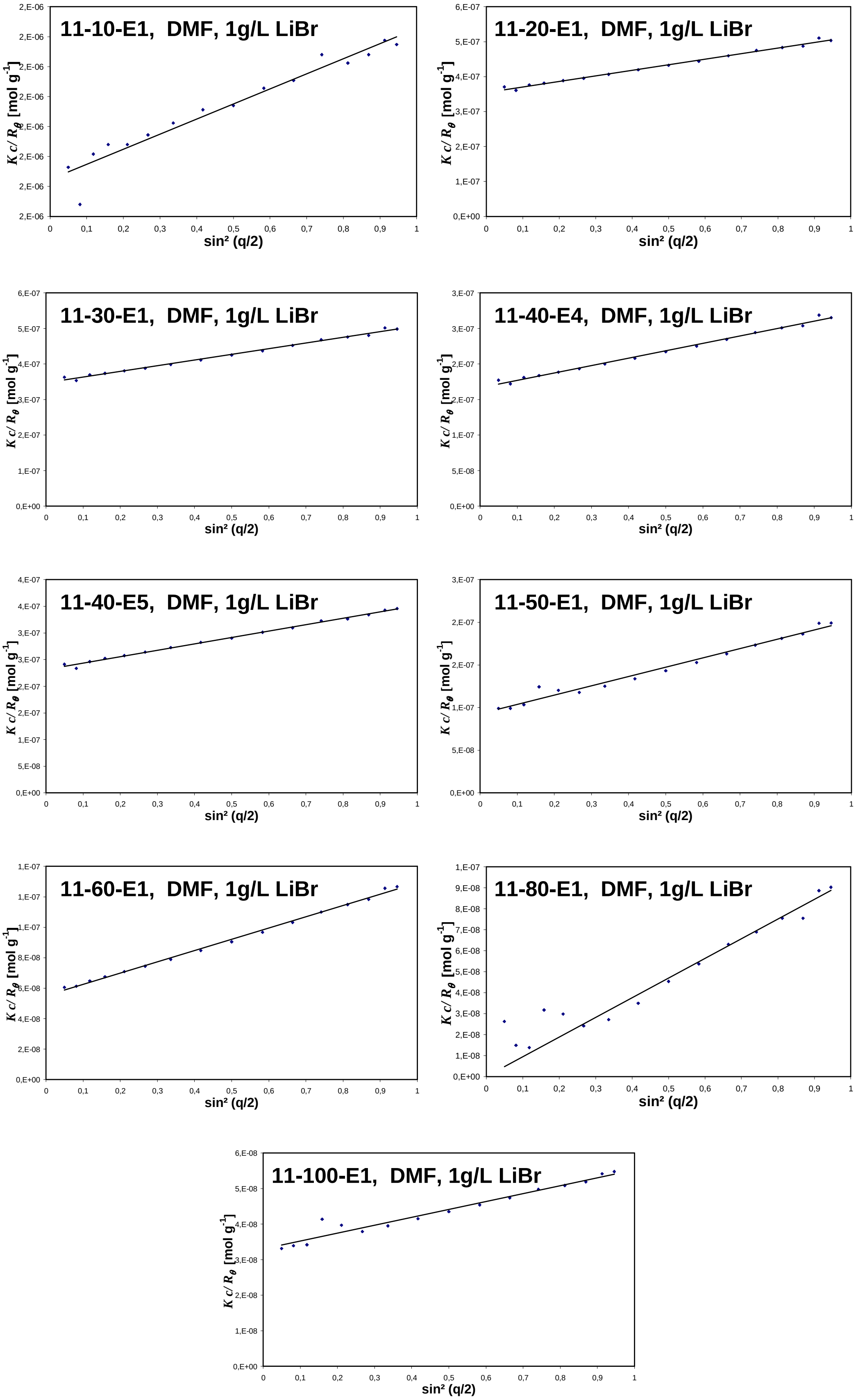

Fig. 15.2.2.1.: $K\,c/R_\theta$ versus q^2 plot for a central slice from the GPC-MALLS elugram for the **PSSE** brushes, all measurements in DMF/1g/L LiBr

For the poly(styrene sulfonate ethyl ester) brushes, the plots of ***Kc/R$_\theta$*** versus ***sin^2 (θ/2)*** (for a representative slice from near the peak maximum) are given in Fig. 15.2.2.1.. A linear dependence is found for all other slices throughout the peak except at the edges of the elugram as discussed in section 15.2.1..

15.2.3. Polyelectrolyte Brushes

For the poly(styrene sulfonate) brushes, the plots of ***Kc/R$_\theta$*** versus ***sin^2 (θ/2)*** (for a representative slice from near the peak maximum) are given in Fig. 15.2.3.1.. A linear dependence is found for most slices throughout the peak except at the edges of the elugram as discussed in section 15.2.1.. As expect for light scattering in aqueous solution, the values deviate more strongly from the regression line as those measured in THF and DMF, yet the linearity and a positive slope are retained.

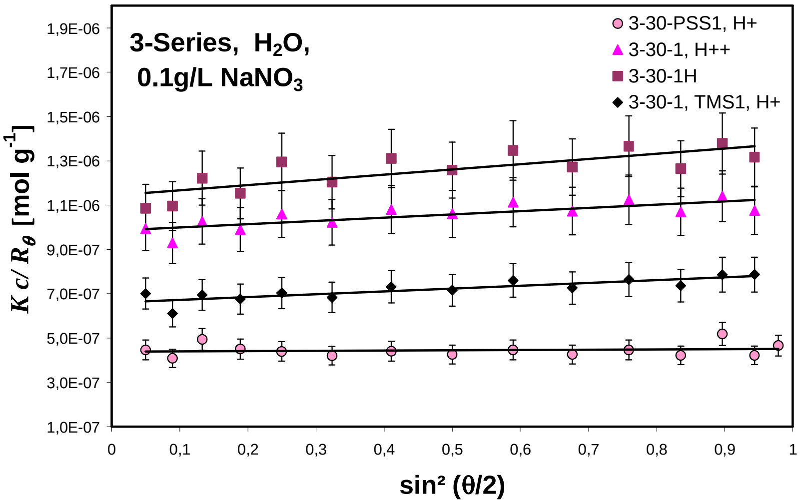

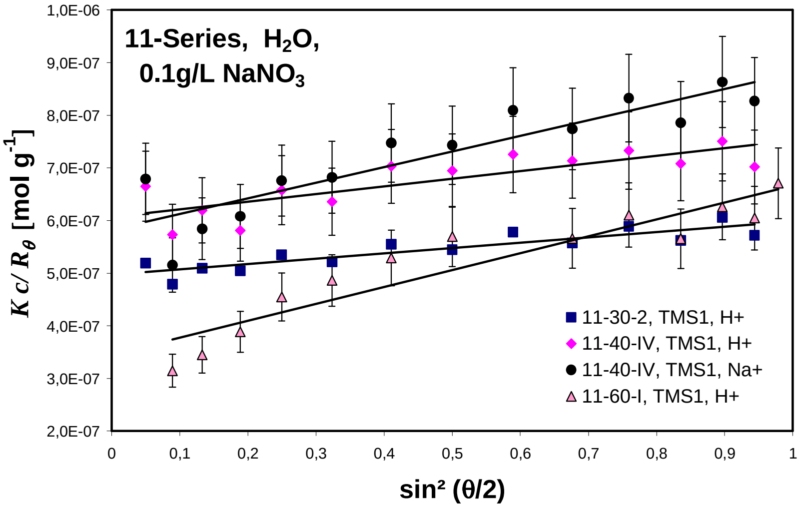

Fig. 15.2.3.1.: ***K c/R$_\theta$*** versus ***q^2*** plot for a central slice from the GPC-MALLS elugram for the **PSS** brushes, all measurements in water/0.1g/L NaNO$_3$